EFFECTS OF EAR-CANAL GEOMETRY AND MIDDLE-EAR PRESSURE ON WIDEBAND ACOUSTIC REFLECTANCE

BY

SARAH R. ROBINSON

DISSERTATION

Submitted in partial fulfillment of the requirements
for the degree of Doctor of Philosophy in Electrical and Computer Engineering
in the Graduate College of the
University of Illinois at Urbana-Champaign, 2017

Urbana, Illinois

Doctoral Committee:

       Professor Jont B. Allen, Chair
       Professor Stephen Boppart
       Professor Michael Oelze
       Professor Susan Voss, Smith College

ABSTRACT

In this thesis, complex wideband acoustic immittance (WAI) measurements of the middle ear are studied. The body of work presented here has three major components: (1) design of a hearing measurement probe and probe tip, (2) extraction of the effects of the residual ear canal (REC) and estimation of the WAI at the tympanic membrane (TM), and (3) analysis of the TM-WAI to characterize middle-ear conditions. Major contributions of this thesis include a pole-zero modeling method to estimate WAI at the TM (Robinson et al., 2013), and analysis of changes in WAI with static negative middle-ear pressure (NMEP) (Robinson et al., 2016). Additionally, an extensive review of the literature and theory underlying WAI measurements is presented, using both time- and frequency-domain analyses.

(1) Measurement probe: The design of a WAI measurement probe and probe tip was conducted with Mimosa Acoustics (Champaign, IL). The inclusion of this work in the present document is primarily limited to the probe-tip project. Two-port network modeling techniques were applied to describe and extract the effects of a variable-area probe tip on WAI measurement. This procedure is effective up to at least 3-5 [kHz], depending on the quality of the probe calibration.

(2) Reflectance factorization: Complex reflectance data may be fit to a pole-zero model, and factored into its all-pass and minimum-phase parts, representing the lossless ear canal and complex middle-ear reflectance respectively (Robinson et al., 2013). This provides an intuitive analysis of reflectance, which is computationally efficient and adaptable to non-ideal (e.g. bandlimited or noisy) data. A detailed comparison is performed between this method and other TM-WAI estimation methods in the literature.

(3) Negative middle-ear pressure (NMEP): Thompson et al. (2015) trained eight subjects with normal middle-ear function to induce consistent NMEPs, quantified by the tympanic peak pressure (TPP), to study the effects of NMEP on distortion-product otoacoustic emissions. WAI data were also collected in that study, and are analyzed in this thesis using the reflectance factorization method (Robinson et al., 2016). For the 8 ears presented here, NMEP has the largest and most significant effect across ears from 0.8 to 1.9 [kHz], resulting in reduced power absorbance by the middle ear and cochlea. On average, NMEP causes a decrease in the power absorbance level for low- to mid-frequencies, and a small increase above about 4 [kHz]. The

effects of NMEP on WAI quantities, including the absorbance level and TM impedance, vary considerably across ears. The complex WAI at the TM and fitted model parameters show NMEP effects consistent with an increased stiffness in the middle ear, which could originate from the TM, tensor tympani, annular ligament, or other middle ear structures.

To female engineers everywhere - may there be more of us in the future.
To Paul Ergler, Ph.D., to whom those three letters meant so much.
To Erik Johnson - I'm so lucky this path brought me to you.

ACKNOWLEDGMENTS

TABLE OF CONTENTS

LIST OF ABBREVIATIONS

AMEP	Ambient Middle Ear Pressure
DP	Distortion Product
ETD	Eustachian Tube Dysfunction
ITE	In-the-ear
LHP	Left Half Plane
ME	Middle Ear
MEPA	Middle Ear Power Assessment
MSE	Mean Squared Error
NMEP	Negative Middle Ear Pressure
OAE	Otoacoustic Emission
OM	Otitis Media
OME	Otitis Media with Effusion
PTA	Pure-tone Audiometry
REC	Residual Ear Canal
RHP	Right Half Plane
RMS	Root Mean Squared
SNHL	Sensorineural Hearing Loss
SSCD	Superior Semicircular Canal Dehiscence
TM	Tympanic Membrane
WAI	Wideband Acoustic Immittance

LIST OF SYMBOLS

Presented here is an incomplete list of symbols used in this thesis, grouped by topic.

A note about subscripts. Immittance quantities (e.g. impedance, admittance, reflectance) without a subscript are typically those measured at the probe location. Subscripts may denote a quantity at another location, such as Z_{tm}, the impedance at the tympanic membrane. Subscripts may also denote separation into parts, for instance, $\Gamma = \Gamma_{mp}\Gamma_{ap}$ where subscripts indicate the minimum-phase and all-pass components, respectively. Other common subscripts include 's' for Thévenin source parameters (e.g. P_s, Z_s) and L for a transmission-line load (e.g. Z_L).

A note about double usage. Every effort has been made to use distinct symbols to represent distinct quantities. In some cases, this is virtually impossible, and one must consider the subscript or context of the quantity in question.

Time-frequency analysis

f	Frequency in [Hz]
$s = \sigma + j\omega$	Complex frequency
σ	Real component of the complex Laplace frequency
t	Time
τ	Group delay
$\omega = 2\pi f$	Frequency in radians (imaginary component of the complex Laplace frequency)

Operators

$\vec{\nabla}$	Gradient
∇^2	Laplacian
$\mathcal{F}, \mathcal{F}^{-1}$	Fourier transform and its inverse
$\Im$	Take imaginary component
$\mathcal{L}, \mathcal{L}^{-1}$	Laplace transform and its inverse

$$\Re \qquad \text{Take real component}$$

Impedance quantities

$b(t) \xrightarrow{\mathcal{L}} B(s)$ Susceptance (imaginary part of the admittance)

$\gamma(t) \xrightarrow{\mathcal{L}} \Gamma(s)$ Reflectance

$g(t) \xrightarrow{\mathcal{L}} G(s)$ Conductance (real part of the admittance)

g_0 Characteristic conductance, 'surge' conductance (real constant)

$r(t) \xrightarrow{\mathcal{L}} R(s)$ Resistance (real part of the impedance)

r_0 Characteristic resistance, 'surge' resistance (real constant)

$r_v(s),\, r_t(s)$ Viscous and thermal boundary layer ratios (unitless)

$x(t) \xrightarrow{\mathcal{L}} X(s)$ Reactance (imaginary part of impedance)

$\mathcal{Y}$ Per-unit-length shunt admittance of a transmission line

$y(t) \xrightarrow{\mathcal{L}} Y(s)$ Admittance

$y_0(s)$ Characteristic admittance

$\mathcal{Z}$ Per-unit-length series impedance of a transmission line

$z(t) \xrightarrow{\mathcal{L}} Z(s)$ Impedance

$\zeta_0(t) \xrightarrow{\mathcal{L}} z_0(s)$ Characteristic impedance

Acoustic quantities

$\kappa(s)$ Wave propagation function

$p(t) \xrightarrow{\mathcal{F}} \mathcal{P}(\omega)$ Pressure displacement ($p_{tot} - P_0$)

$\psi(t) \xrightarrow{\mathcal{F}} \Psi(\omega)$ Average pressure over a volume-slice (forward- and retrograde-propagating solutions given by $\Psi = \Psi^+ + \Psi^-$)

ρ Density displacement ($\rho_{tot} - \rho_0$)

$\sigma(t) \xrightarrow{\mathcal{F}} \mathcal{E}(\omega)$ Condensation

$\theta(t)$ Temperature displacement ($\theta_{tot} - \theta_0$)

$\vec{u}(t) \xrightarrow{\mathcal{F}} \vec{\mathcal{U}}(\omega)$ Particle velocity

$v(t) \xrightarrow{\mathcal{F}} \mathcal{V}(\omega)$ Volume velocity of a volume-slice (forward- and retrograde-propagating solutions given by $\mathcal{V} = \mathcal{V}^+ - \mathcal{V}^-$)

Physical constants

c_0	Speed of sound
c_p	Heat capacity at constant pressure
c_v	Heat capacity at constant volume
η_0	Adiabatic gas constant
κ_0	Thermal conductivity
μ_0	Viscosity ($\mu_0' = \mu_0/\rho_0$, $\mu_0'' = (1/3)\mu_0/\rho_0$)
ν_0	Thermal constant equal to $\kappa_0/(\rho_0 c_v)$
P_0	Equilibrium pressure
Pr	Prandtl number
R_g	Gas constant
ρ_0	Density
θ_0 or T	Equilibrium temperature

Coordinates and spatial descriptors

a	Planar radius
A	Area
d	Planar diameter
L	Length
$\hat{n}$	Unit vector normal to a surface
Π	Perimeter
r, θ, z	Cylindrical coordinates
r, θ, ϕ	Spherical coordinates
S	Surface area
x, y, z	Cartesian coordinates
x_k	Curvilinear coordinates (with differential thicknesses given by $h_k(x_1, \ldots, x_N)$)

CHAPTER 1

INTRODUCTION

The middle ear is a critical part of the auditory pathway. Malfunction of the middle ear can lead to conductive hearing loss (CHL), a problem with acoustical or mechanical transmission of sound to the cochlea. This type of hearing loss is very different from sensorineural hearing loss (SNHL), which is characterized by damage along the auditory pathway to the brain, beginning with the 'hair cell' sensory receptors in the cochlea. Many tests of hearing deliver acoustic stimuli to the cochlea via the ear canal. Therefore, assessment of the middle ear is key to differentiating SNHL from CHL. Furthermore, the accuracy and variability of such hearing tests depend upon delivery of acoustic stimuli to the cochlea. CHL or individual variation in the middle ear can cause the actual level of a stimulus in the cochlea to vary from target. Using acoustic measurements made in the ear canal, sound transmission to the cochlea, including specific dysfunctions of the middle ear, may be modeled. This thesis describes techniques for making and modeling such measurements.

Figure 1.1 shows the outer, middle, and inner ear. Generally, the middle ear may be defined as beginning at the eardrum and ending at the oval window of the cochlea. Pressure waves propagate down the ear canal to the eardrum, or tympanic membrane (TM), and cause it to vibrate. This vibration drives the ossicular chain (malleus, incus, and stapes) via the connection of the malleus to the TM at the umbo. The ossicles function as a mechanical lever system, delivering an amplified pressure wave to the cochlea via the stapes footplate at the oval window. For low frequencies (up to 2-4 [kHz]) the footplate of the stapes moves approximately like a piston (Voss et al., 2000), creating pressure waves in the fluid of the cochlea. All components of this system, including the cochlea itself (Wegel & Lane, 1924), may be modeled as a series of transmission lines. Therefore, we may study this system by measuring its acoustic input impedance as a function of frequency.

1.1   Conductive hearing loss (CHL)

Numerous dysfunctions of the middle-ear system can result in CHL. Research has shown that CHL can have a frequency-specific pattern, depending on its physical cause (Feeney, Grant, & Marryott, 2003; Allen et al., 2005). Middle ear pathologies can affect all age groups and have a variety of causes. Some conditions associated with CHL are given in Table 1.1. Examples of CHL in infant, child and adult populations are given in the following paragraphs. Many audiometric
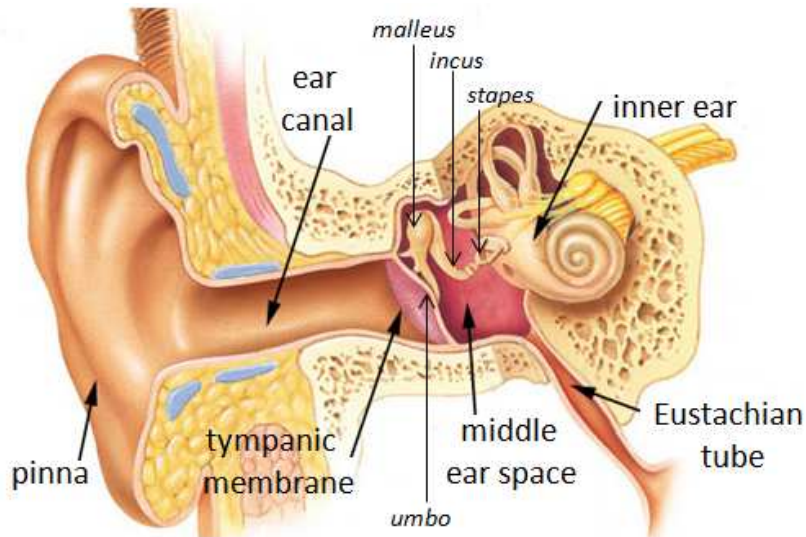
Figure 1.1: The human ear (including outer, middle, and inner ear), which may be modeled as a series of transmission lines. *Image edited from http://www.kidsent.com/pediatricent/ear_infections/index.html*

measurements cannot bypass the middle ear,[1] thus a correct diagnosis of middle-ear function is needed to distinguish SNHL from CHL.

One important example of this need arises in newborn hearing screening programs. Such programs are intended to identify candidates for cochlear implants as early as possible, since implant efficacy diminishes rapidly with age (Fallon et al., 2008). As infants are unable to cooperate with traditional perceptual threshold testing, an objective measure of hearing function is required. Typically an acoustic measurement is taken, which detects stimulus-dependent otoacoustic emissions (OAEs) from the cochlea. These low-level signals are indicative of a healthy cochlea. However, fluids associated with birth (i.e. amniotic fluid) can lead to temporary CHL. This disrupts the round-trip travel of the acoustic stimulus and OAEs, causing false positive detections of hearing loss. Hunter et al. (2010) found that the distortion-product (DP) OAE pass rate increased drastically in the hours following birth, from about 50% within the first 20 hours to about 85% by 36 hours, as transient cases of middle-ear fluid are resolved. Thus, identification of transient CHL cases reduces the need for more extensive audiometric tests, and frees necessary clinical resources for infants with SNHL, or persistent middle-ear infections.

Otitis media (OM), any inflammation of the middle ear, is especially common in infants and children. OM or Eustachian tube dysfunction (ETD) can be accompanied by a fluid effusion or middle-ear pressure (MEP), which can impede the motion of the ossicles and cause temporary CHL. Otitis media with effusion (OME) can cause a hearing loss of 27 [dB] on average, or up to 60 [dB] depending on the fluid level (Bluestone & Klein, 2007). This can become a serious problem, as chronic CHL due to middle-ear effusion can impair or delay speech and language abilities in

---

[1]Some exceptions include bone-conducted stimuli, and measurement of the auditory brainstem response (ABR).

Table 1.1: An incomplete list of middle-ear conditions that can affect sound transmission from the ear canal to the cochlea.

Condition	Description
Bacterial Biofilm	A bacterial colony on the middle-ear side of the eardrum, which hinders the vibration of the TM. It can result from and/or cause chronic recurring otitis media (OM).
Middle-Ear Pressure	Static pressure in the middle ear space, which can occur due to Eustachian tube dysfunction (ETD), or as a mild transient condition in normal middle ears. Negative pressure (NMEP) is more common than positive (PMEP).
Ossicular Discontinuity	Partial or complete separation of the ossicle joints, which most commonly occurs at the incudo-stapedial joint.
Otitis Media (OM)	Any inflammation of the middle ear. When accompanied by fluid in the middle-ear space, it is OM with effusion (OME).
Otosclerosis	Abnormal bone growth in the middle ear, which most commonly occurs at the stapes (this can result in 'stapes fixation').
Superior Semicircular Canal Dehiscence (SSCD)	A condition of the *inner* ear, involving a thinning or absence of part of the temporal bone. This can cause CHL and may be detected via ear-canal measurements (Nakajima et al., 2012).
Tympanic Membrane (TM) Perforation	A hole in the eardrum. Acoustically, this behaves as a Helmholtz resonator (Voss et al., 2001).

children (Bluestone & Klein, 2007). High effusion levels or large middle-ear pressures can also lead to eardrum bursts (TM perforation[2]). Finally, chronic or recurring OM can, in some cases, be related to biofilm, a bacterial colony on the middle-ear side of the TM. Biofilm interferes with the motion of the TM, causing a conductive hearing loss, and is resistant to antibiotic treatments (Nguyen et al., 2010, 2012, 2013). Some of these conditions may be visible[3] during an otoscopic examination, while others may require acoustic measurements to differentiate or diagnose.

Adult populations can be afflicted by a wide range of middle-ear pathologies (Feeney, Grant, & Marryott, 2003). In adults, extreme noise trauma (e.g. battlefield explosions) can cause both TM perforation and ossicular discontinuity (Rronenberg et al., 1993), a separation of the ossicle joints. Otosclerosis, abnormal bone growth in the ossicles, causes the ossicular chain to stiffen and can even immobilize the stapes (this is called 'stapes fixation'). This causes CHL due to an impedance change in the middle ear (Shahnaz et al., 2009). Pathologies such as otosclerosis, ossicular discontinuity and superior semicircular canal dehiscence (SSCD) can be difficult to diagnose using traditional audiological methods (Nakajima et al., 2012). This can lead to surgical exploration of the middle ear, which is expensive and unnecessary for some patients. For instance, SSCD cannot be remedied

---

[2]Sometimes a perforation is created on purpose, to relieve pressure or fluid in the middle ear; this surgical procedure is called a myringotomy.

[3]The healthy TM appears clear, whereas OM, fluid, biofilm, or pressure may cause it to appear inflamed, cloudy, or retracted.

Table 1.2: Impedance-based tests and quantities for describing sound transmission in the ear canal and middle ear. All tests are made with a probe that is acoustically or hermetically sealed in the ear canal.

Test/Quantity	Description
Tympanometry	Impedance is measured at a single low frequency (e.g. 226[Hz]) while the static ear canal pressure is varied (e.g. over a ±400 [daPa] range; often swept from 200 to -400 [dPa]).
Multi- or High-Frequency Tympanometry	Impedance is measured as a function of pressure at multiple frequencies, such as 226 [Hz], 600 [Hz], 1 [kHz], or 2 [kHz]. High-frequency (e.g. 1 [kHz]) tympanometry is sometimes used in infants due to low-frequency compliance effects of the soft tissue in the ear canal. However, tympanograms are more complicated to interpret at higher frequencies (Vanhuyse et al., 1975).
Wideband Acoustic Reflectance or Immittance (AR, WAI)	Impedance is measured over a broad range of frequencies (e.g. 0.2 to 8 [kHz]). This can be measured at ambient pressure, or with static pressure applied in the ear canal.
Wideband Tympanometry	WAI is measured as a function of pressure (e.g. over 0.2 to 8 [kHz] and 200 to -400 [daPa]). Immittance quantities are typically represented as a 3D contour plot.
Forward Pressure Level (FPL)	The forward-going pressure at the probe (Eq. 2.32), calculated from WAI. This can be used for in-the-ear (ITE, or *in situ*) calibration.

by middle ear surgery.

1.2 Middle-ear assessment

Conductive hearing loss may be identified by an 'air-bone gap,' which is a difference in the audiometric thresholds for sound conducted in air versus sound conducted in bone. Bone-conducted stimuli are typically delivered via a 'bone driver' oscillator placed on the mastoid bone or forehead (Weece & Allen, 2010). Aside from invasive (i.e. surgery) and non-invasive visual diagnoses, non-invasive acoustic techniques have been adopted to identify the causes of CHL. These non-invasive tests are based on measurements of the acoustic impedance of the ear, and quantities that may be derived from it. The set of impedance-related quantities, including impedance, admittance, reflectance, conductance, and so on, is often collectively referred to as the acoustic 'immittance.' Table 1.2 describes multiple impedance-based tests and quantities currently used in clinical audiometry or research.

All immittance-based measurements share a common obstacle for middle-ear assessment. The stimulus must be transmitted to the middle ear and back via the ear canal, which can have variable effects on the measured impedance across populations, individuals, and probe insertions. The two primary methods of accounting for this variability are

1. controlling the ear canal pressure while measuring the impedance, and

2. estimating and removing ear-canal delay in the reflectance domain.

Method 1 requires a hermetic seal while method 2 may be performed under both pressurized and ambient pressure conditions. Impedance, reflectance, and the acoustic effects of the ear canal will be described further in the following chapters. In this thesis, the portion of the ear canal between the probe and TM will be referred to as the residual ear canal (REC).

Tympanometry, developed for clinical use in the 1960s (Shanks & Shohet, 2009), measures the admittance of the TM at a single frequency as the ear-canal pressure is varied. This procedure accounts for the impedance effects of the ear canal by assuming that the TM becomes rigid at extreme pressures (method 1). Low-frequency tympanometry can estimate middle-ear pressure because the impedance is minimum (admittance is maximum, or 'peak') when the pressure on both sides of the TM is equal. In normal adult ears at 226 [Hz], the admittance tympanogram has a single peak at the tympanic peak pressure (TPP), and decreases as the pressure increases or decreases from the TPP. Tympanometry can often detect CHL, but cannot always differentiate between middle ear conditions (Nakajima et al., 2012). In part, this is because middle-ear malfunctions can have many different frequency-dependent effects on the measured impedance, not necessarily at 226 [Hz]. Additionally, the assumptions of 'method 1' to account for the REC are not generally valid above 500 or 600 [Hz]. Still, some middle-ear conditions may be identified by considering tympanogram shape as a function of pressure (Shanks & Shohet, 2009).

Multiple- or 'high'-frequency[4] tympanometry (e.g. 660 [Hz], 1 [kHz], 2 [kHz]) is sometimes used to obtain impedance information over a broader range of frequencies. However, tympanograms have much more complicated shapes at higher frequencies, requiring detailed interpretation (Vanhuyse et al., 1975). In normal adult ears at low frequencies, the admittance is dominated by its imaginary part (the susceptance). However, this will not necessarily be true in pathological ears or at higher frequencies. Therefore, Vanhuyse et al. (1975) consider the susceptance and conductance (real part of the admittance) tympanograms separately. Tympanometry at 1 [kHz] is also used to assess middle-ear function in newborns and infants, since it produces more reliable tympanogram patterns than low-frequency tymponometry (Shanks & Shohet, 2009; Prieve et al., 2013). In general, tympanometric measurement and interpretation in infants are problematic because the ear-canal walls are much more compliant in this population.[5] In some cases, pressurization of the ear canal

---

[4]Note that 1 [kHz] is not actually that high, as the human hearing range extends out to 15 or 20 [kHz].

[5]However, Prieve et al. (2013) suggest that the ear-canal effect may be less variable across newborns and infants due to less variability in ear canal volume, presumably due to similar body size. They found that subtracting the tympanogram tail from the peak to account for the ear canal did not change their statistical results.

can even cause it to collapse. Measurements made at ambient pressure, discussed next, may avoid some of these complications.

Wideband acoustic immittance (WAI) can be measured at ambient pressure using a probe that is acoustically (but not necessarily hermetically) sealed in the ear canal. These 'wideband' measurements are typically made from 0.2 to 6 [kHz], or higher in frequency (e.g. up to 8, 10, or 15 [kHz]). The measurable bandwidth depends on accurate Thévenin calibration of the measurement probe. This calibration typically depends on probe geometry and transducer selection, as will be discussed later in this thesis. A subject of research for decades, WAI has been used in a growing number of clinical studies in the past 20 years, and demonstrates promise for differentiating between various types of conductive hearing loss (Møller, 1960; Rabinowitz, 1981; Allen, 1986; Keefe et al., 1993; Voss & Allen, 1994; Feeney, Grant, & Marryott, 2003; Allen et al., 2005; Nakajima et al., 2012; Feeney et al., 2013). An important factor in the advent of clinical reflectance technology was the ability to estimate the contribution of the REC to WAI. In the reflectance domain, the ear-canal effect is approximately that of a lossless delay (Voss & Allen, 1994; Voss et al., 2008; Abur et al., 2014), therefore, the magnitude reflectance or power reflectance may be used to study clinical populations across ears and probe insertions. This is the simplest example of method 2 for removing the effects of the REC.

Studies have shown systematic changes in the power reflectance for various pathological conditions of the middle ear, including disarticulation or fixation of middle ear joints, tympanic membrane (TM) perforations, or degrees of fluid in the middle-ear cavity (Feeney, Grant, & Marryott, 2003; Allen et al., 2005; Shahnaz et al., 2009; Nakajima et al., 2012; Voss et al., 2012; Prieve et al., 2013). However, more analyses and normative databases are required before WAI can reach its full clinical potential (Feeney et al., 2013). Additionally, more sophisticated algorithms and models may be employed when implementing method 2 to remove the effects of the REC (Robinson et al., 2013; Rasetshwane & Neely, 2011; Lewis & Neely, 2015). Many of these methods are intended to estimate the complex immittance at the eardrum, rather than just the magnitude reflectance. The ability to analyze the complex immittance of the eardrum is expected to improve differential diagnoses. Furthermore, improved characterization of the REC acoustics will decrease measurement variability across ears and probe insertions for multiple types of insert-earphone hearing measurements. This thesis presents a comparison of methods to remove the REC effect and estimate the middle-ear immittance.

Wideband tympanometry, reviewed in Keefe et al. (2015), combines the elements of tympanometry and WAI. The pressure is swept over range similar to that of tympanometry (e.g. 200 to -400 [daPa], or sometimes 300 to -600 [daPa]), and instead of measuring the impedance at a single frequency for each pressure, a wideband impedance measurement is made. Keefe et al. (2015) discuss how eardrum immittance may be estimated; typically, a combination of methods 1 and 2 is employed. Advantages to this technique include the ability to analyze the results by frequency or by ear-canal pressure. Disadvantages of such measures include increased complexity of the acquired data, the need to pressurize the ear canal, and the effects pressurization can have on subsequent

measurements due to preconditioning of the TM (Burdiek & Sun, 2014). Clinical efficacy is still being established; for example, Keefe et al. (2012) did not find an advantage to adding pressurization in detecting CHL in children with OME.

WAI measurements may also be used for in-the-ear (ITE) calibration of hearing measurements, such as otoacoustic emissions[6] (OAEs) or pure-tone audiometry (PTA). ITE calibration is a natural extension of OAE probe functionality. OAE measurement requires the probe to include a microphone, thus the only significant extra step required for ITE calibration is Thévenin calibration of the probe. Then, a WAI measurement is made to calibrate the probe *in situ*. This is not an extra step, since all OAE measurements require calibration, either ITE or in an ear simulator, to set the stimulus level. From the measured WAI, the steady-state forward-traveling pressure wave may be calculated. Forward pressure level (FPL) calibration has proven to be the most effective method for characterizing ear-canal standing waves, and setting the target stimulus level at the TM (Scheperle et al., 2008; Lewis et al., 2009; Scheperle et al., 2011; Souza et al., 2014). Furthermore, WAI models of the ear canal for reverse transmission of OAEs (the 'emitted pressure level,' EPL) improve test-retest reliability of OAE measurements at high frequencies (Charaziak & Shera, 2017). FPL calibration also improves reliability of PTA (McCreery et al., 2009; Lapsley Miller et al., 2017). Currently, most PTA testing is done with headphones and earphones; therefore, widespread adoption of FPL calibration for PTA would require the use of probes containing microphones instead of just loudspeakers.

1.3 Focus of this thesis

Clinical uses of WAI include estimation of the middle-ear impedance (diagnosis of TM and ossicle function) and characterization of the acoustic effects of the residual ear canal and middle ear (ITE calibration). This thesis explores these topics. First, the desired characteristics and design of a clinical measurement probe are described. Effects of variable-area horns on immittance measurements are studied in the context of a measurement probe tip, which extends beyond the point of Thévenin calibration. Then, multiple methods for removing the effects of the ear canal and estimating the middle-ear impedance are analyzed. Finally, the middle-ear impedance is studied, using measurements of WAI in normal ears with ambient and negative middle-ear pressure.

---

[6]The most common types of OAE measurements include distortion product (DP), stimulus frequency (SF), and transient evoked (TE) OAEs. Measurement of DPOAEs requires two loudspeakers, due to loudspeaker harmonic distortion.

CHAPTER 2

BACKGROUND: ACOUSTIC IMMITTANCE OF THE EAR

Wideband acoustic immittance (WAI) measurements can be made with a probe containing at least one microphone and loudspeaker (Møller, 1960; Allen, 1986). The design and characteristics of such a probe will be described in the following chapter. The probe can be either acoustically or hermetically sealed in the ear canal; in this thesis, all measurements are made at ambient ear-canal pressure. Note that the probe must be calibrated in order to make immittance measurements. The calibration procedure is designed to find the Thévenin equivalent 'source' parameters of the probe, given the loudspeaker voltage.

To make a measurement, a wideband stimulus such as a steady-state periodic chirp is played via the loudspeaker. The acoustic signal is partially reflected, in a frequency-dependent manner, by the ear. The largest reflection will come from the tympanic membrane (TM) and middle ear. However, any changes in impedance along the ear canal (such as area changes) will also cause sound reflections. The probe microphone signal records these reflections, and may be used to calculate acoustic 'immittance' quantities, including the impedance, reflectance, admittance, and so on. The relationships between these immittance quantities will be described in this chapter, along with the typical immittance of the human ear. Understanding the relationships between immittance quantities is key to modeling the effects of the residual ear canal (REC) and estimating the immittance of the middle ear.

In this thesis, plane-wave propagation is assumed for measurements and models of the middle-ear immittance. The assumption is that, in a constant-area horn waveguide, only the 0th order plane-wave mode propagates below some cutoff frequency. Above this cutoff frequency, waves are evanescent, and their amplitudes decay rapidly (e.g. over a few millimeters). The cutoff frequency is determined by the dimensions of the horn. For example, in a cylindrical horn the cutoff frequency is given by

$$f_c = \frac{1.841 c_0}{2\pi a_0}, \tag{2.1}$$

where a_0 is the radius of the cylinder (Pierce (1981), p. 317).[1] In the ear canal, which is approximately cylindrical with an average diameter of 7.5 [mm], $f_c \approx 27$ [kHz]. For smaller diameters,

---

This chapter is loosely based on "Middle-ear reflectance: Concepts and clinical applications" by J. B. Allen, S. R. Robinson, J. A. Lapsley Miller, P. S. Jeng and H. Levitt in Scientific Foundations of Audiology: Perspectives from Physics, Biology, Modeling, and Medicine (p. 1-18) by A. Cacace, E. de Kleine, A. Holt, & P. van Dijk (Eds.). Copyright ©2016 Plural Publishing, Inc. All rights reserved. Used with permission.

[1] The constant 1.841 is the first root of the Bessel function derivative $\frac{d}{dx} J_1(x)$.

such as a sound delivery tube or port leading to the microphone, this frequency only increases.

Note that acoustic variables discussed in the following sections may be defined either in the time or frequency domain. It is important to always be aware of which domain is under consideration. Typically, uppercase variables are used to describe frequency-domain signals and lowercase variables are used to describe time-domain signals. Often these variables are also a function of location. For measurements in the ear canal, we define $x = 0$ as the probe location[2] and $x = L$ as the location of the TM 'load.'

2.1 Acoustic impedance and reflectance

Appendix A gives a detailed description of the acoustics principles relevant to the analyses in this thesis. These include wave propagation in cylindrical and variable-area horns, with and without viscous and thermal energy dissipation. Note that the following derivation of reflectance assumes that the horn in question is uniform, at least in the region where reflectance is defined.

2.1.1 Definition of reflectance

When sound is presented via a probe sealed in the ear canal, the pressure plane wave travels toward the TM, where it is reflected back toward the probe in a frequency-dependent manner. The probe also reflects the sound back toward the TM, and so on *ad infinitum*. Therefore, the forward- and reverse-traveling pressure waves discussed here are those at steady state. The following transmission-line description of the reflectance is discussed in detail in Section 3.1.2.

The average pressure across a cross-sectional slice of the ear canal is denoted as Ψ. The forward-traveling pressure wave will be denoted as $\Psi^+(f, x)$ [Pa]. This wave is a function of both frequency f [Hz] and location x [m], and has units of pascals [Pa]. Similarly, the reverse-traveling pressure wave is denoted $\Psi^-(f, x)$. At any location x in the ear canal, the total steady-state pressure $\Psi(f, x)$ is defined as

$$\Psi(f, x) = \Psi^+(f, x) + \Psi^-(f, x). \tag{2.2}$$

Note that the pressure is a scalar quantity. However, any change in the pressure results in a force, which is a vector quantity; this force leads to the motion of air particles. A related variable is the acoustic volume velocity $\mathcal{V}(f, x)$, defined as the velocity of an infinitesimally thin cross-section of air particles any point x in the canal. It may also be decomposed into forward- and reverse-traveling components, as

$$\mathcal{V}(f, x) = \mathcal{V}^+(f, x) - \mathcal{V}^-(f, x). \tag{2.3}$$

The volume velocity is a vector quantity, which accounts for the change in sign of the retrograde wave in Equation 2.3.

---

[2]The front end of the probe. This is also the point of Thévenin calibration.

The complex pressure reflectance is defined as

$$\Gamma(f,x) = \frac{\Psi^-(f,x)}{\Psi^+(f,x)}, \tag{2.4}$$

the ratio of reverse- to forward-traveling pressure waves. The acoustic impedance is defined as the ratio of the total pressure to the total volume velocity,

$$Z(f,x) = \frac{\Psi(f,x)}{\mathcal{V}(f,x)}. \tag{2.5}$$

The acoustic admittance is given by $Y(f,x) = \frac{1}{Z(f,x)}$, and various other WAI quantities may be readily calculated from $\Gamma(f,x)$, $Z(f,x)$ and $Y(f,x)$. Assuming the canal area is of uniform area at the measurement point, the complex reflectance and impedance are related by

$$\Gamma(f,x) = \frac{Z(f,x) - z_0(f,x)}{Z(f,x) + z_0(f,x)} \quad \text{and} \quad Z(f,x) = z_0(f,x)\frac{1+\Gamma(f,x)}{1-\Gamma(f,x)}, \tag{2.6}$$

where the function $z_0(f)$ is the characteristic acoustic impedance[3] of the ear canal. If the ear canal has a locally varying area function at the measurement point, this formula is not exact, as will be described in Section 3.2.

In the case of lossless wave propagation through a cross-sectional area A_0,

$$z_0(f) = r_0 = \frac{\rho_0 c_0}{A_0} \quad \text{(lossless case)}, \tag{2.7}$$

where $\rho_0 \approx 1.2$ [kg/m^3] is the density of air at 20 [^{o}C], $c_0 \approx 343$ [m/s] is the speed of sound. Note that the density will decrease and the speed of sound will increase as the temperature increases.[4] In a human ear, the ear-canal area A_0 will vary with distance x along the canal, thus z_0 will also vary. The exact area of the ear canal at the measurement location is unlikely to be known. However, variation due to the use of an incorrect area to define z_0 has been shown to have a relatively small effect on reflectance and impedance measurements, compared to individual variation across ears (Keefe et al., 1992; Voss & Allen, 1994). Therefore, it is often sufficient to use the average area of the adult ear canal, about 44.2×10^{-6} [m^2] (corresponding to a diameter of 7.5 [mm]), to calculate A_0.

Expressions for the characteristic impedance z_0 including viscous and thermal losses are given in Section A.2.2. For a tube of relatively large diameter (e.g. greater than 0.1 [mm]; see Fig. A.1),

---

[3]Note that acoustic impedance is defined as the ratio of the average pressure to the volume velocity. This is different from a *specific* acoustic impedance, which is defined the pressure over the *particle* velocity. The specific acoustic impedance of air is $\rho_0 c_0$.

[4]The human body temperature is 37 [^{o}C]; the temperature in the ear canal is expected to be closer to body temperature than the environmental temperature.
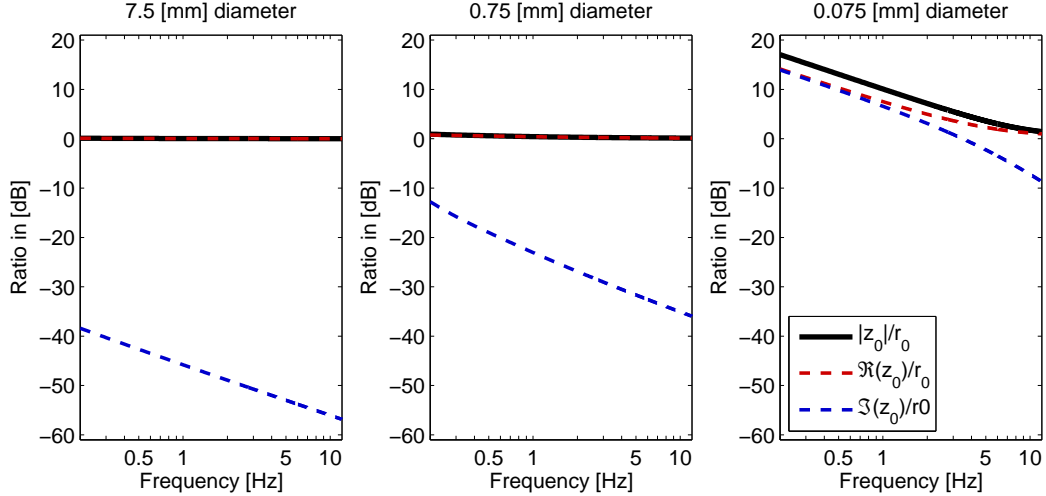
Figure 2.1: Difference between the complex characteristic impedance z_0 and real 'surge' resistance r_0 for different diameters. Except in the case of extremely narrow tubes (e.g. diameter less than 0.1 [mm]), $z_0 \approx r_0$.

the characteristic impedance is given by

$$z_0(f) = r_0 + H(f), \quad \text{(lossy case, 'large' diameter)} \quad (2.8)$$

where the function $H(f)$ is a complex series in $f^{-1/2}$. Figure 2.1 relates the complex, frequency-dependent z_0 to the real constant r_0 for various diameters. For 'large' diameters such as the ear canal, the imaginary component of z_0 is small, and the real component is approximately equal to r_0. For very small diameters below about 0.1 [mm], viscous and thermal losses contribute much more to the characteristic impedance, and it is no longer simply related to r_0. This can be seen in Section A.2.2, considering the 'small' diameter approximation of z_0.

2.1.2 Time-frequency properties of the reflectance and impedance

The reflectance by definition must be strictly causal ($\gamma(t) = 0$ for $t < 0_+$), meaning that there can be no reflection exactly at $t = 0$ (Claerbout, 1985). The impedance must also be causal ($z(t) = 0$ for $t < 0$), meaning that the pressure can depend only on current or past values of the volume velocity. The characteristic impedance must be causal as well. Note that, due to their causal nature, impedances should be analyzed using the Laplace transform. Therefore, the impedance $z(t) \leftrightarrow Z(s)$ and characteristic impedance $\zeta_0(t) \leftrightarrow z_0(s)$ may be expressed in terms of the complex Laplace frequency s.

The relationship between these quantities may be analyzed in the time domain, given the fact

that the reflectance must be strictly causal ($\gamma(0) = 0$). In the time domain, Equation 2.6 becomes

$$z(t) \star [\delta(t) - \gamma(t)] = \zeta_0(t) \star [\delta(t) + \gamma(t)]$$

$$z(t) - z(t) \star \gamma(t) = \zeta_0(t) + \zeta_0(t) \star \gamma(t)$$

$$z(t) - \int_{-\infty}^{t_-} z(\tau)\gamma(t - \tau)d\tau = \zeta_0(t) + \int_{-\infty}^{t_-} \zeta_0(\tau)\gamma(t - \tau)d\tau, \tag{2.9}$$

where the boundaries of the convolutions (∞ to t_-) are due to the fact that $\gamma(t - \tau) = 0$ when $\tau \geq t$. Due to the causal property of both impedances, at $t = 0$ these convolutions become

$$\int_{-\infty}^{0_-} z(\tau)\gamma(-\tau)d\tau = \int_{-\infty}^{0_-} \zeta_0(\tau)\gamma(-\tau)d\tau = 0, \quad (t = 0) \tag{2.10}$$

because $z(\tau) = \zeta_0(\tau) = 0$ for $\tau < 0$. Therefore, at $t = 0$

$$z(0) = \zeta_0(0). \tag{2.11}$$

Lossless case. In the lossless case, the characteristic impedance is a constant r_0, and

$$\zeta_0(x, t) = r_0(x)\delta(t) \leftrightarrow z_0(x, f) = r_0(x). \tag{2.12}$$

Therefore, the impedance at $t = 0$ is given by

$$z(0) = \zeta_0(0) = r_0\delta(0). \tag{2.13}$$

The surge impedance (Campbell, 1922) is defined as the amplitude of the $\delta(t)$ component of the time-domain impedance. Therefore, r_0 may be referred to as the 'surge impedance' or 'surge resistance.'

Lossy case. When viscous and thermal losses are considered, the characteristic impedance becomes a complex function of frequency, as shown in Section A.2.2. The time-domain characteristic impedance remains real, but is no longer just a delta function.

Considering Sections A.2.2 and A.4.5, when the radius is large compared to the visco-thermal boundary layer,

$$z_0(x, s) = r_0(x)\left[1 + \frac{\alpha'_{-1}}{a(x)\sqrt{s}} + \frac{\alpha'_{-2}}{a^2(x)s} + \frac{\alpha'_{-3}}{a^3(x)s^{3/2}}\right], \tag{2.14}$$

where the $a(x)$ is the radius of a cylindrical horn and $\alpha'_k = \alpha_k(\rho_0/\mu_0)^{k/2}$ are constants defined in Appendix A for a 'large' diameter tube. If the ratio of the tube radius to the boundary layer is sufficiently large, $a(x)$ may be generalized to

$$a(x) = \frac{2A(x)}{\Pi(x)}, \tag{2.15}$$

where $\Pi(x)$ is the horn perimeter at location x (Richards, 1986).

The Laplace transforms of the $\sqrt{s}$ terms are given as follows:

$$\frac{1}{\sqrt{\pi t}}u(t) \leftrightarrow \frac{1}{\sqrt{s}}, \quad u(t) \leftrightarrow \frac{1}{s}, \quad 2\sqrt{\frac{t}{\pi}}u(t) \leftrightarrow \frac{1}{s^{3/2}}, \tag{2.16}$$

where $u(t)$ is the Heaviside step function, which means that these functions are causal. Therefore, in the time domain the characteristic impedance becomes

$$\zeta_0(t) = r_0\delta(t) + r_0\left[\frac{\alpha'_{-1}}{a(x)}\frac{1}{\sqrt{\pi t}}u(t) + \frac{\alpha'_{-2}}{a^2(x)}u(t) + \frac{\alpha'_{-3}}{a^3(x)}2\sqrt{\frac{t}{\pi}}u(t)\right]. \tag{2.17}$$

Thus r_0 is still the 'surge resistance,' as it is the magnitude of the $\delta(t)$ component. Note that the time-domain characteristic impedance diverges as $t \to \infty$, which gives an unstable result for $\psi^{\pm}(t) = v^{\pm}(t) \star \zeta_0(t)$. Keefe (1984) derived the frequency-domain expression for $z_0(x, s)$ using an asymptotic expansion for the 'large-r' case. He states that a property of asymptotic expansions is that the approximation can degrade as more terms in the series are included. In this case, it appears this has very serious implications in the time domain.

When the radius is small compared to the boundary layer, the characteristic impedance becomes (Sec. A.2.2)

$$z_0(x, s) = r_0(x)\left[\alpha'_1 a(x)\sqrt{s} + \frac{\alpha'_{-1}}{a(x)\sqrt{s}}\right], \tag{2.18}$$

which requires the Laplace transform pair

$$\frac{d}{dt}\left[\mathcal{L}\left\{\frac{1}{\sqrt{s}}\right\}\right] = -\frac{1}{2\sqrt{\pi}t^{3/2}}u(t) \leftrightarrow \sqrt{s} = s\left[\frac{1}{\sqrt{s}}\right]. \tag{2.19}$$

In this case, the time-domain characteristic impedance becomes

$$\zeta_0(t) = r_0\left[-\alpha'_1 a(x)\frac{1}{2\sqrt{\pi}t^{3/2}}u(t) + \frac{\alpha'_{-1}}{a(x)}\frac{1}{\sqrt{\pi t}}u(t)\right]. \tag{2.20}$$

Thus for the 'small-r' case where visco-thermal losses play a larger role, there is no $\delta(t)$ ('surge') component of the characteristic impedance.

2.1.3 Utility of the magnitude reflectance

Compared to other immittance quantities, the reflectance quantifies sound transmission in the ear somewhat more intuitively. This is because the magnitude reflectance describes the ratio of reflected to incident pressure, while its phase codifies the latency of the pressure reflections (e.g., the depths at which reflections occur). Additionally, the ratio of power absorbed by ear (including the ear

canal, middle, and inner ear) may be calculated. Acoustic power is proportional to the square of pressure, so the ratio of power reflected is $\Gamma\Gamma^* = |\Gamma|^2$. Thus, the ratio of power absorbed by the ear is $1 - |\Gamma|^2$. In the healthy middle ear, most of the power absorbed by the ear is transmitted to the cochlea (Rosowski et al., 1986). Various conductive hearing loss (CHL) conditions may cause more power to be reflected from the middle ear, or to be absorbed by the middle ear instead of transmitted to the cochlea (Lewis & Neely, 2015).

For the middle ear, the magnitude reflectance $|\Gamma|$ and the power reflectance $|\Gamma^2|$ will never be greater than 1. For a passive system, the real part of the impedance must always be non-negative (Brune, 1931; Van Valkenburg, 1964). The corresponding constraint on the reflectance magnitude is proved as follows:

$$
\begin{aligned}
0 &\leq \mathrm{Re}\{Z(f)\} = \frac{Z(f) + Z^*(f)}{2} \\
0 &\leq \frac{z_0}{2}\left[\frac{1 + \Gamma(f)}{1 - \Gamma(f)} + \frac{1 + \Gamma^*(f)}{1 - \Gamma^*(f)}\right] \\
0 &\leq \frac{z_0}{2}\left[\frac{(1 + \Gamma(f))(1 - \Gamma^*(f)) + (1 + \Gamma^*(f))(1 - \Gamma(f))}{(1 - \Gamma(f))(1 - \Gamma^*(f))}\right] \\
0 &\leq z_0\left[\frac{(1 - |\Gamma(f)|^2)}{|1 - \Gamma(f)|^2}\right].
\end{aligned} \tag{2.21}
$$

For this inequality to hold, it is required that $|\Gamma| \leq 1$. It follows that a purely imaginary impedance ($\mathrm{Re}\{Z\} = 0$) must have a reflectance magnitude of 1. If the reflectance measured in any passive system is found to be greater than 1, there may be errors in the Thévenin calibration, or nonlinearities in the loudspeaker(s) or microphone.

2.2 Effects of the ear canal: A simple model

The clinical utility of WAI depends on its ability to characterize and separate the ear-canal and middle-ear effects on the complex immittance measured at the probe. The residual ear canal (REC) dimensions between the probe and TM have a large impact on these measurements. As REC dimensions vary across ears and probe insertions, it is necessary to estimate the TM immittance in order to diagnose middle-ear pathologies. Furthermore, characterization of sound transmission (magnitude and phase) in the ear canal and middle ear can improve the accuracy of stimulus delivery for other tests of hearing. In this section, a simplified model of the ear canal and middle ear is presented to describe the effects of the REC on WAI measurements.

The ear canal may be most simply modeled as a rigid-walled cylindrical tube, shown in Figure 2.2b. The tube is terminated in a load $Z_{tm}(\omega)$, the lumped impedance of the middle ear beginning at the TM. This model assumes plane-wave propagation, which is valid up to about 27 [kHz] depending on the speed of sound and the area of the canal (Voss & Allen, 1994; Pierce, 1981).
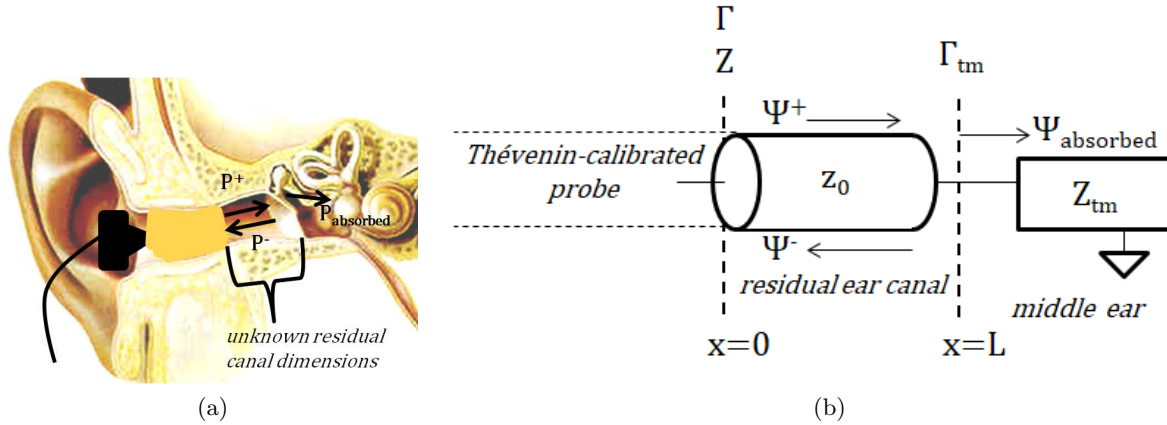
Figure 2.2: Measuring WAI in the ear canal. (a) Probe placement in the ear canal, (b) a simple model for immittance measurements in the ear canal.

Above this frequency, higher-order modes can significantly contribute to the measured pressure. This is typically not a problem, since the human hearing range is about 20 [Hz] to 15 or 20 [kHz]. Note that in Figure 2.2 the TM is approximated as perpendicular to the canal, even though it is actually approximately 45 to 60 degrees from perpendicular (Stinson & Lawton, 1989). Nonplanar modes exist close to the TM due to its angle and vibration, but they are well attenuated within a few [mm] (Voss & Allen, 1994). Thus, it is convenient that measurements are typically made at a canal location relatively far from the TM.

Take the distance between the probe tip and the TM to be L. The acoustic impedance at any point along the cylindrical horn is related to the impedance at the TM by the acoustic transmission line relation

$$
\begin{aligned}
Z(x, f) = \frac{\Psi(x, f)}{\mathcal{V}(x, f)} &= \frac{\Psi^+(x, f) + \Psi^-(x, f)}{\mathcal{V}^+(x, f) - \mathcal{V}^-(x, f)} \\
&= \frac{\Psi_{tm}^+ e^{-\kappa(x-L)} + \Psi_{tm}^- e^{\kappa(x-L)}}{\mathcal{V}_{tm}^+ e^{-\kappa(x-L)} - \mathcal{V}_{tm}^- e^{\kappa(x-L)}},
\end{aligned}
\tag{2.22}
$$

where $\Psi_{tm}^\pm$ and $\mathcal{V}_{tm}^\pm$ are the forward- and reverse-traveling pressure and volume-velocity waves at the eardrum. A nice derivation of this equation is given by Staelin et al. (1998) for an electrical transmission line. The complex wavenumber κ depends on the cross-sectional dimensions of the horn when visco-thermal losses are present. For lossless transmission κ is purely imaginary,

$$
\kappa = \frac{s}{c} = j\frac{2\pi f}{c} \qquad \text{(lossless propagation)}.
\tag{2.23}
$$

Note that even a hard-walled cylinder is expected to have some viscous and thermal losses (W. Mason, 1928; Keefe, 1984).

Using the relations in Equation 2.22 and the definitions presented in the previous section, it is

possible to estimate the effect of a REC of length L on the measured impedance and reflectance. The goal is to determine the difference between immittance measured at the probe and the immittance of the middle ear at the TM. Starting from Equation 2.22,

$$Z(x, f) = \frac{\Psi^+(x, f)}{\mathcal{V}^+(x, f)} \left[\frac{1 + \frac{\Psi^-(x,f)}{\Psi^+(x,f)}}{1 - \frac{\mathcal{V}^-(x,f)}{\mathcal{V}^+(x,f)}} \right] = \frac{\Psi^+(x, f)}{\mathcal{V}^+(x, f)} \left[\frac{1 + \frac{\Psi_{tm}^-}{\Psi_{tm}^+} e^{2\kappa(x-L)}}{1 - \frac{\mathcal{V}_{tm}^-}{\mathcal{V}_{tm}^+} e^{2\kappa(x-L)}} \right]$$

$$= z_0(f) \frac{1 + \Gamma(x, f)}{1 - \Gamma(x, f)} = z_0(f) \frac{1 + \Gamma_{tm}(f) e^{2\kappa(x-L)}}{1 - \Gamma_{tm}(f) e^{2\kappa(x-L)}}, \qquad (2.24)$$

where $z_0(f)$ does not vary with location x because the cylinder is of uniform area. Examining this relationship at the probe location $(x = 0)$,

$$Z(0, f) = z_0(f) \left[\frac{1 + \Gamma(0, f)}{1 - \Gamma(0, f)} \right] = z_0(f) \left[\frac{1 + \Gamma_{tm}(f) e^{-2\kappa L}}{1 - \Gamma_{tm}(f) e^{-2\kappa L}} \right]$$

$$= z_0(f) \left[\frac{(Z_{tm}(f) + z_0(f)) e^{\kappa L} + (Z_{tm}(f) - z_0(f)) e^{-\kappa L}}{(Z_{tm}(f) + z_0(f)) e^{\kappa L} - (Z_{tm}(f) - z_0(f)) e^{-\kappa L}} \right]$$

$$= z_0(f) \left[\frac{Z_{tm}(f) \cosh(\kappa L) + j z_0(f) \sinh(\kappa L)}{j Z_{tm}(f) \sinh(\kappa L) + z_0(f) \cosh(\kappa L)} \right]. \qquad (2.25)$$

Thus, according to this simplified model, the impedance and reflectance measured at the probe location in the ear canal are related to the impedance and reflectance at the TM by

$$\Gamma(f) = \Gamma_{tm}(f) e^{-2\kappa L} \qquad (2.26a)$$

$$Z(f) = z_0(f) \left[\frac{Z_{tm}(f) + j z_0(f) \tanh(\kappa L)}{z_0(f) + j Z_{tm}(f) \tanh(\kappa L)} \right]. \qquad (2.26b)$$

Note that in this thesis, if x is not specified or there no subscript, it may be assumed that the quantity in question is at $x = 0$ (the probe location). From Equation 2.26b, it follows that the variable REC length between subjects makes it difficult to compare impedance measurements at the probe. However, the reflectances $\Gamma(f)$ and $\Gamma_{tm}(f)$ only differ by a phase delay.

The reflectance phase, $\angle\Gamma(f)$, is a measure of signal latency. The 'group delay'

$$\tau(f) = -\frac{d}{d\omega} \angle\Gamma(f) = \frac{-1}{2\pi} \frac{d}{df} \angle\Gamma(f) \qquad (2.27)$$

is a frequency-dependent measure of round-trip signal delay in the ear canal and middle ear. Assuming a lossless ear canal of uniform area,

$$\Gamma(f) = \Gamma_{tm}(f) e^{-j2\pi f \tau_{rec}} \qquad (2.28a)$$

$$\angle\Gamma(f) = \angle\Gamma_{tm}(f) - 2\pi f \tau_{rec} \qquad (2.28b)$$

16

$$\tau(f) = \tau_{tm}(f) + \tau_{rec} \tag{2.28c}$$

$$\tau_{rec} = 2L/c_0. \tag{2.28d}$$

Thus the cylindrical 'ear canal' in this model contributes a pure delay τ_{rec} that is constant for all frequencies. Note that for a REC of varying area (i.e. a human ear canal) the ear canal will not contribute a pure delay. The effects of a variable-area horn may be modeled using two-port network techniques as described in Appendix B. A variable-area ear canal can also affect the magnitude reflectance measured at the probe, and the severity of these effects depends on the size of the area change, and the relative delays of the ear canal and the load impedance (in this case, the middle ear).

Taking the magnitude of Equation 2.28a yields

$$|\Gamma(f)| = |\Gamma_{tm}(f)| \tag{2.29}$$

for a lossless, cylindrical ear canal. Equation 2.29 indicates that, if the simple model is a good approximation for the REC effect, the reflectance magnitude does not depend on probe depth in the ear canal. This has proven to be a reasonable assumption for adult ears (Voss & Allen, 1994; Voss et al., 2008; Abur et al., 2014), which allows for comparisons across ears and probe insertion depths. Deviations from this relationship may increase with REC length due to the compliance of the ear canal tissue (Voss et al., 2008), particularly when the probe is seated outside of the bony portion of the ear canal. In many ears, canal compliance losses are relatively small compared to the variability of measurements across ears. Equation 2.29 is a standard assumption for WAI analysis of the middle ear, which often considers only the power reflectance or absorbance level.

Given the measured $\Gamma(f)$ and an estimated canal length L, one may estimate $\Gamma_{tm}(f)$ and $Z_{tm}(f)$. Voss and Allen (1994) used the complex reflectance to estimate the acoustic properties of the TM, by removing pure delay from the reflectance phase. However, as the eardrum is expected to contain a significant amount of delay (Puria & Allen, 1998; Parent & Allen, 2010), it is difficult to determine how much to remove. Furthermore, when the area of the canal depends on position (as in a real ear canal), estimating the immittance of the middle ear at the TM requires two-port modeling techniques. This subject will be addressed in detail in Chapter 4.

The ear-canal standing wave. A standing wave is created when the forward and retrograde pressures in the ear canal are out of phase, nearly canceling each other and creating a deep minimum in the total pressure (Eq. 2.2). The frequency at which this cancellation occurs is dependent upon the round-trip delay from the probe source ($x = 0$) to the TM ($x = L$), and varies significantly across probe insertions. To understand the standing-wave effect, consider the cylindrical ear-canal model presented previously in this section. The retrograde pressure at the microphone is related to the forward pressure by $\Psi^-(0, f) = \Psi^+(0, f)\Gamma_{tm}(f)e^{-j2\pi f \tau_{rec}}$. Therefore, the total pressure at

the microphone is

$$\Psi(f) = \Psi(0, f) = \Psi^+(0, f)(1 + \Gamma_{tm}(f)e^{-j2\pi f\tau_{rec}}).$$ (2.30)

If Γ_{tm} is real-valued, this quantity is at its minimum when $e^{-j2\pi f\tau_{rec}} = -1$ (i.e. $f\tau_{rec} = n/2$ for odd integers n). Any delay in Γ_{tm} will modify the locations of these minima.

Below 8 kHz, insert-earphone measurements are typically only affected by the lowest standing wave frequency, corresponding to a distance of one-quarter wavelength. The one-quarter wavelength standing wave occurs in a tube that is closed at one end and open at the other. For an insert-earphone configuration, the eardrum represents the closed end of the tube, while the earphone represents the open end due to the earphone sound source. For example, a standing wave at 6 kHz corresponds to a distance of about 14 [mm]. This distance is not well-defined for in-the-ear measurements due to the angled eardrum, and any eardrum delay (Puria & Allen, 1998) may make the earphone-eardrum distance appear longer, decreasing the standing wave frequency. For example, Parent & Allen (2010) attribute 24 [μs] of one-way delay to the TM (the speed of sound is much slower on the TM than in air), and 9 [μs] to the ossicles. This gives a round-trip delay of 66 [μs], which corresponds to a length of about 11 [mm] for sound traveling in air.

2.3   Immittance of the human middle ear

Major physical mechanisms that contribute to the measured immittance of the middle ear include the TM, ossicle chain, middle-ear cavities, and cochlear load. As described in the previous section, the acoustic impedance measured in the ear canal is dominated by a standing wave related to the ear-canal length. Therefore, this section will show experimental measurements of the reflectance magnitude, and refer to models to describe the complex impedance.

2.3.1   Immittance of the middle ear

The impedance of the middle ear is stiffness-dominated below about 1 [kHz]. This stiffness causes the impedance to be higher, and the magnitude reflectance to approach 1 at low frequencies. It originates from multiple middle-ear features, including the ossicle joints and ligaments, TM, and middle-ear cavities. The middle-ear stiffness maybe be altered by a number of pathologies, or by the acoustic reflex[5] (Feeney & Keefe, 2001; Feeney, Keefe, & Marryott, 2003).

In the mid-frequency range (e.g. 1 to 5 [kHz]), the middle-ear impedance is more closely matched to the ear-canal impedance, causing a broad minimum in the power reflectance (Parent & Allen, 2010; Rosowski et al., 2012). In this region, and at higher frequencies, immittance quantities tend to have variable local minima and maxima, due to the transmission characteristics of individual ears. At high frequencies, the impedance may be mass-dominated, but it is difficult to measure precisely due probe insertion and transducer frequency response (Parent & Allen, 2010). Additionally,

---

[5]The acoustic reflex is a contraction of the stapedius muscle in reaction to a high stimulus level.
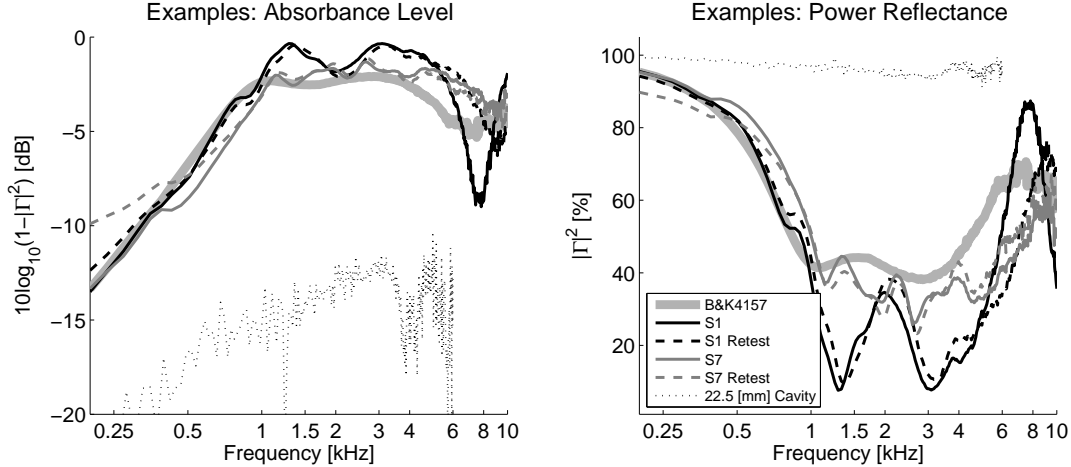
Figure 2.3: Absorbance level (left) and power reflectance (right) for 2 normal ears (with retest measurements) from Voss & Allen (1994). Additionally, a measurement of the B&K 4157 ear simulator from that study is presented, where the ear simulator is intended to mimic the response characteristics of the average adult ear. Finally, a measurement of a rigid cylindrical cavity (22.5 [mm] long) is shown. *From "Middle-ear reflectance: Concepts and clinical applications" by J. B. Allen, S. R. Robinson, J. A. Lapsley Miller, P. S. Jeng and H. Levitt in Scientific Foundations of Audiology: Perspectives from Physics, Biology, Modeling, and Medicine (p. 10) by A. Cacace, E. de Kleine, A. Holt, & P. van Dijk (Eds.). Copyright © 2016 Plural Publishing, Inc. All rights reserved. Used with permission.*

area variation in the ear canal may have an effect on high-frequency minima and maxima of the impedance and reflectance (Lewis & Neely, 2015).

As previously described, the magnitude reflectance measured at the probe location in the ear canal $|\Gamma(f)| = |\Gamma(0, f)|$ is assumed to be approximately equal to the magnitude reflectance at the TM $|\Gamma_{tm}(f)| = |\Gamma(L, f)|$, while its phase is highly variable across ears. Therefore, many clinical studies have focused on the power reflectance, $|\Gamma(f)|^2$. Because this value is between 0 and 1, expressing the ratio of power reflected from the middle ear, it is often expressed as a percentage.

A related quantity, the power absorbance, $1 - |\Gamma(f)|^2$, is a measure of middle-ear energy transmission. Assuming low-loss transmission in the ear canal, it approximately quantifies power absorption by the middle ear and cochlea (Allen et al., 2005; Rosowski et al., 2012). In the case of some middle-ear conditions, power can be absorbed or dissipated in the middle ear, and does not reach the cochlea. The power absorbance expressed in decibels, $10 \log_{10}(1 - |\Gamma(f)|^2)$, is referred to as the "power absorbance level," and has a distinctive shape for normal ears. This quantity has also been referred to as the "transmittance" (Allen et al., 2005). In normal ears, it is expected to be closely related to the middle-ear transfer function.

Figure 2.3 shows example power reflectance and absorbance level measurements from normal ears (Voss & Allen, 1994), an ear simulator (the Brüel & Kjær 4157), and a rigid cylindrical cavity. The cavity has a power reflectance close to 100% across all frequencies, as expected, with some small losses due to viscous and thermal effects of air flow along the cylinder walls (Keefe, 1984).

19

For normal ears, the absorbance level has a distinctive shape, with a rising slope below about 1 [kHz], a flat region with small individual variations between about 1 and 5 [kHz], and a falling slope at high frequencies.

2.3.2   Middle-ear models

The complex acoustic impedance of the middle ear is traditionally modeled using electrical networks. Resistor elements represent resistive losses in the middle ear, while capacitors and inductors correspond to compliance (stiffness) and mass, respectively. These impedance elements represent analogous differential equations in electrical, mechanical, and acoustical dynamics. When modeling electrical and mechanical parts together, such as for a loudspeaker (Kim & Allen, 2013) it is necessary to take the 'dual' of the mechanical portion, or use a gyrator. In the case of the middle-ear, only transformers are required to convert between the mechanical and acoustical parts of the model.
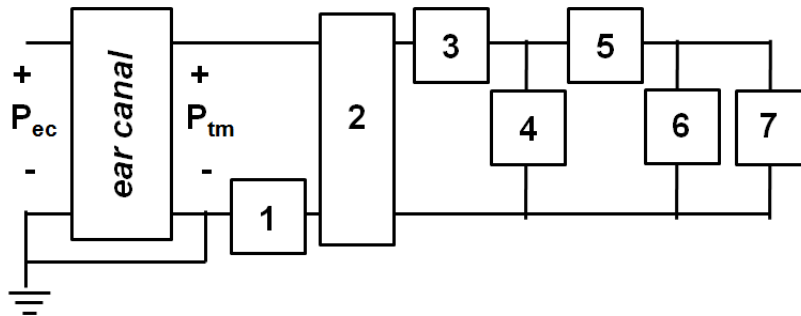

Figure 2.4: Block diagram of the major acoustic components of the middle ear. Tables 2.1 and 2.2 show how various published models account for each of these blocks. (1) middle-ear cavities (including the tympanic cavity, antrum, and mastoid air cells), (2) tympanic membrane (TM), (3) malleus (and any part of the TM that moves as one unit with the malleus), (4) incudomalleolar joint, (5) incus, (6) incudostapedial joint, and (7) stapes and cochlea.

Figure 2.4 shows a block diagram of the major acoustic components of the middle ear. These are represented as either series or shunt impedance blocks, or as two-port networks (for a review of two-port networks, see Appendix A). The ear canal is an acoustic horn of variable area, and may also be modeled as a two-port network. The major components of the middle ear represented by the numbered blocks are the (1) middle-ear cavities, (2) tympanic membrane (TM), (3) malleus, (4) incudomalleolar joint, (5) incus, (6) incudostapedial joint, and (7) stapes and cochlea. This section describes blocks 1-7 (not the ear canal), as models of the ear canal will be explored in more detail in future chapters.

Tables 2.1 and 2.2 summarize a selection of middle-ear models from the literature. These models are primarily used to describe middle-ear immittance, and the middle-ear transfer function from the TM to the cochlea. Table 2.1 focuses on Zwislocki-type models, which are quasi-static, lumped-element models, while Table 2.2 shows models that combine distributed delay-line models of the

Table 2.1: Models of the middle-ear using lumped-element network models to represent the eardrum (numbered blocks correspond to Fig. 2.4). Note that + and || denote series and parallel combinations of elements, and C, R, and L denote capacitors (stiffness, $Z_c = \frac{1}{sC}$), resistors ($Z_R = R$), and inductors (masses, $Z_L = sL$). For simplicity, the parameter values given are adjusted to eliminate transformers.

Block	Zwislocki (1962)[a]	Kringlebotn (1988) (used by Voss et al. (2012))	Lewis & Neely (2015) (simplified from Kringlebotn (1988))	Shaw (1977), Shaw & Stinson (1983)
1: Middle-ear cavities	$(C_p[5.1\mu F] + R_a[60\Omega] + L_a[14mH]) \| R_m[1000\Omega]) \| C_t[0.35\mu F]$	$(C_a[3.9\mu F] + R_a[60\Omega] + L_a[1mH]) \| C_t[0.4\mu F]$	[short circuit]	$(C_p + R_a + L_a) \| R_m \| C_t$ (no values provided)
2: Tympanic membrane (2-port)	$\begin{bmatrix} 1 & 0 \\ 1/Z & 1 \end{bmatrix}$ Z (shunt): $C_{d1}[0.23\mu F] + L_d[15mH] \| R_{d1}[40\Omega] + (C_{d2}[0.4\mu F] + R_{d2}[220\Omega])$	$\begin{bmatrix} 1 & Z_1 \\ 0 & 1 \end{bmatrix}\begin{bmatrix} 1 & 0 \\ 1/Z_2 & 1 \end{bmatrix}$ Z_1 (series): $L_d[7.5mH] + (C_s[0.3\mu F] + R_s[20\Omega] + L_s[66mH]) \| (C_r[1.3\mu F] + R_r[120\Omega])$ Z_2 (shunt): $C_m[0.38\mu F] + R_m[120\Omega]$	$\begin{bmatrix} 1 & 0 \\ 1/Z & 1 \end{bmatrix}$ Z (shunt): $C_m[0.38\mu F] + R_m[120\Omega]$	$\begin{bmatrix} 1 & Z_1 \\ 0 & 1 \end{bmatrix}\begin{bmatrix} 1 & 0 \\ 1/Z_2 & 1 \end{bmatrix}$ Z_1 (series): $C_d + R_d + L_d$ Z_2 (shunt): $C_{do} + R_{do}$ This is the "two-piston" model, rearranged to eliminate transformer (no values provided).
3: Malleus	$C_o[1.4\mu F] + R_o[70\Omega] + L_o[40mH]$ (model assumes malleus and incus move as one unit)	$C_o[\infty F] + R_o[20\Omega] + L_o[22mH]$ (model assumes malleus and incus move as one unit)	$L_o[22mH]$ (model assumes malleus and incus move as one unit, no values provided)	$C_o + R_o + L_o$ (model assumes malleus and incus move as one unit, no values provided)
4: Malleus-incus joint	[open circuit]	[open circuit]	[open circuit]	[open circuit]
5: Incus	[short circuit]	[short circuit]	[short circuit]	[short circuit]
6: Incus-stapes joint	$C_i[0.25\mu F] + R_i[3000\Omega]$	$C_i[0.3\mu F] + R_i[6000\Omega]$	$R_i[6000\Omega]$	$C_i + R_i$ (no values provided)
7: Stapes & cochlea	$C_c[0.6\mu F] + R_c[600\Omega] + L_c[0H]$	$C_c[0.56\mu F] + R_c[330\Omega] + L_c[46mH]$	$C_c[0.56\mu F] + R_c[330\Omega]$	$C_c + R_c + L_c$ (no values provided)

[a]Some precursors of this model included Onchi (1949), Zwislocki (1957) and Møller (1961).

Table 2.2: Models of the middle-ear using delay-line models to represent the eardrum (numbered blocks correspond to Fig. 2.4). Note that + and || denote series and parallel combinations of elements, and C, R, and L denote capacitors (stiffness, $Z_c = \frac{1}{sC}$), resistors ($Z_R = R$), and inductors (masses, $Z_L = sL$). For simplicity, the parameter values given are adjusted to eliminate transformers.

Block	O'Connor & Puria (2008)	Parent & Allen (2010)	Goll & Dalhoff (2011)	Keefe (2015b)
1: Middle-ear cavities	[short circuit]	[short circuit]	[short circuit]	Transmission line model; many branches (Keefe, 2015a).
2: Tympanic membrane (2-port)	$\begin{bmatrix} A & B \\ C & D \end{bmatrix}$ Uniform Tube	$\begin{bmatrix} A & B \\ C & D \end{bmatrix}\begin{bmatrix} N & 0 \\ 0 & 1/N \end{bmatrix}$ TM discretized into rings	TM represented as a 1D radial string	$\frac{1}{z_{21}}\begin{bmatrix} A'(s) & B'(s,\tau) \\ C'(s) & D'(s,\tau) \end{bmatrix}\begin{bmatrix} N & 0 \\ 0 & 1/N \end{bmatrix}$ where $z_{21} = C_1 + C_2 e^{-s\tau}$, $B' = B_1 + B_2 e^{-s\tau}$, and $D' = D_1 + D_2 e^{-s\tau} + D_3 e^{-2s\tau}$. All B_k, C_k, D_k are functions of s. TM is represented by 2 segments coupled by a time-delayed compliance.
3: Malleus	$C_m + R_m + L_m$	$2C_m + R_m/2 + L_m/2$	$C_{me} + R_{me} + L_{me}$	$C_m + R_m + L_m$
4: Malleus-incus joint	$C_{im} + R_{im}$	$C_{im} + R_{im}$	[short circuit]	$C_{im} + R_{im}$
5: Incus	L_i	$(2C_m + R_m/2 + L_m/2) + L_i/2$	[short circuit]	L_i
6: Incus-stapes joint	$C_{is} + R_{is}$	$C_{is} + R_{is}$	[short circuit]	$C_{is} + R_{is}$
7: Stapes & cochlea	$C_{al} + R_{al} + L_s + R_c + C_{rw}$	$L_i/2 + L_s + C_{al} + R_{al} + (R_c \,\|\, (R_o + L_o)) + C_{rw}$	[short circuit]	$C_{al} + R_{al} + L_s + \hat{Z}_c$ where $\hat{Z}_c$ is not simply a series element, but a network with other connections to ground.

TM with lumped-element models of the ossicles. Note that Figure 2.4 and Tables 2.1 and 2.2 do not show all transformers included in these models. However, any acoustical-mechanical impedance change will have a transformer related to the cross-sectional area of the acoustical section, and some models include a transformer for the lever ratios between ossicles. In many cases, the parameter values given are adjusted to eliminate transformers. An example of how these network models may be simplified by removing low-sensitivity components is given by Lewis & Neely (2015), as compared to the other models in Table 2.1.

Modeling the middle-ear cavities, ossicles, and cochlea. The first block represents the middle-ear cavities. These include the tympanic cavity, antrum, and mastoid air cells. Zwislocki (1953) models this as the parallel combination of a C-R-L circuit, a resistor, and a capacitor. In the C-R-L circuit, the inductor and resistor represent the constricted passage between the tympanic cavity and the antrum, and the capacitor represents the volume of the antrum and pneumatic cells. The other capacitor represents the volume of the tympanic cavity, which is the space where the ossicles reside. Finally, the resistor represents general absorption by the cavity walls. This resistor value is large (e.g. approaching a short circuit), and is often left out in other models, such as that of Kringlebotn (1988). Stepp & Voss (2005) used Kringlebotn's model to characterize their measurements of the middle-ear cavities in cadaver ears, and found it suitable to capture the acoustic effects of these cavities, though their parameter values differed from those of Kringlebotn. While many models omit the middle-ear cavities, Stepp & Voss (2005) found that they can affect the impedance measured at the tympanic membrane by up to 10 [dB] above 1 [kHz].

Blocks 3, 5, and 7 of Figure 2.4 represent the malleus, incus and stapes. Blocks 4 and 6 represent the incudomalleolar and incudostapedial joints, respectively. While most of the models in Table 2.2 include the incus and incudomalleolar joint, the Zwislock-based models in Table 2.1 represent the malleus and incus as one unit (Zwislocki, 1957). Assuming that the incudomalleolar joint is very stiff, this may be a good approximation at frequencies below 1 or 2 [kHz]. However, as the goal of many distributed TM models (Table 2.2) is to model the middle-ear immittance at high frequencies, it is necessary to include this joint. Puria & Allen (1998) suggest that both joint compliances should be chosen to minimize reflections between the ossicles, given the proven efficiency of the normal middle ear.

Block 3, representing the malleus, may also include any portion of the TM that is rigidly coupled to the malleus at the umbo. Likewise block 7, which represents the stapes, also includes the impedance of the cochlea in series with the stapes impedance. When modeling ear-canal immittance measurements, it is typically sufficient to represent the cochlea as a resistor. Furthermore, the cochlear load provides the main resistive component of the model (Zwislocki, 1962; Lynch et al., 1982), as it should be the primary place where power is dissipated in an efficient middle ear.

The elements of block 7 may be broken out into separate series blocks to model the cochlea or middle-ear transfer function in more detail. For instance, Pascal et al. (1998) include separate nonlinear capacitors in series, representing the stapes and annular ligament, in order to model the

nonlinear acoustic reflex. Note that in the model of Keefe (2015b), the model of the cochlea is much more detailed. Therefore, block 7 of Figure 2.4 is not merely a series impedance. Instead, it contains numerous branches to ground allowing for shunt sound pathways in the scala tympani and scala vestibuli.

Modeling the TM. In the literature, the TM (block 2) is primarily modeled in one of two ways: as a lumped-element or distributed model. Table 2.1 shows models where the TM is represented as a quasistatic, lumped-element network. In the models listed, the TM is represented either as a shunt impedance element, or a series element followed by shunt element. In Zwislocki's model, a portion of the TM is assumed to vibrate in concert with the malleus (block 3), while the portion that is not directly coupled to the malleus is represented by a shunt impedance.[6] Shaw & Stinson (1983) suggest that the TM be modeled using two pistons[7] to accommodate its mechanical complexity. In this model, one piston represents the portion of the TM that is rigidly attached to the malleus, and the other piston represents the rest of the TM, including its inertance (mass) and periphery (which has capacitance and resistance). Rearranging the schematic given in Shaw & Stinson (1983), the first piston may be combined with the malleus (block 3), the second piston is in series, and the coupling between these pistons is a shunt impedance. Kringlebotn's model is quite similar to the two-piston model, except that the series block is more complicated. Kringlebotn (1988) includes a series inertance for the TM, then represents its suspension as a parallel combination including the suspension and rim.

Table 2.2 shows hybrid models which incorporate lumped-element networks and transmission-line delay to represent the middle ear. Given the experimental evidence for TM delay (Puria & Allen, 1998; O'Connor & Puria, 2008; Milazzo et al., 2017), such a model should be vastly superior to purely lumped-element model. The four models shown have similar middle-ear network models, with varying levels of simplification. For instance, the model of Goll & Dalhoff (2011) is primarily intended to characterize the TM, and a single mass-spring-damper system is attributed to the middle ear. Alternatively, the model of Keefe (2015b) is extremely detailed, particularly in its representation of the cochlea. Keefe's model is also the only one of these models to include the middle-ear cavities and mastoid air cells, which he represents using a transmission line containing many branches as described in Keefe (2015a).

O'Connor & Puria (2008), similar to Puria & Allen (1998), model the TM as a uniform tube transmission line. This model therefore attributes a frequency-independent group delay to wave propagation from the ear canal to the umbo. This is an over-simplification, but is the easiest way to add delay to the middle-ear model. Keefe (2015b) adds a simple delay quite differently. Beginning with an expanded version of the two-piston model (Shaw, 1977; Shaw & Stinson, 1983; Shera & Zweig, 1991), Keefe inserts a time-delayed compliance (e.g. a spring with delay) between the two

---

[6]Zwislocki (1962) suggests that the TM should be modeled as a transmission line above low- to mid-frequencies.

[7]Shaw's first versions of this model were presented as conference abstracts, Shaw (1977) and Shaw & Stinson (1981). In Table 2.1, this model has been rearranged to show its functional similarity to the models of Zwislocki (1962) and Kringlebotn (1988).

portions of the TM.

The model of Parent & Allen (2010), constructed in the time domain using wave digital filters, presents a highly intuitive representation for the TM. In this model, the TM is discretized into annular rings, which are split in half and attributed to either the near or far side of the angled TM as viewed from the ear canal. In this model, sound waves impinge on each of these annular rings, traveling a variable distance to reach the umbo. One downside to this model is that the reflection coefficients between the annuli have been heuristically rather than analytically determined (Parent & Allen (2010), Fig. 2).

Goll & Dalhoff (2011), who extensively cite Parent & Allen (2010) and praise the intuition behind their model, attempt to provide a rigorous physical model using a string to represent an arbitrary radial component of the TM. During forward excitation, a driving force due to the ear-canal pressure is applied uniformly over the length of the string. For reverse excitation, the force is applied at one point, the umbo-end of the string. Goll & Dalhoff (2011) explore two boundary conditions for the rim of the TM, finding that it is best modeled as a non-rigid boundary.

Model verification and finite-element modeling. Note that comparing these middle-ear models to their input impedances is only one method of verification. In fact, to fully validate any of these models, extensive invasive measurements are needed. Some possible measurements include transfer functions between the ear-canal pressure and umbo or stapes velocities, using techniques such as laser Doppler vibrometry. Many such experiments have been performed in animal models, or cadaveric human ears, due to the need to invasively modify the middle ear. While the scope of this thesis is limited to measurements of the middle-ear input impedance, it is important to consider how these models are developed.

Also note that the transmission-line models described in this section all describe one-dimensional transmission lines, using the average pressure and volume velocity. Extremely detailed three-dimensional models may be developed using finite-element modeling. However, such complicated models do not always lend more insight into the physics of the problem. Often, simple phenomenological models are adequate to model the data, and are much easier to interpret.

2.4   Limitations and sources of measurement error

There are many possible sources of error for clinical impedance measurements of human ears. These include calibration, noise, probe-tip insertion and air leaks, and normal variation across ears. In the design of a probe and analysis of measurements, the goal is to detect and mitigate these errors as much as possible.

2.4.1 Probe calibration

Acoustic measurements can be very sensitive to probe calibration, described in the following chapter. The calibration procedure measures the acoustic Thévenin parameters of the probe. Any errors in this measurement will be propagated to measurements of the middle-ear immittance, and in-the-ear (ITE) calibrations for other tests such as OAEs. For instance, any noise or vibration present in the environment throughout the calibration can cause measurement error.

It would be advantageous for the Thévenin parameters to be stable over time, so that the probe may be calibrated as infrequently as possible (e.g. to save time in a busy clinical setting). However, any acoustic or electrical changes in the measurement system, or changes in the environment, can impact the stability of the Thévenin parameters. For example, the speed of sound is dependent on temperature, so large variations in temperature can impact the calibration. The calibration is dependent on the voltage provided to the loudspeaker, so any significant changes in the electrical path could also cause errors. For instance, errors could arise when using measurement probes and hand-held modules (containing loudspeaker or microphone circuitry) interchangeably.

Finally, changes in the probe tip geometry will also alter the Thévenin parameters. In the case of a foam-tipped probe such as the ER-10C[8], parameters characterizing the sound source may drift over time with expansion and compression of the foam. Furthermore, insertion of the foam tip into the ear canal may cause changes in the foam geometry, such as large creases or even blockage of the sound path, that were not present during calibration. The Thévenin parameters may also be sensitive to differences across replaceable tips, which may not have perfectly identical geometries.

2.4.2 Noise

Acoustic measurements are sensitive to environmental noise, which can include both audible noise and mechanical vibration. In a clinic or hospital, such noise is often inescapable. In these cases, some ways to obtain better data include increasing averaging times, and taking retest measurements. A set of retest measurements may in some cases be averaged (e.g. using the power reflectance), or the measurement with lowest noise may be selected during analysis. An example of this is given in Appendix D.1 for test-retest measurements of ears with negative middle-ear pressure (NMEP).

In addition to noise in the environment, acoustic noise from vocalizations and physical movements of a the subject may also affect measurements. Infant data often has the most measurement noise because it is taken in busy hospitals, and infants cannot be asked to sit still and be quiet during measurement. Additionally, movement of the probe cable can contribute acoustical or electrical noise, which means it is important to choose a cable with good flexibility and electrical shielding.

---

[8]Etymotic Research, Elk Grove, IL

2.4.3 Probe insertion

Both the depth of the probe in the ear canal and the probe seal may affect the measured reflectance, though the effect of probe depth is typically assumed to be small. Power reflectance at low frequencies has been shown to decrease (absorbance level increases) with the probe distance from the eardrum (Lewis & Neely, 2015; Voss et al., 2008, 2013). In adult ears, this effect is relatively small[9] when the probe is situated in or close to the bony portion of the ear canal because this region is most similar to a rigid-walled cavity and thus has smaller acoustic losses. Outside of the bony region, the cartilaginous section of the ear canal has much greater compliance, leading to more acoustic losses. Therefore, it is best if the probe tip is inserted deeply enough to reach the bony part of the ear canal. Probe location in the ear canal may also vary due to different probe tip types across measurement systems. For instance, 'umbrella' tips which may be used for pressurized tympanometry measurements are placed against the opening to the ear canal. Thus, measurements made with these tips will be more affected by the ear canal than those made with more deeply inserted ear tips.

Air leaks around the probe tip can also cause measurement error, particularly at low frequencies. Most leaks occur because the probe tip does not properly seal in the ear canal, or may shift in the ear canal over the course of the measurement. An example of an acoustic leak is given in Figure 2.5. These measurements come from a normal ear from (Thompson, 2013), where the probe insertion drifted across tests made over the course of a few minutes. As the leak in the probe seal increases in size, the low-frequency absorbance level increases, and the impedance phase increases (Groon et al., 2015). This increased absorbance is due to power dissipating through the leak around the probe tip. The impedance phase is perhaps a better indicator, as it should be close to $-\pi/2$ at low frequencies in a sealed cavity.

2.4.4 Normal variation

Normal middle ears are known to have a fairly wide range of variation in power reflectance and absorbance level (Rosowski et al., 2012). The largest source of intrasubject variability (e.g. test-retest) is probe placement in the ear canal (Voss et al., 2013), though this variability is smaller than the variability across a population of normal ears (Rosowski et al., 2012; Abur et al., 2014), partucularly when the probe is deeply inserted. Middle-ear pressure within a normal range may also cause intrasubject variations (Shaver & Sun, 2013).

Intersubject variation (e.g. across ears) is assumed to be due largely to differences in middle-ear physiology. Variability in the small minima and maxima exhibited in the power reflectance and absorbance level in the mid-frequency region is likely related to the acoustics of the TM, ossicles,

---

[9]Acoustic losses due to canal wall compliance are larger in reflectance measurements made in infants and newborns. The most rapid changes occur in the first six months of life, as the inner two-thirds of the ear canal ossify during maturation (Kei et al., 2013). This fact differentiates low-frequency reflectance norms of newborns from older populations.
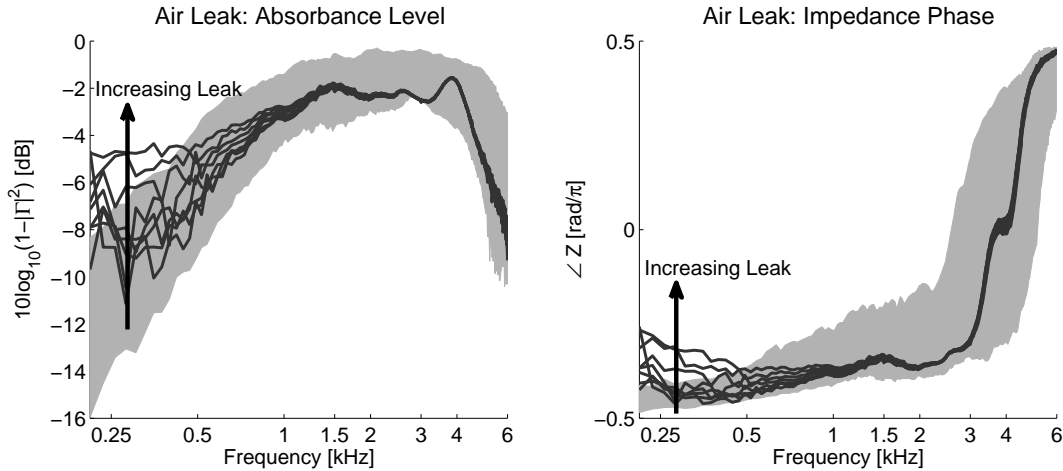
Figure 2.5: Example of the effects of a leak in probe insertion on the absorbance level and impedance phase in a normal ear, plotted against the 10-90th percentile (gray region) for normal ears from Rosowski et al. (2012). As the size of the acoustic leak increases (e.g. the probe insertion slowly loosens), there is an increase in the low-frequency absorbance level, and an increase in the impedance phase. The effect propagates upward in frequency as the leak size increases. *Left plot from "Middle-ear reflectance: Concepts and clinical applications" by J. B. Allen, S. R. Robinson, J. A. Lapsley Miller, P. S. Jeng and H. Levitt in Scientific Foundations of Audiology: Perspectives from Physics, Biology, Modeling, and Medicine (p. 17) by A. Cacace, E. de Kleine, A. Holt, & P. van Dijk (Eds.). Copyright ©2016 Plural Publishing, Inc. All rights reserved. Used with permission.*

and middle-ear space (Rosowski et al., 2012; Stepp & Voss, 2005). When expressed as absorbance level, mid-frequency variations occur over a small decibel range (Fig. 2.3). Voss et al. (2008) found, using manipulations in cadaveric ears, that variations in the volume of the middle-ear space produced larger variability in power reflectance measurements than variation in probe insertions. The middle-ear cavities can affect the power reflectance and absorbance level over a broad frequency range, and may play a role in variability across normal subjects.

2.5 In-the-ear (ITE) calibration for hearing measurements

Many acoustic assessments of the inner ear, including OAE and hearing threshold (e.g. audiogram) measurements, rely on the transmission of sound stimuli to the cochlea via the ear canal and middle ear. Therefore, proper calibration of such stimuli requires an understanding of the magnitude and phase effects introduced by propagation through the ear canal and middle ear. It follows that WAI, which quantifies the impedance of the ear canal and middle ear, may be applied to improve stimulus delivery.

Standard practice to account for middle-ear effects is to calibrate stimuli using a middle-ear simulator, often referred to as 'reference equivalent threshold sound pressure level' (RETSPL) calibration (ISO, 1997). However, ear simulators do not account for variation of the middle-ear

properties across individuals. More importantly, they do not account for the specific probe insertion depth, which varies across ears and measurement sittings. Probe insertion depth is of particular importance because of acoustic standing waves in the ear canal between the measurement probe and the TM (Siegel, 1994), as described in Section 2.2.

Two other quantities, the initial forward pressure and emitted pressure, are also described in this section. These are not specifically used for ITE calibration, but have other applications to measurements of hearing. Initial forward pressure was first defined by Keefe (1996), and can be used to Thévenin calibrate an acoustic probe using a single long tube.[10] However, initial forward pressure is not as effective for ITE calibration as FPL (Souza et al., 2014). Emitted pressure is defined by Charaziak & Shera (2017), and describes the retrograde propagation of OAEs in the ear canal.

2.5.1 Forward pressure level

Research shows that the *forward pressure level* (FPL) should be used for ITE stimulus calibrations, to account for standing wave effects on the stimulus magnitude and phase in individual ears (Scheperle et al., 2008; Souza et al., 2014; Withnell et al., 2009). FPL has been shown to limit intrasubject variability for pure-tone audiometry, which can improve long-term monitoring of hearing (McCreery et al., 2009; Lapsley Miller et al., 2017). The FPL is defined as the steady-state forward component of the pressure wave, $\Psi^+(x, f)$, as previously described. One may determine the forward pressure at the microphone from the total pressure as

$$
\begin{aligned}
\Psi(f) = \Psi(0, f) &= \Psi^+(0, f) + \Psi^-(0, f) \\
&= \Psi^+(0, f)\left(1 + \frac{\Psi^-(0, f)}{\Psi^+(0, f)}\right) \\
&= \Psi^+(0, f)(1 + \Gamma(0, f)).
\end{aligned}
\tag{2.31}
$$

Solving for $\Psi^+(0, f)$ gives

$$
\Psi^+(f) = \frac{\Psi(f)}{1 + \Gamma(f)}.
\tag{2.32}
$$

Therefore, given the measured pressure $\Psi(f)$ and the measured complex reflectance $\Gamma(f)$, the forward pressure $\Psi^+(0, f)$ can be computed. This is accomplished by varying the loudspeaker voltage so that $\Psi^+(0, f)$ is constant at the desired level. Using the FPL, the ear-canal standing wave can be precisely removed. Figure 2.6 shows the magnitude of the normalization factor $|1+\Gamma(f)|$ in decibels for 10 human ears and 2 ear simulators, taken from Voss & Allen (1994).

Considering Figure 2.6, at low frequencies, the forward and retrograde pressures are approximately in phase, requiring little correction. At frequencies above 3 [kHz], the phase of $\Gamma(f)$ plays a very important role, as it results in a deep null in the correction factor, due to the quarter-

---

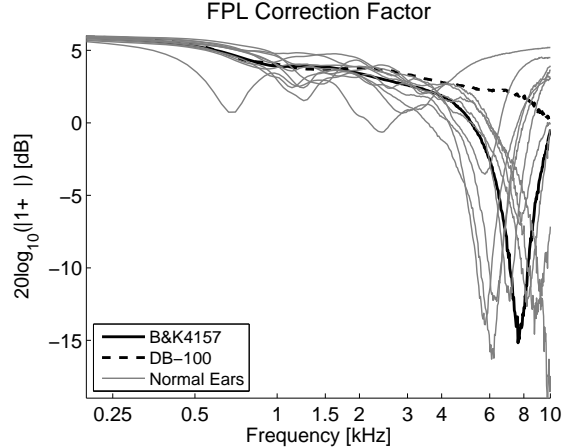[10]A better calibration may be found using at least two tubes (Keefe & Simmons, 2003).

Figure 2.6: Forward pressure level normalization factor $|1 + \Gamma|$, which corrects for the ear-canal standing wave, for 10 normal ears and two ear simulators from Voss & Allen (1994). At the frequency of the null, the phase of the complex reflectance is approximately 180 degrees (Withnell et al., 2009). The frequency of the null critically depends on the round-trip delay between the probe tip and the TM (Eq. 2.28d). This delay is different for each ear, as it depends on the insertion depth of the probe and the geometry of the ear canal and TM. As the ear-canal delay decreases, the standing-wave null shifts upward in frequency.

wavelength ear-canal standing wave. The frequency of the correction factor null increases as the distance between the probe and TM decreases.[11] For example, the null associated with the DB-100 ear simulator, measured with a very short 'canal,' is above the frequency range shown. To understand the effect of the TM reflectance on the standing-wave null frequency, consider a distance of 10 [mm] between the probe and TM. This gives a round-trip delay of about 58 [μs], thus the standing wave null might be estimated to occur at 8.6 [kHz]. However, including the additional delay of the TM and ossicles (about 33 [μs] (Parent & Allen, 2010)), the actual null frequency will be lower.

Based on the deep nulls in the FPL correction factor (due to ear canal standing waves) observed in Figure 2.6, it would not be reasonable to normalize the total pressure $\Psi(f)$ to be a constant for delivering stimuli to the cochlea. Such a normalization would boost the stimulus level at the standing-wave null frequency by as much as 25 [dB]. For instance in Equation 2.32, if $\Psi(f)$ is held constant, there is a peak in the forward pressure corresponding to the null of $|1 + \Gamma(f)|$. Calibration using an ear simulator will typically not be effective either, even if an artificial ear canal of similar length is included in the measurement. Consider the correction factors for the two ear simulators shown in Figure 2.6. The DB-100 has a very short ear canal, such that the correction factor is nearly constant. In the case of a longer simulated canal, the B&K 4157, it is unlikely that the length of the simulator canal will precisely equal the distance between the probe microphone and TM. Because the correction factor minima are so narrow and deep, this length must be extremely precise to avoid introducing a deep attenuation at the false null frequency, in addition to boosting

---

[11]In a rigidly terminated tube, the quarter-wavelength null frequency is given by $f_{null} = c/(4L)$.

the forward pressure level much too high at the true null frequency.

The low-frequency factor of 2.   Note that the correction factor in Figure 2.6 approaches 6 [dB] at low frequencies, where the eardrum is nearly rigid and $|1 + \Gamma| \to 2$. However, at this frequency there is approximately no effect due to the ear-canal standing wave, so it would seem that this factor of 2 is in error. One way to eliminate this factor is to define a modified forward pressure,

$$\widetilde{\Psi}^+ = \Psi \left(\frac{1 + |\Gamma|}{1 + \Gamma} \right), \tag{2.33}$$

where the modified correction factor $(1 + |\Gamma|)/|1 + \Gamma| \approx 1$ at low frequencies. This modified forward-pressure expression does not appear to be tested in the literature, but seems worthy of consideration.

First, $1 \leq 1 + |\Gamma| \leq 2$, meaning that the modified FPL results will never differ by more than 6 [dB] from traditional FPL, which has proven to be effective. Second, this formula is closely related to another ear-canal compensation method, the integrated pressure level (IPL), which has proven just as effective as FPL (Lewis et al., 2009; Souza et al., 2014). Lewis et al. (2009) define the IPL as

$$\text{IPL} = |\Psi^+| + |\Psi^-|, \tag{2.34}$$

which is insensitive to the ear-canal standing wave because the phases of the forward and retrograde pressure waves have been eliminated. However, this loss of phase information is sub-optimal for many types of stimuli. Therefore, it may be improved.

In fact, the IPL is intimately related to Equation 2.33,

$$\begin{aligned}
\text{IPL} &= |\Psi^+| + |\Psi^-| \\
&= \left| \frac{\Psi}{1 + \Gamma} \right| + \left| \frac{\Psi}{\frac{1}{\Gamma} + 1} \right| \\
&= |\Psi| \left(\left| \frac{1}{1 + \Gamma} \right| + \left| \frac{\Gamma}{1 + \Gamma} \right| \right) \\
&= |\Psi| \left(\frac{1 + |\Gamma|}{|1 + \Gamma|} \right) \\
&= \left| \Psi \left(\frac{1 + |\Gamma|}{1 + \Gamma} \right) \right|.
\end{aligned} \tag{2.35}$$

Therefore, the IPL is the magnitude of the modified FPL given in Equation 2.33. It would seem that the modified FPL is not likely to perform worse than traditional FPL, and accounts for the low-frequency factor of 2 in a rigorous way.

2.5.2 Initial (incident) forward pressure level

The incident, or initial, forward pressure is a property of a measurement probe for a given voltage stimulus, similar to (and derived from) the Thévenin equivalent source pressure and impedance. Keefe (1996) defines the initial forward pressure in the time domain,

$$\psi(t) = \psi_i^+(t) + \psi_r(t), \tag{2.36}$$

as the component of the pressure measured before any reflected signal (from the load) arrives back at the microphone. To derive an expression for $\psi_i^+(t) \leftrightarrow \Psi_i^+(f)$, Keefe (1996) used the following frequency-domain relations:

$$\Psi(f) = \frac{Z(f)\Psi_s(f)}{Z_s(f) + Z(f)}, \quad Z(f) = z_0(f)\frac{1 + \Gamma(f)}{1 - \Gamma(f)}, \quad Z_s(f) = z_0(f)\frac{1 + \Gamma_s(f)}{1 - \Gamma_s(f)}, \tag{2.37}$$

where Ψ is the average pressure measured at the probe, Z and Γ are the measured impedance and reflectance of a load, and Z_s and Γ_s are the impedance and reflectance looking into the probe. At the interface between the probe and the load, there is a shared characteristic impedance z_0.

Combining these relations gives an expression for the pressure in terms of the source pressure, source reflectance, and load reflectance,

$$\Psi = \frac{1}{2}\Psi_s(1 - \Gamma_s)\frac{1 + \Gamma}{1 - \Gamma\Gamma_s} \tag{2.38a}$$

$$= \frac{1}{2}\Psi_s(1 - \Gamma_s)\left[1 + (1 + \Gamma_s)\Gamma + \ldots + (1 + \Gamma_s)\Gamma^n\Gamma_s^{n-1} + \ldots\right], \tag{2.38b}$$

where the term $1/(1 - \Gamma\Gamma_s)$ has been expanded into a geometric series and rearranged. In the time domain, this expression becomes

$$\psi(t) = \frac{1}{2}\psi_s(t) \star (\delta(t) - \gamma_s) \star \left[\delta(t) + (1 + \gamma_s) \star \gamma + \ldots\right]. \tag{2.39}$$

Because the initial forward pressure is defined as the time-domain pressure in the absence of any reflections, it is given by the above expression when all terms convolved with the load reflectance γ are set to zero,

$$\psi_i^+(t) = \frac{1}{2}\psi_s(t) \star (\delta(t) - \gamma_s). \tag{2.40}$$

Thus in the frequency domain, the initial forward pressure is given by

$$\Psi_i^+(f) = \frac{1}{2}\Psi_s(f)(1 - \Gamma_s(f)). \tag{2.41}$$

Though the initial forward pressure is not as effective as FPL for ITE calibration, it has other utility. Keefe (1996) uses it to perform a Thévenin calibration in a single long cavity, a procedure

that usually requires at least two measurements (to solve for two unknown source parameters). Furthermore, the incident pressure is closely related to the source pressure. Separating the incident pressure from the load reflections provides a good measure of how much energy is sent into the system, independent of the load impedance. Therefore, this quantity might be used to adjust the speaker voltage in order to help balance the pressure response over a broad range of load impedances.

2.5.3 Emitted pressure level

Charaziak & Shera (2017) define the emitted pressure level for OAEs propagating out of the middle ear towards the probe as

$$\Psi_{OAE,EPL} = \Psi_{OAE} \left(\frac{1 - \Gamma\Gamma_s}{e^{-j\omega L_{rec}/c_0}(1 + \Gamma_s)} \right), \tag{2.42}$$

where the ear canal is modeled is a uniform cylinder of length L_{rec}. They found that using this measure to quantify OAEs allowed for smaller test-retest variability across probe insertions, particularly at high frequencies. Note that the stimuli were all calibrated ITE using the FPL.

In a similar manner to the initial forward pressure calculation, this formula separates the initial signal propagating out of the middle ear (back towards the TM) from the steady-state solution. To use this method, it is necessary to estimate the ear-canal length, which is accomplished in Charaziak & Shera (2017) using the method proposed by Rasetshwane & Neely (2011).[12]

---

[12]Note they did not try to estimate the ear-canal area function; rather, they determined L_{rec} by locating the first major reflection from the TM in the time-domain reflectance $\gamma(t)$.

CHAPTER 3

METHODS AND THEORY: VARIABLE-AREA ACOUSTIC TRANSMISSION LINES

3.1 Transmission line analysis for acoustic horns

In acoustic horn waveguides, only plane waves propagate for frequencies below a diameter-dependent 'cuttoff frequency.' This plane-wave propagation can be analyzed using transmission-line techniques. Therefore, in many cases, it is only necessary to solve for the impedance characteristics of the horn. In such cases (assuming linearity), the wave amplitude does not matter, and the impedance may be described using the axial propagation characteristics. For plane-wave propagation, transmission-line analysis methods may be used to describe the pressure and velocity, which are analogous to the voltage and current, respectively. To do this, the problem must first be cast in one dimension along the axis of the horn.

3.1.1 Volume velocity and average pressure

It is helpful to cast the problem in one dimension, the axis of propagation or 'range' variable x. This is accomplished by describing the motion of an infinitesimally thin 'slice' of air particles. This 'slice' width is assumed to be very small compared to the wavelength. Wave propagation in a slice may be described by the 'volume velocity' and the average pressure over the slice. The volume velocity is defined as

$$v(x,t) = \iint_{A_{slice}} \vec{u} \cdot \hat{x} dA \leftrightarrow \mathcal{V}(x,\omega), \tag{3.1}$$

where $\vec{u}$ is the particle velocity and $\hat{x}$ is normal to the slice. The average pressure is defined as

$$\psi(x,t) = \frac{1}{A(x)} \iint_{A_{slice}} p dA \leftrightarrow \Psi(x,\omega). \tag{3.2}$$

The geometry of the slice is very important. The slices are defined to be 'iso-pressure.' Except in the case of a cylindrical horn, the iso-pressure contours will not be planar cross-sections. This distinction becomes important when working with variable-area horns. When the pressure is constant over the slice

$$\psi(x,t) = p(x,t) \quad \text{(iso-pressure slice).} \tag{3.3}$$

3.1.2 Acoustic telegrapher's equations and the wave equation

A computationally convenient method for impedance analysis is to form two one-dimensional equations in the average pressure Ψ and volume velocity $\mathcal{V}$ (using x to represent the axial direction of propagation). In the frequency domain,

$$\frac{\partial}{\partial x}\begin{bmatrix}\Psi(x,\omega)\\\mathcal{V}(x,\omega)\end{bmatrix} = -\begin{bmatrix}0 & \mathcal{Z}(x,s)\\\mathcal{Y}(x,s) & 0\end{bmatrix}\begin{bmatrix}\Psi(x,\omega)\\\mathcal{V}(x,\omega)\end{bmatrix},\tag{3.4}$$

where $\mathcal{Z}$ is the per-unit-length series impedance, and $\mathcal{Y}$ is the per-unit-length shunt admittance of the transmission line. The two equations in Ψ and $\mathcal{V}$ are the acoustic analogue of the telegrapher's equations. These equations are developed from the lossless or lossy equations of state, continuity, and force, which are described in Appendix A.

Equation 3.4 gives the wave equations[1]

$$\Psi = \frac{1}{\mathcal{Y}}\frac{\partial}{\partial x}\frac{1}{\mathcal{Z}}\frac{\partial \Psi}{\partial x} \quad \text{or} \quad \mathcal{V} = \frac{1}{\mathcal{Z}}\frac{\partial}{\partial x}\frac{1}{\mathcal{Y}}\frac{\partial \mathcal{V}}{\partial x}.\tag{3.5}$$

The following analyses consider the pressure wave equation and its general solutions. Note that an analogous derivation may be performed beginning with the velocity wave equation and its general solutions.

Wave equation for a uniform-area horn. If the acoustic horn in question is of uniform area, then $\mathcal{Z}$ and $\mathcal{Y}$ are independent of the axial coordinate x, and may be factored out of the wave equation,

$$\frac{\partial^2 \Psi}{\partial x^2} = \mathcal{Z}\mathcal{Y}\Psi.\tag{3.6}$$

This differential equation gives the homogeneous solutions

$$\Psi^{\pm} = \alpha_{\pm}e^{\mp\sqrt{\mathcal{Z}\mathcal{Y}}x},\tag{3.7}$$

where the coefficients $\alpha_{\pm}$ can be functions of frequency. Therefore, for a uniform acoustic transmission line the wave-propagation function $\kappa(s)$ is defined as

$$\kappa(s) = \sqrt{\mathcal{Z}\mathcal{Y}}.\tag{3.8}$$

The lossless and lossy solutions for a uniform-area horn are discussed at length in Section A.2.

---

[1]These equations may also be written as $\frac{\partial^2 \Psi}{\partial x^2} - \left(\frac{\partial}{\partial x}\ln\mathcal{Z}\right)\frac{\partial \Psi}{\partial x} = \mathcal{Z}\mathcal{Y}\Psi$ and $\frac{\partial^2 \mathcal{V}}{\partial x^2} - \left(\frac{\partial}{\partial x}\ln\mathcal{Y}\right)\frac{\partial \mathcal{V}}{\partial x} = \mathcal{Z}\mathcal{Y}\mathcal{V}$.

Webster horn equation for a variable-area horn. When $\mathcal{Z}$ and $\mathcal{Y}$ are spatially dependent, the wave equation will not have the form of Equation 3.6. For lossless wave propagation,

$$\mathcal{Z} = \frac{s\rho_0}{A(x)} \quad \text{and} \quad \mathcal{Y} = \frac{sA(x)}{\eta_0 P_0}, \tag{3.9}$$

due to the conservation of momentum and conservation of mass equations, respectively. With this dependence on the area function $A(x)$, the wave equation (Eq. 3.5) may be simplified as

$$\frac{1}{A(x)} \frac{\partial}{\partial x} A(x) \frac{\partial \Psi}{\partial x} = \mathcal{Z}\mathcal{Y}\Psi. \tag{3.10}$$

This is the Webster horn equation (Webster, 1919), and its solutions $\Psi^{\pm}$ will have more than an exponential dependence on x (e.g. Eq. 3.7), if they exist at all. The existence of solutions to this differential equation depends on the existence of an orthogonal coordinate system describing $A(x)$ (Agulló et al., 1999; Keefe & Barjau, 1999), or preferably a separable coordinate system. This is discussed in some detail in Section A.4. The Webster horn equation is also studied in detail in Allen (2016).

For wave propagation with thermal and viscous losses (described in Appendix A), the parameters $\mathcal{Z}$ and $\mathcal{Y}$ have a more complicated dependence on x,

$$\mathcal{Z} = \frac{s\rho_0}{A(x)} \left[1 - F(r_v(x,s)) \right]^{-1} \tag{3.11a}$$

$$\mathcal{Y} = \frac{sA(x)}{\eta_0 P_0} \left[1 + (\eta_0 - 1)F(r_t(x,s)) \right], \tag{3.11b}$$

where r_v and r_t represent ratios of the effective radius of the wavefront to the viscous and thermal boundary layers, respectively. The function F will depend on the cross-sectional geometry of the horn. For circular cross sections, F is a ratio of Bessel functions, and for rectangular cross sections it is a tangent function, as described in Section A.3. For large enough values of r_v and r_t, F is small. In this case, Equation 3.10 is approximately true, and use of the lossy value for κ in the final solution will approximate the effect of visco-thermal losses.

3.1.3 Forward- and reverse-traveling waves

In general the wave-equation solutions take the form

$$\Psi(x,\omega) = \Psi^+ + \Psi^- \tag{3.12a}$$

$$\mathcal{V}(x,\omega) = \mathcal{V}^+ - \mathcal{V}^-$$

$$= \left(\frac{\mathcal{V}^+}{\Psi^+}\right)\Psi^+ - \left(\frac{\mathcal{V}^-}{\Psi^-}\right)\Psi^-$$

$$= y_c^+\Psi^+ - y_c^-\Psi^-. \tag{3.12b}$$

In many applications, the average pressure Ψ and volume velocity $\mathcal{V}$ are specified for some input impedance (e.g. one-port network) of interest at point x, where the positive direction is defined as into the port. The characteristic impedance at the test point x is defined as the ratio of pressure to volume velocity for a single plane wave propagating in one direction, in the absence of any reflections.[2] This is the same as the input impedance of a semi-infinite horn having an area function consistent with the local area variation. It is defined as

$$z_c^\pm(f,x) \equiv \frac{\Psi^\pm(f,x)}{\mathcal{V}\pm(f,x)} = \frac{1}{y_c^\pm(f,x)}. \tag{3.13}$$

Equation 3.4 can be used to determine $y_c^\pm$ by relating $\Psi^\pm$, $\mathcal{V}^\pm$, $\mathcal{Z}$ and $\mathcal{Y}$. These equations yield

$$\mathcal{V}^\pm = \mp\frac{1}{\mathcal{Z}}\frac{\partial\Psi^\pm}{\partial x} \tag{3.14a}$$

$$\Psi^\pm = \mp\frac{1}{\mathcal{Y}}\frac{\partial\mathcal{V}^\pm}{\partial x} \tag{3.14b}$$

$$y_c^\pm = \mp\frac{1}{\mathcal{Z}}\frac{\partial}{\partial x}\ln\Psi^\pm = \mp\left[\frac{1}{\mathcal{Y}}\frac{\partial}{\partial x}\ln\mathcal{V}^\pm\right]^{-1} = \frac{1}{z_c^\pm}. \tag{3.14c}$$

For a horn of uniform area, the characteristic impedance is independent of direction,

$$z_c^+ = z_c^- = \sqrt{\frac{\mathcal{Z}}{\mathcal{Y}}} \equiv z_0 \quad (\text{constant } A(x) = A_0). \tag{3.15}$$

In the wideband acoustic immittance (WAI) literature, the reflectance is traditionally defined using z_0 as in Equation 2.6. However, using this definition, the characteristic impedances of the forward- and reverse-traveling waves are not equal $(z_c^+ \neq z_c^-)$ if the local area function $A(x)$ is not uniform. For example, a conical horn has the general pressure solutions and directional characteristic

---

[2]This is one common definition (https://en.wikipedia.org/wiki/Characteristic_impedance).

impedances given by

$$\Psi^{\pm} = \alpha_{\pm} \frac{e^{\mp \kappa r}}{r} \tag{3.16a}$$

$$y_c^{\pm}(r) = \sqrt{\frac{\mathcal{Y}}{\mathcal{Z}}} \left(1 \pm \frac{1}{\kappa r} \right) = y_0 \left(1 \pm \frac{1}{\kappa r} \right) = \frac{1}{z_c^{\pm}(r)}, \tag{3.16b}$$

where $\alpha_{\pm}$ are functions of frequency and r is the distance from the vertex of the cone ($x = r - R_0$). These equations and further derivations for the conical horn are given in Appendices A and B. In the time domain, given lossless propagation ($\kappa = s/c_0$), the time-domain characteristic admittances and impedances are given by

$$y_c^{\pm}(r, f) \leftrightarrow \frac{1}{r_0} \left(\delta(t) \pm \frac{c_0}{r} u(t) \right) \tag{3.17a}$$

$$z_c^{\pm}(r, f) \leftrightarrow r_0 \left(\delta(t) \mp \frac{c_0}{r} e^{\mp c_0 t/r} u(t) \right). \tag{3.17b}$$

The surge resistance r_0 and conductance $1/r_0$ are defined as the coefficient of the $\delta(t)$ function of the time-domain impedance and admittance. This component does not vary with direction. However, at time $t = 0^+$, the local curvature of the horn contributes to the characteristic impedance and admittance. The forward-traveling component has a positive time-domain step function (diverging wave) while the reverse-traveling component has a negative time-domain step function (converging wave).

The fact that the characteristic impedance depends on direction, $z_c^+ \neq z_c^-$, has implications for the definition of reflectance. The reflectance must be carefully defined in the presence of a locally varying $A(x)$, as discussed next.

3.2   A strict definition for reflectance in horns

The reflectance can be derived using a frequency-domain factorization of the impedance,

$$Z = \frac{\Psi}{\mathcal{V}} = \frac{\Psi^+ + \Psi^-}{\mathcal{V}^+ - \mathcal{V}^-} = \left(\frac{\Psi^+}{\mathcal{V}^+} \right) \frac{1 + \Psi^-/\Psi^+}{1 - \mathcal{V}^-/\mathcal{V}^+}. \tag{3.18}$$

Note that here we consider only the plane-wave solutions for Ψ and $\mathcal{V}$. Also note that there is an implicit direction in which we are viewing the system; let the impedance Z (and reflectance Γ) be that of the load looking in the '+' direction from the test point. Typically, it is assumed that the ratios of reverse- to forward-traveling pressure and velocity are the same. However, if $z_c^+ \neq z_c^-$, then

$$\frac{\Psi^+}{\mathcal{V}^+} \neq \frac{\Psi^-}{\mathcal{V}^-} \implies \Gamma_{\Psi} = \frac{\Psi^-}{\Psi^+} \neq \frac{\mathcal{V}^-}{\mathcal{V}^+} = \Gamma_{\mathcal{V}}, \tag{3.19}$$

where the pressure and velocity reflectances are defined as Γ_Ψ and $\Gamma_\mathcal{V}$ respectively, to acknowledge that their values will be different if the characteristic impedance depends on direction. In this case, the impedance and reflectance are related by

$$Z = z_c^+ \left(\frac{1 + \Gamma_\Psi}{1 - \Gamma_\mathcal{V}} \right). \tag{3.20}$$

Therefore, the relationship between the impedance and pressure (or velocity) reflectance must be carefully defined using the directionally dependent characteristic impedance $z_c^\pm$.

3.2.1 Reflectance definition given a locally varying area function

To define a consistent reflectance given a locally varying area function, it is necessary to choose whether to work with the pressure or velocity reflectance. Here we choose to work with the pressure reflectance Γ_Ψ. Note that typically Γ is defined as the pressure reflectance in WAI literature. Additionally, the primitive spherical wave solutions in the conical horn (Sec. A.4) indicate that the pressure reflectance may have a simpler form than $\Gamma_\mathcal{V}$, since the primitive velocity solutions have two terms.

We will work with the pressure reflectance Γ_Ψ, the admittance Y and the characteristic admittances $y_c^\pm$ for this derivation. In this case, the admittance formula may be factored as

$$
\begin{aligned}
Y(x, s) &= y_c^+ \frac{1 - \mathcal{V}^-/\mathcal{V}^+}{1 + \Psi^-/\Psi^+} \\
&= \frac{y_c^+}{1 + \Gamma_\Psi} \left(1 - \frac{y_c^- \Psi^-}{y_c^+ \Psi^+} \right) \\
&= \frac{y_c^+ - y_c^- \Gamma_\Psi}{1 + \Gamma_\Psi}.
\end{aligned}
\tag{3.21}
$$

A rearrangement of these terms yields the following definitions of the pressure reflectance (looking in the '+' direction):

$$\Gamma_\Psi(x, s) = \frac{y_c^+ - Y}{y_c^- + Y} = \frac{Z/z_c^+ - 1}{Z/z_c^- + 1}. \tag{3.22}$$

The formulas to calculate impedance and admittance from the pressure reflectance are

$$Y(x, s) = \frac{y_c^+ - y_c^- \Gamma_\Psi}{1 + \Gamma_\Psi} \quad \text{and} \quad Z(x, s) = z_c^+ z_c^- \left(\frac{1 + \Gamma_\Psi}{z_c^- - z_c^+ \Gamma_\Psi} \right). \tag{3.23}$$

Note that Y, Γ_Ψ, $y_c^\pm$ and $z_c^\pm$ are all functions of frequency (ω or s) and space (x). This result is consistent with the formula given by Farmer-Fedor & Rabbitt (2002), and simplifies to Equation 2.6 for a uniform-area horn.

Some examples of $y_c^\pm = 1/z_c^\pm$ are given for different area functions $A(x)$ in Table 3.1 for lossless

Table 3.1: Re-defining the characteristic impedance for a consistent definition of reflectance, for uniform, parabolic, conical, and exponential horns. Note that $\kappa = \sqrt{\mathcal{Z}\mathcal{Y}}$ and $z_0 = \sqrt{\mathcal{Z}/\mathcal{Y}}$. For a lossless horn, $\kappa = s/c_0$ and $y_0 = A(x)/\rho_0 c_0$. For the conical and exponential horns, the term $1/k \propto 1/s$, and has the inverse Laplace transform of a unit step.

Type	Area function	Pressure $\Psi^{\pm}$	Characteristic admittance $y_c^{\pm} = \mp \frac{1}{\mathcal{Z}} \frac{\partial}{\partial x} \ln \Psi^{\pm}$
Uniform	$A(x) = A_0$	$\Psi^{\pm} \propto e^{\mp \kappa x}$	y_0
Parabolic	$A(x) \propto x$	$\Psi^{\pm} \propto J_0(\kappa x) \mp Y_0(\kappa x)$, where J_n are Bessel functions and Y_n are Neumann/Weber functions	$y_0 \left[\frac{\pm J_1(\kappa x) - Y_1(\kappa x)}{J_0(\kappa x) \mp Y_0(\kappa x)} \right]$, which is a ratio of Hankel functions.
Conical	$A(r) \propto r^2$, where $r = R_0 + x$ is the distance from the cone apex	$\Psi^{\pm} \propto \frac{e^{\mp \kappa r}}{r}$	$y_0 \left[1 \pm \frac{1}{\kappa r} \right]$
Exponential	$A(x) \propto e^{2mz}$	$\Psi^{\pm} \propto e^{-(m \pm \sqrt{m^2 + \kappa^2})x}$	$y_0 \left[\sqrt{1 + \frac{m^2}{\kappa^2}} \pm \frac{m}{\kappa} \right]$

horns. The uniform-line characteristic admittance $y_0 = \sqrt{\mathcal{Y}/\mathcal{Z}}$ is widely used to define reflectance in the literature. However, it appears that any local area variation at the measurement location may cause errors in the calculation of reflectance.

3.2.2 Supporting evidence and applicability

To our knowledge, the formula for the reflectance given in Equation 3.22 is not widely known. Some instances of this and related formulas in the literature are discussed in this section. Equation 3.22 will be exact when exact solutions to the Webster horn equation (a Sturm-Liouville problem with integrating factor $A(x)$) are available, such that $y_c^{\pm}$ may be calculated. Benade (1988) gives the formula for z_c^{+} for a conical horn, but does not note that z_c^{-} is different. Agulló et al. (1988) and Amir et al. (1995) give the strict reflectance formula for the conical horn, but do not generalize it

to other horn shapes.

Note that when the local horn curvature is unknown, or is discontinuous at the point of interest, it is impractical to define the reflectance in this manner. In this case, it is better to use the surge resistance r_0 (lossless case) or the equivalent uniform-horn characteristic impedance $z_0 = \sqrt{\mathcal{Z}/\mathcal{Y}}$ (lossy case) since these quantities do not depend on the direction of the wave (they only depend on the local cross-sectional area).

Equivalence to Farmer-Fedor & Rabbitt (2002) result. Farmer-Fedor & Rabbitt (2002) derived the same result, but it is heavily obscured by their notation. They defined

$$\Psi^{\pm}(f,x) = \alpha_{\pm}(f)B(x)e^{\mp\phi(f,x)}, \tag{3.24}$$

separating the pressure waves into a frequency-dependent coefficient $\alpha_{\pm}(f)$, an amplitude function $B(x)$ which depends on the axial coordinate x, and an exponential function with a phase $\phi(f,x)$ which depends on both frequency and location (e.g. for a conical horn, $B(x) = 1/(x + R_0)$ and $\phi(f,x) = \kappa(x + R_0)$). For non-separable coordinate systems, Farmer-Fedor & Rabbitt (2002) calculated a solution of this form using the Wentzel, Kramers, and Brillouin (WKB) approximation, which did not yield a robust solution (this problem with the WKB approximation is well known).

Farmer-Fedor & Rabbitt (2002) found that the pressure reflectance may be derived by taking the spatial derivative $\frac{\partial}{\partial x}\ln(\Psi^+ + \Psi^-)$ and re-grouping the terms to form the ratio

$$\Gamma = \frac{\alpha_-}{\alpha_+}e^{2\phi} = \frac{\frac{\partial}{\partial x}\ln\Psi - \frac{\partial}{\partial x}\ln B + \frac{\partial}{\partial x}\phi}{-\frac{\partial}{\partial x}\ln\Psi + \frac{\partial}{\partial x}\ln B + \frac{\partial}{\partial x}\phi}. \tag{3.25}$$

This equation relates to the transmission-line parameters via

$$\frac{\partial}{\partial x}\ln\Psi = -\mathcal{Z}Y \tag{3.26a}$$

$$\pm\frac{\partial}{\partial x}\ln B + \frac{\partial}{\partial x}\phi = \mathcal{Z}y_c^{\pm}, \tag{3.26b}$$

which yields Equation 3.22 for the pressure reflectance. We feel that the derivation given here is much easier to follow, and more intuitive for researchers who are familiar with transmission-line theory.

The step admittance and 'type-II' reflectance of Rasetshwane & Neely (2011). Rasetshwane & Neely (2011) found they needed to define reflectance using a Heaviside step function $u(t) \leftrightarrow 1/s$ in addition to $y_0 = \sqrt{\mathcal{Y}/\mathcal{Z}}$ in simulations and measurements of horns; they give an equation similar to Equation 3.22 and refer to it as type-II reflectance.[3] However, they did not properly derive the origin of the $1/s$ term. As discussed in this section, the $1/s$ term originates from the characteristic

---

[3]Note that Rasetshwane & Neely (2011) was published first, but the inverse method is detailed in the later publication Rasetshwane et al. (2012). This method is also used in Rasetshwane & Neely (2015).

admittance $y_c^{\pm}$ and their type-II reflectance is equivalent to Equation 3.22 when there is a local conical flare. Using Equation 3.22, there need only be one definition of reflectance.

Rasetshwane & Neely (2011) used a lossless, reflectance-based inverse solution method to determine $A(x)$ from the impedance at the mouth of the horn. For calculations with reflectance, they found it was necessary to define

$$\Gamma(x,\omega) = \frac{y_0(x) - [Y(x,\omega) - Y_s(x,\omega)]}{y_0(x) + [Y(x,\omega) - Y_s(x,\omega)]}, \qquad (3.27)$$

where $y_0(x) = \sqrt{\mathcal{Y}/\mathcal{Z}} = A(x)/(\rho_0 c_0)$ is the characteristic admittance of a uniform transmission line having the same area, Y is the measured (simulated) admittance, and the 'step admittance' Y_s was calculated from Y via

$$Y_s(x,\omega) = \frac{y_0}{j\omega} \lim_{\omega \to \infty} j\omega \left[\frac{Y(x,\omega)}{y_0} - 1 \right]. \qquad (3.28)$$

This formula appears to be related to the initial value theorem of the Laplace transform (Lundberg et al., 2007). Ideally the limit would be taken as $\Re(s) = \sigma \to \infty$, but the full admittance $Y(s)$ is not available for measured data (though Y could be fit with a pole-zero rational approximation (Gustavsen & Semlyen, 1999; Robinson et al., 2013)). This calculation yielded a 'step admittance'

$$Y_s(x,s) = \frac{y_0(x)}{\kappa} \beta(x) \qquad (3.29)$$

$$= \frac{c_0 y_0(x)}{s} \beta(x) \quad \text{(lossless)}, \qquad (3.30)$$

where β is a constant that depends on the axial depth x at which the reflectance is calculated. This function is called the step admittance because it is the Laplace transform of the Heaviside function $u(t) \leftrightarrow 1/s$. Note that when analysis is conducted using Fourier transforms (necessary with real data) the step function $u(t) \leftrightarrow \pi\delta(\omega) + 1/j\omega$, since the Fourier transform is not well-equipped to treat causal functions. The subtle problem with the Fourier transform is not addressed in Rasetshwane & Neely (2011) or Rasetshwane et al. (2012).

When Y_s is combined with y_0 rather than Y, it gives

$$y_0 \pm Y_s = y_0 \left(1 \pm \frac{\beta}{\kappa} \right). \qquad (3.31)$$

This term is same as the characteristic admittances $y_c^{\pm}$ of a conical horn, as given in Table 3.1. Under this interpretation, $r_e = 1/\beta$ is the effective distance to the cone apex, which describes the local flare of the horn as a first-order approximation. This term is also approximately equal to the

characteristic admittances $y_c^{\pm}$ for an exponential horn of area $A(x) = e^{2\beta x}$,

$$y_0 \pm Y_s \approx y_0 \left(\sqrt{1 + \frac{\beta^2}{\kappa^2}} \pm \frac{\beta}{\kappa} \right). \tag{3.32}$$

In their calculation of the area function, Rasetshwane & Neely (2011) implicitly attribute exponential curvature to each area segment calculated, as will be discussed in Section 3.4.2.

The results of this section suggest that Rasetshwane & Neely (2011) calculated the pressure reflectance correctly according to Equation 3.22, but should attribute Y_s to the characteristic admittance,

$$\Gamma(x, \omega) = \frac{[y_0(x) + Y_s(x, \omega)] - Y(x, \omega)}{[y_0(x) - Y_s(x, \omega)] + Y(x, \omega)} = \frac{y_c^+ - Y}{y_c^- + Y}. \tag{3.33}$$

Therefore, Rasetshwane & Neely (2011) find

$$\beta(x) = \frac{1}{2} \frac{\partial}{\partial x} \ln(A(x)) = \frac{1}{2A(x)} \frac{\partial A(x)}{\partial x}, \tag{3.34}$$

which is equal to $1/r$ in the case of a conical horn and equal to m in the case of the exponential horn (Table 3.1). For the parabolic horn this conical approximation would overestimate the local flare, which seems to have led to some computational problems for Rasetshwane & Neely (2011).

3.3 Synthesis of acoustic horns of known area function

This section treats the problem of describing the properties of an acoustic horn, such as its impedance and transfer function, given its area function $A(x)$. The primary method described is that of two-port network modeling. This has applications for modeling the ear canal and estimating the WAI of the middle ear. Additionally, it can be used to describe sound-delivery systems such as the measurement probe, as described in the next chapter. Particularly, a probe tip that is added on as part of the measured impedance is studied.

Exact calculation of plane-wave solutions in variable-area horns is not usually possible, due to limitations of the wave-equation solutions. Exact solutions are generally only available when there is a separable coordinate system describing the entire horn, and the system is assumed to be lossless. Typically, a variable-area horn may be adequately described using a concatenation of conical or cylindrical horns, which have known impedance properties. For low frequencies and constricted passages, where the viscous and thermal boundary layer is more than one-tenth of the effective radius, thermo-viscous losses should be approximated. Note that these methods may or may not take into account curvature of the iso-pressure wavefront in a given horn.

Alternatively, approximations to the wave equation may be made in order to describe a special, tractable coordinate system for the given area function. One example of such a method is the curvilinear horn equation (Agulló et al., 1999; Keefe & Barjau, 1999). This equation allows adjoining

orthogonal curvilinear coordinate systems to be sewn together via a 'thickness function.' In theory, this should provide more exact results, though in practice is likely to yield small corrections at the cost of a much higher complexity. A simple theory approximating the area function as a Fourier series is also presented in this section.

3.3.1   Two-port network modeling

A two-port network model, described by Figure 3.1, describes the impedance and transfer properties from an input (port 1) to an output (port 2). These properties can be completely described in the frequency domain using a 2×2 matrix. Matrices for cylindrical tubes, conical horns, and step discontinuities are given in Appendix 3.3.1. These networks may be connected in cascade to approximate any area function, resulting in a single 2×2 matrix. Properties of two-port matrices are discussed at length in Appendix B.
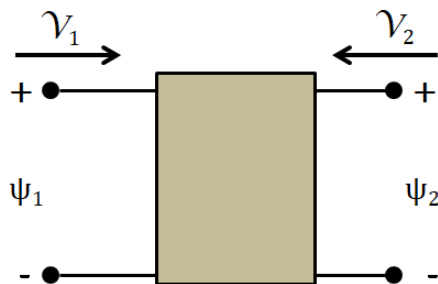
Figure 3.1:   An acoustic two-port network showing the average pressures Ψ and volume velocities $\mathcal{V}$ at the input (1) and output (2). The direction of $\mathcal{V}_2$ is defined as into the port, as required by the definition of the impedance matrix. Two-port properties and solutions for cylindrical tubes, conical horns, and step discontinuities are discussed at length in Appendix B.

Transmission parameters for the conical horn were originally given by Benade (1988), and step discontinuities in area were described by Karal (1953). When the effective radius of the cross-section is much larger than the boundary layer, lossless models suffice. To include the effects of viscous and thermal losses, typically the lossy propagation function and characteristic impedance may be calculated using the exact Bessel-function solution (e.g. Keefe (1984)) for circular cross-sections, as described in Section A.2.2. For non-circular cross-sections, the propagation function can usually be approximated using an 'effective radius' and the cylindrical or parallel plate solution for visco-thermal losses (Richards, 1986), as described in Section A.3. A similar solution for arbitrary geometry was first given by Rayleigh (1896).

Typically, a smoothly varying area function can be approximated by the concatenation of many short conical or cylindrical segments. Mapes-Riordan (1993) approximated horn functions using both of these methods, and found that conical horns provided the best approximation. However, he did not include the Karal (1953) correction for step discontinuities in the cylindrical model,

which would likely improve the approximation.

A small number of conical horns may also be used to determine an area function via least-squares model fitting. For example, Lewis & Neely (2015) use seven conical sections and a low-order model for the middle ear to fit WAI data measured in the ear canal. However, this fitting procedure relies heavily on knowledge of the terminating impedance, the TM and ossicles, to accurately determine the ear-canal area function. The next section describes inverse methods that rely on the time-domain impedance and reflectance. Using these methods, the terminating impedance does not affect the estimated area function, because the area function is estimated up to some point using time-domain information preceding the round-trip travel time to that point and back.

General two-port solution. For wave propagation in a tube ($A(x) = A_0$) or horn ($A(x)$), first represent the average pressure and volume velocity by a matrix. Assume that the solutions are separable into a frequency-dependent amplitude term, and a frequency- and space-dependent term with axial coordinate x, such that [4]

$$\Psi(x,\omega) = \alpha_+(\omega)\widehat{\Psi}^+(x,\omega) + \alpha_-(\omega)\widehat{\Psi}^-(x,\omega). \tag{3.35}$$

If the horn is terminated in a load at port 2 (e.g. Fig. B.1), $x = L = x_2$, the amplitude terms will be related by a reflection coefficient $\Gamma_2(\omega) = \alpha_-(\omega)/\alpha_+(\omega)$. The pressure and volume velocity are given by

$$\begin{bmatrix} \Psi(x,\omega) \\ \mathcal{V}(x,\omega) \end{bmatrix} = \begin{bmatrix} \widehat{\Psi}^+(x,\omega) & \widehat{\Psi}^-(x,\omega) \\ y_c^+(x,\omega)\widehat{\Psi}^+(x,\omega) & -y_c^-(x,\omega)\widehat{\Psi}^-(x,\omega) \end{bmatrix} \begin{bmatrix} \alpha_+(\omega) \\ \alpha_-(\omega) \end{bmatrix}. \tag{3.36}$$

Recall that $y_c^\pm(x,\omega) = \mathcal{V}^\pm(x,\omega)/\Psi^\pm(x,\omega)$ is the characteristic admittance, which depends on direction for a variable-area horn. It is possible to solve for the coefficients $\alpha_\pm(\omega)$ in terms of the load pressure and volume velocity, Ψ_2 and $\mathcal{V}_2$. At this step, we may also define the direction of $\mathcal{V}_2$ as 'into the port,' which is convenient for analysis of the corresponding impedance matrix. This gives

$$\begin{bmatrix} \Psi_2 \\ -\mathcal{V}_2 \end{bmatrix} = \begin{bmatrix} \widehat{\Psi}^+(x_2,\omega) & \widehat{\Psi}^-(x_2,\omega) \\ y_c^+(x_2,\omega)\widehat{\Psi}^+(x_2,\omega) & -y_c^-(x_2,\omega)\widehat{\Psi}^-(x_2,\omega) \end{bmatrix} \begin{bmatrix} \alpha_+(\omega) \\ \alpha_-(\omega) \end{bmatrix}$$

$$\begin{bmatrix} \alpha_+(\omega) \\ \alpha_-(\omega) \end{bmatrix} = \frac{1}{\widehat{\Psi}_2^+\widehat{\Psi}_2^-(y_{c,2}^- + y_{c,2}^+)} \begin{bmatrix} y_{c,2}^-\widehat{\Psi}_2^- & \widehat{\Psi}_2^- \\ y_{c,2}^+\widehat{\Psi}_2^+ & -\widehat{\Psi}_2^+ \end{bmatrix} \begin{bmatrix} \Psi_2 \\ -\mathcal{V}_2 \end{bmatrix}. \tag{3.37}$$

---

[4]In terms of Equation 3.24, $\widehat{\Psi}^\pm(x,\omega) = B(x)e^{\mp\phi(x,\omega)}$.

By substituting the expression for $\alpha_\pm(\omega)$ back into Equation 3.36, the following expression may be obtained:

$$\begin{bmatrix} \Psi_1 \\ \mathcal{V}_1 \end{bmatrix} = \frac{1}{\widehat{\Psi}_2^+ \widehat{\Psi}_2^- (y_{c,2}^- + y_{c,2}^+)} \begin{bmatrix} \widehat{\Psi}_1^+ & \widehat{\Psi}_1^- \\ y_{c,1}^+ \widehat{\Psi}_1^+ & -y_{c,1}^- \widehat{\Psi}_1^- \end{bmatrix} \begin{bmatrix} y_{c,2}^- \widehat{\Psi}_2^- & \widehat{\Psi}_2^- \\ y_{c,2}^+ \widehat{\Psi}_2^+ & -\widehat{\Psi}_2^+ \end{bmatrix} \begin{bmatrix} \Psi_2 \\ -\mathcal{V}_2 \end{bmatrix}$$

$$= \begin{bmatrix} A & B \\ C & D \end{bmatrix} \begin{bmatrix} \Psi_2 \\ \mathcal{V}_2 \end{bmatrix} = \begin{bmatrix} A & B \\ C & D \end{bmatrix} \begin{bmatrix} \Psi_2 \\ -\mathcal{V}_2 \end{bmatrix}. \tag{3.38}$$

The input impedance $Z_1 = \Psi_1/\mathcal{V}_1$, and the load impedance $Z_2 = -\Psi_2/\mathcal{V}_2$. Using the two-port model, the input impedance may determined given the load impedance, and vice versa.

3.3.2 Fourier series analysis of the area function

The differential equation for an exponential horn is separable and easily solved[5] (Pierce, 1981; Beranek & Mellow, 2012; Allen, 2016). This offers an interesting solution to the Webster horn equation (Eq. A.91), as an arbitrary area function of finite length L may be represented using a Fourier series,

$$A(x) = \sum_{n=-\infty}^{\infty} a_n e^{j\nu_n x}, \qquad \nu_n = 2\pi n/L \tag{3.39}$$

where ν_n are discrete spatial frequencies. Note that the use of a Fourier series implies that the area function is periodically extended. Applying this series expansion to the Webster horn equation gives

$$\frac{\partial}{\partial x} \left[\sum_{n=-\infty}^{\infty} a_n e^{j\nu_n x} \right] \frac{\partial}{\partial x} \Psi = \left[\sum_{n=-\infty}^{\infty} a_n e^{j\nu_n x} \right] \kappa^2 \Psi. \tag{3.40}$$

By superposition, this yields a (potentially infinite) sum of primitive pressure solutions Ψ_n, as the equation for each spatial mode is

$$\frac{1}{e^{j\nu_n x}} \frac{\partial}{\partial x} e^{j\nu_n x} \frac{\partial}{\partial x} \Psi_n = \kappa^2 \Psi_n \tag{3.41a}$$

$$j\nu_n \frac{\partial \Psi_n}{\partial x} + \frac{\partial^2 \Psi_n}{\partial x^2} = \kappa^2 \Psi_n. \tag{3.41b}$$

This equation is the familiar equation for a horn with an exponentially varying area function $A(x) = e^{2mz} = e^{j\nu_n z}$ which has a well-known solution (e.g. Table 3.1). The nth equation has the forward- and reverse-traveling pressure solutions

$$\Psi_n^\pm \propto e^{-(j\nu_n/2 \pm \sqrt{\kappa^2 + (j\nu_n/2)^2})x}. \tag{3.42}$$

---

[5]When not accounting for the curvature of the iso-pressure wavefronts (Agulló et al., 1999; Keefe & Barjau, 1999)

Therefore, the total pressure may be described by

$$\Psi(\omega, x) = \sum_{n=-\infty}^{\infty} \left[\alpha_{n,+}(\omega) e^{-(j\nu_n/2 + \sqrt{\kappa^2 - \nu_n^2/4})x} + \alpha_{n,-}(\omega) e^{-(j\nu_n/2 - \sqrt{\kappa^2 - \nu_n^2/4})x} \right], \qquad (3.43)$$

where the coefficients $\alpha_{n,\pm}(\omega)$ must be determined by the impedance boundary conditions of the horn.

This method bears resemblance to the work of Schroeder (1967) and Mermelstein (1967), who estimated the area function of the vocal tract using measured vowel formant frequencies. Schroeder (1967) specifically mentions that the area function may be represented by a Fourier series, but fails to note that this would lead to an exact solution (due to the fact that when the area function is exponential, the Sturm-Louisville equation has an exact solution). Thus this expansion is a key result, presented here for the first time. Note that solutions to this method require assumptions regarding the terminating load impedance.

3.4   Inverse solution for horns of unknown area function

The area function of an unknown acoustic horn may also be estimated using time-domain inverse methods. These methods are far less dependent on knowledge of the load impedance (e.g. the middle ear), as they consider the early-time signal, prior to any reflections from the load. In general, the area function up to some point x_a in the horn can be estimated from the first $2t_a$ [s] of the time signal, defined as the time it takes for an impulse at the input to travel to the point x_a and back. Two inverse methods are presented in this section. The first method is based on the time-domain impedance impulse response, and was developed by (Sondhi & Gopinath, 1971), though preceded by similar methods such as that of Youla (1964). The second method is based on the time-domain reflectance and the Webster horn equation, as described by Rasetshwane et al. (2012). This method appears to be similar to the 'step reflectance' method given in Sondhi & Resnick (1983).
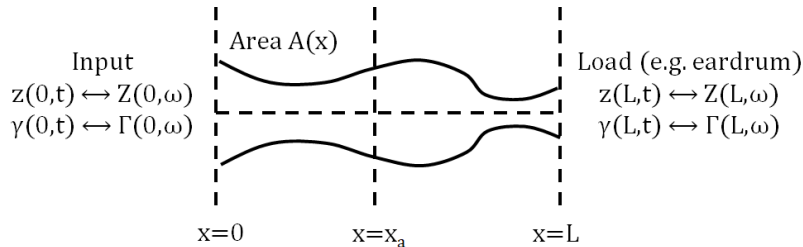
Figure 3.2:   Diagram of an arbitrary variable-area acoustic horn of area function $A(x)$. The x coordinate represents the central axis; typically slight curvature of this axis does not have a large effect on the acoustic results. The coordinate $x = x_a$ represents an arbitrary point of analysis. The horn is terminated in an unknown acoustic load at $x = L$.

Consider the variable-area horn shown in Figure 3.2. To analyze the area at x_a in the time domain, it can be related to the time-of-travel t_a to that point for an impulse entering the system at $x = 0$,

$$t_a = \int_0^{x_a} \frac{1}{c_0} dx = \frac{x_a}{c_0}, \tag{3.44}$$

where c_0 is the speed of sound in a lossless acoustic horn. As noted by Youla (1964), if the velocity depends on position, this may be described by the integral over the function $c(x)$,

$$t_a = \int_0^{x_a} \frac{1}{c(x)} dx. \tag{3.45}$$

For a lossless acoustic system, a spatially dependent speed of sound $c(x)$ would be due to spatial changes in equilibrium pressure, density, temperature or other gas properties. For the systems considered in this thesis, such changes do not apply. It is important to note that lossy acoustic horns will have dispersion, such that the phase velocity is a function of frequency as well as position,

$$c(x, \omega) = \frac{\omega}{\Im[\kappa(x, \omega)]}. \tag{3.46}$$

In this case, the travel time t_a for a plane wave to the point x_a will be frequency-dependent. Sondhi & Resnick (1983) offer a modified inverse method accounting for visco-thermal losses, but note that the solutions computed will be non-unique.

Note that time-domain analysis is limited by the bandwidth of the WAI measurement. Good resolution in the time domain and description of the signal near $t = 0$ (e.g. delta function and unit-step behavior) is contingent upon a broad frequency range of measurement, and the high-frequency signal. Additionally, WAI measurements are very sensitive to low-frequency noise, so data below 100-200 Hz is not typically available, which limits the accuracy of the time-domain reflectance estimation.

3.4.1 Impedance method

The impedance-based method proposed by Sondhi & Gopinath (1971) is based on the convolution relationship between the time-domain impedance at $x = 0$ (e.g. Fig. 3.2) and the average pressure and volume velocity,

$$\psi(0, t) = z(0, t) \star v(0, t), \tag{3.47}$$

and the time-domain continuity equation

$$\frac{\partial v}{\partial x} = -\frac{A(x)}{\rho_0 c_0^2} \frac{\partial \psi}{\partial t}. \tag{3.48}$$

Area function from the continuity equation. To solve for the area function from the continuity equation, both sides of the equation are integrated over $x \in (0, x_a)$ and $t \in (t_0, t_0 + t_a)$.

These intervals describe the depth x_a and time of travel t_a to some point along the horn for an impulse entering the system at $t = t_0$. This gives

$$\int_{t_0}^{t_0+t_a} dt \int_0^{x_a} dx \frac{\partial v}{\partial x} = -\frac{1}{\rho_0 c_0^2} \int_0^{x_a} dx A(x) \int_{t_0}^{t_0+t_a} dt \frac{\partial \psi}{\partial t} \tag{3.49a}$$

$$\int_{t_0}^{t_0+t_a} dt \left[v(x_a,t) - v(0,t) \right] = -\frac{1}{\rho_0 c_0^2} \int_0^{x_a} dx A(x) \left[\psi(x, t_0+t_a) - \psi(x,t_0) \right]. \tag{3.49b}$$

A crucial step in simplifying these equations requires some intuition regarding the behavior of a wave propagating through space and time in the horn. For an impulse entering the system at $t = t_0$ and $x = 0$, no disturbance is expected at $x = x_a$ until time $t = t_0 + t_a$. Therefore, $v(x_a, t)$ is expected to be 0 over the time range of integration on the left-hand side of this equation. Consequently, at $t = t_0$ there should be no disturbance for $x > 0$; therefore, $\psi(x, t_0)$ is equal to 0 over the spatial range of integration on the right-hand side of this equation. This gives

$$\int_{t_0}^{t_0+t_a} v(0,t)dt = \frac{1}{\rho_0 c_0^2} \int_0^{x_a} A(x)\psi(x, t_0+t_a)dx. \tag{3.50}$$

In order to relate the velocity $v(0,t)$ at the input to the area function, it is necessary to impose the condition

$$\psi(x, t_0+t_a) = 1, \quad 0 \le x \le x_a. \tag{3.51}$$

For clarity, we will use the subscript a to denote the velocity function $v_a(0,t)$ that produces this condition

$$\psi(0, t_0+t_a) = 1 = z(0,t) \star v_a(0,t) \Big|_{t=t_0+t_a}. \tag{3.52}$$

Under the unity condition on the spatial pressure function, the integral of the time-domain velocity at the input gives the volume of the horn up to x_a,

$$V(x_a) = \int_0^{x_a} A(x)dx = \frac{1}{\rho_0 c_0^2} \int_{t_0}^{t_0+t_a} v_a(0,t)dt. \tag{3.53}$$

Therefore, in order to determine the area function, it is possible to solve for the volume function over a discrete set of values x_a, and find the area function by taking the derivative of $V(x)$. Note that a new function $v_a(0,t)$ leading to the condition $\psi(x, t_0+t_a) = 1$ for $x \in [0, x_a]$ must be found for each x_a.

Time-domain volume velocity $v_a(0,t)$ for constant pressure at time $t_0 + t_a$. The solutions $v_a(0,t)$ for various values of x_a are obtained using the convolution formula for the impedance

impulse response at $x = 0$,

$$\psi(0, t) = v(0, t) \star z(0, t)$$

$$= \int_{-\infty}^{\infty} v(0, \tau)z(0, t - \tau)d\tau$$

$$= \int_{t_0}^{t} v(0, \tau)z(0, t - \tau)d\tau. \tag{3.54a}$$

The bounds of the convolution are determined by the fact that the impedance is causal ($z(0, t-\tau) = 0$ when $\tau > t$) and the velocity must be zero before the system is excited at t_0. This is a Volterra integral equation of the first kind, whose solution is the function $v(0, t)$ given known functions ψ and z. Decomposing the impedance into a delta-function and remainder component, setting $t_0 = 0$, and taking the pressure at $t = t_0 + t_a = t_a$,

$$z(0, t) = r_0\delta(t) + \hat{z}(t) \tag{3.55a}$$

$$\psi(0, t_a) = 1 = r_0 v_a(0, t_a) + \int_0^{t_a} v_a(0, \tau)\hat{z}(0, +t_a - \tau)d\tau. \tag{3.55b}$$

This is a Volterra integral of the second kind, which can be solved to find $v_a(0, t)$ for $t \in [0, t_a]$. The advantage of using this equation over the previous one is that it specifically treats the $\delta(t)$ function at $t = 0$ in the time-domain impedance.

Using the functions $v_a(0, t)$ for $t \in [0, t_a]$, the discrete solution for the area is

$$A(x_{a_n}) = \frac{1}{\rho_0 c_0^2} \left[\frac{\int_0^{t_{a_{n+1}}} v_{a_{n+1}}(0, t)dt - \int_0^{t_{a_n}} v_{a_n}(0, t)dt}{x_{a_{n+1}} - x_{a_n}} \right]. \tag{3.56}$$

Symmetric solution. Sondhi & Gopinath (1971) create a symmetric Fredholm integral equation by constructing symmetric functions such that

$$\widetilde{\psi}(x, t) = \psi(x, t) + \psi(x, -t) \tag{3.57a}$$

$$\widetilde{v}(x, t) = v(x, t) - v(x, -t), \tag{3.57b}$$

which still satisfy the equations of continuity and motion (e.g. Eq. 3.4). To proceed, the following relationship is necessary:

$$\widetilde{\psi}(0, t) = 2 \ \& \ \widetilde{v}(0, t) = 0, \ |t| \leq t_a \implies \psi(x, 0) = 1, \ 0 \leq x \leq x_a. \tag{3.58}$$

This proof relates to the Cauchy problem for differential equations, and is discussed in detail in Gopinath & Sondhi (1971). Under these conditions, the solution is also unique. It follows from Equation 3.58 that $v(0, t) = v(0, -t)$.

Begin with the convolution relationship

$$\widetilde{\psi}(0,t) = v(0,t) \star z(0,t) + v(0,-t) \star z(0,-t)$$

$$= \int_{t_0}^{t} v(0,\tau)z(0,t-\tau)d\tau + \int_{t_0}^{-t} v(0,-\tau)z(0,-t-\tau)d\tau$$

$$= r_0 v(0,t) + \int_{t_0}^{t} v(0,\tau)\hat{z}(0,t-\tau)d\tau + r_0 v(0,-t) + \int_{t_0}^{-t} v(0,-\tau)\hat{z}(0,-t-\tau)d\tau. \quad (3.59)$$

If $t_0 = -t_a$, it is possible to simplify this equation using Equation 3.58,

$$\widetilde{\psi}(0,t) = 2 = 2r_0 v(0,t) + \int_{-t_a}^{t} v(0,\tau)\hat{z}(0,t-\tau)d\tau + \int_{-t_a}^{-t} v(0,-\tau)\hat{z}(0,-t-\tau)d\tau$$

$$= 2r_0 v(0,t) + \int_{-t_a}^{t} v(0,\tau)\hat{z}(0,t-\tau)d\tau - \int_{t_a}^{t} v(0,\tau')\hat{z}(0,-t+\tau')d\tau', \quad \tau' = -\tau$$

$$= 2r_0 v(0,t) + \int_{-t_a}^{t} v(0,\tau)\hat{z}(0,t-\tau)d\tau + \int_{t}^{t_a} v(0,\tau')\hat{z}(0,-(t-\tau'))d\tau'$$

$$= 2r_0 v(0,t) + \int_{-t_a}^{t_a} v(0,\tau)\hat{z}(0,|t-\tau|)d\tau. \quad (3.60)$$

To form the final equation, we allow the impedance kernel $\hat{z}$ to be a symmetric function. Since the impedance z is causal, and the delta-function component has been removed, this is an acceptable construction (the postive- and negative-time functions do not overlap).

This gives the Fredholm integral equation

$$r_0 v_a(0,t) + \frac{1}{2}\int_{-t_a}^{t_a} v_a(0,\tau)\hat{z}(0,|t-\tau|)d\tau = 1, \quad |t| \le t_a, \quad (3.61)$$

whose solutions are the functions $v_a(0,t)$, $|t| \le t_a$. The symmetry of this equation helps to simplify discrete solution methods (e.g. Caflisch (1981)). Given a numerical impulse response $z(t)$, the solution to this integral is the inversion of a convolution matrix. `Matlab` packages for numerically solving such Fredholm integrals for continuous functions are also available online (Atkinson & Shampine, 2008).

Tracking the constants. As Sondhi & Gopinath (1971) set all constants to 1, it is helpful to determine what the solution is in terms of these constants. Putting the above equations in the

51

same form as Sondhi & Gopinath (1971) gives

$$\frac{1}{r_0 \rho_0 c_0^2} = f_a(0,t) + \frac{1}{2} \int_{-t_a}^{t_a} f_a(0,\tau) h(0, |t-\tau|) d\tau, \qquad |t| \le t_a \tag{3.62a}$$

$$V(x_a) = \int_0^{x_a} A(x) dx = \int_0^{t_a} f_a(0,t) dt, \tag{3.62b}$$

$$f_a(0,t) = \frac{1}{\rho_0 c_0^2} v_a(0,t) \tag{3.62c}$$

$$h(0, |t|) = \frac{1}{r_0} \hat{z}(0, |t|) = \frac{1}{r_0} \left[z(0, |t|) - r_0 \delta(t) \right]. \tag{3.62d}$$

Taking the derivative of Equation 3.62a, Sondhi & Gopinath (1971) showed that

$$A(x_a) = \left[f_a(0, t_a) \right]^2. \tag{3.63}$$

Therefore, the area function may be determined directly from the solution f_a, given that the Fredholm integral is solved in the form given in Equation 3.62a.

3.4.2 Reflectance method

The inverse solution of Rasetshwane & Neely (2011) (developed in Rasetshwane et al. (2012)) uses the time-domain reflectance to determine the unknown area function, assuming lossless wave propagation. This is accomplished via a formulation of the Webster horn equation (Eq. A.91) in terms of the forward and retrograde pressure signals. Recall that

$$\Gamma(0,f) = \frac{\Psi^-(0,f)}{\Psi^+(0,f)} \quad \leftrightarrow \quad \psi^-(0,t) = \psi^+(0,t) \star \gamma(0,t). \tag{3.64}$$

Due to the convolution relationship between the forward and retrograde pressures, if $\psi^+(0,t) = \delta(t)$ then

$$\psi^-(0,t) = \gamma(0,t). \tag{3.65}$$

The reflectance method takes advantage of this fact, using the theoretical (or measured) time-domain reflectance impulse response at the input.

Note that a correct definition of reflectance is critical to the success of this method. As discussed in Section 3.2.2, Rasetshwane et al. (2012) ultimately used the correct definition,

$$\Gamma = \frac{y_c^+ - Y}{y_c^- + Y}. \tag{3.66}$$

Rasetshwane et al. (2012) did not correctly identify the contribution of the term $y_c^{\pm} \pm y_0$, attributing it to the measured (or simulated) admittance Y rather than to the characteristic admittance.

However, their final solution is correct. The following derivations will be stated in terms of $y_c^{\pm}$ for clarity. Rasetshwane et al. (2012) effectively approximated the characteristic admittance $y_c^{\pm}$ at each spatial step as

$$y_c^{\pm}(x,\omega) \approx \frac{A(x)}{\rho_0 c_0}\left[1 \pm \frac{c_0\beta(x)}{j\omega}\right] \tag{3.67a}$$

$$\beta(x) = \lim_{\omega \to \infty} j\omega\left[\frac{Y(x,\omega)}{y_0} - 1\right]. \tag{3.67b}$$

Wave variables. The forward and retrograde wave variables Ψ^+ and Ψ^- may be derived from the pressure and velocity equations

$$\Psi = \Psi^+ + \Psi^- \tag{3.68a}$$

$$\mathcal{V} = y_c^+\Psi^+ - y_c^-\Psi^-. \tag{3.68b}$$

Solving these equations for $\Psi^{\pm} \leftrightarrow \psi^{\pm}$ yields

$$\Psi^{\pm}(x,\omega) = \frac{1}{2}\left[\left(1 \mp \frac{c_0\beta(x)}{j\omega}\right)\Psi(x,\omega) \pm \frac{1}{y_0(x)}\mathcal{V}(x,\omega)\right] \tag{3.69a}$$

$$\psi^{\pm}(x,t) = \frac{1}{2}\left[\psi(x,t) \mp c_0\beta(x)\int_0^t \psi(x,t')dt' \pm \frac{1}{y_0(x)}v(x,t)\right]. \tag{3.69b}$$

By differentiating the time-domain pressures in time and space, and using the conservation of mass and momentum equations,

$$\frac{\partial\psi}{\partial x} = -\frac{\rho_0}{A(x)}\frac{\partial v}{\partial t} \quad \text{and} \quad \frac{\partial v}{\partial x} = -\frac{A(x)}{\rho_0 c^2}\frac{\partial\psi}{\partial t},$$

they define the directional derivatives

$$\left[\frac{\partial}{\partial x} \pm \frac{1}{c_0}\frac{\partial}{\partial t}\right]\psi^{\pm} = -\frac{1}{2}\beta(x)\psi(x,t) \mp \left[\left(\frac{1}{2}\frac{1}{A(x)}\frac{\partial A}{\partial x} - \frac{1}{2}\beta(x)\right)\frac{v(x,t)}{y_0(x)} + \frac{c_0}{2}\frac{\partial\beta}{\partial x}\int_0^t \psi(x,t')dt'\right]$$

$$= -\frac{1}{2}\beta(x)\psi(x,t) \mp \left[\left(\varepsilon(x) - \frac{1}{2}\beta(x)\right)\frac{v(x,t)}{y_0(x)} + \eta(x)\int_0^t \psi(x,t')dt'\right]. \tag{3.70}$$

Solution. Beginning with Equation 3.70 and $\psi^{\pm}(x,t)$, $A(x)$ and $\beta(x)$ at $x = 0$, they used a finite-difference time-domain method to solve for these parameters (and $\varepsilon(x)$ and $\eta(x)$) at each spatial step. Note that each spatial step $\Delta x = c_0\Delta t$ for lossless propagation, where Δt is the time-of-travel across a distance of Δx.

At each step of the algorithm, the total pressure and volume velocity were recalculated as

$$\psi = \psi^+ + \psi^- \tag{3.71a}$$

$$\begin{aligned} v &= y_c^+ \star \psi^+ - y_c^- \star \psi^- \\ &= y_0(x) \left[\psi^+ - \psi^- + c_0 \beta(x) \int_0^t \psi(0, t') dt' \right]. \end{aligned} \tag{3.71b}$$

Additionally, a boundary condition requiring the retrograde pressure to vanish at the wavefront was imposed,

$$\psi^-(x, t) = 0, \quad x \geq c_0 t. \tag{3.72}$$

This boundary condition states the no wave is propagating back from beyond the wavefront, since the wave has not penetrated the system past this point. These equations provided sufficient information to calculate $\varepsilon(x)$ and $\eta(x)$ at each step.

The area function and flare parameter were incrementally adjusted at each step of the algorithm via

$$A(x_{n+1}) = A(x_n) e^{2c_0 \varepsilon_n \Delta t} = A(x_n) e^{2\varepsilon_n \Delta x} \tag{3.73a}$$

$$\beta(x_{n+1}) = \beta(x_n) + 2\eta_n \Delta t = \beta(x_n) + \frac{\Delta \beta}{\Delta x} c_0 \Delta t = \beta(x_n) + \Delta \beta. \tag{3.73b}$$

Note that the area solution has an exponential form,

$$A(x_N) = \prod_{n=1}^{N} e^{2\varepsilon_n \Delta x} = e^{2\Delta x \sum_{n=1}^{N} \varepsilon_n}. \tag{3.74}$$

For a continuous function $\beta(x)$, this expression becomes

$$A(x) = e^{2 \int_0^x \beta(x') dx'}. \tag{3.75}$$

Rasetshwane et al. (2012) found $\varepsilon(x) = \beta(x)$, which they said was unexpected. However, arguably this occurs by design rather than coincidence. The characteristic impedance is fitted at each step to a conical (or approximately exponential) flare. Therefore, by construction

$$\varepsilon = \frac{1}{2} \frac{1}{A(x)} \frac{\partial A(x)}{\partial x} \approx \frac{1}{2} \frac{1}{e^{2\beta x}} \frac{\partial e^{2\beta x}}{\partial x} = \beta. \tag{3.76}$$

This exponential form of the area function was therefore determined by the choice of the form of $y_c \pm$. Consequently, it is probably not necessary to solve for both $\epsilon(x)$ and $\beta(x)$.

As previously noted, the formulation of $y_c^\pm$ is exact for a conical horn, and only approximate for an exponential horn. Therefore, we suggest a correction to the area function calculation to match the conical horn case. It requires more computational operations, but may provide better stability

for the inverse method. Let $a(x_n)$ be equal to the planar radius,

$$a(x_n) = \sqrt{\frac{A(x_n)}{\pi}}. \tag{3.77}$$

The effective distance to the cone apex at each algorithm step is given by $r_{e,n} = 1/\beta_n$, as shown in Figure 3.3. At step $n+1$, the new effective apical distance is estimated. This gives the relationships

$$\sin(\theta_{n+1}) = a_n \beta_{n+1} \tag{3.78a}$$

$$\tan(\theta_{n+1}) = \frac{\Delta a}{\Delta x}. \tag{3.78b}$$

Therefore, the change in cross-sectional radius is described by

$$a(x_{n+1}) = a(x_n) + \Delta a \tag{3.79a}$$

$$\Delta a = \Delta x \frac{a(x_n)\beta(x_{n+1})}{\sqrt{1 - (a(x_n)\beta(x_{n+1}))^2}}. \tag{3.79b}$$

Prior to the next algorithm step, it seems that β_{n+1} should be adjusted as well, to maintain the angle θ_{n+1} when it is paired with the new radius a_{n+1}. This increment should be

$$r'_{e,n+1} = r_{e,n+1} + \sqrt{(\Delta a)^2 + (\Delta x)^2} \tag{3.80a}$$

$$\beta'_{n+1} = \frac{\beta_{n+1}}{1 + \sqrt{(\Delta a)^2 + (\Delta x)^2}}. \tag{3.80b}$$
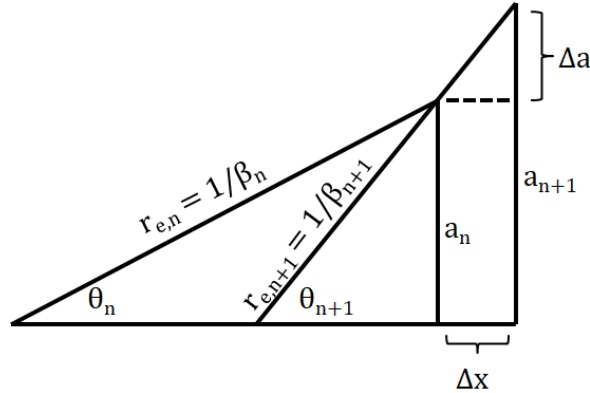
Figure 3.3: A description of incremental changes in local flare, using $r_e = 1/\beta$ as the effective distance to the apex of a cone. This approximates the local change in radius via straight line of some slope described by the angle θ_{n+1}.

Relationship to the 'step reflectance' of Sondhi & Resnick (1983). Sondhi & Resnick

(1983) formulate the inverse problem in terms of a function

$$S(t) = \int_0^t \gamma(t')dt'. \tag{3.81}$$

They form directional derivatives similar to Equation 3.70, but impose a different condition on the forward time-domain pressure,

$$\psi^+(0,t) = \begin{cases} u(t) & \text{Sondhi \& Resnick (1983)} \\ \delta(t) & \text{Rasetshwane et al. (2012).} \end{cases} \tag{3.82}$$

Given the relationships $\psi = \psi^+ + \psi^-$ and $\psi^- = \psi^+ \star \gamma$, the function $S(t)$ using the pressure condition for Rasetshwane et al. (2012) becomes

$$S(t) = -1 + \int_0^t \psi(0,t')dt', \qquad \text{Rasetshwane et al. (2012).} \tag{3.83}$$

The time integral of $\psi(0,t)$ appears throughout the method of Rasetshwane et al. (2012) to account for the local curvature of the area function. Therefore, we can hypothesize that the 'step reflectance' of Sondhi & Resnick (1983) meets a similar need.

3.5 Pole-zero fitting and reflectance factorization

This section details a method described in Robinson et al. (2013) for analysis of WAI measurements made in the ear canal. This method consists of two main operations:

1. Fitting poles and zeros to the frequency-domain reflectance data using the method of Gustavsen & Semlyen (1999),

2. Factoring the pole-zero fit into its minimum-phase and all-pass components to estimate the WAI at the TM.

An important assumption of this method is that there is very little area variation in the ear canal, such that the measurement

$$\Gamma(\omega) \approx e^{-j\omega(2L/c_0)}\Gamma_{tm}(\omega). \tag{3.84}$$

The method allows for a lossless, frequency-dependent delay to be removed from the reflectance measured at the input. A non-uniform-area canal will cause both magnitude and phase effects on the measured WAI, as reviewed later in this section. However, this factorization appears to remove some phase effects due to variable area, and yields reasonable estimates of the TM impedance. Additionally, it preserves the magnitude reflectance, which is the current diagnostic standard for WAI.

3.5.1 Pole-zero representation

Poles and zeros may be expressed in terms of a rational polynomial fraction, as the roots of the denominator and numerator, respectively. Such a function will have the form

$$\hat{F}(s) = \frac{b_{N_z}s^{N_z} + b_{N_z-1}s^{N_z-1} + ... + b_1 s + b_0}{s^{N_p} + a_{N_p-1}s^{N_p-1} + ... + a_1 s + a_0}$$
$$= b_{N_z}\frac{\prod_{i=1}^{N_z}(s - z_i)}{\prod_{i=1}^{N_p}(s - p_i)}, \tag{3.85}$$

where s is the complex angular frequency variable ($s = \sigma + j\omega$), a_i and b_i are the polynomial coefficients, N_p is the number of poles, N_z is the number of zeros, p_i are the poles, and z_i are the zeros (Van Valkenburg, 1964). Note that the coefficients a_i and b_i must be real for $\hat{f}(t)$ to be real. The poles and zeros give

$$\hat{F}(s)|_{s=z_i} = 0 \tag{3.86a}$$
$$\hat{F}(s)|_{s=p_i} \to \infty. \tag{3.86b}$$

When these poles and zeros have non-zero real parts, $\hat{F}(s)|_{s=j\omega}$ will have minima and maxima rather than zeros and poles. Therefore, the poles and zeros generally describe the local minima and maxima of the fitted data $F(\omega)$. The closer the poles and zeros lie to the $j\omega$ axis, the more extreme these minima and maxima become. Therefore, the real part of a pole or zero describes the 'damping' of that extremum.

Poles and zeros are a familiar concept in impedance analysis. Considering Equation 2.6, the reflectance must also have poles and zeros via a simple algebraic transformation. Thus, $\hat{F}(s)$ may fit the impedance Z, the reflectance Γ, or some other simple algebraic transformation of the data. Robinson et al. (2013) found that fitting the data in the reflectance domain typically yielded the best results, due to the small dynamic range and smooth behavior of the reflectance function.

3.5.2 Pole-zero fitting method

While it is more common to fit poles and zeros in the time domain, using methods such as au-toregressive moving-average (ARMA) modeling (e.g. Recio-Spinoso et al., 2011), this is not usually practical for WAI data. This is because WAI data is usually bandlimited (e.g. 0.2 to 6 or 8 [kHz]), particularly for clinical systems. This bandwidth limitation is due to a number of factors, including transducer output and noise floor, range of accurate Thévenin calibration, and noisy environments (particularly in clinics and hospitals). This typically prevents the acquisition of a quality time-domain impedance or reflectance signal. Therefore, pole-zero fitting was accomplished using a frequency-domain method.

$\hat{F}(s)$, where $s = \sigma + j\omega$ is the complex angular frequency variable, will be used to denote the

complex frequency-domain fit, and $F(\omega)$ will be used to denote the measured complex frequency-domain data. It is important to note that the data is only available as a function of ω, thus the data is related to the fitted function by

$$F(\omega) \approx \hat{F}(s)|_{s=j\omega}. \tag{3.87}$$

Because the middle ear is not a lossless system, the poles and zeros of the fit are typically located off the ω axis (have non-zero σ values related to the damping). Thus $\hat{F}(s)|_{s=j\omega}$ typically has minima and maxima instead of zero and infinite values.

The data (e.g. the complex reflectance $\Gamma(\omega)$, impedance $Z(\omega)$, or admittance $Y(\omega) = 1/Z(\omega)$) is fit to a causal, stable residue expansion of the form

$$\hat{F}(s) = \sum_{i=1}^{N_p} \frac{C_i}{s - A_i} + D + Es, \tag{3.88}$$

where the constants D and E are real quantities, while the constant poles and residues, A_i and C_i, are either real or occur in complex conjugate pairs. Note that if E is non-zero, the numerator order (N_z, as in Eq. 3.85) is one greater than the denominator order ($N_z = N_p + 1$). Similarly, if E is zero and D is non-zero the numerator and denominator orders are equal ($N_z = N_p$), and if both D and E are zero the numerator order is one less than the denominator order ($N_z = N_p - 1$). Since the poles and zeros of a 1-port network impedance are restricted to first order, with a relative order of $|N_z - N_p| \leq 1$, the functional form of Equation 3.88 is sufficient for fitting impedance domain data (Van Valkenburg, 1964). The reflectance does not have the same constraints, but given its relationship to impedance (Eq. 2.6) we assume it will also fit well to this form.

It is important to note that while the total number of parameters may seem daunting, there are typically fewer 'degrees of freedom' than it seems because the complex poles and zeros are constrained to come in complex conjugate pairs. For instance, if a fit has twelve poles and ten of them are complex, there are only seven 'degrees of freedom' related to the poles because five (half) of the complex poles are constrained by conjugate symmetry. This constraint is preserved under the transformation in Equation 2.6. Most WAI data with a (0.2 to 6 [kHz]) range can be fit with 10-20 unique parameters, with a mean-squared error of less than 3% (Robinson et al., 2013).

The vector fitting procedure derived by Gustavsen & Semlyen (1999) is a two-step process, which converts a nonlinear least squares problem to a linear least squares problem by introducing an unknown scaling function with known poles. This procedure is detailed in Appendix C. Given a fixed number of poles, the algorithm converges very rapidly, usually within a few iterations. The algorithm may be re-run with an increasing number of poles, until some error criterion is met. For some measurements, the fitting procedure may return a set of poles and zeros with nearly overlapping pole-zero pairs, due to small extrema from measurement noise. Such pairs may be considered to 'overfit' the data, and it is often possible to eliminate them from the fit without causing an appreciable increase in the fitting error.

3.5.3 Characteristics of the pole-zero fit

The pole-zero fitting method is limited by the data provided, and will typically not be accurate outside of the measured frequency range (either above or below). For example, the appropriate relative order of the fit (N_z vs. N_p) is related to high-frequency asymptotic behavior of the data, which may be unknown. As stated in Section 3.5.2, the relative order is determined by the values of D and E in Equation 3.88; these fit the high-frequency data because all other terms (e.g. $C_i/(s-A_i)$) go to zero for large ω values.

Pole-zero fits to the data are also impacted by the estimated surge resistance r_0 (Eq. 2.6) because the complex reflectance depends on this parameter. The use of an incorrect area value to calculate r_0 will cause errors in the calculation of the reflectance (Rasetshwane & Neely, 2011). For the Mimosa Acoustics HearID system, the canal area A_0 is set according to the size of the foam tip used. It has been shown that small variations in the ear canal area relative to the calibration cavity area, within 20%, cause a negligible change in the reflectance measurement (Keefe et al., 1992; Voss & Allen, 1994). Nonetheless, such a change will impact the pole-zero approximation of the reflectance.

Correction to the surge impedance r_0. Robinson et al. (2013) determined empirically that the fit parameter E (Eq. 3.88) should be set to zero when fitting in the reflectance domain, while the value D should not (though it is typically small). When E is forced to zero, the inverse Laplace transform of the reflectance fit $\hat{\Gamma}(s)$ is

$$\hat{\gamma}(t) = D\delta(t) + \sum_{i=1}^{N_p} C_i e^{A_i t} u(t). \tag{3.89}$$

Thus, a non-zero fit parameter D corresponds to an initial Dirac δ-function singularity of the time domain reflectance (Lundberg et al., 2007); this value D is related to the reflectance fit via

$$\lim_{\sigma \to \infty} \left[\hat{\Gamma}(s) \right] = D. \tag{3.90}$$

Now consider the surge resistance r_0, which is defined as the magnitude of the initial δ-function singularity of the time domain impedance. For a transmission line model of the ear canal and middle ear (e.g. having wave propagation) the impedance $Z(s)$ at the probe tip has the property

$$\lim_{\sigma \to \infty} \left[Z(s) \right] = \bar{r}_0, \tag{3.91}$$

where $\bar{r}_0$ is the true surge resistance, a real-valued constant. Considering Equation 2.6 in this limit (assuming lossless propagation, $z_0 = r_0$), we find

$$\lim_{\sigma \to \infty} \left[\Gamma(s) \right] = \frac{\bar{r}_0 - r_0}{\bar{r}_0 + r_0}. \tag{3.92}$$

If r_0 is equal to the true surge resistance $\bar{r}_0$, the limit of $\Gamma(s)$ as $\sigma \to +\infty$ must be zero. This means there must be no initial δ-singularity in the time domain reflectance. Thus, considering Equation 3.90 and 3.92, D should be zero; a non-zero value of D may indicate a fitting inaccuracy, or the use of an incorrect r_0 value. In the latter case, if the fitting procedure yields a good approximation of the initial singularity in the time-domain reflectance (due to an incorrect r_0 value), D might be used to estimate the true surge resistance value from the complex reflectance data via

$$\bar{r}_0 = r_0 \frac{1+D}{1-D}. \tag{3.93}$$

In practice, the bandwidth of the data is too limited to achieve accurate estimates of D. This is consistent with the observed low sensitivity to variations in r_0 (or equivalently, A_0).

Network modeling application. Pole-zero fits may also be used to synthesize network models of the complex impedance (e.g. Brune (1931) and Van Valkenburg (1964)). However, such RLC networks will not necessarily be unique. Networks synthesized from pole-zeros fits of complex reflectance measurements will often lack direct physical interpretations present in other models, such as the Zwislocki (1962), Kringlebotn (1988), or Parent & Allen (2010) models. Therefore, network synthesis using the pole-zero fits is outside the scope of this thesis.

3.5.4 Reflectance factorization

Under the assumption that the ear canal is approximately a lossless uniform tube, and the rest of the middle ear system has loss, the reflectance may be factored such that the residual ear canal effect is approximately removed. Using the Weiner spectral factorization technique

$$\hat{\Gamma}(s) = \hat{\Gamma}_{ap}(s)\hat{\Gamma}_{mp}(s) \tag{3.94a}$$

$$\hat{\Gamma}_{ap}(j\omega) \approx e^{-j\omega(2L/c_0)} \tag{3.94b}$$

$$\hat{\Gamma}_{mp}(j\omega) \approx \Gamma_{tm}(\omega), \tag{3.94c}$$

where $\hat{\Gamma}_{mp}(s)$ is the 'minimum-phase' component and $\hat{\Gamma}_{ap}(s)$ is the 'all-pass' component of the pole-zero fit $\hat{\Gamma}(s)$. Using this factorization, it is possible to preserve the magnitude reflectance while removing variable residual canal delay. Note that by design of the pole-zero fitting method and the definition of the Laplace transform, the reflectance fit is causal and stable.

Construction of minimum-phase and all-pass components. By definition, it is required that all poles and zeros of a minimum-phase function lie in the LHP. To construct the minimum-phase component $\hat{\Gamma}_{mp}(s)$, we must factor a component out of $\hat{\Gamma}(s)$ that accounts for all zeros that lie in the RHP (if the fit was performed in the reflectance domain, all poles will be constrained to the LHP by the fitting algorithm). Let the function $\hat{\Gamma}_{LHP}(s)$ contain all the poles and zeros of $\hat{\Gamma}(s)$ that lie in the LHP; let $N_{z,RHP}$ be the number of RHP zeros of $\hat{\Gamma}(s)$, with values q_i. The

reflectance fit may be factored as follows:

$$\hat{\Gamma}(s) = \hat{\Gamma}_{LHP}(s) \prod_{i=1}^{N_{z,RHP}} (s - q_i)$$

$$= \hat{\Gamma}_{LHP}(s) \prod_{i=1}^{N_{z,RHP}} (s - q_i) \frac{(s + q_i^*)}{(s + q_i^*)}$$

$$= \underbrace{\left[\hat{\Gamma}_{LHP}(s) \prod_{i=1}^{N_{z,RHP}} (s + q_i^*) \right]}_{\hat{\Gamma}_{mp}(s)} \underbrace{\left[\prod_{i=1}^{N_{z,RHP}} \frac{(s - q_i)}{(s + q_i^*)} \right]}_{\hat{\Gamma}_{ap}(s)}. \tag{3.95}$$

Considering Equation 3.95, overlapping poles and zeros are introduced in the LHP at $s = -q_i^*$. Grouping the terms, a component emerges with LHP poles and RHP zeros symmetrically placed about the ω axis. This is called the *all-pass* component because its magnitude $|\hat{\Gamma}_{ap}(j\omega)|$ is 1 for all frequencies in the fitting range; it passes all frequencies with no attenuation. The factorization required to form the all-pass component is unique. The remaining terms contain only poles and zeros in the LHP and form the minimum-phase factor $\hat{\Gamma}_{mp}(s)$. When working with poles and zeros, this factorization requires no additional calculations.

The minimum-phase and all-pass factors have the following properties:

$$|\hat{\Gamma}_{mp}(j\omega)| = |\hat{\Gamma}(j\omega)| \tag{3.96a}$$

$$|\hat{\Gamma}_{ap}(j\omega)| = 1 \tag{3.96b}$$

$$\angle\hat{\Gamma}_{mp}(j\omega) + \angle\hat{\Gamma}_{ap}(j\omega) = \angle\hat{\Gamma}(j\omega). \tag{3.96c}$$

The reflectance magnitude is maintained in the minimum-phase component of the fit, while the component of the reflectance that is uniformly lossless across the frequency range of the fit, including any pure delay, is accounted for in the all-pass component. Because the factors are multiplied, their phases add.

Estimating other WAI quantities at the TM. Using the estimated $\Gamma_{tm}(\omega)$, and assuming that the canal area is approximately the same at the TM and the probe, all WAI quantities may be estimated at the TM. For example, the normalized TM impedance can be calculated using Equation 2.6 (assuming the ear canal is lossless),

$$\frac{Z_{tm}(s)}{r_0} = \frac{1 + \Gamma_{tm}(s)}{1 - \Gamma_{tm}(s)}. \tag{3.97}$$

When the approximate residual ear canal contribution has been removed, the magnitude TM impedance $|Z_{tm}(j\omega)|/r_0$ typically has no high-frequency notch due to ear canal standing waves (Robinson et al., 2013, 2016). The TM impedance estimate is similar to the 'propagated impedance'

function described by Voss & Allen (1994), calculated by removing a pure delay from the reflectance. The advantage of the pole-zero factorization procedure is that it allows for a method to estimate the pure delay present in the reflectance frequency response, without necessitating the use of the high-frequency phase, which may not be available.

In theory, this factorization does not work for a variable-area horn because the reflectance magnitude will be altered as well as the phase. In practice it seems to work well for measurements made in the ear canal (Robinson et al., 2016), which we expect will generally have small variations in area compared to, for instance, a measurement probe tip such as that described in Section 4.3. If the all-pass component has a frequency-dependent phase, it may be indicative of area variations in the ear canal.

Note that any lossless TM delay, as described by Puria & Allen (1998) and modeled by Parent & Allen (2010), may also be included in the REC component. Conversely, because we enforce $\Gamma_{rec} \approx \Gamma_{ap} = 1$ for all frequencies, thermoviscous losses due to the walls of the ear canal will be mistakenly attributed to the middle ear. The longer the residual ear canal, the more pronounced these losses will be, particularly if the probe is seated outside of the bony portion of the ear canal.

3.5.5 Minimum-phase/all-pass decomposition for a variable-area ear canal.

Consider a variable-area horn, which can be expressed as an $ABCD$ transmission matrix, according to Figure 3.1 in Section 3.3.1. If this network is terminated in a load impedance $Z_2 = Z_L$, then the input impedance $Z_1 = Z_{in}$ is related to the load impedance via

$$Z_{in} = \frac{AZ_L + B}{CZ_L + D}. \tag{3.98}$$

To assess the minimum-phase/all-pass decomposition of the input reflectance, we must first calculate Γ_{in} and Γ_L using Equation 2.6. Let the characteristic impedance at the input be $z_{0,in}$, and that at the load be $z_{0,L}$.

It can be shown that the input and load reflectances are related via

$$\Gamma_{in} = \frac{\widetilde{A}\Gamma_L + \widetilde{B}}{\widetilde{C}\Gamma_L + \widetilde{D}}. \tag{3.99}$$

Therefore, the load and input reflectances are only related by a multiplicative factor when $\widetilde{B} = \widetilde{C} = 0$. Furthermore, this factor is 'all-pass' only when $|\widetilde{A}/\widetilde{D}| = 1$.

The coefficients of this möbius transformation are given by

$$\widetilde{A} = Az_{0,L} - B - Cr_{in}z_{0,L} + Dz_{0,in} \tag{3.100a}$$

$$\widetilde{B} = Az_{0,L} + B - Cz_{0,in}z_{0,L} - Dz_{0,in} \tag{3.100b}$$

$$\widetilde{C} = Az_{0,L} - B + Cz_{0,in}z_{0,L} - Dz_{0,in} \tag{3.100c}$$

$$\widetilde{D} = Az_{0,L} + B + Cz_{0,in}z_{0,L} + Dz_{0,in}. \tag{3.100d}$$

The reason factorization seems to work for the ear canal is that the ear canal in many cases may be reasonably approximated by a uniform cylinder, for which $\widetilde{B} = \widetilde{C} = 0$ and $|\widetilde{A}/\widetilde{D}| = |e^{-j\omega(2L/c_0)}| = 1$.

Thus, reflectance factorization will be a good approximation when

$$|\widetilde{B}| << |\widetilde{A}| \tag{3.101a}$$

$$|\widetilde{C}| << |\widetilde{D}| \tag{3.101b}$$

$$|\widetilde{A}| \approx |\widetilde{D}|. \tag{3.101c}$$

For large variations in area, like those seen for the probe tip (Sec. 4.3), this method will not be nearly precise enough, and two-port modeling or inverse techniques must be used instead.

Restrictions on the TM-WAI imposed by reflectance factorization. Considering the real and imaginary parts of the impedance ($Z = R + jX$) and the admittance ($Y = G + jB$), and the typical definition of reflectance (Eq. 2.6), the following set of relationships holds:

$$\frac{R}{r_0} = \frac{1 - |\Gamma|^2}{|1 - \Gamma|^2} \tag{3.102a}$$

$$\frac{X}{r_0} = \frac{2\Im\{\Gamma\}}{|1 - \Gamma|^2} \tag{3.102b}$$

$$Gr_0 = \frac{1 - |\Gamma|^2}{|1 + \Gamma|^2} \tag{3.102c}$$

$$Br_0 = \frac{-2\Im\{\Gamma\}}{|1 + \Gamma|^2}. \tag{3.102d}$$

Thus, normalized impedance and admittance quantities will be bounded based on the values of $\Gamma(\omega)$. Restricting reflectance of the TM to minimum phase narrows the ranges the real and imaginary parts of $\Gamma_{tm} = \Gamma_{mp}$ can occupy.

Consider Figure 3.4. The reflectance measured at the probe is bounded by $|\Gamma| \leq 1$, thus values of the complex function $\Gamma(\omega)$ may fall anywhere within the unit circle. However, the minimum phase function $\Gamma_{mp}(\omega)$ must fall within the grey region shown because its phase is constrained by
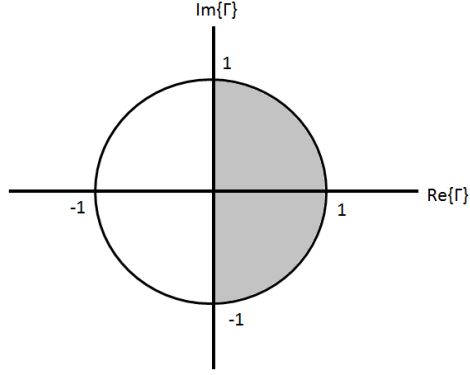
Figure 3.4: The reflectance is bounded by $|\Gamma| \leq 1$, thus values of the complex function $\Gamma(\omega)$ may fall anywhere within the unit circle. The minimum phase function $\Gamma_{mp}(\omega)$ must fall within the grey region shown because its phase is constrained by $-\pi/2 \leq \angle \Gamma_{tm}(\omega) \leq \pi/2$.

Table 3.2: Bounds on impedance and admittance quantities for the probe and estimated TM responses.

Probe quantities	TM quantities
$0 \leq R/r_0 \leq \infty$	$0 \leq R_{mp}/r_0 \leq \infty$
$-\infty \leq X/r_0 \leq \infty$	$\infty \leq X_{mp}/r_0 \leq \infty$
$0 \leq Gr_0 \leq \infty$	$0 \leq G_{mp}r_0 \leq 1$
$-\infty \leq Br_0 \leq \infty$	$-2 \leq B_{mp}r_0 \leq 2$

$-\pi/2 \leq \angle \Gamma_{tm}(\omega) \leq \pi/2$. Thus the following inequalities must be true:

$$0 \leq |1 + \Gamma| \leq 2 \tag{3.103a}$$

$$1 \leq |1 + \Gamma_{tm}| \leq 2 \tag{3.103b}$$

$$0 \leq |1 - \Gamma| \leq 2 \tag{3.103c}$$

$$0 \leq |1 - \Gamma_{tm}| \leq \sqrt{2}. \tag{3.103d}$$

Thus, the impedance and admittance quantities are bounded as shown in Table 3.2. These bounds may partially explain why the conductance G_{tm} bears a greater similarity to the absorbance $(1 - |\Gamma|^2)$ as discussed in Section 6.4.2, since it is bounded between 0 and 1.

CHAPTER 4

METHOD AND RESULTS: MEASUREMENT-PROBE DESIGN

For clinical use, a wideband acoustic immittance (WAI) measurement probe should have stable Tévenin parameters (or be easy to calibrate), fit into adult, child, and infant ear canals, and have disposable single-use ear tips or covers to keep the probe clean between subjects. For other measurements such as otoacoustic emissions (OAEs), it is important that the probe have low harmonic distortion and distortion products, and a low noise floor across the frequency range of interest. Additionally, we require low acoustic crosstalk between transducer channels and a rugged, acoustically sealed housing.

For the purposes of this thesis, the following discussion is limited to the WAI measurement capabilities of the prototype probe. Specifically, the use of a probe-tip extension, beyond the point of Thévenin calibration,[1] is studied. This is different from the traditional method of probe calibration, where a probe is calibrated with the complete ear tip on, and thus the microphone channel must be separated up to the front end of this tip. Single-use foam and rubber tips meeting this criteria, such as those used with the ER-10C (Etymotic Research, Elk Grove Village, IL), have very small central sound outlets so that they can fit in the smallest (infant) ear canals. These tips lead to a wave-spreading effect at the outlet of the probe into the ear canal (e.g. Karal (1953)). The purpose of the probe-tip extension studied here is to allow the loudspeaker output to spread as much as possible before entering the ear canal, by choosing an appropriately sized tip for the subject in question. This study is a feasibility study, and does not represent the performance of the current commercial probe supported by Mimosa Acoustics.

4.1   Thévenin calibration

WAI can be derived using many calibration methods such as the 'two microphone' method, or the 'standing-wave tube' method (Beranek & Mellow, 2012; Shaw, 1980). The two microphone method requires a precise calibration of the microphones, and precise knowledge of their relative placement; the standing wave tube method requires manual manipulation of the microphone placement with reference to the end of a tube. Many of these methods have been shown to be relatively inaccurate due to their sensitivity to precise placement of the microphone(s). The four-cavity Thévenin method

---

[1]The point of Thévenin calibration is where the microphone and speaker channels are separated. The probe cannot be Thévenin calibrated beyond the point where the channels have mixed.

is suitable for clinical use because it is less sensitive to precise placement of the microphone.

Typically, a WAI measurement is made by playing a broadband sound stimulus in the ear canal, such as a chirp, and measuring the sound pressure at the probe microphone. The sound source must be calibrated in order to correctly interpret the ear-canal sound pressure response. Most techniques for measuring reflectance use multiple cylindrical cavities of known lengths to calibrate the probe; various approaches differ primarily in terms of the size, length and the number of calibration cavities used (Keefe et al., 1992; Neely & Gorga, 1998). For instance, Mimosa Acoustics' HearID (Champaign, IL) uses a four-cavity method described by Allen (1986). In this method, the pressure responses of four cylindrical cavities, and their theoretical cavity impedances, are used to determine the Thévenin equivalent source parameters, which characterize the output of the probe loudspeaker(s) in response to a stimulus voltage level.
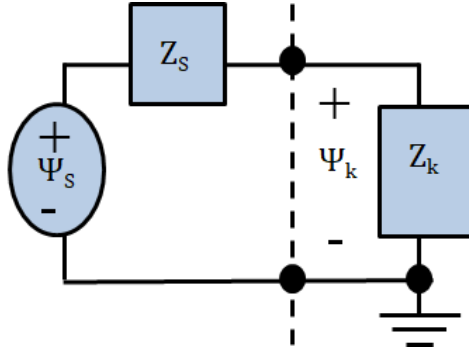
Figure 4.1: Thévenin equivalent circuit for calibration of a WAI measurement probe. Ψ_s and Z_s are the source pressure and impedance, while Ψ_k and Z_k are the measured pressures and theoretical impedances of the cylindrical calibration cavities. All of these quantities will vary with frequency ω.

A diagram of the Thévenin equivalent circuit is shown in Figure 4.1. The measured pressure responses and the theoretical impedances of the known cavities, considering thermal and viscous losses (Keefe, 1984), are used to determine the source pressure and impedance by solving the overdetermined system of equations

$$
\begin{bmatrix} Z_1 & -\Psi_1 \\ Z_2 & -\Psi_2 \\ Z_3 & -\Psi_3 \\ Z_4 & -\Psi_4 \end{bmatrix} \begin{bmatrix} \Psi_s \\ Z_s \end{bmatrix} = \begin{bmatrix} Z_1\Psi_1 \\ Z_2\Psi_2 \\ Z_3\Psi_3 \\ Z_4\Psi_4 \end{bmatrix},
\tag{4.1}
$$

at each frequency. As this system is of the form $A\mathbf{x} = \mathbf{b}$, the solution is $\mathbf{x_{opt}} = (\mathbf{A^t A})^{-1}\mathbf{A^t b}$. Once the Thévenin parameters of the source, $Z_s(f)$ and $\Psi_s(f)$, have been calculated, the impedance measured at the ear canal is simply

$$
Z = Z_s \frac{\Psi}{\Psi_s - \Psi},
\tag{4.2}
$$

where $\Psi(f)$ is the measured pressure.

Determination of the cavity lengths. The lengths of the calibration cavities are needed to calculate the impedance models Z_k. These lengths may be determined by one of two methods.

1. Minimization of the least-squares error of Equation 4.1.

2. Determination of the acoustic length from the pressure null.

When these two methods yield equivalent lengths, it is more straightforward to calculate the lengths directly from the pressure nulls. However, in some cases these lengths are not in agreement, due to the length effect of the Karal (1953) spreading mass at high frequencies. This occurs for short cavities with the ER10C, when the pressure null is above 8 or 9 [kHz].

A further complication is that the acoustic lengths do not always match the physical lengths. In general, it was found that the acoustic lengths determined for the ER10C probe were usually 1-2 [mm] longer than the measured lengths, while the acoustic lengths for the Mimosa Acoustics prototype probe were typically about 1 [mm] shorter than the measurement lengths. Either length difference may need to be accounted for when modeling measurements (e.g. two-port probe-tip models). However, this difference may create more problems for the Mimosa probe, since its effective plane of Thévenin calibration is therefore about 1 [mm] in front of the probe.

Evaluating the calibration. To evaluate the performance of the calibration (Allen, 1986) as a function of frequency, we consider the following normalized, complex, frequency-dependent cavity length:

$$\widehat{L}_k(f) = \frac{\ln \Gamma_k(f)}{-2L_k\kappa(f)} \tag{4.3}$$

where L_k is the cavity length determined by the calibration and $\kappa(f)$ is the complex propagation function accounting for lossy sound propagation in a cylindrical cavity. The measured cavity reflectance $\Gamma_k(f)$ of the kth cavity is theoretically $\Gamma_k(f) = e^{-2L_k\kappa(f)}$. Therefore, it is possible to define $\widehat{L}_k$ using the measured Γ_k for each cavity defined by the Thévenin solution, the determined length L_k, and the theoretical value for κ.

Thus, we may place a calibration 'pass' criterion on the normalized length $\widehat{L}_k(f)$ such that its magnitude must be correct within 1%, and its phase must be within 1 degree of 0

$$|\widehat{L}_k(f) - 1| < 0.01 \tag{4.4a}$$

$$\angle\widehat{L}_k(f) < 1°. \tag{4.4b}$$

Figure 4.2 shows an example calibration. The top-left quadrant shows the cavity pressure responses and the magnitude $|\widehat{L}_k(f) - 1|$ for each cavity. Note that the phase of this quantity always 'passes' calibration when the magnitude passes, so it is not shown. The upper-right quadrant shows the measured cavity reflectances compared to their theoretical values. The bottom-right quandrant shows the fit of the model (dashed line) to the pressure data (dots) at the pressure null. Finally,
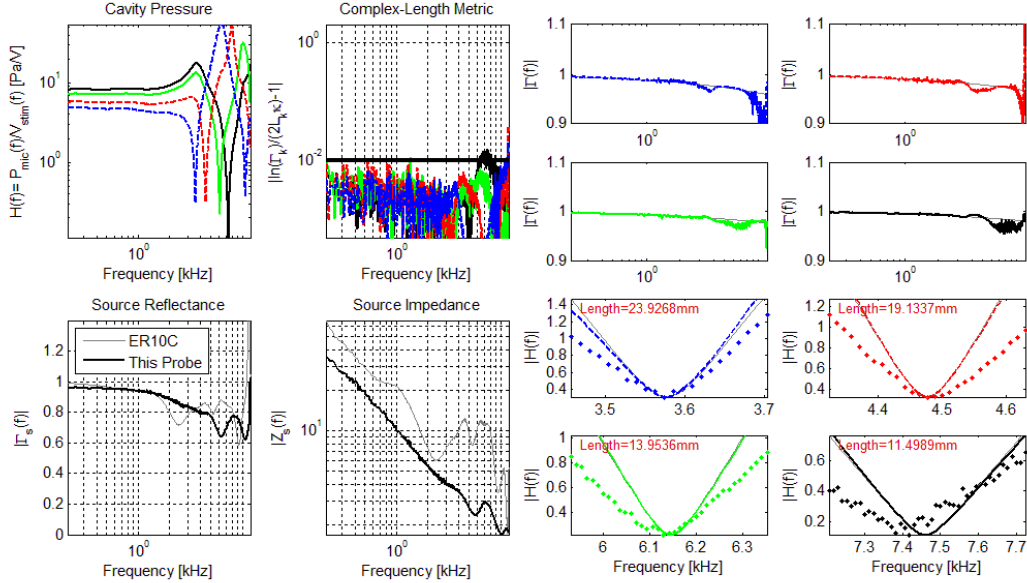
Figure 4.2: Example of a successful calibration of a prototype Mimosa Acoustics probe. The top-left plots show the magnitude response (in [Pa/V]) and the magnitude normalized length $\widehat{L}_k(f)$ for each cavity. The bottom-left plots show the magnitude source impedance and source reflectance of this probe, compared with the ER10C. The top-right plots show the magnitude reflectances and the bottom-right plots show the measured pressure response nulls, compared with the cavity models.

the bottom-left quadrant shows the magnitude source relfectance and impedance of the current probe, as compared to an example calibration of the ER10C.

The cavities causing large errors in the least-squares solution may typically be identified using the $\widehat{L}_k$ metric. Alternatively, the least-squares solution may be analyzed to determine how each two-cavity solution is weighted in the final answer (Haghighatshoar et al., 2015). It is best to detect and remove error-prone cavities or regions from the solution, particularly near pressure poles, which may be affected by level-dependent nonlinearities in the microphone, and the pressure nulls, which may dip into the noise floor.

4.2 Effects of microphone nonlinearity

Both the loudspeaker and microphones used in the measurement probe exhibit nonlinear behavior. Typically the loudspeaker impedance is nonlinear with level, but this nonlinearity can generally be avoided by sticking to one operating voltage across measurement levels. Nonlinearities of the microphone can cause much more serious problems, in response to pressure poles and, for some microphones, mild mechanical shock.

Electret microphones. Microphones used in insert-earphone measurement probes tend to be electret microphones (Sessler & West, 1962). However, the type of bias circuit used for the microphone's transistor can determine whether or not the microphone gain is stable over time, and how fast it settles back to equilibrium. This time-dependent gain may be acceptable for certain applications (e.g. cell phones), but is unacceptable for WAI devices. If the microphone gain changes over time, a stable Thévenin calibration cannot be achieved. Figure 4.3 shows example cavity measurements over time, using a probe build with a Knowles EM series microphone.
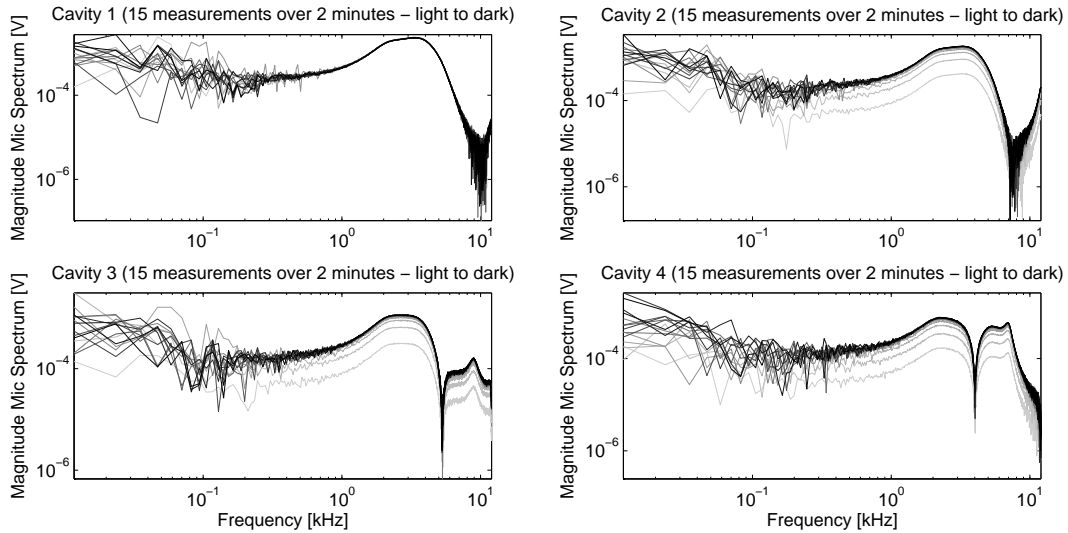
Figure 4.3: Knowles EM microphone with changing gain. The calibration may be achieved and applied using measurements where the microphone gain has settled back to equilibrium. However, every time the probe is touched during calibration, the microphone gain will change.

The EM microphone transistor is biased using a diode circuit, which improves the signal to noise ratio of the measurements (Van Rhijn, 2003), but causes a time-varying gain. Alternatively, Knowles' EK series microphones, which are used in the ER10C probe, have a very stable output over time due to resistor-biasing of the internal transistor. This increases the total size of the microphone, but eliminates this gain instability. Some microphones employ a back-to-back diode circuit, which dramatically reduces the microphone recovery time (Van Rhijn, 2003). However, it can be difficult to determine which microphones are built this way (for instance, some FG microphones by Knowles have this fast recovery time, while others behave more like the EM shown in Fig. 4.3).

Pressure poles. A related type of nonlinearity is caused by high-level signals, typically due to the pressure response poles of the impedance load being measured. If the microphone has a fast settling time, it will recover from the effect of the pole within one time-averaged signal block. However, a nonlinear artifact appears locally in the de-chirped impulse response, as shown in Figure 4.4. This artifact will appear when the pole frequency is excited by the measurement chirp.

69
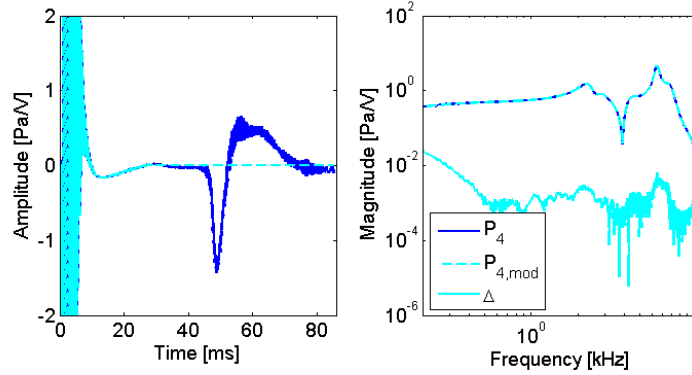
Figure 4.4: Time and frequency effects of a high-amplitude pressure pole for cavity 4 (about 22 [mm] long). The left-hand plot shows the original cavity impulse response (solid blue). The impulse response decays rapidly in the first 5-10 [ms], and should not get larger. However, an artifact of the non-linearity occurring when the chirp frequency passes through the cavity pole is seen between 40 and 60 [ms]. The signal $P_{4,mod}$ (dashed cyan) is calculated by removing this time-domain artifact. The corresponding frequency-domain quantities are shown in the right-hand plot, along with the difference in the spectra, given by Δ (solid cyan). This demonstrates that the nonlinearity causes a low-frequency error in the frequency-domain pressure.

Figure 4.5 shows the chirp frequency as a function of group delay, indicating which frequencies are played at which times. Comparing this to Figure 4.4, it is clear that the cavity 4 pole frequency of about 8 [kHz] falls about 50 [ms] into each block. Therefore, this pole is responsible for the nonlinear artifact appearing near 50 [ms] in Figure 4.4. Furthermore, all frequencies of the cavity 4 measurement falling in the affected time region of the chirp may be contaminated by this nonlinearity.

This time-domain signature can be used to help identify nonlinear pressure measurements, as the nonlinearity can result in an inaccurate Thévenin calibration at the affected frequencies. This effect is of particular importance when modeling the probe tip because the lengthened probe-tip system, particularly when placed in a rigidly terminated cavity, can produce very large pressure poles.

70
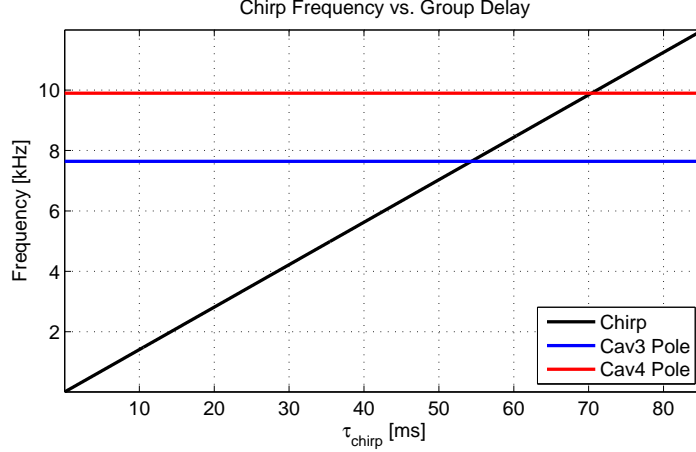
Figure 4.5: Chirp frequency as a function of group delay. The approximate pole frequencies are marked in red and blue for cavities 3 (about 18 [mm] long) and 4 (about 22 [mm] long).

4.3   Model for a removable probe tip

The probe tip may be described by a cascade of frequency-dependent two-port matrices, as shown in Figure 4.6. Two-port transmission matrices for the uniform tube, conical horn, and step discontinuities in area are given in Appendix B; the general derivation for such matrices is described in Section 3.3.1. The models used in this chapter include viscous and thermal losses, though their effects on sound transmission are minimal for relatively wide ducts such as the test probe tip ($d_1 = 7.5$ [mm], $d_2 = 4.0$ [mm]). Figure 4.6 shows the general configuration for a measurement in the ear canal using the probe tip. The goal of modeling the probe tip is to accurately estimate the load impedance Z_L (or preferably the TM impedance Z_{tm}, as discussed in the next chapter) using the impedance measured in the plane of Thévenin calibration.

Theoretical effect of the load impedance on the measured WAI.   When the load impedance Z_L of Figure 4.6 is infinite, there is a non-uniform delay effect due to the non-uniform area of the probe tip, but the reflectance measured at the probe is 1 for all frequencies in the lossless case (e.g. equivalent to the reflectance of the load). However, when the load impedance is not infinite, the reflectance at the probe and that at the TM have a much more complicated relationship, which is governed by the two-port properties of the probe tip (e.g. Eq. 3.99).

First, we examine the effect of a variable-length ear canal on the measured WAI, using a simulated load impedance as shown in Figure 4.7. A simple, smooth model approximating the average middle-ear absorbance is used to represent the middle ear. This model is given by

$$Z_{tm} = R + \frac{1}{j2\pi fC} = \frac{\rho_0 c_0}{A_0}\left[3 + \frac{2400}{jf}\right]. \tag{4.5}$$

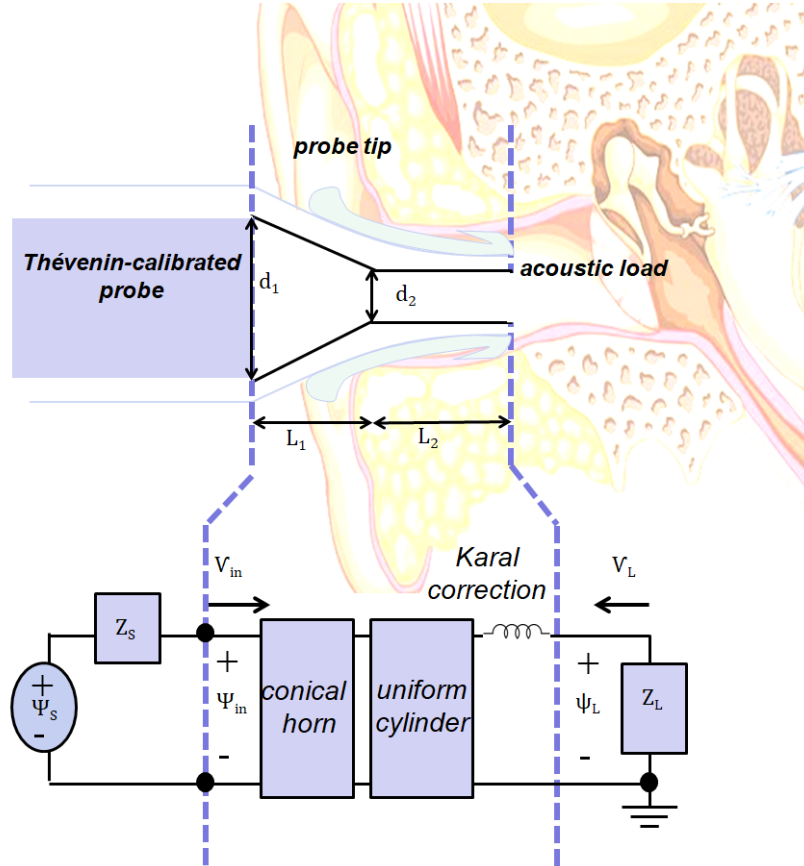This quasi-static model must be concatenated with a delay in order to approximate measurements

71

Figure 4.6: Configuration and model for a middle-ear WAI measurement made using the probe tip. The original probe tip studied had $d_1 = 7.5$ [mm], $d_2 = 4.0$ [mm], $L_1 = 6.5$ [mm], and $L_2 = 13.3$ [mm]. This tip is somewhat large for adult ears.

made in the Mimosa Acoustics average-ear simulator, or in human ears. This is accomplished using a uniform cylinder model of length L_{ec} and a diameter of 7.5 [mm]. Using a simple, smooth middle-ear model, it is easier to observe the effects of the probe tip on the measured WAI. The only parameter varied in the following simulation will be the ear-canal length.

Figure 4.8 shows the effect of different ear-canal lengths on the WAI measured in the plane of Thévenin calibration, given the area function of the probe tip and the average middle ear. The longer the ear canal, the greater the effect of the probe tip on the measured absorbance level (left). Therefore, it is not only the change in area that matters, but also the relative delays of segments of different areas. These results predict that the area function can cause a high-frequency decrease in the measured absorbance level. This high-frequency roll-off is known to vary across ears (sometimes it is not present), and thus may be related to ear-canal area variations (Lewis & Neely, 2015). Finally, note that the total transfer function across the probe tip and ear canal (right) indicates an up to 10 [dB] attenuation of the signal delivered to the middle ear at high frequencies. This may cause problems for stimulus delivery in OAE measurements.
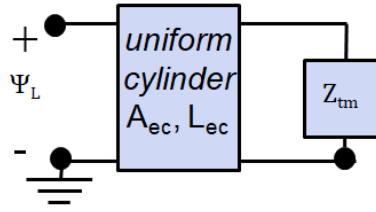
Figure 4.7: Model for the ear-canal and middle-ear load, assuming a uniformly cylindrical ear canal. The middle-ear impedance $Z_{tm} = R + [j2\pi fC]^{-1}$, where $R = 3r_0$ and $C \approx 6.6 \times 10^{-5} r_0$. To approximate measurements in the Mimosa Acoustics average-ear simulator, or a human ear, it is necessary to add acoustic delay representing the ear canal (and TM). This is accomplished using a uniform cylinder model of length L_{ec} and diameter 7.5 [mm].

Theoretical effect of the probe-tip dimensions on the measured WAI. With the ear-canal length held constant at 10 [mm], the effects of the cone length relative to the total probe-tip length, and the effects of the total tip length, were simulated. The results are displayed in Figure 4.9.

The left-hand plot shows the effects of varying the total probe tip length. In this case, a shorter probe tip leads to a lower absorbance (higher reflectance) at high frequencies. A longer probe tip has less dramatic effects on the measured absorbance magnitude, but these effects appear lower in frequency. The right-hand plot shows the effect of the cone angle, for a probe tip of fixed total length. The extrema of this variation occur when the area discontinuity is located at the point of Thévenin calibration (cone length goes to zero) and when the area discontinuity is located at the outlet of the probe tip (there is no decrease in area except for a constriction at the end of the tip). The range of variation of these simulations is relatively small, indicating that the relative dimensions of the taper matter less than the total length of the tip and the total change in area.
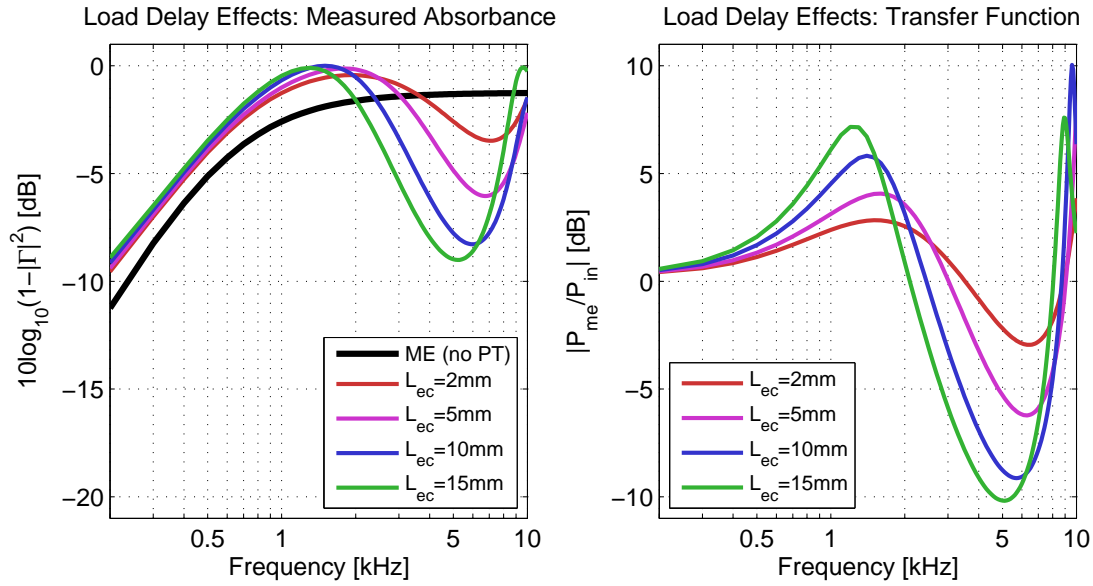
Figure 4.8: Effects of varying load (ear-canal) delay on the measured absorbance at the point of Thévenin calibration (left), and the transfer function across the probe tip and ear canal, from the calibration point to the middle ear (right). Longer ear-canal models (with more delay) produce more extreme changes (from the black curve) due to the variable-area tip. Based on these simulations we conclude that these changes are due to the combination of the jump discontinuity and the delays of the probe tip and ear canal.
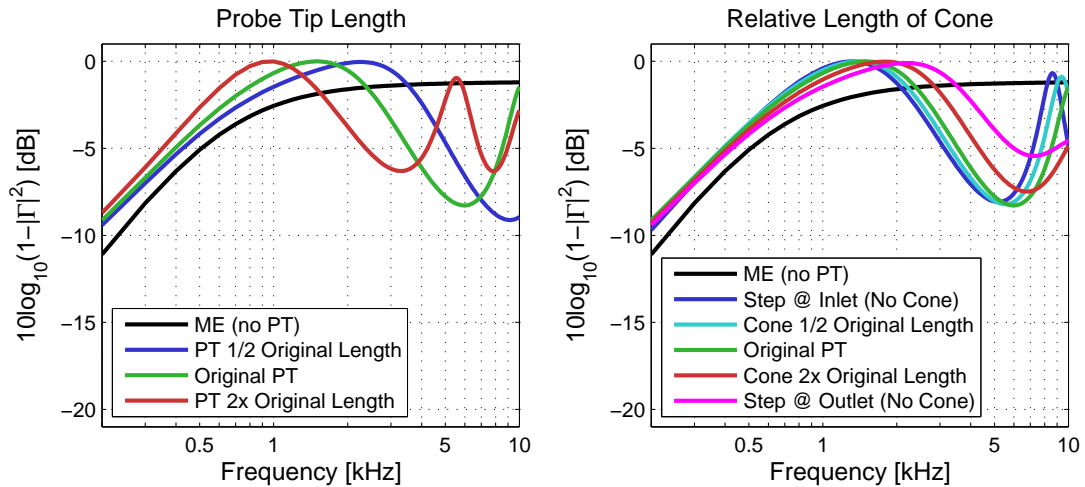

Figure 4.9: Variation in the measured WAI (absorbance level) with probe-tip dimensions. Only one parameter is varied at a time. For both plots, the ear canal length is always 10 [mm]. When the probe-tip length is varied (left), the cone and cylinder are scaled equally, and when the cone length is varied (right) the cylinder (L_2) is varied so that the total length ($L_1 + L_2$) remains constant. The relative length of the cone (e.g. steepness of taper) causes much less variation than the total length (delay) of the tip.

4.4   Probe-tip measurements

The following section describes two types of measurements:

1. Ear-simulator measurements using the probe tip, from which the tip effect was extracted using its theoretical two-port model (e.g. Appendix B).

2. A two-port matrix calibration of the probe tip, using three cylindrical-cavity loads (described in Sec. B.3).

Figure 4.10 shows the probe tip sealed into a cylindrical cavity, with the aid of a metal washer and a glue gun. This configuration is used to perform the two-port matrix calibration of the probe tip.
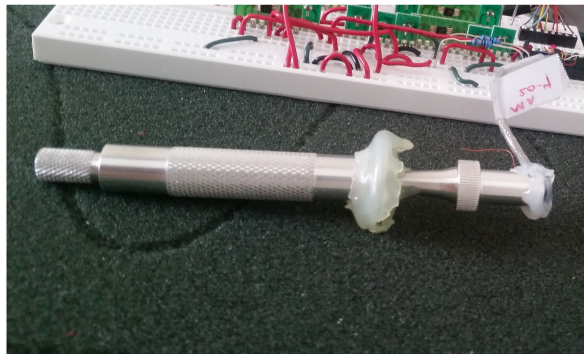
Figure 4.10:   Probe tip connected to a uniform cylindrical syringe of 7.5 [mm] diameter. A jump discontinuity between the probe tip and the syringe was created using a washer as a flat plane, fused to the probe tip using a glue gun. To measure the two-port parameters of the probe tip, the plunger depth was varied (and carefully measured) to create test cavities of known impedance.

4.4.1   Extracting the probe-tip effects

Figures 4.11 and 4.12 examine measurements of an ear simulator using the probe tip. In Figure 4.11, the green lines show the original measurement of an ear simulator without the probe tip (solid), and a simulation of the corresponding WAI that would be measured with the probe tip on (dashed). Conversely, the black lines show a measurement of the same ear simulator with the probe tip on (dashed), and with the probe tip computationally extracted (solid). These results agree with each other in general, but the process of adding (rather than extracting) the probe tip seems to be more computationally stable. This may be due in part to the high reflectance measured at high frequencies with the probe tip on. This high reflectance is due to the constriction of the tip, which limits access to the response on the other side.

Figure 4.12 shows multiple measurements of the ear simulator using the probe tip and two different probes. The ear simulator measured without the probe tip (solid black) is the load absorbance we hope to calculate via extraction of the probe tip. For the measurements shown here,
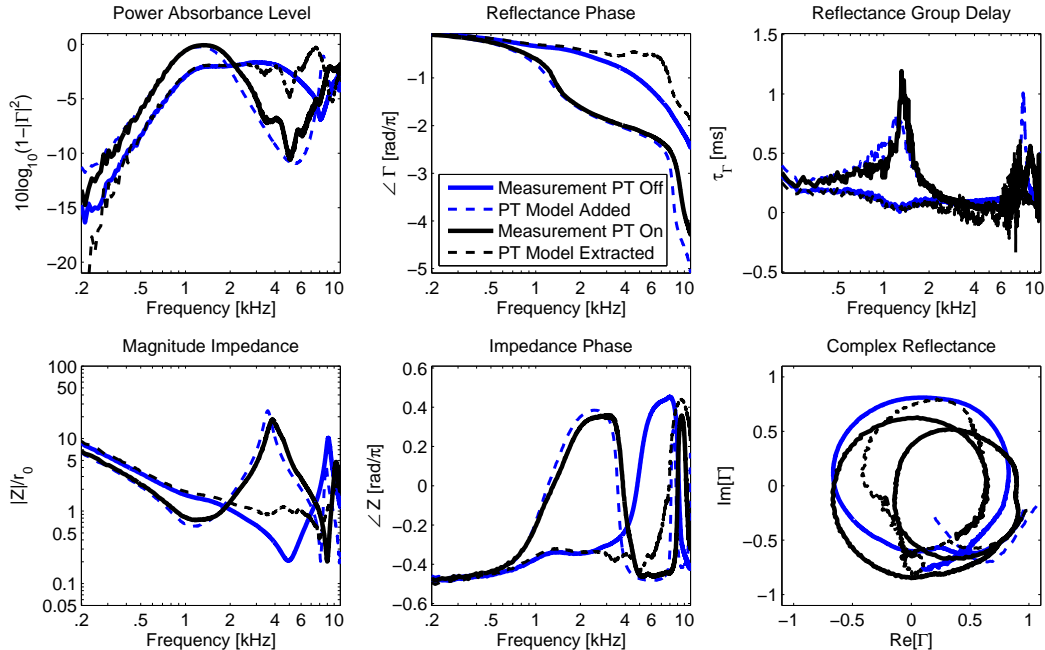
Figure 4.11: Measurements of the Mimosa Acoustics average-ear simulator with (solid black) and without (solid blue) the probe tip. By adding or extracting (subtracting) the computational model for the probe tip (Fig. 4.6), each measurement is used to predict the other (dashed lines). The estimate is better when adding the probe tip on (dashed blue), rather than extracting its effects (dashed black).

this extraction works well up to 3-4 [kHz]. Above this frequency, the extraction fails. This failure could be due to inaccuracies in the probe-tip model (e.g. Figs. 4.13 and 4.14) or inadequacy of the probe calibration. The fact that the effective calibration point of the Mimosa prototype probe is about 1 [mm] in front of the probe (e.g. inside the probe tip) may also play a role. In similar experiments using the ER10C, it was possible to accurately extract the effect of the probe tip up to 4-5 [kHz] (a small improvement over the Mimosa Acoustics prototype probe).

4.4.2 Measuring the $ABCD$ parameters of the probe tip

The two-port parameters of the probe tip were measured using three known cylindrical loads, assuming that the probe tip is reciprocal. Note that the lossy conical model is not quite reciprocal (as explained in Sec. B.2.2), but this may be due to the approximations made to obtain solutions to the lossy wave equation, rather than physical reality. Reciprocity is a fair approximation (Van Valkenburg, 1960), as any transmission line composed of series and shunt impedance elements is by definition reciprocal, and the probe tip could be modeled to high accuracy in this fashion. Figures 4.13 and 4.14 show the results of these calibrations for 3 combinations of 3 (out of 4) cavity loads (corresponding to approximately 2.5, 5, 7.5, and 10 [mm]). The experiment was performed
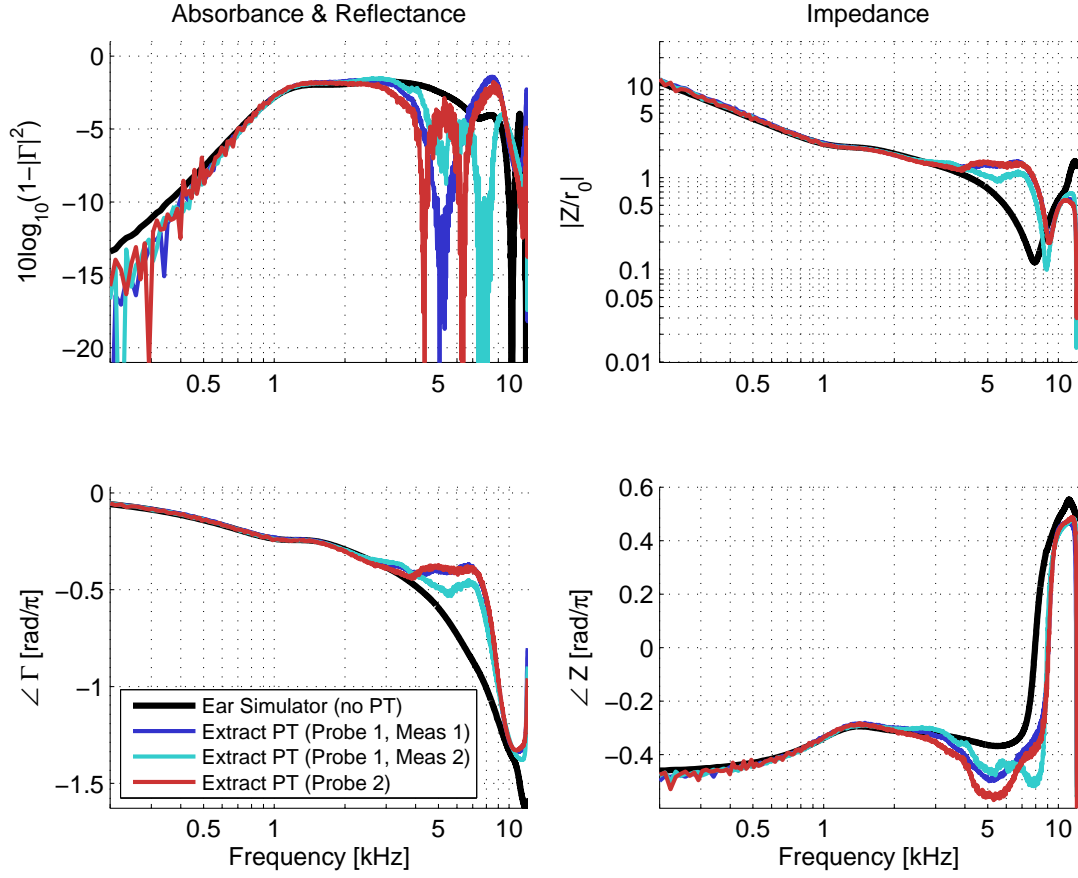
Figure 4.12: Attempt to extract the probe-tip effect from measurements of the Mimosa Acoustics average-ear simulator, made with the probe tip on. The simulator response without the probe tip is shown as a solid black line. Three colored curves show measurements made with the probe tip on, and mathematically extracted using the two-port probe-tip model. The WAI at the output of the tip can be accurately estimated from measurements with the tip on up to 3-4 [kHz].

twice using two different Mimosa Acoustic prototype probes.

Considering Figure 4.13, the measured $ABCD$ matrix is very similar to the theoretical matrix (solid black line). A significant deviation of the data from the model occurs for the B parameter. This effect appears to be that of a series compliance placed between the probe tip and the load, such that

$$T_{pt} = \begin{bmatrix} A' & B' \\ C' & D' \end{bmatrix} = \begin{bmatrix} A & B \\ C & D \end{bmatrix} \begin{bmatrix} 1 & Z_C \\ 0 & 1 \end{bmatrix} = \begin{bmatrix} A & (Z_C A + B) \\ C & (Z_C C + D) \end{bmatrix}. \tag{4.6}$$

Using a compliance in parallel with a resistor,

$$Z_C(f) = \frac{R_0}{1 + j2\pi f C_0 R_0}, \tag{4.7}$$

with $C_0 \approx 6.3 \times 10^{-12}$ and $R_0 \approx 3.6 \times 10^7$, the behavior of the element B may be approximated, without degrading the model fit for the other $ABCD$ (and Z matrix) elements. It is unclear whether this model addition is attributable to problems with this specific test system, to the probe tip itself, or to non-ideal properties of the plane of the area discontinuity. The compliance C_0 corresponds to a volume with cubed root $V^{-1/3} \approx 1$ [mm], while the resistance R_0, if taken to equal $\rho_0 c_0 / A_0$ for a cylindrical area, corresponds to a radius of 1.9 [mm]. Such dimensions could be related to crevices in the interface between the probe tip and cavity load. Or, the added compliance could instead be due to non-rigid properties of the glue-gun glue.

Considering Figure 4.14, the measured impedance matrix elements are similar to the model, though they are slightly lower at low frequencies. This low-frequency deviation may be easily approximated by adding a very small leak to the model, between the probe tip and the test load, as

$$T_{pt} = \begin{bmatrix} A' & B' \\ C' & D' \end{bmatrix} = \begin{bmatrix} A & B \\ C & D \end{bmatrix} \begin{bmatrix} 1 & 0 \\ Y_R & 1 \end{bmatrix} = \begin{bmatrix} (A + Y_R B) & B \\ (C + Y_R D) & D \end{bmatrix}, \tag{4.8}$$

where Y_R is the impedance of an infinite tube with a radius of approximately 0.1 [mm]. It is quite likely this leak is present in this test setup, which was difficult to acoustically seal. However, it is unlikely that the leak also exists when the probe tip is sealed in the ear simulator using an ear-tip.

4.5 Summary

Variable-area horns are known to present computationally difficult problems, particularly when constrictions are present (Sondhi & Resnick, 1983). In the current study, the two-port modeling strategy is insufficient for estimating the ear-canal WAI at high frequencies. In the following chapter, it will be shown that this direct synthesis of the known area function still performs better than many inverse methods.

In this chapter, it was shown that the relative length of the conical section has little effect on the measured impedance. Decreasing the probe-tip length shifts its effects upward in frequency, due to the reduced delay. Additionally, the measured impedance and transfer function are highly dependent on the load impedance; they are adversely affected when more delay is present in the load. With these considerations in mind, a probe tip may be designed to minimize these sources of variation. Additionally, a model-fitting procedure might be used to relate the experimental measurements of the two-port network with the computational model.

The probe-tip effects on WAI (Fig. 4.8) coincidentally demonstrate the effect of an area constriction in the ear canal. Such effects are seen in real ears (Lewis et al., 2009; Voss & Allen, 1994; Allen et al., 2005), though they are typically less severe. The high-frequency roll-off of the absorbance level is often attributed to mass-like characteristics of the middle ear (Allen et al., 2005). However, these simulations show that ear-canal area variations might cause similar effects.
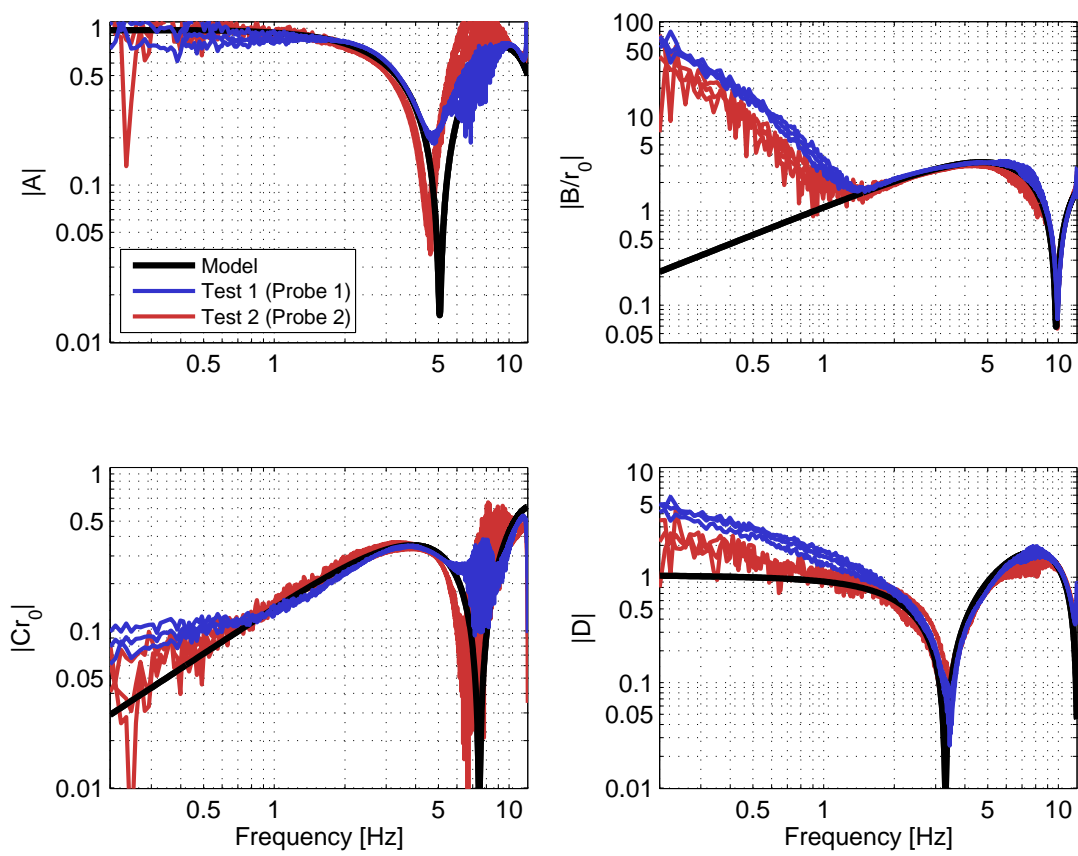
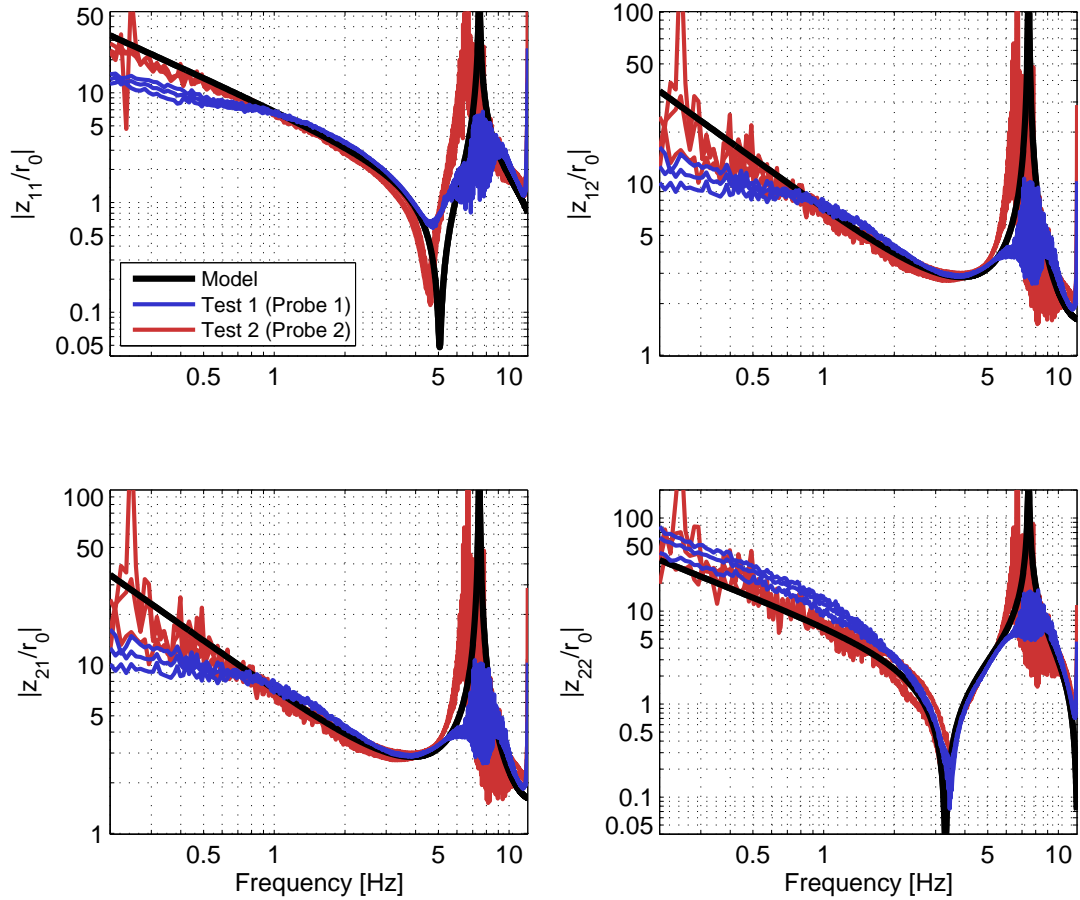Figure 4.13: Transmission (ABCD) matrix calibrations of the probe tip for two different prototype probes, calibrated using three known loads according to Section B.3 (assuming that the lossy probe tip is approximately reciprocal). Multiple combinations of three-load calibrations were calculated using the measured 2.5, 5, 7.5, and 10 [mm] cylindrical loads; three of four load combinations were shown for each probe. The measurements and model are in reasonable agreement, except for B (top right) at low frequencies. As discussed in the text, the large deviation in B is likely due to the compliance of the glue holding the probe tip and cylindrical cavity together.

Figure 4.14: Impedance matrix calibrations of the probe tip for two different prototype probes, calibrated using three known loads according to Section B.3 (assuming that the lossy probe tip is approximately reciprocal). Multiple combinations of three-load calibrations were calculated using the measured 2.5, 5, 7.5, and 10 [mm] cylindrical loads; three of four load combinations were shown for each probe. The measurements and model are in reasonable agreement. The measurements fall slightly below the model at low frequencies; this phenomenon is easily modeled by adding a small leak between the output of the probe tip and the two-port calibration load.

CHAPTER 5

RESULTS: EFFECTS OF THE EAR CANAL

To compare wideband acoustic immittance (WAI) measurements across ears, it is necessary to remove or avoid the effects of the residual ear canal (REC), which is of unknown dimensions. The goal is to estimate the WAI at the tympanic membrane (TM). As described in Chapters 1 and 2, it is possible to (mostly) avoid the effects of the REC by considering the magnitude reflectance only. This chapter compares methods for estimating the complex WAI at the TM by accounting for magnitude and phase effects of the REC. Additionally, delay effects of the TM itself are analyzed using the distributed models given in Table 2.2.

The pole-zero fitting and reflectance factorization method described in Section 3.5 was originally used to analyze REC effects and measurements of negative middle-ear pressure (NMEP), described in the following chapter (Robinson et al., 2013, 2016). In this chapter, it is shown that this method compares favorably to other methods of characterizing the ear canal (Rasetshwane & Neely, 2011; Lewis & Neely, 2015). As a computationally fast, frequency-domain method, pole-zero fitting appears to be the most straightforward way to estimate the complex WAI at the TM, particularly when the frequency range of the data is limited.

5.1   Pole-zero fitting and reflectance factorization

In this section, the reflectance factorization into minimum-phase and all-pass parts is examined. Recall that the magnitude of the all-pass component is constrained to be one,

$$|\Gamma_{ec}| \approx |\Gamma_{ap}| = 1. \tag{5.1}$$

Therefore, the ear canal is assumed to have the magnitude effects of a lossless, uniform tube. In the case of a uniform-area ear canal, the group delay is expected to be constant, $\tau = 2L/c_0$. However, the phase of the all-pass component may contain a frequency-dependent group delay,

$$\Gamma_{ec} = e^{-j\omega\tau}, \tag{5.2}$$

where τ is a function of frequency $s = \sigma + j\omega$. Intuitively, this factorization can capture the phase effects of a variable-area canal, even though it cannot account for the magnitude effects.

The pole-zero method will first be validated using known volumes in a syringe. Then, the all-pass

factors for middle-ear data from Robinson et al. (2016) will be examined. In the next section, this method will be compared to other methods for estimating the ear-canal area function and WAI at the TM.

5.1.1 Verification in a syringe

The reflectance factorization algorithm was experimentally verified by measuring the WAI of known volumes in a syringe. For each of two calibrated probe tips, 32 measurements were made, for a total of 64 measurements. The foam tipped probe was sealed in the syringe, which was terminated by a rubber stopper attached to a plunger, and the volume was controlled by changing the plunger depth. Note that this termination, which is acoustically rigid, is expected to be different from the eardrum because it has no delay or acoustic loss. The syringe diameter was about 8.7 [mm], slightly larger than the average diameter of the adult ear canal (about 7.5 [mm]). The rubber stopper had small conical peak, with a negligible volume of approximately 0.03 [mL].
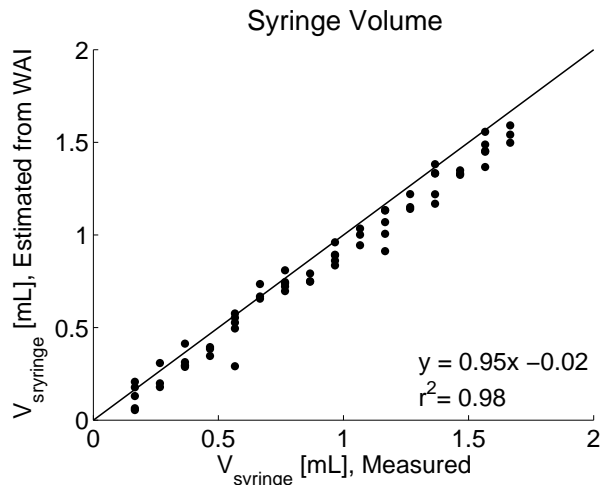
Figure 5.1: Volumes in a syringe, estimated from WAI using the reflectance factorization method (Robinson et al., 2013). The volume range of 0.2 to 1.7 [mL] corresponds to a length range of about 3 to 29 [mm]. Variability in the measured lengths may be partially due to visual estimation of the syringe length, as the measured lengths appear to be quantized. Considering only the lossless delay, the volumes estimated from WAI are about 5% smaller than the measured volumes.

Figure 5.1 shows WAI estimates of the syringe volume made over a range of 0.2 to 1.7 [mL], corresponding to a length range of about 3 to 29 [mm]. Some variability in the WAI estimates versus the measured lengths may be due to visual estimation of the syringe length, as the measured volumes appear to be quantized according to the volume markings on the syringe. A linear regression ($r^2 = 0.98$) shows that the volumes estimated via reflectance factorization are about 5% less than the measured volumes. This is likely due to acoustic losses in the syringe (Keefe, 1984), as the reflectance factorization considers only lossless delay. Using the raw, unfiltered measurements (including losses), the regression line is $y = 0.98x + 0.06$ ($r^2 = 0.99$).

5.1.2 Residual ear canal group delays

Recall that the group delay factor, when constant, corresponds to a time-domain delay. By the time-delay property of the Fourier (or Laplace) transform

$$\Gamma_{tm}e^{j\omega\tau} \leftrightarrow \gamma_{tm}(t-\tau). \tag{5.3}$$

Therefore, the group-delay function $\tau(\omega)$ describes the ear-canal delay, and lends much more insight than the phase.

Figure 5.2 shows group delay functions for ears from Robinson et al. (2016). This study examined the effects of negative middle-ear pressure (NMEP) on WAI in normal ears. The details of the experimental procedures and inducement of NMEP are described in the following chapter. In brief, eight ears were measured at both ambient middle-ear pressure (AMEP) and NMEP. AMEP and NMEP measurements were interleaved, with each subject experiencing a consistent NMEP level. In general, little to no change in ear-canal sound propagation is expected between the two conditions, unless the TM is significantly deformed by NMEP.
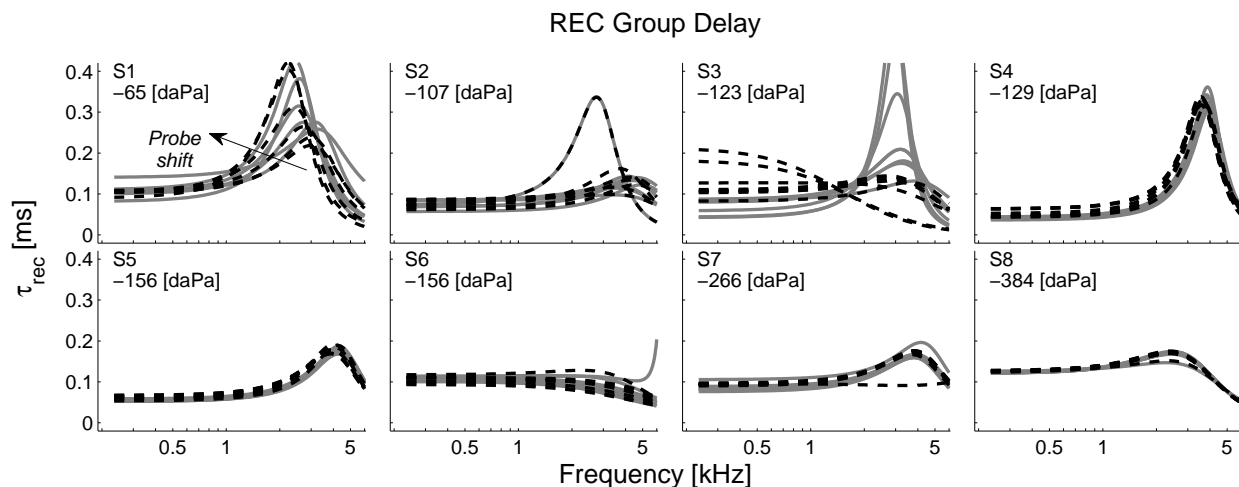
Figure 5.2: The estimated residual ear canal (REC) group delay, $\tau_{rec}(f)$ (Eq. 2.28c), is shown for all ears. Ambient middle ear pressure (AMEP, gray solid) and negative middle ear pressure (NMEP, black dashed) states are shown, ordered by mean NMEP tympanic peak pressure (TPP). Note that these responses are smooth due to the parametric fit to the complex reflectance, $\Gamma(f)$, from which $\tau_{rec}(f)$ is derived. Some ears, particularly ear S1, show differing responses across measurements which do not depend on the pressure state. As discussed in the text, this is likely due to changes in the probe insertion.

The residual ear canal (REC) delays shown in Figure 5.2 are ordered by mean NMEP. AMEP and NMEP states are shown as gray solid and black dashed lines, respectively. As expected, the frequency-dependent REC delays, $\tau_{rec}(f)$, are relatively constant across pressure conditions and retest measurements for most ears. These responses are smooth due to the parametric fit to the complex reflectance, $\Gamma(f)$, from which $\Gamma_{rec}(f)$ and subsequently $\tau_{rec}(f)$ are derived. All ears show

some frequency-dependent variation in group delay, though the range of this change varies by ear. We hypothesize that this frequency dependence relates to area variations in the ear canal.

Though probe insertions were not intentionally modified between measurements, a few ears show changes in $\tau_{rec}(f)$ that are independent of pressure state. For example, ear S1 (top left plot) shows a varying $\tau_{rec}(f)$ function across measurements, meaning the estimated REC length changed during data collection. The largest change in $\tau_{rec}(f)$ for S1 occurred between 2 and 3 [kHz], where there is a peak in $\tau_{rec}(f)$ that changed with time.
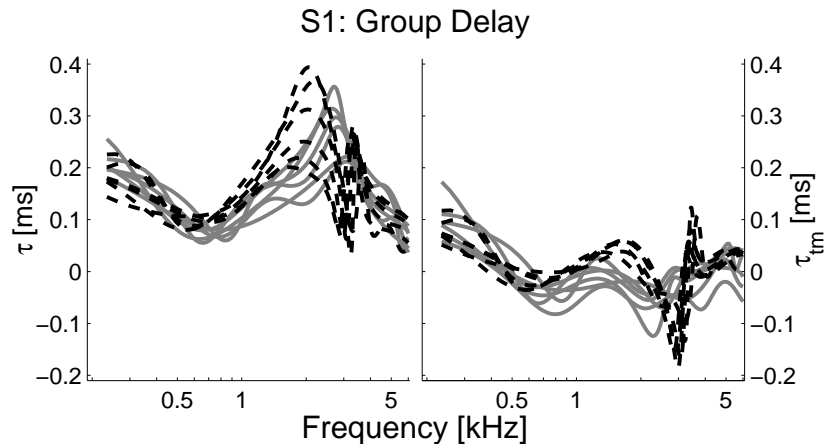
Figure 5.3: The total group delay, $\tau(f)$, and tympanic membrane (TM) group delay, $\tau_{tm}(f)$, for subject S1. Ambient middle ear pressure (AMEP, gray solid) and negative middle ear pressure (NMEP, black dashed) states are shown. Removing the group delay due to the residual ear canal (REC), $\tau_{tm}(f) = \tau(f) - \tau_{rec}(f)$, visibly reduces variability in $\tau_{tm}(f)$ with respect to $\tau(f)$. Note that these responses are smooth due to the parametric fit to the complex reflectance, $\Gamma(f)$, from which $\tau(f)$ and $\tau_{tm}(f)$ are derived.

The TM delay, $\tau_{tm}(f)$, and the total delay, $\tau(f)$, are also shown for ear S1 in Figure 5.3. When the REC delay is removed from the total delay (left), the resulting TM delay, $\tau_{tm}(f) = \tau(f) - \tau_{rec}(f)$ (right), is more coherent across trials. The variation in $\tau_{tm}(f)$ is slightly greater in the AMEP state. This is consistent with a greater variation of the absorbance level, which will be shown in the following chapter (Fig. 6.2). This variation may be due to an inadequate release of the NMEP between trials.

As shown in Figure 5.2, some ears show changes in $\tau_{rec}(f)$ that are independent of pressure state, which may indicate 'drift' in the probe insertion. Such drifts could be caused by small movements of a subject's head between measurements, or the weight of the cable slowly pulling the probe out of the ear canal. Considering $\tau_{rec}(f)$ for subject S1 (top left plot), the REC group delay changed systematically with time during data collection, showing an increasing mid-frequency peak. Such a peak is functionally consistent with an area constriction in the REC (Karal, 1953; Puria, 1991), which could be due to the angle of the probe in the ear canal (e.g. a drooping probe insertion). Considering Figure 5.3, removing the time-varying REC delay gives a more consistent estimate of the complex WAI at the TM, which indicates that the reflectance factorization method can account

Table 5.1: Methods for computing the ear-canal area function and middle-ear immittance.

Acronym	Method
RN2011	Time-domain inverse solution using reflectance (Rasetshwane & Neely, 2011; Rasetshwane et al., 2012; Rasetshwane & Neely, 2015). This method typically yields a very smooth estimation of the area function. Matlab code is publicly available at `http://audres.org/cel/refl/measures.html`.
LN2015	Frequency-domain fitting procedure using impedance (Lewis & Neely, 2015). This method fits the data to a seven-conical-segment model of the ear canal, and a simplified middle-ear impedance described by Kringlebotn (1988). Matlab code for this method was generously provided by the authors.
SG1971	Time-domain inverse solution using impedance (Sondhi & Gopinath, 1971). This solution calculates the area function by solving a Fredholm integral equation. The problem may be cast as a Fredholm integral of either the 1st or 2nd kind. The stability of the solution depends on the inversion of a convolution matrix.
SR1983	Time-domain inverse solution using 'step' reflectance estimate of impedance impulse response (Sondhi & Resnick, 1983). This method uses a Fredholm integral of the 2nd kind as in Sondhi & Gopinath (1971). However, the time-domain impedance is estimated from the step reflectance (described in Sec. 3.4.2).
RNA2013	Frequency-domain fitting procedure using reflectance or impedance (Robinson et al., 2013, 2016). The WAI at the TM is determined by factoring out the all-pass component of the reflectance fit, as described in Section 3.5.

for variation in the REC dimensions.

5.2   Comparison of methods

In this section, the reflectance factorization method is validated via comparison to other published methods for computing the ear-canal area function and WAI at the TM. These methods were previously described in Chapter 3. They include the inverse solutions of Sondhi & Gopinath (1971), Sondhi & Resnick (1983), and Rasetshwane & Neely (2011); the frequency-domain fitting of an ear-canal and middle-ear model by Lewis & Neely (2015); and the pole-zero fitting and factorization procedure given by Robinson et al. (2013). A summary of the methods and their corresponding acronyms is given in Table 5.1.

5.2.1   Simulation results

Figure 5.4 shows the results of these assorted inverse methods for a simulation of a variable-area horn, with dimensions shown by the thick black line. These dimensions were chosen to mimic the probe tip tested in Chapter 4. The left-hand plot shows a variable area system terminated in an

infinite-tube matched load, while the right-hand plot shows the same system terminated in a rigid wall at about 30 [mm]. These simulations are only performed up to 20 [kHz], since WAI typically is not measured above this frequency. This imposes a serious limitation on time-domain methods, and we expect the time-domain inverse method results would improve if the bandwidth of the simulation were extended.
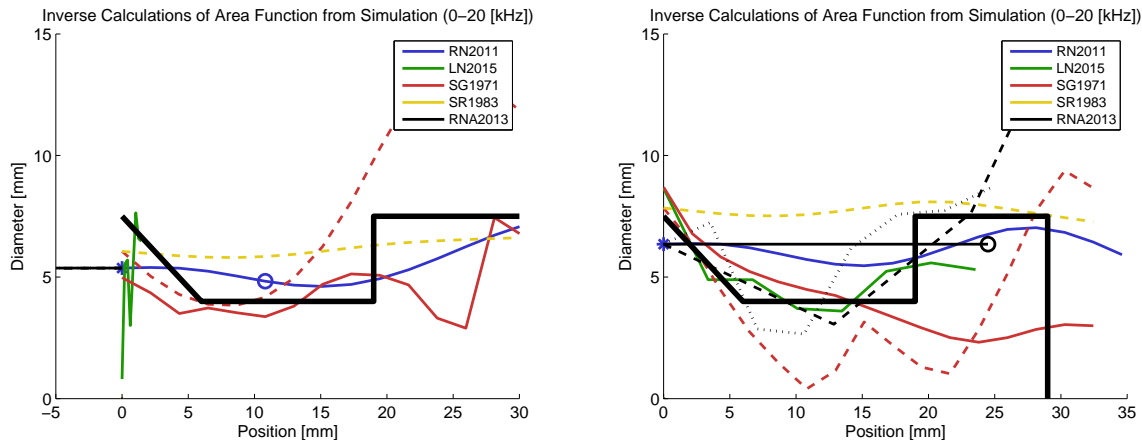

Figure 5.4: Determination of a simulated area function (thick black line) using multiple inverse methods. A variable area horn resembling the probe tip of Chapter 4 is terminated in an infinite-tube matched load (left) and a rigid wall (right). The simulation was performed over a 0-20 [kHz] range, mimicking the typical maximum range of WAI data. Line colors denote the method used to estimate the area function, with line styles representing variations of the same method.

Note that when the system is terminated in an infinite-tube matched load, the pole-zero method (RNA2013) and the method of Lewis et al. (2009) (LN2015) fail. This not surprising, as both of these methods expect a terminating impedance causing a major reflection. The remaining methods show relatively poor fits to the area function. The reflectance inverse method (RN2011) produces an overly smooth result which is stable, but does not accurately capture the minimum and maximum values of the area function, or the sharp corners. A circle marks the estimated length of the system, which is determined from the peak value of the time-domain reflectance (Rasetshwane & Neely, 2011).

The remaining three curves show the time-domain inverse methods of Sondhi & Gopinath (1971) and Sondhi & Resnick (1983), denoted as SG1971 and SR1983.[1] The dashed lines denote solutions computed from Fredholm integrals of the second kind, where the surge component of the impedance, $r_0\delta(t)$, has been removed from the time-domain impedance convolution integral, as described in Section 3.4.1. Similar to the RN2011 method, these methods provide relatively smooth, but inaccurate, solutions. The Sondhi & Gopinath (1971) method was also implemented using a Fredholm integral of the first kind (solid line). As the bandlimited reponse will have an ill-defined delta-function behavior at $t = 0$, this method was intended to relax the assumptions of

---

[1]These methods were regularized as suggested by Sondhi & Resnick (1983). These inverse methods are notoriously computationally unstable (Allen & Sondhi, 1979).

the Fredholm integral of the second kind by not attempting to remove the surge component of the impedance. This results in a better, though less stable estimate of the area function.

The right-hand plot shows the results for the rigidly terminated simulation. As the time-domain inverse methods RN2011, SG1971 and SR1983 depend on the early-time signal for round-trip propagation to a point x and back, these results are similar to the matched-load case. As a major point of reflection has been included in this model, the RNA2013 and LN2015 methods now also provide solutions. The LN2015 method provides a more accurate approximation of the area function than the time-domain inverse methods. It is worth noting that the model-fitting procedure for this method had an average fit time 3.8 minutes per measurement for the canonical data set of Voss & Allen (1994), and failed catastrophically for one ear (subject 6). In comparison, the remaining methods all run for less than 0.2 seconds on average.

An initial solution and two further interpretations are given for the pole-zero factorization method. Note that this method benefits from an improved estimate of the surge resistance, as given by the RN2011 method.

1. (solid line) $A(x) = \rho_0 c_0 / r_0$ for $0 \leq x \leq L_{ec}$, where the ear-canal length is estimated from the difference in low-frequency volume compliances (Y versus Y_{mp}), as described in Section 6.4.1.

2. (dashed line) $A(x)$ was determined from the group delay of the all-pass component Γ_{ap}, by fitting a three-segment lossless cone model of varying segment lengths using Matlab's `fminsearch` with the terminating boundary impedance $Z_{mp} = r_0(1 + \Gamma_{mp})/(1 - \Gamma_{mp})$.

3. (dotted line) $A(x)$ was determined from the group delay of the all-pass component Γ_{ap}, by fitting a seven-segment lossless cone model of equal segment lengths using Matlab's `fminsearch` with the terminating boundary impedance $Z_{mp} = r_0(1 + \Gamma_{mp})/(1 - \Gamma_{mp})$.

The cone-model fits were performed using the two-port modeling techniques described in Section 3.3.1 and Appendix B. The fits were constrained such that diameters and volumes far outside of the initial estimates incurred an error penalty. This fitting procedure demonstrates that group delays such as those shown in Figure 5.2 may be associated with area variations in the ear canal. In Figure 5.4 (right), the dashed-line fit to the all-pass group delay yields $A(x)$ similar to that of the LN2015 method. This method might be refined in the future to estimate the effects of $A(x)$ on the magnitude reflectance, using the pole-zero method. Note that these `fminsearch` methods, similar to LN2015, require far more computational time than the pole-zero fit.

5.2.2 Human-ear and ear-simulator measurements

This section compares the estimated TM admittance using different methods to extract the ear-canal effect. Note that the inverse methods of Sondhi & Gopinath (1971) and Sondhi & Resnick (1983) are not used because they are too computationally unstable, even using regularization techniques. Therefore, the pole-zero fitting method (RNA2013) is compared to the RN2011 and

LN2015 methods only. Not that for the examples shown here, the fitting range was limited to 7.0 [kHz], to avoid over-fitting of high-frequency noise ripples in the reflectance.
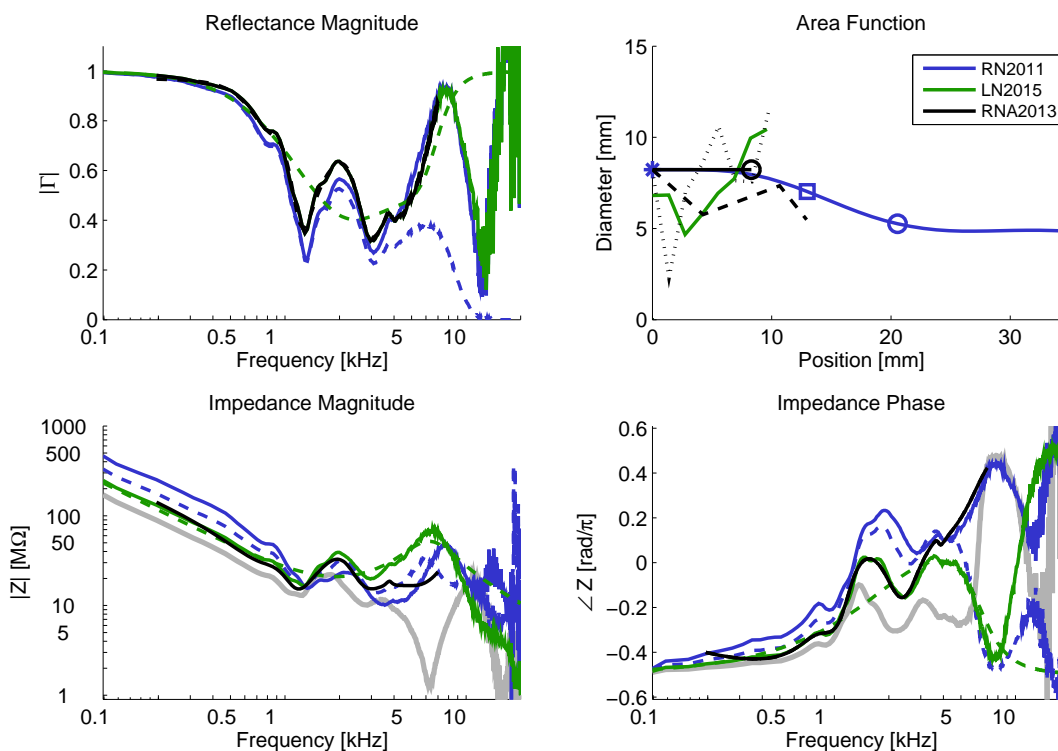

Figure 5.5: Estimated area function and TM impedance for RN2011, LN2015, and pole-zero (RNA2013) methods for Subject 1 of Voss & Allen (1994). For the magnitude reflectance (upper left), solid lines are used to represent the raw/smoothed data for each method. The dashed line for RN2011 indicates the frequency-domain window, and the dashed lines for RNA2013 and LN2015 indicate the final model fit. The area functions (upper right) are displayed in the style of Figure 5.4. Estimated ear-canal lengths are marked with circles, and the dashed and dotted lines show $A(x)$ determined from the all-pass group delay (RNA2013). The impedance plots (bottom) show the original measured impedance (gray), and the TM impedance estimated by each model. The dashed line for LN2015 represents the fitted model, while the solid lines for RN2011 and LN2015 show the result of extracting $A(x)$ using $ABCD$ modeling. The dashed blue lines in the bottom plots show when an ear-canal length corresponding to the blue square (top-right) with $A(x)$ specified by RN2011 has been removed.

Figure 5.5 shows the results for subject 1 of Voss & Allen (1994). Line colors indicate the estimation method, while line styles (described in the caption) indicate variations of, or quantities related to, a particular method. Considering the impedance magnitude and phase (bottom), the pole-zero method agrees closely with the LN2015 method up to about 3 [kHz]. The estimated ear-canal length (top right) from the pole-zero method is similar to the length estimated by LN2015, and corresponds to the flat portion of the area function determined by RN2011. Additionally, the dashed-line fit to the all-pass group delay yields an area function similar to that of LN2015. Note

that the impedance-smoothing procedure used by RN2011 creates a low-frequency aberration in the magnitude reflectance.
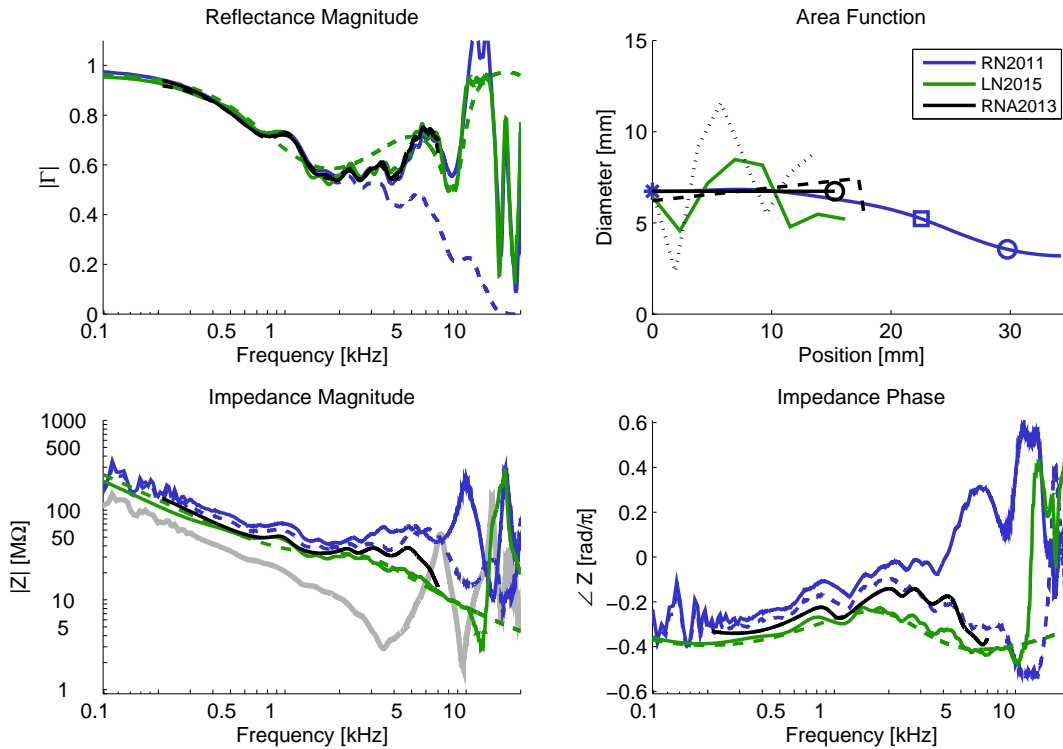

Figure 5.6: Estimated area function and TM impedance for RN2011, LN2015, and pole-zero (RNA2013) methods for an ear provided with the RN2011 code. For the magnitude reflectance (upper left), solid lines are used to represent the raw/smoothed data for each method. The dashed line for RN2011 indicates the frequency-domain window, and the dashed lines for RNA2013 and LN2015 indicate the final model fit. The area functions (upper right) are displayed in the style of Figure 5.4. Estimated ear-canal lengths are marked with circles, and the dashed and dotted lines show $A(x)$ determined from the all-pass group delay (RNA2013). The impedance plots (bottom) show the original measured impedance (gray), and the TM impedance estimated by each model. The dashed line for LN2015 represents the fitted model, while the solid lines for RN2011 and LN2015 show the result of extracting $A(x)$ using $ABCD$ modeling. The dashed blue lines in the bottom plots show when an ear-canal length corresponding to the blue square (top-right) with $A(x)$ specified by RN2011 has been removed.

Figure 5.6 shows the results for a measurement provided by the authors of RN2011[2] for running their inverse method code. This data is compatible with the impedance-smoothing method used in the inverse code, such that the low-frequency reflectance is not altered by the RN2011 method. Considering the impedance magnitude and phase (bottom), the pole-zero result lies in between the RN2011 and LN2015 methods. The estimated ear-canal length (top right) from the pole-zero method is similar to that estimated by LN2015 and roughly corresponds to the flat portion of the

---

[2]http://audres.org/cel/refl/measures.html

area function determined by RN2011. Additionally, the fits to the all-pass group delay yield an area function similar to that of LN2015.
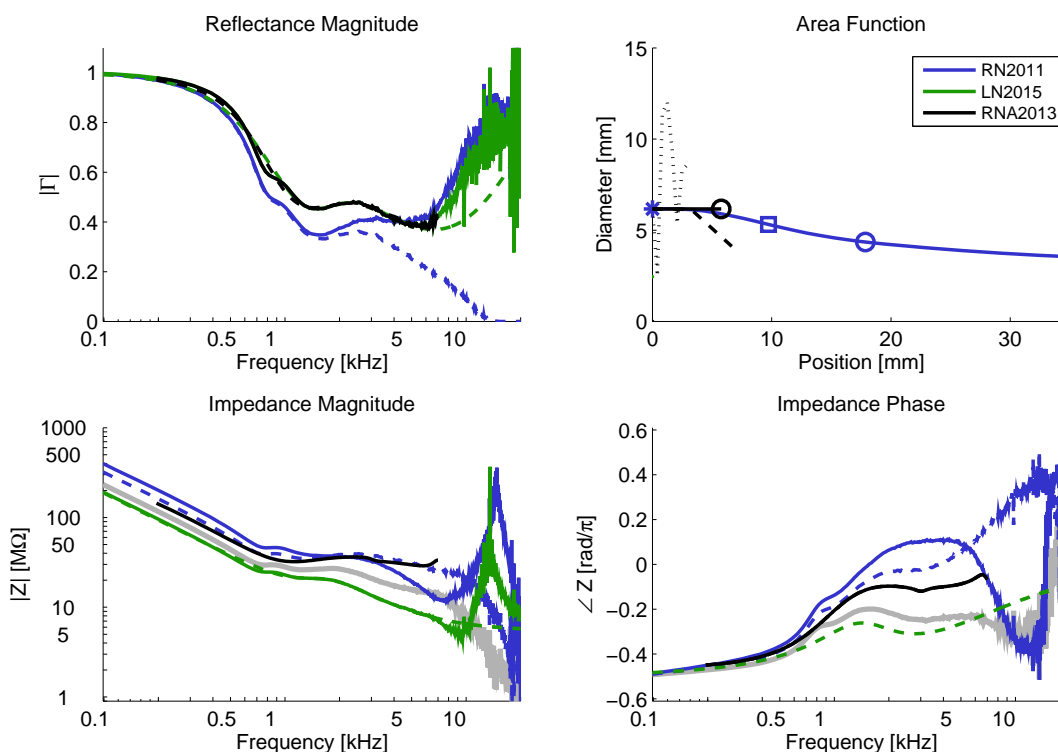

Figure 5.7: Estimated area function and TM impedance for RN2011, LN2015, and pole-zero (RNA2013) methods for the DB-100 ear simulator as measured by Voss & Allen (1994). For the magnitude reflectance (upper left), solid lines are used to represent the raw/smoothed data for each method. The dashed line for RN2011 indicates the frequency-domain window, and the dashed lines for RNA2013 and LN2015 indicate the final model fit. The area functions (upper right) are displayed in the style of Figure 5.4. Estimated ear-canal lengths are marked with circles, and the dashed and dotted lines show $A(x)$ determined from the all-pass group delay (RNA2013). The impedance plots (bottom) show the original measured impedance (gray), and the TM impedance estimated by each model. The dashed line for LN2015 represents the fitted model, while the solid lines for RN2011 and LN2015 show the result of extracting $A(x)$ using $ABCD$ modeling. The dashed blue lines in the bottom plots show when an ear-canal length corresponding to the blue square (top-right) with $A(x)$ specified by RN2011 has been removed.

Finally, Figure 5.7 shows the results for the DB-100 ear simulator ('Zwislocki ear') as measured by Voss & Allen (1994). Considering the impedance magnitude (bottom left), the pole-zero method agrees closely with both other methods. Considering the impedance phase, the pole-zero method agrees more closely with the LN2015 method at low frequencies, and the RN2011 method at higher frequencies. The estimated ear-canal length (top right) from the pole-zero method is very short for this ear (3 [mm]), which is expected for this ear simulator. Note that the LN2015 method estimates the ear-canal length to be 0 [mm].

In contrast, the RN2011 method estimates the ear canal of the DB-100 simulator to be over 10 [mm] long. This area taper appears in all three measurements fitted here, and in the results presented in Rasetshwane & Neely (2011). In general, it estimates the ear canal to be 10-15 [mm] longer than that estimated by LN2015 or the pole-zero method. Therefore, this taper may be related to the taper in the area under the TM, sound transmission on the TM, or some signal processing artifact related to the apparent over-smoothing of the area function. When the LN2011 area function $A(x)$ is used with a shorter length estimated (blue square, Figs. 5.5, 5.6, and 5.7, top-right), the TM impedance estimates match the RNA2013 and LN2015 estimates more closely (dashed blue line, Figs. 5.5, 5.6, and 5.7, bottom).

5.3 Other factors influencing area function and delay

This section investigates two other factors which may impact estimation of the ear-canal area function: TM delay and ear-canal curvature. Based on a quick test measurement, curvature appears to have a minimal impact on the measured WAI when compared to area variations. Therefore, it is not studied in great detail.

5.3.1 Tympanic membrane delay

Tympanic membrane delay, as described in Chapter 2, may contribute a large delay to the measured WAI. Therefore, it would be helpful to determine how the ear-canal estimation methods interpret this delay. As no data of an isolated TM was available at the time of this writing, the distributed TM models described in Figure 2.2 are analyzed. These models include a uniform tube terminated in a transformer (Puria & Allen, 1998; O'Connor & Puria, 2008), a wave-digital-filter model (Parent & Allen, 2007, 2010), a string model (Goll & Dalhoff, 2011; Milazzo et al., 2017), and a two-piston model (e.g. Shaw (1977)) with added delay (Keefe, 2015b).

Model preparation. For comparison and simulations, all TM models were cast in two-port form. This form is known for the uniform tube model, and was specified exactly in the model of Keefe (2015b). The $ABCD$ model of Parent & Allen (2010) was computed using simulation code provided by the authors, by modifying boundary conditions at the umbo.

The model of Goll & Dalhoff (2011), based on the intuition of Parent & Allen (2010), models wave propagation on a one-dimensional string. In this case, one end of the string is fixed (either rigidly or non-rigidly) at the rim of the TM, and the other end represents the umbo boundary condition. This model was transformed into $ABCD$ form by imposing boundary conditions on the given differential equations for the string. Note that Milazzo et al. (2017) suggested a slightly different boundary condition for the pressure at the TM, making it constant instead of linearly increasing along the string length. The $ABCD$ models for both pressure conditions, with rigid and

non-rigid suspension at the TM rim, were calculated for this analysis.

Two-port models. Figures 5.8 and 5.9 show the frequency-dependent transmission and impedance matrix parameters for the TM models described above, simulated over a 0-12 [kHz] range. Considering the transmission matrix, many of these models are similar to the uniform-tube model. This is due to the delay present in each of the models. The B parameter experiences the most variation across models. The Parent & Allen (2010) model has very different magnitudes for the A and C quantities, which is likely a transformer effect, such that the overall transformer ratio from the ear canal to the umbo is different for this model. The pressure conditions distinguishing the Goll & Dalhoff (2011) and Milazzo et al. (2017) models cause much less variation in the two-port properties of the TM than the flexibility of the TM rim boundary condition.
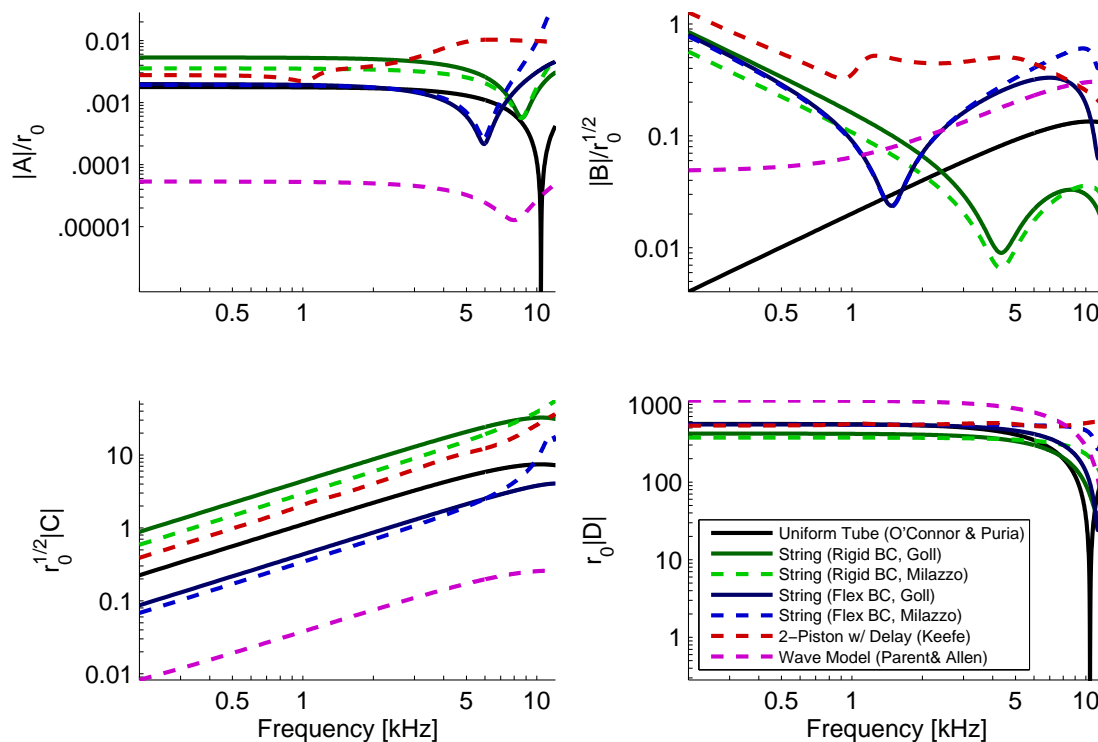

Figure 5.8: Transmission-matrix parameters for various models of the eardrum. Many models bear similarity to the uniform-tube model, including a high-frequency minimum in the A parameter due to delay (with the exception of the Keefe (2015a) model). The models of Goll & Dalhoff (2011) and Milazzo et al. (2017) use different boundary conditions for the pressure distribution at the eardrum (dashed vs. solid), but this condition has far less impact on the model than the rigidity of eardrum-rim boundary condition. The B parameter experiences the most variation across models.

Considering the impedance matrix (Fig. 5.9), these models look very similar. Note the high-frequency standing wave nulls in these impedances, which indicate TM delay. These delays may

appear to be additional length when using inverse area-function methods. Note that these models all estimate the TM radius to fall somewhere between 3.5 and 5 [mm], corresponding to a quarter-wavelength standing wave frequency of 17 [kHz] or higher. However, the slower wave-speed on the TM makes the distance to the umbo appear longer.
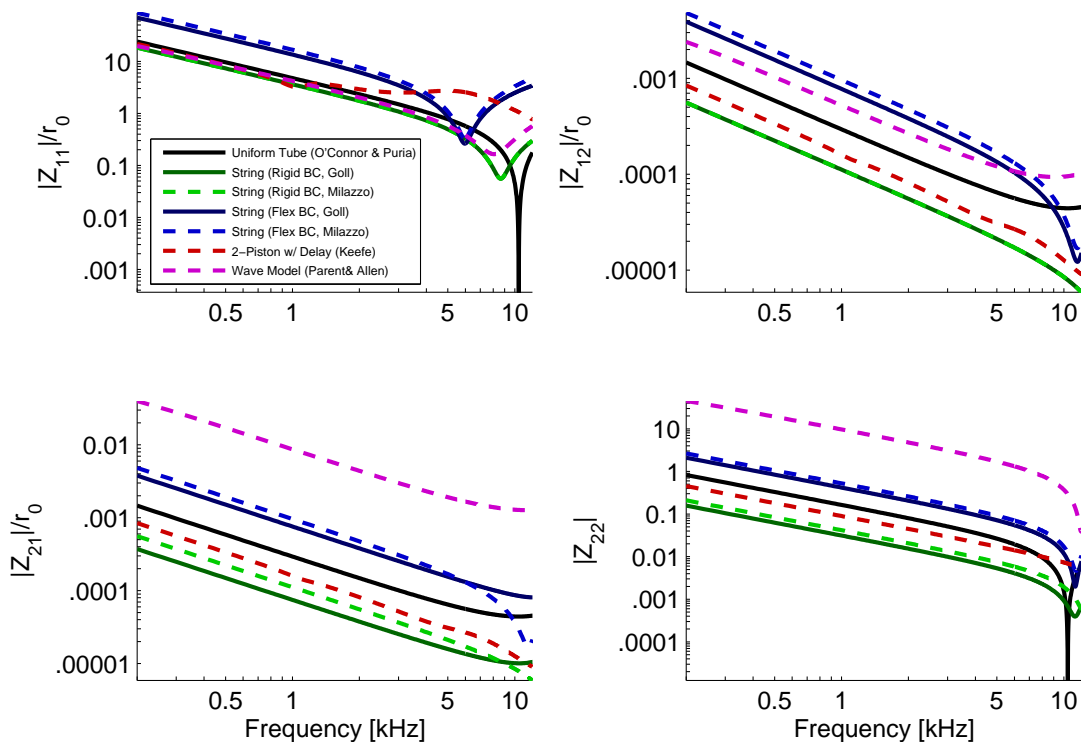

Figure 5.9: Impedance-matrix parameters for various models of the eardrum. Note that Z_{11} is the input impedance of the eardrum when the umbo is blocked (immobilized).

Finally, Figure 5.10 shows the reflectance magnitude and phase of the TM when the umbo is blocked. When there is a flexible boundary condition for the Goll & Dalhoff (2011) and Milazzo et al. (2017) models, a sharp minimum appears in the magnitude at high frequencies, likely due to the string resonance at this boundary. Also note that the reflectance of the Keefe (2015b) model resembles the magnitude reflectance of the normal ear (Fig. 2.3). This seems like it may be fitting some energy absorbance of the middle ear and cochlea to the TM instead.

Application of area methods to the TM. An important question is, What do these distributed TM models look like to inverse-area and area-fitting methods? Since the TM contains delay, it may be mis-identified as an extension of the ear-canal area function rather than a separate entity. It remains unclear whether removing lossless delay from the TM would improve or degrade estimates of the WAI at the TM.

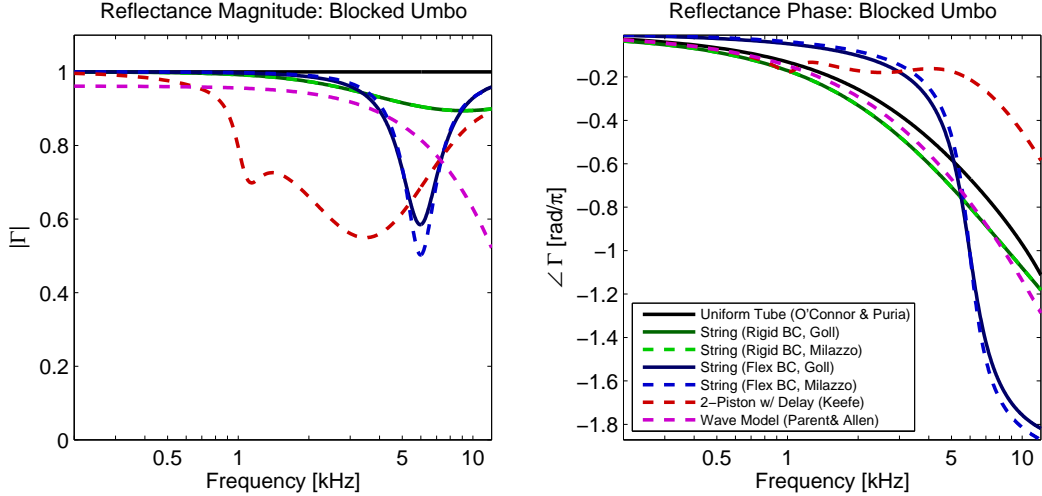Figure 5.11 shows the area function results using a number of methods, as described in Table

Figure 5.10: Input reflectance of the eardrum when the umbo is blocked (immobilized). Note that the reflectance of the Keefe (2015b) model resembles the magnitude reflectance of the normal ear, possibly attributing loss to the eardrum that should be associated with the middle ear.

5.1. The presentation of this data is similar to that of Figure 5.4. For all TM models, the pole-zero method and the fit of Lewis & Neely (2015) predict a much shorter ear canal than Rasetshwane & Neely (2011). As in Figures 5.5, 5.6, and 5.7, the RN2011 method predicts a taper of the area function. Therefore, it is likely that this taper, when it appears in measurements of human middle ears, represents sound transmission on the TM.

5.3.2   Propagation around a bend

Bends in the ear canal may also affect sound propagation and estimation of the ear-canal area function. There is some literature on this topic (Miles, 1947; Keefe & Benade, 1983), but a quick measurement sufficed to show that any effect due to a bend will be small compared to the effects of ear-canal area variation.

Measurement.   Two measurements were made using rapid-prototyped cylinders 3 [cm] in length along their central axes. One cylinder was bent at a 90° angle, as shown in Figure 5.12, such that the diameter remained constant throughout the bend. At one end a measurement probe was sealed into the tube, and at the other the tube was sealed to the input of an ear simulator using poster putty.

  Figure 5.13 shows the resulting complex WAI measurements for the configuration in Figure 5.12, for both the bent tube and a straight tube of the same length. These results show good agreement between the bent and straight tubes. Slight differences in these measurements appear to be due to a small change in the test tube length and, at high frequencies, the putty seal. Note that due to differences in insertion into the ear simulator, and extra delay and losses from the added length,
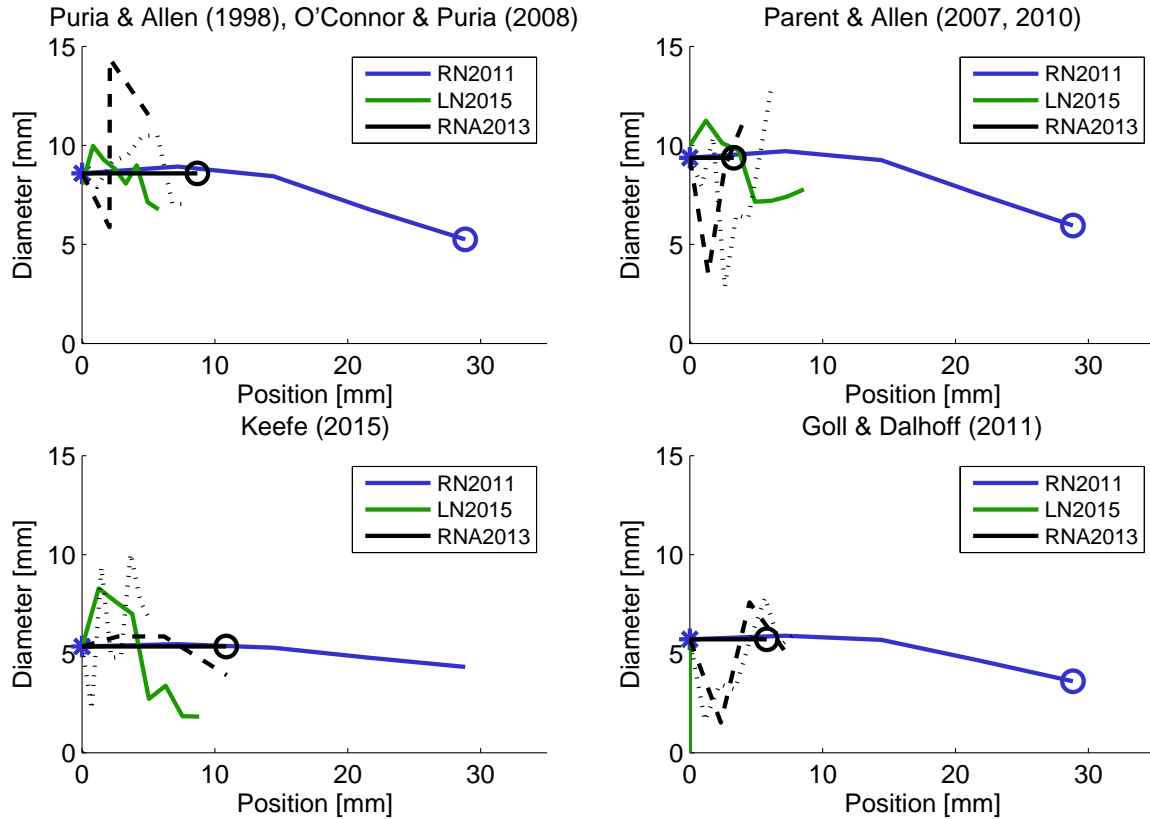
Figure 5.11: Inverse-area and fitted-area solutions for four distributed models of the eardrum, including a uniform tube and transformer (O'Connor & Puria, 2008), a wave-digital-filter model (Parent & Allen, 2007), a two-piston model with delay (Keefe, 2015b), and a string model (Goll & Dalhoff, 2011) with a flexible boundary condition at the eardrum rim. Note that the LN2015 method failed for the (Goll & Dalhoff, 2011) simulation.

both measurements differ from that of the ear simulator with no tube extension.

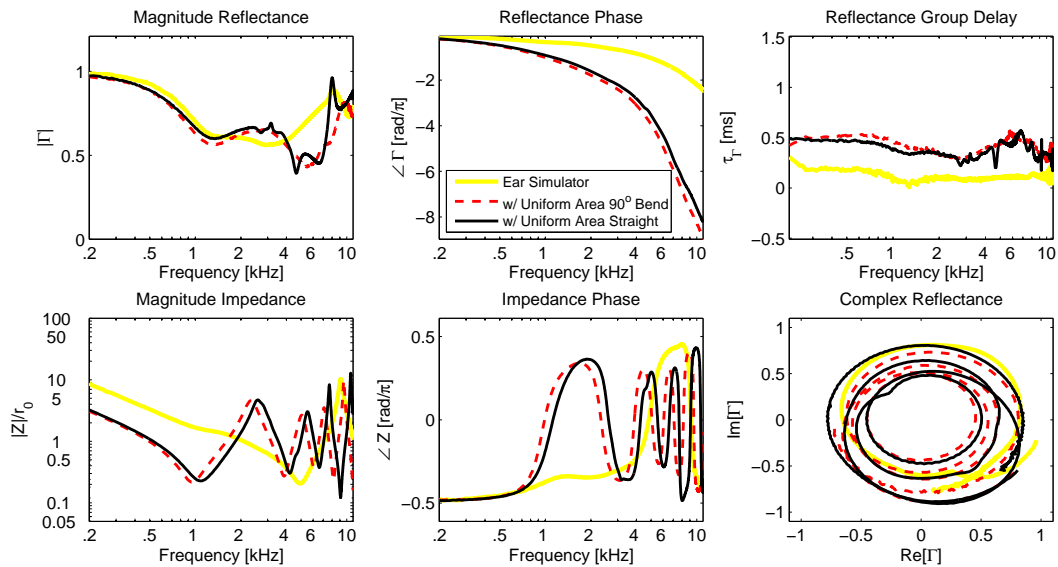Figure 5.12: Measurement of a 90° bend in a uniform-area horn 7.5 [mm] in diameter.

Figure 5.13: Measurements of an average middle-ear simulator with the probe only (solid yellow), a 3 [cm] straight uniform-tube extension (solid black) and a 3 [cm] uniform-diameter extension with a right-angle bend (dashed red). The extensions were sealed to the probe using matched threads and an O-ring, and sealed to the ear simulator using rubber cement and putty. The tube extensions were 7.5 [mm] in diameter. Little change was observed in the WAI response between the straight and bent extensions.

5.4 Comparison to tympanometry

For the assessment of middle ear admittance, tympanometry is the clinical standard. In this procedure, the ear canal admittance, Y (related to the impedance by $Z = 1/Y$, and typically given in milliliters), is measured at a single frequency, typically 226 [Hz], using a probe that is hermetically sealed in the ear canal. The static pressure in the canal is then varied, typically from +200 to -400 [daPa], as described in Chapter 1. A single-frequency precursor to WAI, tympanometry attempts to remove the effects of the ear canal using pressurization. In this section, removal of the ear canal effect in tympanometry is briefly compared to the pole-zero reflectance factorization method, using tympanograms and WAI measurements from Robinson et al. (2016).

Some fundamental assumptions of tympanometry are that (1) at 226 [Hz] the probe admittance is purely compliant (no friction losses), (2) it may be modeled as the sum of two compliances, $|Y_{probe}| \approx 2\pi f(C_{me} + C_{rec})$, where C_{rec} is proportional to the volume of the REC and C_{me} is the aggregate middle ear compliance at the TM, and (3) for extreme canal pressures C_{me} is zero (Shanks et al., 1988). Based on these three assumptions, the high pressure 'tails' of the tympanogram are assumed to be equal to the REC compliance $C_{rec} \approx C_{probe}|_{+200[daPa]}$, which is subtracted from the probe compliance at TPP to obtain the compliance of the middle ear at the TM, $C_{me} = C_{probe}|_{TPP} - C_{probe}|_{+200[daPa]}$.

Assumption (3) has been questioned by several investigators (Rabinowitz, 1981; Shanks & Lilly, 1981; Shanks et al., 1988), who found that C_{me} is underestimated because it does not go to 0 at extreme pressures (thus the volume of the REC is overestimated). Rabinowitz (1981) models this error by relating changes in canal pressure to changes in hearing thresholds. Shanks & Lilly (1981) compare REC volumes estimated by tympanometry with measured volumes to assess this error. They showed that while both methods have errors larger than 20%, the negative tail of the tympanogram is a better estimator of REC volume than the positive tail.

Pressurizing the ear canal to eliminate the REC is a poor approximation above 500 or 600 [Hz] because the admittance at the TM is not a simple compliance (assumption (2)). At higher frequencies, investigators using tympanometry typically consider the conductance G and susceptance B tympanograms, representing the real and imaginary parts of the complex admittance, respectively (Shanks et al., 1988; Vanhuyse et al., 1975).

Here we relate WAI to tympanometry by directly estimating the REC volume and the equivalent compliance at the TM from the complex WAI. In this way we define a relationship between WAI and three parameters derived from the tympanogram: TPP, peak compliance, and REC volume. Using the pole-zero reflectance factorization method (Robinson et al., 2013), we remove REC delay from WAI at all measured frequencies, approximating the WAI response at the TM.

5.4.1 TM Admittance at 226 [Hz]: WAI vs. Tympanometry

Figure 5.14 shows peak compensated static acoustic admittance values estimated via tympanometry at 226 [Hz], $|Y_{tm}|_{f=226[Hz]}$, compared with $|Y_{tm}|_{f=226[Hz]}$ values estimated using WAI at AMEP. WAI estimates include AMEP C_{me} values given in Figure 6.8b, along with r_c values (not shown), according to the model in Figure 6.7b. Boxplots of $|Y_{tm}|_{f=226[Hz]}$ are shown for WAI (gray) and tympanometry (black). Note that the tympanometric measurements were rounded to the nearest 0.1 [mL] by the measurement device; this quantization can be seen in the boxplots. Tympanometric estimates of $|Y_{tm}|_{f=226[Hz]}$ are significantly lower than WAI estimates for all ears except S3 and S8. The variability is similar for both methods of estimating the 226 [Hz] TM admittance, though slightly higher for the WAI measurements. The average standard deviations are 0.10 and 0.08 for WAI and tympanometry, respectively (excluding outliers).
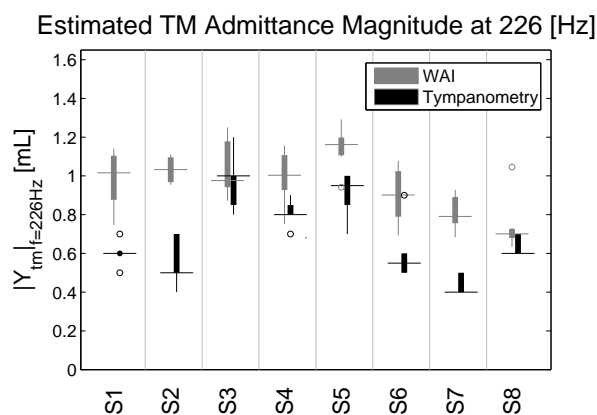

Figure 5.14: Comparison of mean 226 [Hz] tympanic membrane (TM) admittance magnitude values, $|Y_{tm}|_{f=226[Hz]}$, estimated by tympanometry (black box plots) with those estimated from wideband acoustic immittance (WAI, gray box plots) at ambient middle ear pressure (AMEP). The tympanometric estimates are significantly lower than the WAI estimates for all ears except S3 and S8 ($p < 0.005$). On average, tympanometry underestimates the TM compliance by 27%, as previously observed (Rabinowitz, 1981; Shanks & Lilly, 1981).

Figure 5.14 shows that the 226 [Hz] TM admittance is consistently lower when estimated via tympanometry, compared to WAI. As noted by Rabinowitz (1981) and Shanks & Lilly (1981), our results show that it is incorrect to assume that the compliance at the TM is zero at static ear canal pressure extremes, such as +200 [daPa] (assumption (3) of tympanometry, as described above). This assumption causes the admittance (compliance) at the TM to be underestimated. In Figure 5.14, mean tympanometric estimates are 7% to 46% lower than mean WAI estimates (excluding outliers), 27% lower on average, in agreement with Rabinowitz (1981). The variation in these errors is most likely related to individual characteristics of the TM and middle ear when the ear canal pressure is +200 [daPa].

Part of the error in the tympanometric estimates of the 226 [Hz] TM admittance is due to the fact that these estimates are typically lower when the positive tympanogram tail is used to compensate

for the REC volume (Shanks & Lilly, 1981). Shanks & Lilly showed that the error in REC volume estimated at 220 [Hz] was 39% using the positive tail, and 24% using the negative tail. However, in this study it was prudent to compensate for the REC using the positive tail because negative shifts in the TPP due to NMEP could artificially raise the compliance of the negative tail.

Though these results indicate that the tympanometric errors in $|Y_{tm}|_{f=226[Hz]}$ are significant, their clinical relevance is tied to the current utility of the peak compensated static acoustic admittance parameter. In tympanometry, peak compensated admittance is a measure of middle ear compliance, as the admittance at the TM is dominated by stiffness characteristics at 226 [Hz] (Figs. 6.7, 6.4, and 6.5). Low compliance (high stiffness) is linked to middle ear pathologies such as middle ear effusion, otosclerosis, thickened TM, and malleus fixation (Shanks & Shohet, 2009). Therefore, if the estimated value of $|Y_{tm}|_{f=226[Hz]}$ is too low, it could lead to a false positive diagnosis indicating one of these disorders.

According to Shanks & Shohet (2009), the clinical utility of the peak compensated admittance is questionable, due to high normal variability and significant overlap between $|Y_{tm}|_{f=226[Hz]}$ distributions for normal and pathological middle ears. They hypothesize that some of this variability is related to inconsistent compensation methods (e.g. whether the positive or negative tympanogram tail is subtracted from the peak). Further variability is due to the fact that the compliance at the TM does not go to zero at static pressure extremes. Instead, individual ears have varying TM compliance characteristics at the pressure extremes used in tympanometry. It is likely that the error in $|Y_{tm}|_{f=226[Hz]}$ as estimated via tympanometry is one of the primary reasons why the parameter is not clinically useful.

CHAPTER 6

RESULTS: NEGATIVE MIDDLE-EAR PRESSURE

The results of this chapter are drawn from Robinson et al. (2016), and supporting unpublished analyses. In that paper, pole-zero fitting was used to analyze complex WAI data. The results of the previous chapter support the use of this method of analysis instead of inverse methods (Rasetshwane et al., 2012) and large-scale model fitting (Lewis & Neely, 2015). These methods of estimating the TM admittance are typically comparable over the frequency range analyzed (0.2 to 6.0 [kHz]).

The goal of this study was to determine the effects of negative middle-ear pressure (NMEP) on WAI. Identification of these effects has implications for diagnosis of middle-ear conditions and for all measurements of hearing made with an acoustic probe placed in the ear canal. Various types of such measurements are described in Chapters 1 and 2.

6.1 Background

Chronic negative middle-ear pressure (NMEP) is one of the most common middle-ear pathologies (Shaver & Sun, 2013). It typically occurs when the Eustachian tube is dysfunctional, such that the pressure behind the TM cannot be equalized to the ambient atmospheric pressure (Bluestone & Klein, 2007). This pressure imbalance can cause a retraction of the eardrum, resulting in compression of the ossicular chain (Shaver & Sun, 2013). It can result in a combination of NMEP and fluid in the middle ear cavity, and lead to chronic conditions such as otitis media with effusion and bacterial biofilm (Bluestone & Klein, 2007; Nguyen et al., 2012, 2013; Monroy et al., 2015). Middle-ear pressure can be directly measured using tympanometry (Shanks & Shohet, 2009). Middle-ear pressure is approximately equivalent to the tympanic peak pressure (TPP), as described in Chapter 1.

Because negative middle-ear pressure is so common, a number of studies have considered its impact on otoacoustic emissions (OAEs), including transient evoked OAEs (Marshall et al., 1997; Prieve et al., 2008) and distortion product OAEs (DPOAEs, Sun & Shaver (2009); Thompson et al. (2015)). As they require no behavioral response, OAE tests are widely used for infant hearing screening. However, middle-ear pathologies such as middle-ear fluid and NMEP confound the results of OAE tests, which depend on the round trip of a signal to and from the cochlea via the middle ear. Even small NMEPs less negative than -100 [daPa], which are considered to be in the

'normal' range, can compromise OAE test results (Sun & Shaver, 2009).

The middle-ear pressure naturally varies when the Eustachian tube is functioning normally. Typically it is negative during waking hours, and slightly positive when the subject is recumbent or sleeping (Tideholm et al., 1998). When a subject with normal middle-ear function swallows or yawns, the Eustachian tube briefly opens, causing a pressure equalization, leading to a time-varying middle-ear pressure (on the order of minutes). This natural variation, or lack thereof, may be used to diagnose Eustachian tube dysfunction. By having subjects alter their middle-ear pressure, using the Valsalva and Toynbee maneuvers, the Eustachian tube function may be directly assessed (Holmquist & Olen, 1980; Honjo et al., 1981). In the case of extreme dysfunction (e.g. otitis media with effusion) it is not possible to assess the middle-ear pressure via tympanometry, due to extreme changes in the TM admittance resulting in no measurable TPP. As we will show, even in normal ears modest changes around zero TPP (e.g. -65 [daPa]) can produce easily observed changes in the WAI at the TM.

Previous WAI studies.   Two recent studies investigated the effects of static middle-ear pressure on the power reflectance. Voss et al. (2012) showed there was a systematic increase in the power reflectance (decrease in the absorbance level) below 2 [kHz] as a function of the static middle-ear pressure in eight cadaver preparations with controlled MEPs over a ±300 [daPa] range. For individual ears, this increase was monotonic. Above 2.6 [kHz], NMEP caused a decrease in the power reflectance (increase in the power absorbance level). Voss et al. (2012) modeled these acoustic changes using the network model of Kringlebotn (1988), assuming NMEP reduces the compliance of the TM and middle-ear ligaments.

Similar results were obtained from 35 human subjects by Shaver & Sun (2013), who trained subjects to self-induce NMEPs, which they measured using tympanometry. They reported averaged WAI data from four NMEP ranges, but did not show data from individual ears. Shaver & Sun found that the power reflectance increased for low- to mid-frequencies and decreased above 3 [kHz], with the largest changes occurring in the 1.0 to 1.5 [kHz] and 4.5 to 5.5 [kHz] ranges, respectively. They observed that the average magnitude of these changes increased with TPP magnitude. Additionally, they used wideband tympanometry to compensate for NMEP, by measuring WAI while applying an equivalent pressure in the ear canal, which estimates WAI at the TPP. They found that, on average, compensating for the NMEP restored the power reflectance to near-baseline values. Considering the power reflectance results in Figures 1 and 3 of Shaver & Sun (2013), the average absorbance level would be about 2 [dB] higher at the compensated NMEP than at ambient middle-ear pressure (AMEP) around 200 [Hz], and about 0.5 [dB] higher around 1 [kHz]. Sun & Shaver (2009) also show that, averaged across ears, there is no significant difference between compensated-NMEP and AMEP measurements of DPOAEs. These studies show that average WAI measurements made at TPP and ambient ear canal pressure are similar in normal ears.

6.2   Experiment

WAI data in ears with static NMEP were collected by Suzanne Thompson at City University of New York. These data were taken as part of a study designed to investigate the effects of middle-ear pressure on DPOAE measurements (Thompson et al., 2015).

For the measurements presented here, the probe was sealed in the ear canal at ambient atmospheric pressure. As in the Shaver & Sun (2013) study, subjects were trained to induce consistent TPP levels using the Toynbee maneuver (Thompson et al., 2015). Though it was not possible to simultaneously measure the TPP and WAI in the current study, the subjects were able to perform this task consistently and hold the NMEP for the duration of each test.

6.2.1   Subjects

Twenty-six adult subjects were recruited for the study, which was approved by the institutional review board of the City University of New York Graduate Center. All subjects had normal hearing and normal middle ear function, confirmed by a test battery including otoscopic examination, pure-tone threshold testing, tympanometry, and acoustic reflex testing. Subjects had little to no cerumen accumulation, healthy intact TMs, pure-tone air-conduction thresholds below 15 [dB-HL] (in octaves from 125 to 8000 [Hz]), normal 226 [Hz] tympanograms (GSI 33 Middle Ear Analyzer, Grason-Stadler), and acoustic reflex thresholds below 95 [dB].

Of the 26 subjects trained to induce consistent NMEP, eight completed the study. NMEPs more negative than -50 [daPa] were desirable, as NMEPs in this range have been shown to affect middle-ear transmission (Marshall et al., 1997; Prieve et al., 2008; Sun & Shaver, 2009).

6.2.2   Data Collection

Subjects were trained to perform the Toynbee maneuver, in which NMEP is induced by pinching the nose while swallowing to completely block the passage of air, thus sucking air out of the middle-ear cavity via the Eustachian tube. Tympanometry was used to assess subjects' ability to induce and maintain consistent NMEPs. A total of 16 admittance tympanograms were taken at 226 [Hz] for each subject at a sweep rate of -50 [daPa/s], alternating 8 trials at NMEP and 8 trials at AMEP, such that each NMEP measurement was made from a separate attempt of the Toynbee maneuver. Subjects were taught to swallow or yawn between trials to equalize the middle-ear pressure. For each admittance tympanogram, the REC volume was estimated based on the positive pressure tail at +200 [daPa].

Figure 6.1 shows NMEPs induced by the 8 subjects over a -50 to -385 [daPa] range. Each box plot shows 8 TPP measurements, collected from separate performances of the Toynbee maneuver, alternated with pressure equalizations. The measurements are divided into quartiles, with each median measurement shown as a horizontal line, the first and third quartiles as the bottom and
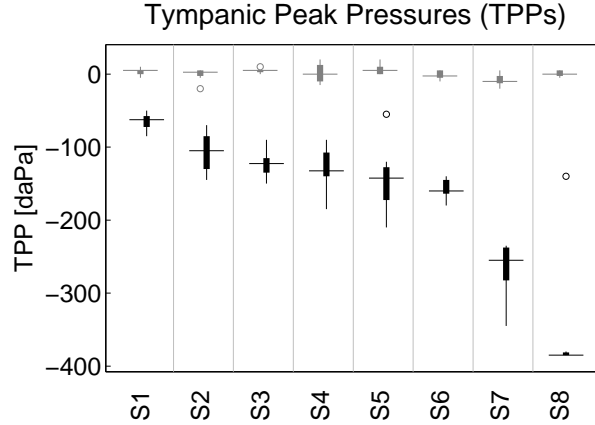
Figure 6.1: Subjects were able to induce consistent negative middle-ear pressures (NMEPs), esti-mated from the tympanic peak pressures (TPPs), using the Toynbee maneuver. Box plots show the measured TPPs at ambient middle-ear pressure (AMEP, gray) and NMEP (black) states. Each box plot divides the measurements into quartiles, showing the median measurement as a horizontal line, and the first and third quartiles as the bottom and top of the thin box. Outliers are shown as circles. TPPs are less variable in the AMEP state, as expected. All box plots show N=8 trials, except for S6 and S8 (N=7, NMEP), and S7 (N=5, AMEP; N=7, NMEP).

top of a thin box, and outliers as circles. The gray box plots show the AMEPs, while the black box plots show the NMEPs. The subjects induced NMEPs with an average standard deviation of 22 [daPa] (individual standard deviations ranged from 2 to 39 [daPa], excluding outliers). For all ears, the standard deviation was less than 25% of the mean NMEP magnitude (16% on average). As expected, there is little variation in the TPP values at AMEP, with an average standard deviation of 6 [daPa] (individual standard deviations ranged from 2 to 13 [daPa]).

WAI was measured during the same session using Mimosa Acoustics' HearID Middle Ear Power Analyzer (MEPA3). The system was calibrated according to the manufacturer's guidelines before collecting measurements. As in the tympanometry trials, eight trials each at AMEP and NMEP conditions were interleaved. During each trial, up to eight test-retest measurements were attempted, for a total of up to 64 measurements per pressure condition in each ear. Though WAI measurements typically have good signal-to-noise ratios, they can be affected, particularly at low frequencies, by mechanical noise in the environment or subject movements. This can be seen in the absorbance level curve below 500 [Hz], where the absorbance is small. Because this frequency range is of interest for data analysis and modeling, WAI measurements presented here are chosen from sets of test-retest measurements to have the smoothest curves at low frequencies. The probe was not re-inserted between trials, so the residual ear canal (REC) volume remained approximately constant for all measurements for a given subject. Finally, the low-frequency phase of the measured impedance was investigated for air-leaks (Groon et al., 2015). At 200 [Hz], nearly all impedance phase measurements fell on the interval $(-\pi/2, -3\pi/8)$ [rad], indicating a good acoustic seal.

6.3 Absorbance level

Figure 6.2 shows absorbance level measurements in decibels for the 8 individual subjects, sorted by mean NMEP TPP (from Fig. 6.1, excluding outliers). Gray solid lines show the absorbance level for AMEP, while black dashed lines show it for NMEP. The light gray region shows normative data (± 1 standard deviation) from Rosowski et al. (2012). For these eight ears, the magnitude change in $A(f)$ with NMEP is 5 [dB] or less in most ears, though it is up to 10 [dB] for ear S8.
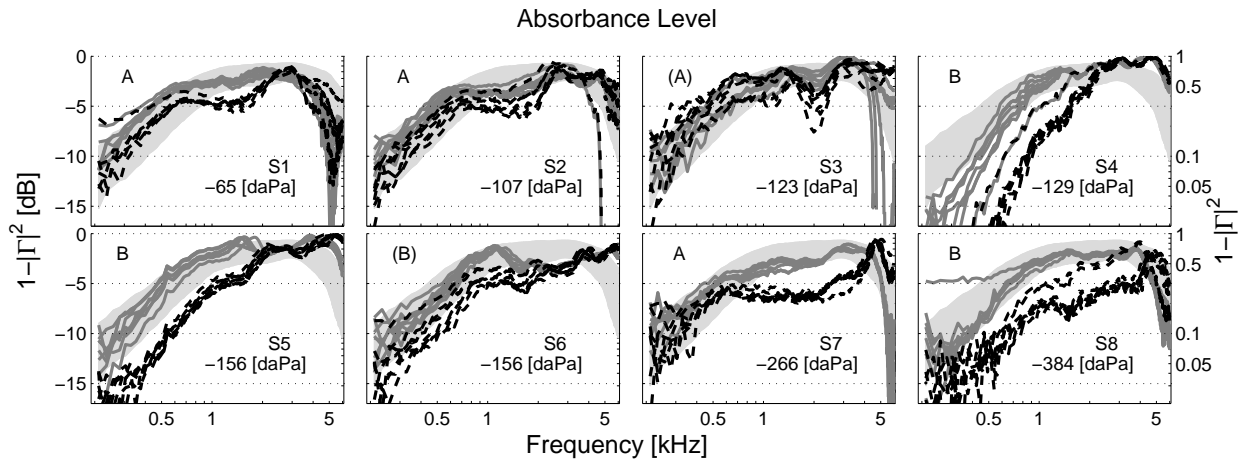

Figure 6.2: Power absorbance level measurements at ambient middle-ear pressure (AMEP, gray solid) and negative middle-ear pressure (NMEP, black dashed) states for all ears, ordered by mean NMEP tympanic peak pressure (TPP). For each ear, N=8 measurements are shown, selected to have the lowest noise from a pool of up to 8 retest measurements (except for ear S1 (N=6, AMEP and NMEP), ear S2 (N=7, NMEP), and ear S7 (N=7, AMEP)). For the majority of the ears there is a decrease in the absorbance level below 2 [kHz] due to NMEP, and a small increase above 4 to 5 [kHz]. The light gray region shows ± 1 standard deviation for normative data from Rosowski et al. (2012).

Most ears show a depression of the absorbance level due to NMEP for some range of frequencies below 2 [kHz]. This depression has a frequency range of at least 1 [kHz] for all ears, and varies in size and location. The ears with the most severe NMEPs, S7 and S8, have the widest frequency ranges of separation between the pressure states, extending from at least 0.6 to 4.0 [kHz]. Above 2 to 3 [kHz] the absorbance is generally similar between the AMEP and NMEP states. Half of the ears, S3, S5, S7, and S8, show a slight increase in absorbance level due to NMEP above 4 [kHz], in agreement with the results of Shaver & Sun (2013) and Voss et al. (2012). For most ears, the absorbance level across trials in each pressure state remains fairly constant. Ear S3 shows the largest variation across measurements for a given pressure state, and the greatest overlap between the pressure states (particularly below 1 [kHz]). Ears S4 and S8 appear to have an intermediate pressure state, likely caused by inconsistencies in subjects' performance of the Toynbee maneuver.

The effects of NMEP may be grouped by similarity across ears. For the first group, ears S1, S2 and S7, NMEP change is characterized by a mid-frequency depression in the absorbance level

beginning around 0.5 to 1.0 [kHz]. In Figure 6.2 we label these ears group A. The group B ears, S4, S5, and S8, show a large separation due to NMEP, extending all the way down to 0.2 [kHz]. For group B, NMEP appears to cause not only a depression of the absorbance level over this frequency range, but a systematic shift of its low-frequency rising slope, upward in frequency. Ears S3 and S6 are less easily grouped. For ear S6 the NMEP curves are most separated from the AMEP curves from 0.8 to 1.5 [kHz], but show slight separation of the states down to the lowest measurement frequencies. Ear S3 shows no absorbance level change below 1.5 [kHz], but has a mid-frequency change due to NMEP around 2 [kHz]. Thus, ear S3 appears to be most similar to group A, while S6 seems most similar to group B (labeled (A) and (B)).

NMEP changes appear to be related to the baseline AMEP measurements. For example, ears S3 and S6 have noticeable small resonances (local minima and maxima) in the mid-frequency region from 1.0 to 4.0 [kHz]. This structure is altered by the NMEP in a systematic way; local resonances in the mid-frequency range become more pronounced, or shift upward in frequency due to the NMEP. Disparities in the effects of NMEP at low frequencies between groups A and B appear to be related to differences in the compliance (stiffness) characteristics of the middle ear, which dominate below 0.6 to 1.0 [kHz]. This is investigated in the following sections by considering the WAI at the TM, which shows that the group B ears experience a greater decrease in the compliance at the TM due to NMEP.
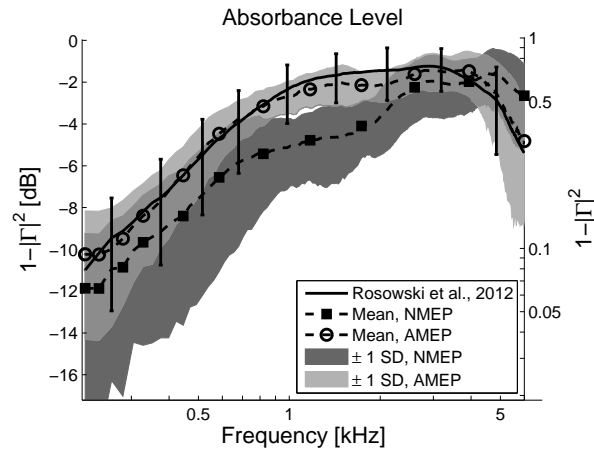

Figure 6.3: Absorbance level distributions showing ±1 standard deviation for the ambient middle-ear pressure (AMEP, light gray, N=61) and negative middle-ear pressure (NMEP, dark gray, N=61) states (medium gray indicates where the standard deviation regions overlap). Mean curves for each state are shown as dashed lines (AMEP, open circles; NMEP, solid squares). Mean and variance calculations were weighted to favor all ears equally. Normative data from Rosowski et al. (2012) are shown as a solid line (mean curve) with error bars showing ±1 standard deviation (N=58). The AMEP mean from this study is in close agreement with the Rosowski et al. (2012) normal mean.

Figure 6.3 summarizes the results across ears, as compared to the study of normal ears by Rosowski et al. (2012). Normative data from Rosowski et al. are displayed using a solid line for the mean curve and error bars showing ±1 standard deviation. Mean curves for the current experiment

are shown as dashed lines for the AMEP (open circles) and NMEP (solid squares) states, along with regions of ± 1 standard deviation (light gray and dark gray, respectively, and medium gray where the regions overlap). Mean and standard deviation calculations were weighted to favor each ear equally. The AMEP distribution from this study shows excellent agreement with normative data from Rosowski et al., as the mean AMEP curve is within 1 [dB] of the Rosowski et al. mean for all measured frequencies. Mean curves show a decrease in the absorbance level for low- to mid-frequencies due to NMEP, and an increase above about 4 [kHz].

Using the eight individual mean curves at both AMEP and NMEP, significance testing was performed at each frequency point. Considering the NMEP change relative to baseline AMEP measurements (using a paired t test), the absorbance level was significantly lower at NMEP from 0.4 to 2.0 [kHz] ($p < 0.01$), and higher from 4.5 to 6.0 [kHz] ($p < 0.05$). Considering the overall separation of NMEP and AMEP results (using an unpaired t test), the absorbance level was significantly lower from 0.6 to 2.0 [kHz] ($p < 0.01$), and the most significant separation occurred from 0.8 to 1.9 [kHz] ($p < 0.002$; $p < 10^{-15}$ using all data in Figure 6.3). In Figure 6.3, there is almost no overlap of the ± 1 standard deviation regions in the 0.8 to 1.9 [kHz] range, where the separation between mean AMEP and NMEP curves is 2 [dB] on average.

6.4 Complex WAI estimated at the eardrum

Figures 6.4, 6.5 and 6.6 show the estimated complex TM impedance, $Z_{tm}(f) = R_{tm}(f) + jX_{tm}(f)$ (Eq. 6.2). Specifically, the resistance, $R_{tm}(f)$, reactance, $X_{tm}(f)$, and magnitude impedance, $|Z_{tm}(f)|$, are shown. Consistent with the absorbance level results in Figure 6.2, these TM impedance estimates show systematic separation of the AMEP and NMEP states.

Figures 6.4 and 6.5 give the estimated wideband TM resistance and reactance for each of the eight ears. As in Figure6.2, the results are ordered by mean NMEP TPP, for the AMEP (gray solid) and NMEP (black dashed) states. From Equation 6.2b the resistance is expected to be approximately independent of frequency. For most of the ears in Figure 6.4, the resistance remains between 2 and 6 times the surge resistance, r_0, of the ear canal (by which the impedance is normalized), especially in the AMEP state. While the TM resistance changes with NMEP for some range of frequencies in all ears, the largest change in R_{tm} occurs in ears S7 and S8, which had the largest NMEPs. The reactance curves in Figure 6.5 all have a $1/f$ dependence up to at least 500 or 600 [Hz], as predicted by Equation 6.2. The NMEP measurements fall below the AMEP measurements, corresponding to a decreased aggregate compliance at the TM (C_{me}, Eq. 6.2c). Ears S4, S5, and S8 (group B) show the largest separation of pressure states at low frequencies, indicating the largest decrease in middle ear compliance due to NMEP.

Note that at frequencies below 400 [Hz], the resistance can be an order of magnitude smaller than the reactance, resulting in unreliable estimates of the TM resistance (Fig. 6.4). Though the low-frequency TM resistance curves appear smooth, due to the parametric fitting procedure, large
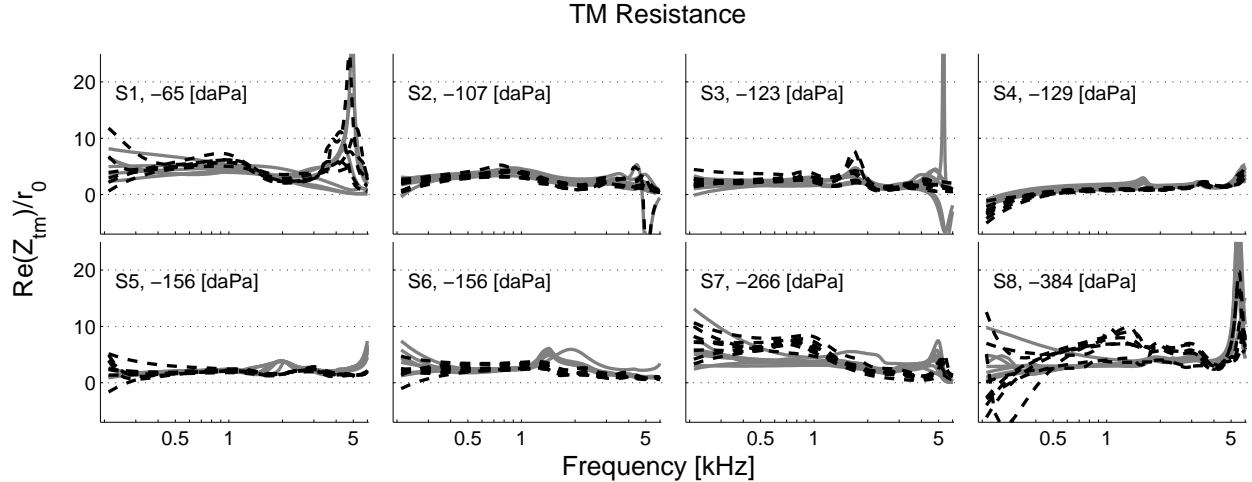
TM Resistance

Figure 6.4: Wideband tympanic membrane (TM) resistance estimates, $R_{tm}(f)$ (the real part of the TM impedance, $Z_{tm}(f)$). Ambient middle ear pressure (AMEP, gray solid) and negative middle ear pressure (NMEP, black dashed) states are shown for all ears, ordered by mean NMEP tympanic peak pressure (TPP). These curves are normalized by the ear canal surge resistance, r_0, defined for Equation 2.6. For most of the ears the resistance remains between 2 and 6 normalized units. These data are smoothed at all frequencies by the parametric fitting procedure; low-frequency variability below 400 [Hz] may be due to measurement noise and to the large disparity in magnitude between the TM resistance and reactance.

variations (e.g. S1, S7, S8) can occur due to measurement noise (e.g. Sec. 2.4.2). For example, the NMEP data for S8 in Figure 6.2 (bottom right) appear to be very noisy (jagged) at frequencies below 400 [Hz]. Considering Figure 6.5, the normalized TM reactance for this ear is very large (less than 20) below 500 [Hz]. Thus, the corresponding TM resistance curves (of much smaller normalized magnitudes) have a wide range of values at low frequencies, including nonphysical negative values.

Figure 6.6 gives the estimated wideband TM impedance magnitudes in the style of Figures 6.4 and 6.5. Below about 0.5 to 1.0 [kHz], $|Z_{tm}(f)|$ is dominated by the compliance at the TM ($|Z_{tm}| \approx |X_{tm}| \approx 1/(2\pi f C_{me})$), which appears as a straight line with a negative slope of 1 on a log-log scale. In the mid-frequency range where the TM reactance (Fig. 6.5) becomes small, the TM resistance (Fig. 6.4) dominates.

Comparing Figures 6.4, 6.5 and 6.6, the largest systematic effect of NMEP is a decreased compliance (increased stiffness) at the TM, characterized by a low-frequency decrease in $X_{tm}(f)$ and increase in $|Z_{tm}(f)|$. NMEP also appears to shift various local middle ear resonances, as in Figure 6.2. For example, ear S5 has a small 3 to 6 [dB] minimum in the TM impedance magnitude at AMEP at 1.5 [kHz] (Fig. 6.6, bottom left). In the NMEP state, this local minimum shifts to 2.5 [kHz], corresponding to a similar shift observed in the NMEP absorbance level (Fig. 6.2, bottom left).
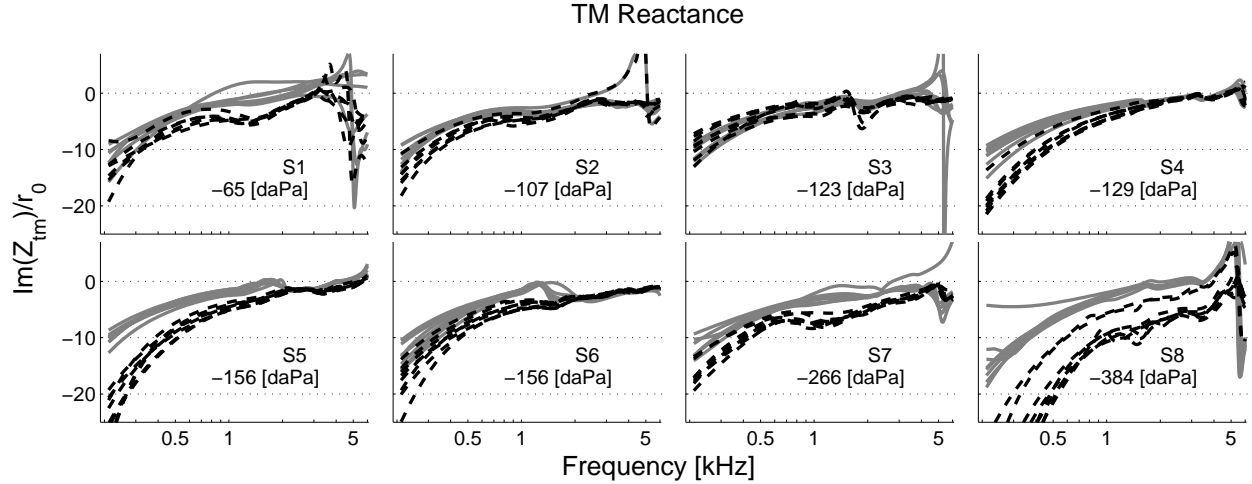
107

Figure 6.5: Wideband tympanic membrane (TM) reactance estimates, $X_{tm}(f)$ (the imaginary part of the impedance, $Z_{tm}(f)$). Ambient middle ear pressure (AMEP, gray solid) and negative middle ear pressure (NMEP, black dashed) states are shown for all ears, ordered by mean NMEP tympanic peak pressure (TPP). These curves are normalized by the ear canal surge resistance, r_0 (Eq. 2.6). The low-frequency reactance has a $1/f$ dependence, as predicted by Equation 6.2c. NMEP causes an increase in the TM reactance magnitude (decrease in C_{me}, Eq. 6.2c) below 2 to 4 [kHz] for most ears.

6.4.1 A simple model

The reflectance factorization results allow us to determine the parameters of a simplified middle ear model shown in Figure 6.7a, consisting of a tube transmission line of length L_{rec} representing the REC, C_{me} representing the aggregate compliance of the middle ear at the TM, and a cochlear load resistance r_c, required to match the transmission lines of the middle ear and cochlea (Møller, 1960; Zwislocki, 1962; Lynch et al., 1982). The compliance C_{me} is nonlinear (represented by an arrow) since its value changes with NMEP. The model in Figure 6.7a qualitatively captures the behavior of the human middle ear up to 4 to 5 [kHz]. Due to its simplicity, the model cannot capture individual variations in the WAI above 600 [Hz].

Figure 6.7b defines a low-frequency (e.g. < 600 [Hz]) network model for Figure 6.7a. The REC volume, V_{rec}, is related to the REC compliance by

$$V_{rec} = C_{rec}\rho_0 c^2, \tag{6.1}$$

where ρ_0 is the density of air and c is the speed of sound (Shanks et al., 1988). The reflectance factorization algorithm analyzes WAI for all frequencies, according to Figure 6.7a. For tympanometry (the industry gold standard for middle ear diagnostics, described in Sec. 5.4), the input impedance of the middle ear is typically modeled by Figure 6.7b, at a single low frequency (e.g. 226 [Hz]), assuming $r_c = 0$. Adding a resistor to this model improves the fit to WAI data.

To relate the WAI results to the model, we first consider the complex TM impedance, $Z_{tm}(f) =$
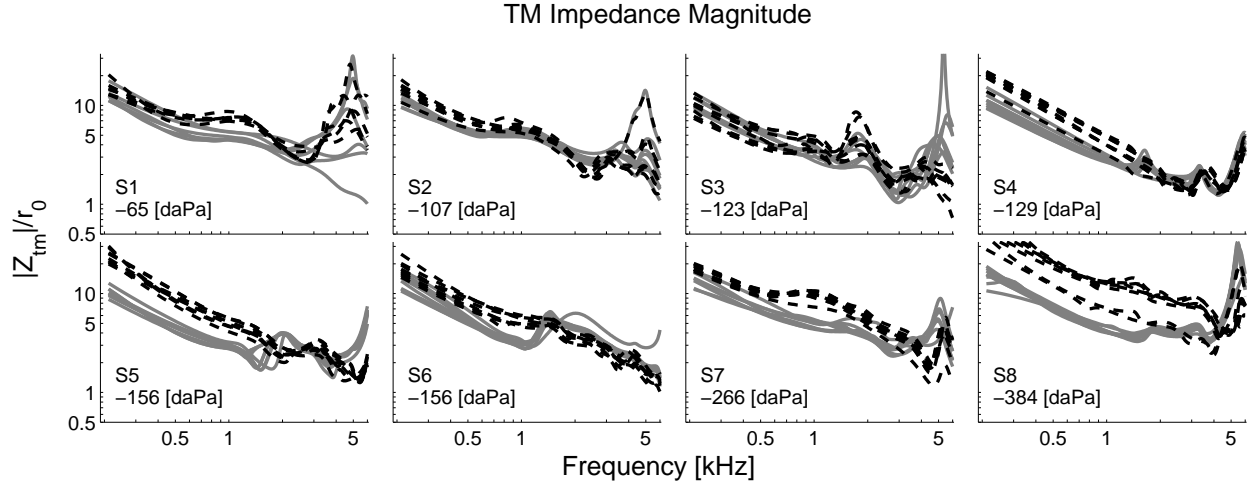
TM Impedance Magnitude

Figure 6.6: Estimated wideband tympanic membrane (TM) impedance magnitudes, $|Z_{tm}(f)|$. Ambient middle ear pressure (AMEP, gray solid) and negative middle ear pressure (NMEP, black dashed) states are shown for all ears, ordered by mean NMEP tympanic peak pressure (TPP). These curves are normalized by the ear canal surge resistance, r_0 (Eq. 2.6). $|Z_{tm}(f)|$ is dominated by the reactance, $X_{tm}(f)$ (Fig. 6.5), at low frequencies, and by the resistance, $R_{tm}(f)$ (Fig. 6.4), at mid-frequencies, where $X_{tm}(f)$ is small.

$1/Y_{tm}(f)$, calculated via reflectance factorization. The TM impedance is considered, rather than the TM admittance, because its mathematical relationship to the model parameters is simpler. The TM impedance (due to C_{me} and r_c, with no REC component) is the same for both models in Figure 6.7,

$$Z_{tm}(f) = \frac{1}{Y_{tm}(f)} = R_{tm}(f) + jX_{tm}(f) \tag{6.2a}$$

$$R_{tm}(f) = r_c \tag{6.2b}$$

$$X_{tm}(f) = \frac{-1}{2\pi f C_{me}}, \tag{6.2c}$$

where the resistance, $R_{tm}(f)$, and reactance, $X_{tm}(f)$, of the middle ear are related to the parameters r_c and C_{me}, respectively. Thus, the model may be used to estimate C_{me}, and r_c from the low-frequency WAI at the TM.

To estimate the REC compliance, C_{rec}, we must consider the reactance at the probe, $X(f)$, which is due to the REC and TM responses combined. Below 500 to 600 [Hz], the compliances dominate the probe response and the reactance is modeled by

$$X(f) \approx \frac{-1}{2\pi f(C_{rec} + C_{me})}, \tag{6.3}$$

from which C_{rec} and subsequently V_{rec} may be estimated (Eq. 6.1). From WAI rather than a single-frequency measurement, such frequency-dependent behavior is easily modeled.
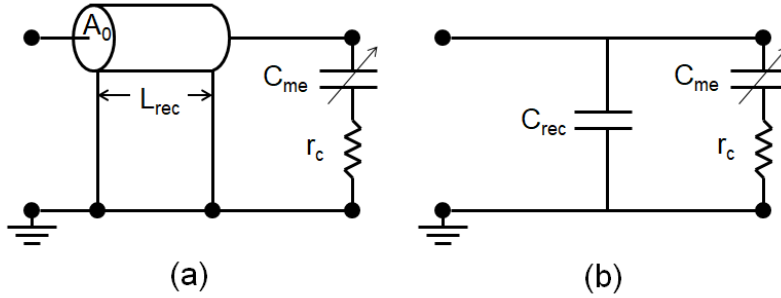
Figure 6.7: (a) A simplified wideband model of the residual ear canal (REC) and middle ear, showing the REC as a tube transmission line and the lumped middle ear compliance C_{me} and resistance r_c at the tympanic membrane (TM). This model qualitatively describes middle ear behavior up to about 4 or 5 [kHz], capturing the general behavior of WAI but not individual variability. (b) A low-frequency approximation of panel (a), where the tube transmission line is replaced by a compliance C_{rec} (proportional to the REC volume, Eq. 6.1). The resistor, r_c, is primarily due to the cochlear load and is necessary to match the transmission lines of the middle ear and cochlea (Zwislocki, 1962; Lynch et al., 1982). The compliance C_{me} is nonlinear (represented by an arrow) and changes with middle ear static pressure.

Model parameters. The REC volumes, V_{rec}, and middle ear compliances, C_{me}, estimated from the WAI data are given in Figure 6.8. The model described by Figure 6.7b (Eq. 6.2) was fit to the complex TM impedance, $Z_{tm}(f)$, below 500 [Hz] (mean fit error was less than 10% for over 90% of the measurements). AMEP and NMEP results are displayed as gray and black boxplots, in the style of Figure 6.1. Figure 6.8a shows the REC volumes (Eq. 6.1), ordered by mean NMEP TPP. These volumes are significantly different ($p < 0.05$ using an unpaired t test) between the AMEP and NMEP states for ears S3, S4 and S5. The change in median REC volume due to NMEP ranges from 0.01 to 0.18 [mL]. Corresponding REC lengths (assuming a constant canal area) are given on the right-side axis.

Considering Figures 5.2 and 6.8a, the frequency dependent REC delays, $\tau_{rec}(f)$, and the estimated volumes, V_{rec}, are relatively constant across pressure conditions and retest measurements for most ears. For six of the ears, V_{rec} is estimated to be slightly larger in the NMEP condition. This could be due to systematic shifts of the probe during the Toynbee maneuver, or to displacement of the TM due to NMEP. Changes in V_{rec} are small compared to the changes in C_{me} with NMEP (ranging from 6% to 35% of the C_{me} value, except for S3).

Figure 6.8b shows the estimated middle ear compliances, C_{me}, ordered by mean NMEP TPP. These values are given in milliliters (calculated using Eq. 6.1), which allows for comparison to tympanometry, and direct comparison of V_{rec} and C_{me} magnitudes. The middle ear compliance values at the TM are significantly lower in the NMEP state ($p < 0.01$, using an unpaired t test), except for ear S3. The change in median C_{me} due to NMEP ranges from 0.21 to 1.34 [mL] (not including S3). Ear S3 has a wide spread of C_{me} and V_{rec} values, likely due to measurement variation and noise, visible in the absorbance curves of Figure 6.2. The group B ears (S4, S5, S8), which
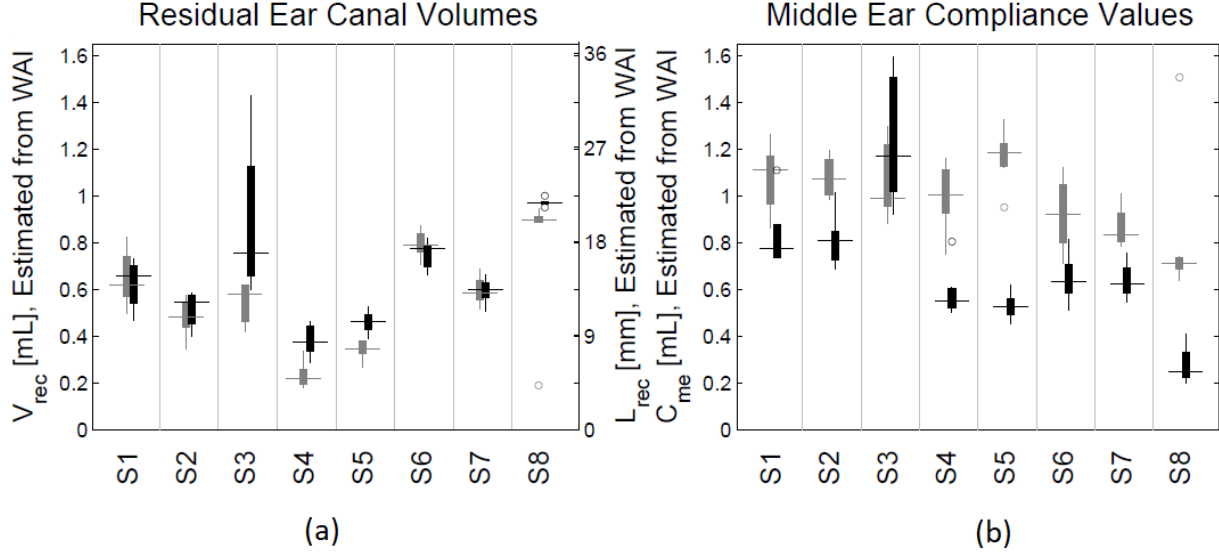
Figure 6.8: (a) Residual ear canal (REC) volumes estimated via reflectance factorization, proportional to C_{rec} (Eq. 6.1). The right-side axis gives the corresponding estimated REC lengths, assuming a uniform ear canal area. (b) Lumped middle ear compliances C_{me} at the tympanic membrane (TM), estimated from the TM impedance, $Z_{tm}(f)$ (Eq. 6.2). These values are given in milliliters (via Eq. 6.1) for easy comparison with the V_{rec} values and tympanometry. Black box plots show the negative middle ear pressure (NMEP) results, and gray box plots show the ambient middle ear pressure (AMEP) results, ordered by mean NMEP tympanic peak pressure (TPP). For all ears (other than the high variance subject S3) the TM compliance, C_{me}, is significantly lower in the NMEP state ($p < 0.01$), and for most ears the V_{rec} estimates show an insignificant or relatively small change between the pressure states.

showed greater separation at low frequencies due to NMEP in Figures 6.2, 6.5 and 6.6, have larger changes in C_{me} than the group A ears.

Median r_c values are shown in Figure 6.9. At AMEP, middle ear resistances, assumed to be due primarily to the cochlea, are between 1.8 and 4.3 times the surge resistance, r_0, except for S4. These values are significantly different in the NMEP state only for ears S4 and S7 ($p < 0.01$). Therefore, NMEP values in the studied range primarily affect the aggregate compliance of the middle ear, but do not create significant acoustic loss.

6.4.2   Detection of NMEP

Figure 6.10 gives a receiver operating characteristic (ROC) analysis of this data, for detection of a NMEP. Figure 6.10a shows ROC curves for the absorbance level $1 - |\Gamma|^2$ at 1.7 [kHz] (black), TM admittance magnitude $|Y_{tm}|$ at 0.7 [kHz] (red), TM conductance G_{tm} at 1.7 [kHz] (green), and TM susceptance B_{tm} at 0.4 [Hz] (blue). The abscissa shows the false positive rate (specificity) and the ordinate shows the true positive rate (sensitivity) for detection of the data with some threshold. Best performance occurs as this curve approaches a right angle ((0,0) to (0,1) to (1,1)). The curves
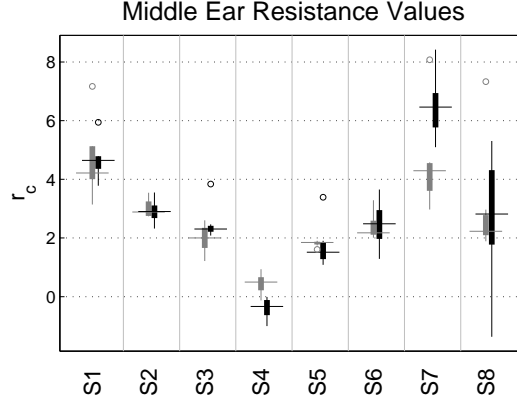
Figure 6.9: Lumped middle ear resistances r_c at the tympanic membrane (TM), assumed to be primarily due to the cochlear load. These values are estimated from the normalized TM impedance, $Z_{tm}(f)/r_0$ (Eq. 6.2), and are therefore unitless. Black box plots show the negative middle ear pressure (NMEP) results, and gray box plots show the ambient middle ear pressure (AMEP) results, ordered by mean NMEP tympanic peak pressure (TPP).

shown are those where the area under the ROC curve was at a maximum.

Figure 6.10b shows the areas under the ROC curves at all frequencies, for various WAI quantities. The susceptance and reactance, B_{tm} and X_{tm}, are the best detectors of NMEP at low frequencies because NMEP decreases the low-frequency TM compliance. The conductance, G_{tm}, performs best at 1-2 [kHz] because NMEP decreases the mid-frequency conductance. G_{tm} has almost the same area under the ROC curve as the absorbance level for all frequencies, indicating that these quantities may have some sort of order-preserving mapping. The reactance, X_{tm}, appears to combine some of the best detection characteristics of the conductance and susceptance, showing the highest A_{ROC} for most frequencies.

The relationship between G_{tm} and the absorbance may be partially explained by the minimum-phase constraint on Γ_{tm}. As shown in Section 3.5.5, the quantities G_{tm} and B_{tm} have a limited range of values based on this assumption, as compared to other quantities (G, B, X, R, X_{tm}, R_{tm}). However, the results of the ROC analysis suggest that there is some more intimate mapping between these two quantities, such that the 'ordering' of measurements remains approximately the same across frequencies.

It is hardly surprising that it is difficult to create a detection criterion for NMEP, even for this small dataset. As middle-ear pressures as low as -100 [daPa] might be considered 'normal,' it may be impossible to detect WAI changes caused by NMEPs in this range. Further, small NMEPs may be present in normative WAI data. Given the variation in frequency-dependence of NMEP effects across ears, small NMEPs may be expected to contribute to both intra-subject and inter-subject variability of normal ears.
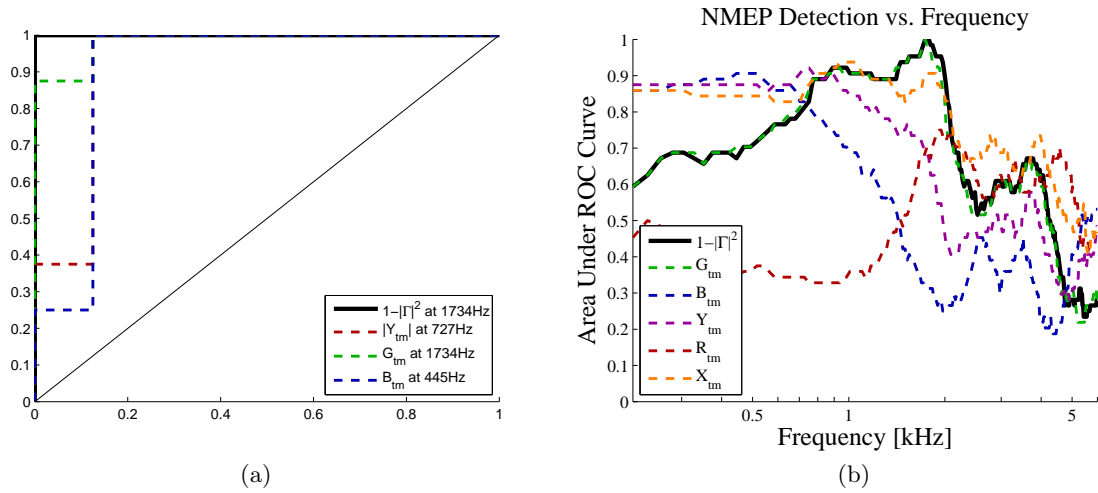
Figure 6.10: (a) ROC curve at a single frequency (see legend) for the absorbance, TM admittance, TM conductance, and TM susceptance. These curves are computed using the median measurement for each ear in each pressure state (16 total measurements). (b) Area under the ROC curve as a function of frequency for various complex TM immittance quantities.

6.5 Discussion

6.5.1 Dependence of WAI changes on NMEP

General changes in the power absorbance level with NMEP, characterized by a depression below about 2 [kHz] followed by a small elevation at higher frequencies, as seen in Figures 6.2 and 6.3, are consistent with the results of Voss et al. (2012) and Shaver & Sun (2013). Figure 6.3, which shows the means and standard deviation regions for the AMEP and NMEP absorbance level measurements across ears, indicates that the mid-frequency region from 0.8 to 1.9 [kHz] is optimal for detecting NMEP in these ears, as shown in Figure 6.3. This is in agreement with the results of Shaver & Sun (2013), who found that the largest change in the power reflectance occurred from 1.0 to 1.5 [kHz]. Based on this observation, for each of the 8 ears we averaged the absorbance level from 0.8 to 1.9 [kHz] to explore its relationship to TPP, as shown in Figure 6.11. Outliers from Figure 6.1 and suspected intermediate pressure states from Figure 6.2 (S4 and S8) are excluded in this analysis. A TPP more negative than -50 [daPa] causes a decrease in the mean 0.8 to 1.9 [kHz] absorbance level for all ears, except S3. There is a significant linear regression of these quantities ($r^2 = 0.79$, $p < 0.001$). However, a quadratic regression provides a similar fit ($r^2 = 0.81$, $p < 0.001$), implying that the relationship between power absorbance level and TPP may be nonlinear.

Though Figure 6.11 yields a significant relationship between TPP and WAI for these 8 ears, investigators should be careful when averaging data in frequency bins. Considering the absorbance level measurements of Figure 6.2, the frequency ranges and magnitudes of NMEP effects vary across ears. For instance, in ear S3, NMEP causes a mean depression of the absorbance level of about -2
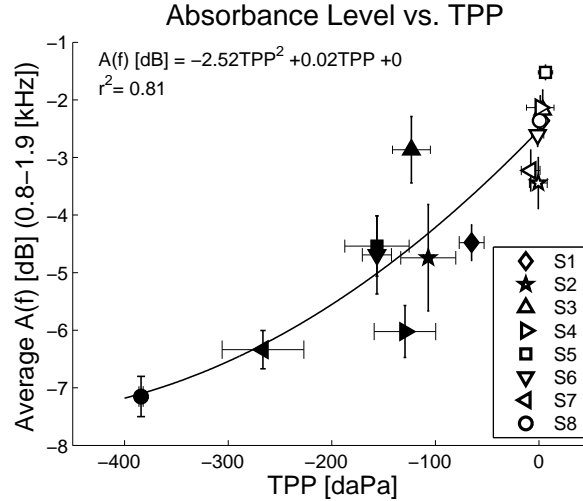
113

Figure 6.11: Mean power absorbance level over the 0.8 to 1.9 [kHz] range as a function of mean tympanic peak pressure (TPP). Error bars show ±1 standard deviation for each quantity (excluding outliers). Ambient middle-ear pressure (AMEP) data are shown as open symbols, and negative middle-ear pressure (NMEP) data are shown as filled symbols. There is a significant quadratic regression ($r^2 = 0.81$, $p < 0.001$). As expected, the AMEP data are clustered around 0 [daPa]; note that the symbols for ears S1 and S4 are partially hidden by those for ears S3, S6, and S8.

[dB] at 2 [kHz]. Though this magnitude change is similar to those observed for the other ears, it occurs outside of the 0.8 to 1.9 [kHz] frequency range over which the absorbance was averaged. Also consider ears S5 and S6, which have similar NMEP TPPs but show disparate NMEP effects at low frequencies (this is true of S3 and S4 as well). Increased stiffness of the middle ear due to NMEP shifts features of the absorbance level (such as the low-frequency rising slope, and local resonances) upward in frequency, but the effect varies due to intersubject variability at AMEP. Thus, the 0.8 to 1.9 [kHz] region merely contains the most overlap of NMEP changes across ears. Alternatively, fitting these data to a parametric model can be a more meaningful approach to characterize WAI change.

Changes in WAI at the TM with NMEP are consistent with increased stiffness (decreased compliance) in the middle ear. This is seen in the TM reactance and magnitude impedance responses in Figures 6.5 and 6.6, as a separation of the AMEP and NMEP states at low frequencies, and shifts in the mid-frequency local resonances. The decrease in compliance due to NMEP is captured by the model parameter C_{me} in Figure 6.8b. The group B ears (S4, S5, S8) show the largest changes in C_{me}, but did not all have the largest pressures. It is likely that the level of change in C_{me} is related to intersubject variability at AMEP. For instance, the middle-ear cavity volume contributes to the compliance at the TM and could be a source of variability across subjects below 2 [kHz] (Voss et al., 2008, 2013), which could affect the NMEP change in C_{me}. Intersubject variability may also be due to the differences in the nonlinear compliance characteristics of the TM and ossicular chain.

6.5.2 Mechanisms for pressure-dependent changes in WAI

As discussed with regard to Figures 6.2, 6.6 and 6.8b, the effect of NMEP on WAI may be primarily described as an increased stiffness in the middle-ear system, characterized by C_{me} (Fig. 6.7). A NMEP-dependent stiffness measured at the TM could be due to many middle-ear structures including the TM, ossicle joints, muscles, and ligaments (Voss et al., 2012). However, it is not fully understood which middle-ear structures contribute to WAI changes due to NMEP, and to what extent. It is commonly assumed that the TM is the largest contributor to nonlinear, NMEP-dependent stiffness characteristics in such data. For example, in assumption (3) of tympanometry it is often stated that the TM itself becomes stiff when pressurized. However, it has been shown that the TM functions primarily as a delay line (Puria & Allen, 1998). Thus it is more likely that the nonlinear NMEP effect is primarily due to the middle-ear ligaments, particularly when the NMEP is within the range of normal variation (Pang & Peake, 1986).

Retraction of the TM due to NMEP is likely similar to TM displacement due to contraction of the tensor tympani muscle. Unlike the stapedius muscle, the tensor tympani is not activated as part of the acoustic reflex in humans (Møller, 1983); thus, how it functions, what causes it to contract, and its effects on the acoustic impedance are not well understood (Mukerji et al., 2010; Aron et al., 2015). Studies in cats, rabbits (Møller, 1983) and humans (Bance et al., 2013; Aron et al., 2015) indicate that the effect of tensor tympani contraction on WAI would be similar to that of stapedius muscle contraction. In vivo measurements in human ears of the acoustic stapedius reflex, which applies a force on the annular ligament, increasing its stiffness and changing the motion of the stapes footplate (Møller, 1983), show similar changes in the WAI to those found here (Feeney & Keefe, 1999; Feeney et al., 2004; Schairer et al., 2007). Thus it seems likely that NMEP is acting on the annular ligament or tensor tympani, or both.

The nonlinear characteristics of the annular ligament have been previously measured and modeled (Lynch et al., 1982; Pang & Peake, 1986; Murakami et al., 1997; Lauxmann et al., 2014). The effects of NMEP on WAI found here are consistent with changes in the stapes response due to a pressure differential across the annular ligament (Lynch et al., 1982; Lauxmann et al., 2014). According to measurements of Lynch et al. (1982) in cat, a partial middle-ear system consisting of the stapes, annular ligament and cochlea gives an impedance change due to static pressure (in the cavity around the stapes) that is similar to the impedance changes observed in Figure 6.6. In human cadaver ears, Murakami et al. (1997) found a decrease in stapes (as well as umbo) vibration at low frequencies (related to an increase in impedance, as in Figure 6.6), and an increase at high frequencies, given a decrease in middle-ear pressure. The same research team also found a decrease in stapes velocity at low frequencies when the pressure in the cochlea was increased instead (Myers et al., 1998).

The overall shift in TM impedance due to increased stiffness, seen here as an increase in the impedance below 1 to 2 [kHz], followed by a small decrease in impedance at high frequencies (for some ears), is described via a simple resonance by Feeney & Keefe (1999). The term 'resonance'

is typically defined by a second-order system, such as a series capacitor-inductor system, modeling a stiffness and mass (e.g. a simple harmonic oscillator). The so-called 'middle-ear resonance' is better characterized as a resistor in series with a capacitor, namely the first-order system described by Figure 6.7a.

As noted in Section 6.4, the resistance at the TM, modeled by r_c, depends on NMEP for some frequencies, particularly at large NMEPs. These changes are related to power dissipation in the middle ear, which could be due to a compression of the ossicle joints. This effect is most severe for ears S7 and S8, which have the largest NMEP TPP values.

6.5.3 Clinical implications

For clinicians and investigators working with WAI, it is important to understand how a wide range of pathologies, including NMEP, may affect their measurements. Here we see a systematic stiffness change due to NMEP, which is similar to that due to otosclerosis or the acoustic stapedius reflex. Understanding the particular effects of NMEP on WAI can aid in better differential diagnoses of similar pathologies. Our results indicate that TPP is not a reliable predictor of immittance changes at the TM over a broad range of frequencies (Figs. 6.2 and 6.11). Future modeling of individual variations in these measurements, due to the stiffness of the middle-ear ligaments and volume of the middle-ear cavity space (Voss et al., 2008, 2013), can greatly improve characterization of NMEP effects.

Unlike traditional 226 [Hz] tympanometry, WAI provides precise, wideband information about acoustic transmission in the presence of NMEP. The effects of NMEP on the absorbance level are relatively small when the NMEP is not extreme (e.g. -400 [daPa], or no measureable TPP); in this study, a mean decrease of 2 [dB] in the region of maximum separation was observed, and the largest effects were about 5 [dB]. Such small changes are unlikely to significantly affect hearing thresholds, as observed by Rabinowitz (1981). However, other diagnostic measurements may be affected. For instance, DPOAE measurements (Sun & Shaver, 2009; Thompson et al., 2015) rely on both forward and reverse transmission through the middle ear, which could double the level effect of NMEP. Note that WAI and OAEs are often measured using the same equipment, which may motivate the use of WAI to evaluate middle-ear function prior to OAE measurements.

One proposed method to circumvent the effects of NMEP on other measurements of hearing is to apply a compensatory pressure in the ear canal, and measure WAI and DPOAEs at the TPP (Sun & Shaver, 2009; Shaver & Sun, 2013). It is important to recognize that there may be subtle differences in middle-ear transmission when using such methods. For instance, the results of Lynch et al. (1982), Lauxmann et al. (2014), and Myers et al. (1998) indicate that the difference between the middle and inner ear pressures may have an effect that is independent of the difference between the ear canal and middle-ear pressures. Using ambient WAI, this experiment has demonstrated that it is possible for subjects to alter their middle-ear pressure without re-insertion of the probe. Thus in some cases, if NMEP is suspected during a measurement sitting, the clinician or researcher

could coach the subject to equalize their middle-ear pressure, and then re-measure WAI.

Ambient WAI estimated at the TM provides a more accurate assessment of acoustic properties of the TM than tympanometry, over a much broader frequency range. In traditional WAI analysis, the effect of the REC is removed by considering only the power reflectance and absorbance level measured in the ear canal. Studies have shown that many properties of the middle ear can be analyzed using these magnitude-only quantities. In this study, we have estimated the phase response at the TM as well, which provides useful information regarding middle-ear signal delay. Such delay information may help to pinpoint the source of disruption in middle-ear sound transmission, via modeling. Refining this and similar methods of estimating the complex acoustic response at the TM should improve differential diagnosis of middle-ear pathology, resulting in increased utility of WAI.

6.5.4 Summary and future directions

Our methods remove REC delay from the complex WAI, allowing for direct estimation of the complex WAI (magnitude and phase) at the TM. For the 8 subjects presented here, NMEP has the largest and most significant effect between 0.8 and 1.9 [kHz], causing a mean reduction of 2 to 3 [dB] in energy absorbed by the middle ear and cochlea. However, WAI results vary considerably in magnitude and frequency range across ears. General changes in the WAI at the TM due to NMEP, characterized by an increase in the TM impedance (decrease in the absorbance level) below 2 [kHz], and a decrease at higher frequencies, appear consistent with previous results, and may be related to a stiffening of the tensor tympani, annular ligament and other middle-ear structures due to middle-ear pressure.

A more detailed model of middle-ear pressure might be fitted to the TM impedance estimates (e.g. Figs. 6.4, 6.5, and 6.6). This could be accomplished using models of the middle ear such as those given in Tables 2.1 and 2.2. Many models can be fit using a widely available error-minimization function such as `fminsearch` in Matlab, similar to the procedure of Lewis & Neely (2015). However, the simple model presented here demonstrates the overall change in WAI due to NMEP, without the danger of over-fitting the data. Furthermore, a more detailed model would benefit from exact measurements of the pressure and middle-ear cavity volume, such as those obtained by Voss et al. (2012) using cadaver preparations.

APPENDIX A

ACOUSTIC WAVE EQUATION AND SOLUTIONS

A.1 Acoustic variables and relationships

In this thesis, models of sound propagation in air are used for multiple purposes. This appendix is intended to summarize the assumptions made by those models. Equations and assumptions are stated for both lossless and lossy cases, and the wave equation and solutions are given for cylindrical and conical horns. A list of physical constants and acoustic variables is given at the beginning of this thesis in the List of Symbols. Approximate values are given for some constants; a list of acoustic constants as a function of temperature is given by Keefe (1984).

For the purposes of this thesis, all vibrations are assumed to be quite small (e.g. pressure wave amplitudes of < 1 [Pa] are very small compared to the ambient pressure of approximately 10^5 [Pa]). Under this assumption, all equations are linearized by neglecting any terms Δ^n for $n \geq 2$, where Δ is a 'small' number. In the lossy cases, there are two primary losses to account for: (1) thermal losses due to heat conduction, and (2) viscous losses to due friction between fluid particles.

In general, an attempt will be made to use lowercase variables in the time domain, and uppercase variables in the frequency domain. This rule may be violated in the case of constants such as P_0 (the ambient air pressure) or volumes and areas (dV, V, dA, A). Vectors will be denoted using an arrow above the letter or symbol.

A.1.1 Variables and relations

The primary variables of concern are the air pressure, density, and particle velocity. Sound waves in air cause small disturbances from the total air pressure p_{tot} and density ρ_{tot}. Typically, air particles are displaced about an equilibrium position, so the particle velocity is also small,[1] as there is no

---

[1] For a plane wave in free space (lossless), $p/|\vec{u}| = \rho_0 c_0 \approx 407$ [Rayls], therefore $|\vec{u}| = \frac{p}{\rho_0 c_0}$ must be small.

net flow. The definitions of interest are

$$p = p_{tot} - P_0 = \text{ excess pressure [Pa]} \tag{A.1a}$$

$$\vec{u} = \text{ particle velocity [m/s]} \tag{A.1b}$$

$$\sigma = \frac{\rho_{tot} - \rho_0}{\rho_0} = \text{ condensation (relative density displacement, unitless)} \tag{A.1c}$$

$$\theta = \theta_{tot} - \theta_0 = \text{ temperature displacement [K].} \tag{A.1d}$$

For the purposes of the following derivations, p, $\vec{u}$, σ and θ are considered to be quite small. Thus, equations in these variables may be 'linearized' by eliminating nonlinear terms (e.g. 'square of the motion' or higher (Rayleigh, 1896)). Condensation is often represented by the variable s in the literature; here σ is used, so that s may be used to represent the complex Laplace frequency. The equilibrium pressure P_0 and density ρ_0 have values of approximately 10^5 [Pa] and 1.2 [kg/m^3] for air at room temperature. Note that the temperature θ is used to relate p and σ when there are thermal losses due to heat conduction.

A 'particle' of the fluid (air) may be thought of as an infinitesimal volume, dV. Because the particle is in motion, any time derivatives related to the particle must take into account any motion of its 'frame of reference.' This is accomplished by using the 'material derivative'

$$\frac{D}{Dt} = \frac{\partial}{\partial t} + \vec{u} \cdot \vec{\nabla}. \tag{A.2}$$

The variables p, $\vec{u}$, and σ, represent three unknowns, thus three equations are necessary to relate them to each other. These equations will differ between the lossless and lossy cases. They are

1. Equation of state (EOS): A thermodynamic equation, typically relating the pressure, condensation (density) and temperature.

2. Equation of continuity (EOC): An equation describing conservation of mass for fluid particles, typically relating velocity to density.

3. Equation of motion (EOM): An equation describing the balance of forces on a fluid particle (conservation of momentum), typically relating force and momentum per unit volume, $\rho\vec{u}$.

By combining these three equations, a differential equation in just one variable (e.g. $p(x,t)$ or $\vec{u}(x,t)$) may be obtained. Using this differential equation along with the boundary conditions, the propagation of pressure or velocity waves in a given geometry can be described. When incorporating the effects of thermal or viscous loss, thermal loss is described by the equation of state (by including heat conduction), and viscous loss is described by the equation of motion (by including frictional forces).

The Theory of Sound, a monumental work by Lord Rayleigh (Baron John William Strutt) was the first text to describe the following acoustics concepts in such thorough detail. Rayleigh drew upon the earlier works of Marin Mersenne, Sir Isaac Newton (who authored *Principia*), Leonhard Euler,

Pierre-Simon Laplace, Hermann von Helmholtz and Gustav Kirchhoff. The works of Helmholtz and Kirchhoff were particularly important for describing lossy wave propagation.

A.1.2 Wave equation: Lossless case

In the 'lossless' case, the following relations are used (Pierce, 1981):

$$\left(\frac{p_{tot}}{P_0}\right) = \left(\frac{\rho_{tot}}{\rho_0}\right)^{\eta_0} \quad \text{(state)} \tag{A.3a}$$

$$0 = \frac{\partial \rho_{tot}}{\partial t} + \vec{\nabla} \cdot (\rho_{tot}\vec{u}) = \frac{D\rho_{tot}}{Dt} + \rho_{tot}(\vec{\nabla} \cdot \vec{u}) \quad \text{(continuity)} \tag{A.3b}$$

$$0 = \rho_{tot}\frac{D\vec{u}}{Dt} + \vec{\nabla}p_{tot} \quad \text{(force)} \tag{A.3c}$$

where $\eta_0 = c_p/c_v$ is the ratio of heat capacities at constant pressure and constant volume. The constant $\eta_0 = (F_0 + 2)/F_0$, where F_0 is the number of degrees of rotational and translational freedom[2] of the air molecules. Air consists primarily of diatomic molecules which have 5 degrees of freedom (3 translational and 2 rotational), thus $\eta_0 \approx 7/5 = 1.4$.

Equation A.3a is a restatement of the adiabatic law for a gas, $PV^{\eta_0} = $ constant. Because the air is not enclosed in a volume V_0, it is necessary to express this law in terms of the density. Sound propagation in air may be approximated as an adiabatic process because it happens so rapidly that heat energy, rather than temperature, remains approximately constant. This equation may be linearized by first approximating

$$p = p_{tot} - P_0 = \left(\frac{dp_{tot}}{d\rho_{tot}}\right)(\rho_{tot} - \rho_0), \tag{A.4}$$

where $(dp_{tot}/d\rho_{tot})$ is calculated from the rearranged Equation A.3a as

$$\frac{d}{d\rho_{tot}}\left[1 = \frac{\rho_0^{\eta_0}}{P_0}p_{tot}\rho_{tot}^{-\eta_0}\right]$$

$$0 = \frac{\rho_0^{\eta_0}}{P_0}\left[p_{tot}(-\eta_0)\rho_{tot}^{-\eta_0+1} + \frac{dp_{tot}}{d\rho_{tot}}\rho_{tot}^{-\eta_0}\right]$$

$$\frac{dp_{tot}}{d\rho_{tot}} = \frac{\eta_0 p_{tot}}{\rho_{tot}} \approx \frac{\eta_0 P_0}{\rho_0}. \tag{A.5}$$

Thus, Equation A.4 becomes

$$p = \frac{\eta_0 P_0}{\rho_0}(\rho_{tot} - \rho_0) = \eta_0 P_0 \sigma, \tag{A.6}$$

where $\eta_0 P_0 \approx 1.4 \times 10^5$ [Pa] is the bulk modulus (incompressibility) of air.

---

[2]This is related to the equipartition theorem in statistical mechanics, formulated by Waterson, and revised by Maxwell and Boltzmann, https://en.wikipedia.org/wiki/Equipartition_theorem.

Substituting $\rho_{tot} = \sigma\rho_0 + \rho_0$ and eliminating 'small' terms, the second equation becomes

$$0 = \frac{\partial}{\partial t}(\sigma\rho_0 + \rho_0) + \vec{\nabla} \cdot ((\sigma\rho_0 + \rho_0)\vec{u})$$

$$0 = \rho_0\frac{\partial\sigma}{\partial t} + \cancel{\frac{\partial\rho_0}{\partial t}}^{0} + \rho_0\vec{\nabla} \cdot (\sigma\vec{u}) + \rho_0\vec{\nabla} \cdot \vec{u}$$

$$0 = \frac{\partial\sigma}{\partial t} + \vec{\nabla} \cdot \vec{u} + \cancel{\sigma\vec{\nabla} \cdot \vec{u}}^{\epsilon} + \cancel{\vec{u} \cdot \vec{\nabla}\sigma}^{\epsilon}$$

$$0 = \frac{\partial\sigma}{\partial t} + \vec{\nabla} \cdot \vec{u}, \tag{A.7}$$

which is the linearized continuity equation. The symbol ϵ is used to denote terms that are negligible. Equation A.3c becomes

$$0 = (\sigma\rho_0 + \rho_0)\left(\frac{\partial\vec{u}}{\partial t} + \cancel{\vec{u}(\vec{\nabla} \cdot \vec{u})}^{\epsilon}\right) + \vec{\nabla}p + \cancel{\vec{\nabla}P_0}^{0}$$

$$0 = \cancel{\rho_0\,\sigma\frac{\partial\vec{u}}{\partial t}}^{\epsilon} + \rho_0\frac{\partial\vec{u}}{\partial t} + \vec{\nabla}p$$

$$0 = \rho_0\frac{\partial\vec{u}}{\partial t} + \vec{\nabla}p, \tag{A.8}$$

which is the linearized force equation.[3] Thus the set of linearized equations in p, $\vec{u}$ and σ is

$$p = \eta_0 P_0 \sigma \tag{A.9a}$$

$$0 = \frac{\partial\sigma}{\partial t} + \vec{\nabla} \cdot \vec{u} \tag{A.9b}$$

$$0 = \rho_0\frac{\partial\vec{u}}{\partial t} + \vec{\nabla}p. \tag{A.9c}$$

Eliminating σ gives two equations in p and $\vec{u}$,

$$0 = \frac{1}{\eta_0 P_0}\frac{\partial p}{\partial t} + \vec{\nabla} \cdot \vec{u} \quad \text{(lossless, linearized continuity equation}[4]) \tag{A.10a}$$

$$0 = \rho_0\frac{\partial\vec{u}}{\partial t} + \vec{\nabla}p \quad \text{(lossless, linearized force equation)}, \tag{A.10b}$$

Combining these two linearized equations yields the scalar pressure wave equation

$$\nabla^2 p = \frac{1}{c_0^2}\frac{\partial p}{\partial t} \tag{A.11}$$

---

[3]This equation is commonly referred to as the 'Euler equation,' or both the force and continuity equations may be referred to as the 'Euler equations.'

[4]This is a combination of the lossless, linearized equation of state and the linearized continuity equation.

and the vector particle velocity wave equation

$$\vec{\nabla}(\vec{\nabla} \cdot \vec{u}) = \frac{1}{c_0^2} \frac{\partial \vec{u}}{\partial t}, \tag{A.12}$$

where the speed of sound $c_0 = \sqrt{\eta_0 P_0/\rho_0}$. Note that Newton's original calculation of the speed of sound was $c_0 = \sqrt{P_0/\rho_0}$ because he assumed sound propagation was isothermal rather than adiabatic.

The solutions of these equations depend on the boundary conditions and the coordinate system. For instance, the gradient and Laplacian depend on the coordinate system. The gradient is given by

$$\vec{\nabla} = \hat{x}\frac{\partial}{\partial x} + \hat{y}\frac{\partial}{\partial y} + \hat{x}\frac{\partial}{\partial x} \qquad \text{(rectangular)} \tag{A.13a}$$

$$\vec{\nabla} = \hat{r}\frac{\partial}{\partial r} + \hat{\theta}\frac{1}{r}\frac{\partial}{\partial \theta} + \hat{x}\frac{\partial}{\partial x} \qquad \text{(cylindrical)} \tag{A.13b}$$

$$\vec{\nabla} = \hat{r}\frac{\partial}{\partial r} + \hat{\theta}\frac{1}{r}\frac{\partial}{\partial \theta} + \hat{\phi}\frac{1}{r\sin\theta}\frac{\partial}{\partial \phi} \qquad \text{(spherical)} \tag{A.13c}$$

$$\vec{\nabla} = \sum_{k=1}^{N} \hat{x}_k \frac{1}{h_k}\frac{\partial}{\partial x_k} \qquad \text{(curvilinear coordinates)}. \tag{A.13d}$$

When cylindrical or spherical waves have angular symmetry, the θ and ϕ terms drop out. In curvilinear coordinates (Kusse & Westwig, 2010), the localized coordinate system is orthogonal, and the differential thicknesses of a volume are scaled by functions $h_k(x_1, x_2, .., x_N)$.

The Laplacian of a quantity is defined as the divergence of the gradient of a scalar field. Note that the similar operation on a vector field (e.g. $\vec{\nabla}(\vec{\nabla} \cdot \vec{u})$) is different from the Laplacian of a scalar function (e.g. $\nabla^2 p$) because of the order of operations of the gradient and divergence (these operators do not commute).

$$\vec{\nabla} \cdot \vec{\nabla} p = \nabla^2 p \tag{A.14a}$$

$$\vec{\nabla}(\vec{\nabla} \cdot \vec{u}) = \nabla^2 \vec{u} + \vec{\nabla} \times (\vec{\nabla} \times \vec{u}) \neq \nabla^2 \vec{u}. \tag{A.14b}$$

A.1.3   Wave equation: Lossy case

Energy losses for wave propagation in air are primarily due to (1) heat conduction (or radiation[5]) and (2) viscous friction. The effects of heat conduction modify the equation of state (Eq. A.3a), such that it is no longer perfectly adiabatic. The effects of fluid viscosity modify the equation of force (Eq. A.3c). The continuity equation, Equation A.3b (or the linearized Eq. A.7), remains unchanged.

---

[5]Rayleigh (1896) states in Section 247 that in free space the effects of heat radiation and conduction are both quite small. Conduction plays a much larger role in a confined space such as a tube. Therefore, heat conduction rather than radiation is of primary interest in this thesis.

Heat conduction. Following the classic work of Helmholtz (1863), who studied the role of viscosity in sound propagation (described next), thermal losses were first addressed by Kirchhoff (1868). He modified the state equation as

$$\frac{p_{tot}}{\rho_{tot}} = \frac{P_0}{\rho_0}(1 + \alpha_0\theta), \tag{A.15}$$

where θ is the excess temperature (e.g. Eq. A.1d), which is assumed to be small, and α_0 is a constant coefficient of gas expansion. Assuming infinitesimal displacements, linearizing this equation gives

$$p_{tot} = \frac{P_0}{\rho_0}(1 + \alpha_0\theta)(\rho_0\sigma + \rho_0)$$

$$P_0 + p = P_0(\sigma + \alpha_0\theta\sigma^{\nearrow\epsilon} + 1 + \alpha_0\theta)$$

$$p = P_0(\sigma + \alpha_0\theta)$$

$$\alpha_0\theta = \frac{p}{P_0} - \sigma. \tag{A.16}$$

Kirchhoff (1868) relates this change in temperature to the conduction of heat via his equation

$$\kappa_0\nabla^2\theta = \frac{1}{\alpha_0\rho_0}\left(c_v\rho_{tot}\frac{\partial p_{tot}}{\partial t} - c_p p_{tot}\frac{\partial \rho_{tot}}{\partial t}\right), \tag{A.17}$$

where κ_0 is the thermal conductivity. Combining Equations A.16 and A.17, Kirchhoff found

$$\nu_0\nabla^2(\alpha_0\theta) = \frac{\partial(\alpha_0\theta)}{\partial t} - (\eta_0 - 1)\frac{\partial\sigma}{\partial t}, \tag{A.18}$$

where the constant ν_0 related to the thermal conductivity by

$$\kappa_0 = \nu_0\rho_0 c_v. \tag{A.19}$$

To arrive at Equation A.18, Kirchhoff would have needed to use $\kappa_0 = \nu_0 P_0 c_v$. Therefore, something is slightly wrong with his derivation. Note that Equation A.18 is stated here in a slightly different form than that given by Kirchhoff (1868) and Rayleigh (1896) (Secs. 247 and 347). Kirchhoff and Rayleigh ultimately solve a differential equation in terms of $\Theta = \alpha_0\theta/(\eta_0 - 1)$. An attempt is made here to fix this and to solve for the relevant equations in terms of p, σ and $\vec{u}$.

Amendment to Kirchhoff's derivation. A thorough derivation of heat conduction effects is given in Stinson (1991). This is a modified version of Kirchhoff's derivation. Stinson begins with

the ideal gas law ($R_{g,specfic}$ is the specific gas constant, which is 287 [J·kg^{-1}·K^{-1}] for air),

$$R_{g,specific} = \frac{p_{tot}}{\rho_{tot}\theta_{tot}} \tag{A.20a}$$

$$\frac{\partial}{\partial t}R_{g,specific} = \frac{\partial}{\partial t}\left(\frac{P_{tot}}{\rho_{tot}\theta_{tot}}\right)$$

$$0 = \frac{1}{\rho_0 T_0}\frac{\partial p_{tot}}{\partial t} + P_0\left[\frac{1}{\rho_0}\left(\frac{-1}{\theta_{tot}^2}\right)\frac{\partial \theta_{tot}}{\partial t} + \frac{1}{\theta_{tot}}\frac{-1}{\rho_{tot}^2}\frac{\partial \rho_{tot}}{\partial t}\right]$$

$$\frac{\partial \theta}{\partial t} = \frac{\theta_0}{P_0}\frac{\partial p}{\partial t} - \theta_0\frac{\partial \sigma}{\partial t} \qquad \text{(linearized)}. \tag{A.20b}$$

Note that this derivation may be simplified by taking the natural logarithm of Equation A.20a before taking the time derivative. The set of equations describing the gas[6] and heat conduction is thus

$$\theta = \frac{\theta_0}{P_0}p - \theta_0\sigma \tag{A.21a}$$

$$\kappa_0\nabla^2\theta = \frac{\theta_0}{P_0}\left(\rho_0 c_v\frac{\partial p}{\partial t} - P_0 c_p\rho_0\frac{\partial \sigma}{\partial t}\right). \tag{A.21b}$$

These equations replace those by Kirchhoff given in Equations A.16 and A.17. Combining the above equations to eliminate θ, the linearized equation of state becomes the diffusion equation

$$\frac{1}{P_0}\nabla^2 p - \nabla^2\sigma = \frac{1}{\nu_0 P_0}\frac{\partial p}{\partial t} - \frac{\eta_0}{\nu_0}\frac{\partial \sigma}{\partial t}. \qquad \text{(lossy, linearized state equation)} \tag{A.22}$$

The same result may be found from Equations A.16 and A.18 by Kirchhoff. Therefore, Kirchhoff's results derived from these equations are correct. However, the relationship he gives for heat conduction (Eq. A.17) is flawed, and he arrives at the correct answer via an algebraic error.

Viscous friction. Frictional losses were first addressed by Stokes (1845). Rayleigh (1896) gives the frictional force density (e.g. force per unit volume) in one dimension,

$$f_{\mu_0,x} = \mu_0\left(\nabla^2 u_x + \frac{1}{3}\frac{d}{dx}(\vec{\nabla}\cdot\vec{u})\right). \tag{A.23}$$

The coefficient of friction (the 'viscosity') is given by μ_0. By applying the linearized continuity equation (Eq. A.7) to the second term,

$$f_{\mu_0,x} = \mu_0\left(\nabla^2 u_x - \frac{1}{3}\frac{d^2\sigma}{dxdt}\right). \tag{A.24}$$

---

[6]When Equation A.20b is taken into the frequency domain, the time-derivative factors cancel out.

Thus, in three dimensions, the equation of motion (for an infinitesimal volume) becomes[7]

$$\rho_0 \frac{\partial \vec{u}}{\partial t} = \text{total force density}$$

$$= -\vec{\nabla} p + \vec{f}_{\mu_0}$$

$$= -\vec{\nabla} p + \frac{1}{3} \mu_0 \vec{\nabla}(\vec{\nabla} \cdot \vec{u}) - \mu_0 \vec{\nabla} \times \vec{\nabla} \times \vec{u}$$

$$= -\vec{\nabla} p + \mu_0 \nabla^2 \vec{u} - \frac{\mu_0}{3} \vec{\nabla}\left(\frac{\partial \sigma}{\partial t}\right). \quad (A.25)$$

This gives the linearized equation of force stated by Kirchhoff and Rayleigh,[8]

$$\frac{\partial \vec{u}}{\partial t} + \frac{1}{\rho_0} \vec{\nabla} p = \mu_0' \nabla^2 \vec{u} - \mu_0'' \vec{\nabla}\left(\frac{\partial \sigma}{\partial t}\right) \quad \text{(lossy, linearized force equation)}, \quad (A.26)$$

where the constants are $\mu_0' = \mu_0/\rho_0$ and $\mu_0'' = \frac{1}{3}\mu_0'$.

The connection between ν_0 and μ_0. The thermal conductivity $\kappa_0 = \nu_0 \rho_0 c_v$ and the viscosity μ_0 affect the equation of state and the equation of motion, respectively. However, they are typically related by molecular properties of the gas (e.g. air). Kirchhoff and Rayleigh claim that thermodynamic constant $\nu_0 = \frac{5}{2}\mu_0'$, citing Maxwell. However, the factor $5/2$ relates c_p to the gas constant for a mono-atomic gas,[9] and is therefore not applicable to air, which is predominantly diatomic (Benade, 1968). Therefore, the following discussion will not relate $\nu_0 = \kappa_0/(\rho_0 c_v)$ to the viscosity. Instead, the thermal conductivity can be looked up directly from a table. For reference, Benade (1968) states that the factor $5/2$ should be approximately $(9\eta_0 - 5)/4 \approx 1.9$. Note that this is a relatively small difference (about 25%), which explains why it remained undetected experimentally (W. Mason, 1928). This gives

$$\nu_0 \approx \left(\frac{9\eta_0 - 5}{4}\right)\mu_0' = \left(\frac{9\eta_0 - 5}{4}\right)\frac{\mu_0}{\rho_0}. \quad (A.27)$$

Final equation. Thus, the full set of linearized equations including thermal and viscous effects is described by Equations A.22, A.7, and A.26. In the frequency domain ($p \leftrightarrow \mathcal{P}$, $\vec{u} \leftrightarrow \vec{\mathcal{U}}$, and

---

[7]This is also stated by Stinson (1991).

[8]Note that Kirchhoff and Rayleigh both give a preliminary equation where the μ_0'' term is positive. However, both use Equation A.26 in their final derivations.

[9]According to http://hyperphysics.phy-astr.gsu.edu/hbase/Kinetic/shegas.html, $c_p = c_v + R_g$, where $c_v = \frac{F_0}{2}R_g$, F_0 is the number of translational and rotational degrees of freedom, and R_g is the gas constant. This gives $c_p = \frac{F_0+2}{2}R_g$, which gives $c_p = \frac{5}{2}R_g$ for a mono-atomic gas.

$\sigma \leftrightarrow \mathcal{E}$), these become

$$sP - \eta_0 P_0 s\mathcal{E} = \nu_0 \nabla^2 P - \nu_0 P_0 \nabla^2 \mathcal{E} \quad \text{(state)} \tag{A.28a}$$

$$s\mathcal{E} + \vec{\nabla} \cdot \vec{\mathcal{U}} = 0 \quad \text{(continuity)} \tag{A.28b}$$

$$\rho_0 s\vec{\mathcal{U}} + \vec{\nabla}P = \rho_0 \mu_0' \nabla^2 \vec{\mathcal{U}} - \rho_0 \mu_0'' s\vec{\nabla}\mathcal{E} \quad \text{(force)}. \tag{A.28c}$$

Eliminating $\mathcal{E}$ by substituting the first equation into the second and third, these equations become

$$\rho_0 s\vec{\mathcal{U}} + \vec{\nabla}P = \rho_0 \mu_0' \nabla^2 \vec{\mathcal{U}} + \rho_0 \mu_0'' \vec{\nabla}(\vec{\nabla} \cdot \vec{\mathcal{U}}) \tag{A.29a}$$

$$\frac{s}{\eta_0 P_0}P + \vec{\nabla} \cdot \vec{\mathcal{U}} = \frac{\nu_0}{\eta_0 P_0}\nabla^2 P + \frac{\nu_0}{\eta_0 s}\nabla^2(\vec{\nabla} \cdot \vec{\mathcal{U}}). \tag{A.29b}$$

Note that in the lossless case when $\mu_0' = \mu_0'' = \nu_0 = 0$, the two equations above become the frequency-domain versions of Equations A.10b and A.10a. By solving for $\vec{\nabla}P$ in the first equation, and substituting this into the gradient of the second equation,

$$\left(\frac{\nu_0}{c_0^2}(\mu_0' + \mu_0'') + \frac{\nu_0}{\eta_0 s}\right)\vec{\nabla}(\nabla^2(\vec{\nabla} \cdot \vec{\mathcal{U}})) - \left(1 + \frac{s}{c_0^2}(\nu_0 + \mu_0' + \mu_0'')\right)\vec{\nabla}(\vec{\nabla} \cdot \vec{\mathcal{U}}) - \frac{s}{c_0^2}\mu_0'\vec{\nabla} \times \vec{\nabla} \times \vec{\mathcal{U}} + \frac{s^2}{c_0^2}\vec{\mathcal{U}} = 0. \tag{A.30}$$

This is a vector wave equation in the frequency-domain particle velocity. In the lossless case, this equation becomes the frequency-domain version of Equation A.12. If $\vec{\nabla} \times \vec{\nabla} \times \vec{\mathcal{U}} = 0$, Equation A.30 has the same coefficients as the scalar wave equation in Θ obtained by Kirchhoff and Rayleigh. Stinson (1991) notes that this similarity is because both $\vec{\mathcal{U}}$ and the temperature displacement θ must vanish at any wall boundaries, under the assumption that the gas behavior at a wall is isothermal (e.g. the walls are an infinite reservoir of the equilibrium temperature, θ_0). In general, the boundary will not be perfectly isothermal; Keefe (1984) derives the effects of a non-isothermal boundary for wave propagation in a cylindrical tube.

Solution in free space. Losses due to heat conduction and viscous friction can affect the wave speed (e.g. dispersion) and introduce attenuation. It may be proved that these losses have the most significant effect when rigid boundaries are present. This is mathematically shown by Kirchhoff (1868) and Rayleigh (1896) (Sec. 349). Here, the free-space case is briefly analyzed; wave propagation in closed spaces such as tubes and horns is described in detail in the following sections.

In free space, there are no significant dispersion effects, but there is a small attenuation effect. Kirchhoff (1868) showed that in free space the solution to Equation A.30, in Cartesian coordinates in one dimension, is

$$\mathcal{U}_x \propto e^{\kappa(s)x} = e^{-mx}e^{sx/c_0}, \tag{A.31}$$

where for $s = j\omega$,

$$m = \frac{\omega^2}{2c_0^3}\left(\mu_0' + \mu_0'' + \nu_0\left(1 - \frac{1}{\eta_0}\right)\right). \tag{A.32}$$

In the lossless case, $m = 0$, so the amplitude of this term is 1 for all x. In the lossy case, the velocity c_0 is the same as the lossless case, and there is no dispersion. At 1 [kHz], $m \approx 1.3 \times 10^{-5}$ [m^{-1}], and at 10 [kHz], $m \approx 1.3 \times 10^{-3}$ [m^{-1}]. Physical constants have been calculated for air at 75° [F] (Keefe, 1984).

The traditional way to evaluate the attenuation is to consider when the wave is attenuated by a factor of $1/e$ (8.7 [dB]), which happens when $mx = 1$. The wave will be attenuated by $1/e$ or more for

$$f > \frac{1}{2\pi} \sqrt{\frac{2c_0^3}{x}\left(\frac{1}{\mu_0' + \mu_0'' + \nu_0(1 - 1/\eta_0)}\right)} = \sqrt{\frac{7.5 \times 10^{10}}{x}}. \tag{A.33}$$

Therefore, this effect increases with distance from the origin point of the wave, and causes the most attenuation at high frequencies. In free space, the distance must be very large, or the frequency very high, for the wave to be significantly attenuated.

Beranek & Mellow (2012) (Sec. 2.2.2) describe the effect of heat conduction in free space in terms of the wavelength and speed of the diffusion wave, compared to the wavelength of the primary vibration. At 1 [kHz], the diffusion wave speed is 0.5 [m/s]; in a half-period, the thermal wave travels just 2.5×10^{-4} [m]. This is small compared to half the wavelength of the primary vibration, which is 0.17 [m] at 1 [kHz].

A.2 Solutions in a constant-area horn waveguide

In this section, solutions are given for wave propagation in a cylindrical horn (Kirchhoff, 1868; Rayleigh, 1896; Benade, 1988; Keefe, 1984). These solutions separate into radial and axial components. In the case of a cylindrical horn, the radial solutions are Bessel functions. In the following derivation, it is assumed that only plane waves (the 0th order mode) propagate. A full discussion of transmission-line notation, including the per-unit-length impedance $\mathcal{Z}$ and admittance $\mathcal{Y}$, is given in Section 3.1.

In a constant-area horn, the plane wave, transmission-line solutions will take the form

$$\Psi(x,\omega) = \alpha_+ e^{-\kappa(x,j\omega)x} + \alpha_- e^{+\kappa(x,j\omega)x} \tag{A.34a}$$

$$\mathcal{V}(x,\omega) = \alpha_+ y_c^+ e^{-\kappa(x,j\omega)x} - \alpha_- y_c^- e^{+\kappa(x,j\omega)x}, \tag{A.34b}$$

where $\kappa(x,s)$ is the analytic propagation function. Equations 3.4 and A.34 give the relations

$$\kappa(x,s)\Psi^\pm = \mathcal{Z}(x,s)\mathcal{V}^\pm$$
$$\kappa(x,s)\mathcal{V}^\pm = \mathcal{Y}(x,s)\Psi^\pm$$
$$\frac{\Psi^\pm}{\mathcal{V}^\pm} = \frac{\kappa(x,s)}{\mathcal{Y}(x,s)} = \frac{\mathcal{Z}(x,s)}{\kappa(x,s)}. \tag{A.35}$$

Therefore, the propagation function and characteristic admittance are given by

$$\kappa(x, s) = \sqrt{\mathcal{Z}(x, s)\mathcal{Y}(x, s)} \tag{A.36a}$$

$$y_c^\pm = \sqrt{\frac{\mathcal{Y}(x, s)}{\mathcal{Z}(x, s)}} = y_0(x, s) = \frac{1}{z_0(x, s)}. \tag{A.36b}$$

Furthermore, the wave attenuation along the horn is described by the real part of κ, with the attenuation given by $e^{-\Re(\kappa(x, j\omega))x}$. The phase velocity $c_p(x, j\omega) = \omega/\Im(\kappa(x, j\omega))$. If c_p is a function of frequency, the system is dispersive.

Note that in general, for a variable-area horn, the characteristic admittance $y_c^\pm \neq \sqrt{\mathcal{Y}/\mathcal{Z}}$. For example, the conical horn has direction-dependent characteristic admittances $y_c^\pm$ which contain the term y_0, along with another function that depends on the axial coordinate (Sec. 3.1.3). For the constant-area horn, $y_c^\pm$ gives the velocity solution

$$\mathcal{V} = y_0\Psi^+ - y_0\Psi^-. \tag{A.37}$$

A negative impedance or admittance is 'illegal' for a passive system (Brune, 1931). In this case, the negative sign of the $y_0\Psi^-$ indicates the direction of flow; the retrograde wave propagates in the negative x direction.

A.2.1   Lossless constant-area solution

For the lossless case, Equations A.10a and A.10b may be recast as a matrix equation

$$\frac{\partial}{\partial x} \begin{bmatrix} p(x, t) \\ u_z(x, t) \end{bmatrix} = - \begin{bmatrix} 0 & \rho_0 \\ \frac{1}{\eta_0 P_0} & 0 \end{bmatrix} \frac{\partial}{\partial t} \begin{bmatrix} p(x, t) \\ u_z(x, t) \end{bmatrix}. \tag{A.38}$$

For a constant cross-sectional area A_0, assuming iso-pressure slices, the volume velocity and average pressure are given by

$$v(x, t) = A_0 u_z(t) \tag{A.39a}$$

$$\psi(x, t) = p(x, t). \tag{A.39b}$$

Thus the matrix equation becomes

$$\frac{\partial}{\partial x} \begin{bmatrix} \psi(x, t) \\ v(x, t) \end{bmatrix} = - \begin{bmatrix} 0 & \frac{\rho_0}{A_0} \\ \frac{A_0}{\eta_0 P_0} & 0 \end{bmatrix} \frac{\partial}{\partial t} \begin{bmatrix} \psi(x, t) \\ v(x, t) \end{bmatrix}. \tag{A.40}$$

This gives the frequency-domain transmission line parameters

$$\mathcal{Z}(x, s) = \frac{s\rho_0}{A_0} \tag{A.41a}$$

$$\mathcal{Y}(x, s) = \frac{sA_0}{\eta_0 P_0} \tag{A.41b}$$

$$\kappa(x, s) = \frac{s}{c_0} \tag{A.41c}$$

$$y_c^{\pm}(x, s) = \frac{A_0}{\rho_0 c_0} \tag{A.41d}$$

$$z_0(x, s) = \frac{1}{y_0(x, s)} = \frac{\rho_0 c_0}{A_0} = r_0 = \frac{1}{g_0}. \tag{A.41e}$$

Thus in the lossless case, there is no attenuation or dispersion, and the characteristic impedance is simply a resistance r_0 (the characteristic admittance is just a conductance g_0).

A.2.2 Lossy cylindrical solution

The transmission line parameters for a lossy cylindrical tube are well known (e.g. Keefe (1984)). They are presented here in terms of the complex frequency s,

$$\mathcal{Z}(x, s) = \frac{s}{c_0} r_0 \left[1 - \frac{2}{r_v} \frac{I_1(r_v)}{I_0(r_v)} \right]^{-1} \tag{A.42a}$$

$$\mathcal{Y}(x, s) = \frac{s}{c_0} \frac{1}{r_0} \left[1 + (\eta_0 - 1) \frac{2}{r_t} \frac{I_1(r_t)}{I_0(r_t)} \right], \tag{A.42b}$$

with dimensionless, frequency-dependent parameters

$$r_v(s) = a_0 \sqrt{\frac{s\rho_0}{\mu_0}} \tag{A.43a}$$

$$r_t(s) = a_0 \sqrt{\frac{s\rho_0 c_p}{\kappa_0}} = \sqrt{\frac{\mu_0 c_p}{\kappa_0}} r_v(s) = \sqrt{\text{Pr}} r_v(s), \tag{A.43b}$$

where Pr= 0.84 is the Prandtl number (unitless), and a_0 is the tube radius. I_0 and I_1 are modified Bessel functions of the first kind, such that $I_n(\phi) = j^{-n} J_n(j\phi)$.

Note that it is not immediately obvious that r_v and r_t are unitless. However, dimensional analysis shows that $\sqrt{s\rho_0/\mu_0}$ indeed has the units [1/m]. Therefore, the thickness of the boundary layer is given by $[s\rho_0/\mu_0]^{-1/2}$ [m]. This is plotted as a function of frequency ($s = j2\pi f$) in the left-hand plot of Figure A.1. The boundary layer has the greatest width at low frequencies; therefore, viscous and thermal effects play the largest role at low frequencies.

The unitless parameters r_v and r_t given here differ from those described by Keefe (1984) by a factor of $\sqrt{j} = e^{\pi/4}$, due to his use of ω instead of s. Keefe states that these parameters are the ratios of the tube radius to the viscous and thermal boundary layers. Examples of this ratio for

different tube radii as a function of frequency are given in the right-hand plot of Figure A.1. From Equations A.42b and A.42a, it is apparent that the viscous losses are described by $\mathcal{Z}$, and the thermal losses are described by $\mathcal{Y}$.
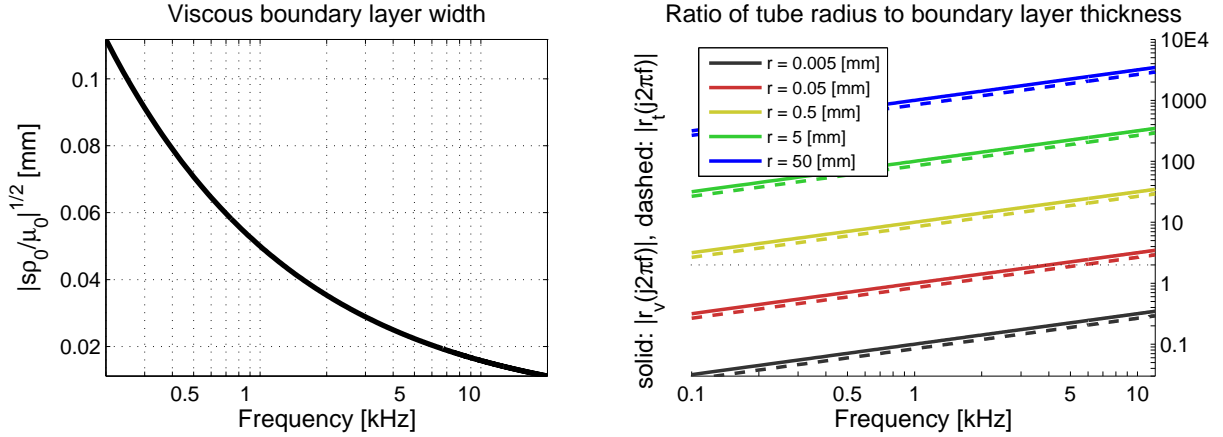

Figure A.1: The left-hand plot shows the boundary-layer width as a function of frequency. The right-hand plot shows the ratios of the viscous $|r_v(s)|$ (solid) and thermal $|r_t(s)|$ (dashed) boundary layers to the tube radius (at each of five different orders of magnitude), for $s = j2\pi f$. In the case of 'small-r' tubes, the tube radius is smaller than the boundary layer. In the case of 'large-r' tubes, the radius is many times the boundary layer width. Keefe (1984) gives $r_v = 2$ as the cutoff between his small- and large-r approximations. Note that the radius of the average adult ear canal is 3.75 [mm].

The ratio $r_t/r_v = \sqrt{\text{Pr}} \approx 0.84$ at 26.85 [^{o}C] (Keefe, 1984). Therefore, r_v and r_t are of the same order of magnitude. Keefe (1984) gives approximations to the Bessel functions of $\mathcal{Z}$ and $\mathcal{Y}$ for small and large r_v. The 'small-r' approximation is a power series for $r_v \to 0$, and the 'large-r' approximation is an asymptotic expansion for $r_v \to \infty$. Keefe determines that the small-r_v expansion may be used for $r_v < 2$, and the large-r expansion may be used for $r_v > 2$, with an accuracy of 1% of the Bessel-function solution. When choosing the small- or large-r approximation, it is important to consider the entire frequency range over which a solution is desired, since r_v is a function of frequency ($\propto \sqrt{s}$). Such approximations can greatly simplify the computational complexity of the solution, though this simplification is no longer necessary on today's computers.

Keefe's series approximations to κ and z_0. Approximations to wavenumber $\kappa(s)$ and characteristic impedance $z_0(s)$ can be given by the following truncated series, derived from Equations A.42a and A.42b. These expressions are modified from Keefe (1984) to accommodate the analytic nature of $r_v(s)$. Allowing the user to substitute the thermal quantities at the appropriate temperature, these complex analytic series in $r_v(s)$ are much easier to use than the formulas given by

Keefe.

$$z_0(x,s) = \frac{\rho_0 c_0}{A(x)} \left[\alpha_1 r_v + \alpha_0 + \alpha_{-1} r_v^{-1} + \alpha_{-2} r_v^{-2} + \alpha_{-3} r_v^{-3} \right] \tag{A.44a}$$

$$\kappa(x,s) = \frac{s}{c_0} \left[\beta_1 r_v + \beta_0 + \beta_{-1} r_v^{-1} + \beta_{-2} r_v^{-2} + \beta_{-3} r_v^{-3} \right]. \tag{A.44b}$$

For large-r $(r_v > 2)$, the coefficients of the series are given by

$$\alpha_1 = 0 \tag{A.45a}$$

$$\alpha_0 = 1 \tag{A.45b}$$

$$\alpha_{-1} = 1 - \frac{(\eta_0 - 1)}{\sqrt{\mathrm{Pr}}} \tag{A.45c}$$

$$\alpha_{-2} = \alpha_{-1} + \frac{1}{2} \frac{(\eta_0 - 1)}{\mathrm{Pr}} + \frac{3}{2} \frac{(\eta_0 - 1)^2}{\mathrm{Pr}} \tag{A.45d}$$

$$\alpha_{-3} = \alpha_{-2} - \frac{1}{8} + \frac{1}{8} \frac{(\eta_0 - 1)}{\mathrm{Pr}^{3/2}} - \frac{3}{2} \frac{(\eta_0 - 1)^2}{\mathrm{Pr}^{3/2}} - \frac{5}{2} \frac{(\eta_0 - 1)^3}{\mathrm{Pr}^{3/2}} \tag{A.45e}$$

$$\beta_1 = 0 \tag{A.46a}$$

$$\beta_0 = 1 \tag{A.46b}$$

$$\beta_{-1} = 1 + \frac{(\eta_0 - 1)}{\sqrt{\mathrm{Pr}}} \tag{A.46c}$$

$$\beta_{-2} = \beta_{-1} - \frac{1}{2} \frac{(\eta_0 - 1)}{\mathrm{Pr}} - \frac{1}{2} \frac{(\eta_0 - 1)^2}{\mathrm{Pr}} \tag{A.46d}$$

$$\beta_{-3} = \beta_{-2} - \frac{1}{8} - \frac{1}{8} \frac{(\eta_0 - 1)}{\mathrm{Pr}^{3/2}} + \frac{1}{2} \frac{(\eta_0 - 1)^2}{\mathrm{Pr}^{3/2}} + \frac{1}{2} \frac{(\eta_0 - 1)^3}{\mathrm{Pr}^{3/2}}. \tag{A.46e}$$

For small-r $(r_v < 2)$, the coefficients of the series are given by

$$\alpha_1 = \sqrt{\frac{2}{\eta_0}} \left[\frac{1}{6} + \frac{(\eta_0 - 1)\,\mathrm{Pr}}{8\eta_0} \right] \tag{A.47a}$$

$$\alpha_0 = 0 \tag{A.47b}$$

$$\alpha_{-1} = 2\sqrt{\frac{2}{\eta_0}} \tag{A.47c}$$

$$\alpha_{-2} = 0 \tag{A.47d}$$

$$\alpha_{-3} = 0 \tag{A.47e}$$

$$\beta_1 = \sqrt{2\eta_0}\left[\frac{1}{6} - \frac{(\eta_0 - 1)\,\mathrm{Pr}}{8\eta_0}\right] \tag{A.48a}$$

$$\beta_0 = 0 \tag{A.48b}$$

$$\beta_{-1} = 2\sqrt{2\eta_0} \tag{A.48c}$$

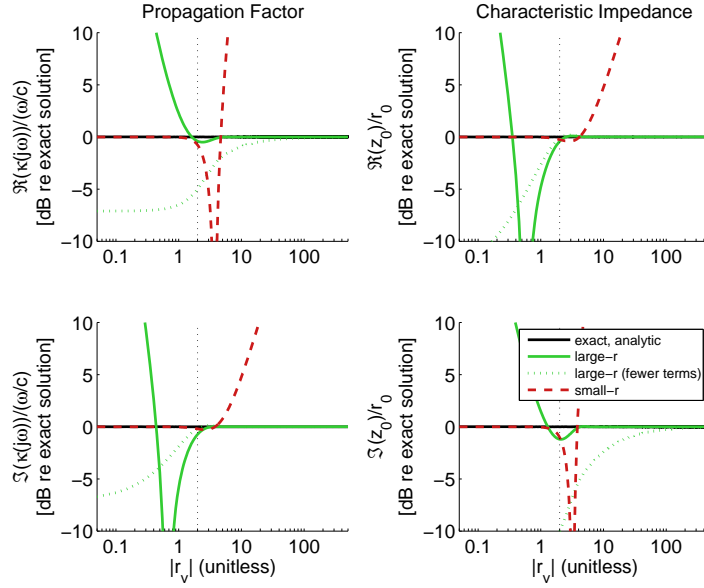$$\beta_{-2} = 0 \tag{A.48d}$$

$$\beta_{-3} = 0. \tag{A.48e}$$

Figure A.2: The propagation function $\kappa(s)$ and characteristic impedance z_0 for the large-r and small-r series approximations. For the large-r approximation, the dotted line shows the result when fewer terms of the series are used ($\alpha_{-2}, \alpha_{-3}, \beta_{-2}, \beta_{-3} = 0$). These values are normalized as $\kappa/(\omega/c_0)$ and z_0/r_0, so that they are dimensionless functions of $|r_v|$ rather than frequency or radius (e.g. Keefe (1984)). Exact solutions (Keefe, 1984; Benade, 1968) are compared with the analytic solution given here (Eqs. A.42a and A.42b).

Figure A.2 compares the small-r (Eqs. A.47 and A.48) and large-r (Eqs. A.45 and A.46) approximations of κ and z_0 to the exact solution. This figure also demonstrates that the analytic solution given in this thesis (Eqs. A.42a and A.42b) is equal to the exact solution given by Keefe (1984) and Benade (1968). The large-r solution using a truncated series ($\alpha_{-2}, \alpha_{-3}, \beta_{-2}, \beta_{-3} = 0$) is also shown. Keefe (1984) uses this truncated series for $\Im(\kappa)$ and $\Re(z_0)$ because it is closer to the exact solution. He says that for an asymptotic series expansion, it is often true that fewer terms lead to a better approximation.

It bears repeating that these approximations are typically unnecessary on a modern computer. However, it is useful to study them in order to understand the trajectory of literature in this field.

A.2.3 Approximation used by Rayleigh and Mason

W. P. Mason (1927); W. Mason (1928) used the solutions of Rayleigh (1896) and Kirchhoff (1868) to approximate the propagation function and characteristic impedance in a tube with thermal and viscous losses. This solution generalizes to a horn of arbitrary cross-sectional shape, and provides some insight that is hard to glean from the fourth-order lossy wave equation and Bessel function solutions for a cylindrical horn. Note that this derivation assumes that the cross-sectional dimensions of the tube are large compared to the thermal or viscous boundary layer (the large-r solution).

The W. Mason (1928) study was particularly important because it was the earliest to validate the model of lossy propagation characteristics (attenuation and sound speed) for a large-r tube, over a range of frequencies relevant to human hearing. Other early experiments included those of Kundt,[10] Stevens (1902), Grüneisen & Merkel (1922), and Simmons & Johansen (1925).

Viscous effects. In Section 347 of his book, Rayleigh (1896) derives the equation of motion for a rigid-walled horn of arbitrary cross-sectional shape. Again, this derivation assumes that the cross-section is much larger than the boundary layer of fluid adhering to the walls. Rayleigh's derivation has been modified to express the equation of motion as a complex function of the frequency s, similar to the previously presented modification to the solutions of Keefe (1984).
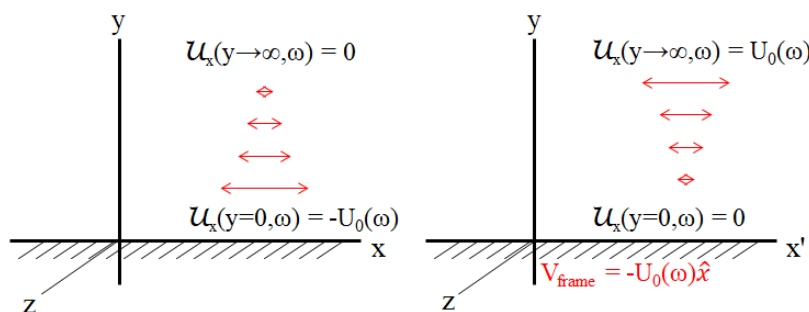

Figure A.3: Infinite, rigid x-y plane, with fluid (air) in the $+y$ half-space. The rigid boundary condition dictates that the fluid (air) immediately next to the plane must adhere to the plane. In the left diagram, the plane moves in the x direction with some velocity $-\vec{\mathcal{U}}_0(\omega) = 0$. The right diagram shows the plane's moving frame of reference, which can be used to describe the force on a moving fluid from a stationary rigid plane.

Rayleigh begins by considering the motion of fluid in contact with an infinite rigid x-z plane, as shown in Figure A.3. The rigid boundary condition dictates that the fluid (air) immediately next to the plane at $y = 0$ must adhere to the plane. As derived by Rayleigh (1896), in the left diagram, the plane moves in the x direction with some velocity $-U_0(\omega) = 0$. The motion of the fluid (in the

---

[10]https://en.wikipedia.org/wiki/Kundt%27s_tube

x direction) is described by the force-density diffusion equation[11]

$$\mu_0 \frac{\partial^2 u_z}{\partial y^2} = \rho_0 \frac{\partial u_z}{\partial t} \leftrightarrow s \rho_0 \mathcal{U}_z. \tag{A.49}$$

Note that this equation is the same as Equation A.26, with p and σ set to 0; thus, assuming that the pressure is constant (and using the lossless equation of state), so is the density. In the frequency domain, this equation becomes

$$\frac{\partial^2}{\partial y^2} \mathcal{U}_z = \left(\frac{s \rho_0}{\mu_0} \right) \mathcal{U}_z = \kappa^2 \mathcal{U}_z, \tag{A.50}$$

where we introduce the square of the propagation constant κ^2 due to the second derivative in space. This equation has the general solution

$$\mathcal{U}_z(y, \omega) = \mathcal{B}_+ e^{-\kappa(j\omega)y} + \mathcal{B}_- e^{\kappa(j\omega)y}, \tag{A.51}$$

where $\mathcal{B}_\pm$ are constants and $\kappa(s) = \sqrt{s \rho_0 / \mu_0}$. The following boundary conditions must be applied:

- as $y \to +\infty$, $\mathcal{U}_z \to 0$

- at the rigid boundary the fluid adheres to the plane, $\mathcal{U}_z|_{y=0} = -U_0(\omega)$

- only considering the solution above the plane, $\mathcal{U}_z|_{y<0} = 0$,

which gives the solution

$$\mathcal{U}_z(y, \omega) = \begin{cases} -U_0(\omega) e^{-\kappa(j\omega)y} & y \geq 0 \\ 0 & y < 0. \end{cases} \tag{A.52}$$

Note that for a 'signal' quantity such as the velocity, the end result should be a function of ω (e.g. substitute $s = j\omega$). However, differential equations describing 'systems' or impedances will be written using the complex Laplace frequency s.

To understand the effect of a stationary plane on fluid moving at velocity $\mathcal{U}_z = U_0$, consider the plane's frame of reference, which moves with a velocity $-U_0(\omega)$ in the x direction. This scenario is pictured in the right diagram of Figure A.3. In this case,

$$\mathcal{U}_z(y, \omega) = -U_0(\omega) e^{-\kappa(j\omega)} - (-U_0(\omega)). \tag{A.53}$$

The per-unit-area tangential force on a stationary plane (Rayleigh, 1896), due to fluid moving with velocity $U_0(\omega)$, is given by

$$\mu_0 \frac{\partial}{\partial y} \mathcal{U}_z \bigg|_{y=0} = -\mu_0 U_0(\omega)(-\kappa(s)) = \mu_0 U_0(\omega) \sqrt{\frac{s \rho_0}{\mu_0}} = U_0(\omega) \sqrt{s \rho_0 \mu_0}. \tag{A.54}$$

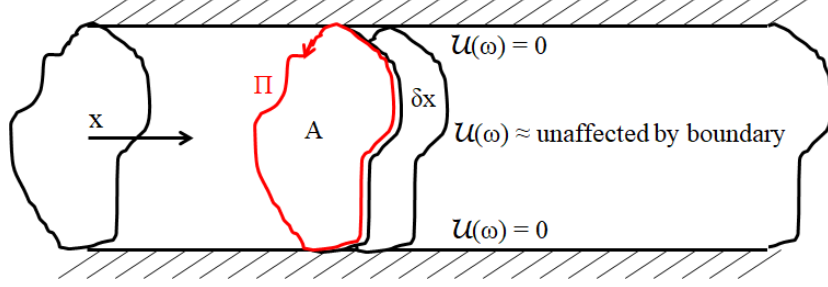[11]The left-hand side of this equation is a statement of 'force = mass × acceleration.'

Figure A.4: Rigid walled tube of cross-sectional area $A(x)$ and perimeter $\Pi(x)$. Rayleigh (1896) derived the equation of motion for a slice of infinitesimal volume, $A\delta x$ and arbitrary cross-sectional shape. It is assumed that $A(x)$ is large compared to the boundary layer of fluid adhering to the walls of the tube.

By Newton's third law, the force of the plane on the fluid is equal to, and opposite of, the force of the fluid on the plane. This result will be applied to a rigid-walled horn of arbitrary cross-sectional shape, as pictured in Figure A.4 (a cylindrical tube is drawn for simplicity). The area of the horn is A, and its perimeter (e.g. circumference) is given by Π. The 'boundary layer' of fluid adhering to the walls of the horn is assumed to be small compared to the cross-sectional dimensions.

Consider an infinitesimal volume of fluid, $A\delta x$. The area related to the tangential force of the wall on the fluid is $\Pi\delta x$. In the frequency domain, the one-dimensional linearized equation of force is

$$(A\delta x)\rho_0 s \mathcal{U}_z = -(A\delta x)\frac{\partial \mathcal{P}}{\partial x} - (\Pi\delta x)\mathcal{U}_z\sqrt{s\rho_0\mu_0}$$

$$\rho_0 s \mathcal{U}_z = -\frac{\partial \mathcal{P}}{\partial x} - \frac{\Pi}{A}\mathcal{U}_z\sqrt{s\rho_0\mu_0}. \tag{A.55}$$

To obtain a differential equation in $\mathcal{U}_z$, it is necessary to use the relation

$$-\frac{\partial \mathcal{P}}{\partial x} = \frac{c_0^2\rho_0}{s}\frac{\partial^2 \mathcal{U}_z}{\partial x^2}, \tag{A.56}$$

which may be derived using the linearized continuity equation $s\mathcal{E} + \partial \mathcal{U}_z/\partial x = 0$ (Eq. A.6) and the lossless equation of state $\mathcal{P} = c_0^2\rho_0\mathcal{E}$ (Eq. A.7). This gives

$$\frac{\partial^2 \mathcal{U}_z}{\partial x^2} = \left[\frac{s^2}{c_0^2}\left(1 + \frac{\Pi}{A}\sqrt{\frac{\mu_0}{s\rho_0}}\right)\right]\mathcal{U}_z$$

$$\frac{\partial^2 \mathcal{U}_z}{\partial x^2} = \kappa^2\mathcal{U}_z, \tag{A.57}$$

where the solutions to this one-dimensional wave equation take the same form as Equation A.51.

135

In this case, taking the positive square root,[12]

$$\kappa(s) \approx \frac{s}{c_0} + \frac{1}{c_0}\left(\frac{\Pi}{2A}\right)\sqrt{\frac{\mu_0 s}{\rho_0}}$$

$$\kappa(s) \approx \frac{s}{c_0} + \frac{\beta_0}{c_0}\sqrt{s}, \qquad \beta_0 = \frac{\Pi\sqrt{\mu_0'}}{2A} = \frac{\Pi}{2A}\sqrt{\frac{\mu_0}{\rho_0}}. \tag{A.58}$$

This approximation holds as long as

$$\left(\frac{\beta_0}{\sqrt{s}}\right)^2 \ll 1. \tag{A.59}$$

Quick calculations show that $(\beta_0/\sqrt{s})^2$, which is unitless, is approximately equal to $-j0.045/f$. Thus, it causes a small error in the phase of $\kappa(s)$. The magnitude of this term is largest at low frequencies, approximately 0.0045 at 100 [Hz], 4.5×10^{-4} at 1 [kHz], and 4.5×10^{-5} at 10 [kHz]. It is even more informative to re-cast this expression in terms of $r_v(s)$, discussed previously. For a cylinder,

$$\frac{\beta_0}{\sqrt{s}} = \frac{2}{r_v(s)}. \tag{A.60}$$

Therefore, the condition given above may be restated as

$$r_v(s) \gg 2, \tag{A.61}$$

which is the same condition given by Keefe (1984) for a large-r tube.

Thermal effects. Kirchhoff (1868) found that in a rigid-walled tube of large radius, the approximate Bessel-function solution depends on the constant

$$\gamma_0' = \sqrt{\mu_0'} + \left(\sqrt{\eta_0} - \frac{1}{\sqrt{\eta_0}}\right)\sqrt{\nu_0}$$

$$= \sqrt{\mu_0'} + (\eta_0 - 1)\sqrt{\frac{\kappa_0}{\rho_0 c_p}}. \tag{A.62}$$

After substituting $\sqrt{\mu_0'} \to \gamma_0'$ into Rayleigh's solution[13] for viscous losses in a horn of cross-sectional area A and perimeter Π, described above, the solution matches the large-r approximate solutions for (1) a cylindrical tube, and (2) infinite parallel walls. Therefore, at the end of Section 350, Rayleigh (1896) notes that the substitution $\sqrt{\mu_0'} \to \gamma_0'$ should be sufficient for any geometry where the cross-sectional dimensions are much larger than the thermal and viscous boundary layer.

Using the definition $\nu_0 = \frac{5}{2}\mu_0'$ for a mono-atomic gas, Rayleigh finds $\gamma_0' = \sqrt{\mu_0'}[1 + \sqrt{5/2}(\sqrt{\eta_0} - $

---

[12]When selecting the sign for κ, the sign of $\pm x\Re(\kappa)$ should always be negative so that a complex propagation factor causes a loss in amplitude.

[13]Benade (1988) says that many papers mistakenly substitute $\mu_0 \to \mu_0[1 + (\eta_0 - 1)(\kappa_0/(\mu_0 c_v))]$, which is not the same as the substitution suggested by Rayleigh.

$1/\sqrt{\eta_0}$)]. W. P. Mason (1927) defines γ_0' using μ_0 instead of $\mu_0' = \mu_0/\rho_0$, and he defines $\nu_0 = \frac{5}{2}\mu_0$ instead of $\nu_0 = \frac{5}{2}\mu_0'$. Because he substitutes this quantity for $\sqrt{\mu_0}$ instead of $\sqrt{\mu_0'}$, his γ_0' is ultimately divided by $\sqrt{\rho_0}$. Therefore, his analysis is equivalent to those of Kirchhoff and Rayleigh. However, all three authors make the same error by defining $\nu_0 = \frac{5}{2}\mu_0'$ instead of defining ν_0 according to Equation A.27 for a (mostly) diatomic gas. To avoid this error, the answer here is left in terms of ν_0 (which could be calculated using Eq. A.27).

Modifying $\kappa(s)$ given in the previous section, the final solution for the wave-propagation factor of a rigid-walled horn of arbitrary shape, including both thermal and viscous effects, is

$$\kappa(s) \approx \frac{s}{c_0} + \frac{\beta_0}{c_0}\sqrt{s} \tag{A.63a}$$

$$\beta_0 = \frac{\Pi}{2A}\sqrt{\frac{1}{\rho_0}}\left[\sqrt{\mu_0} + \left(\eta_0 - 1\right)\sqrt{\frac{\kappa_0}{c_p}}\right]. \tag{A.63b}$$

From Keefe (1984) and Benade (1988), $\kappa_0/c_p = \mu_0/\mathrm{Pr} = [1.846 \times 10^{-5}(1+0.0025\Delta T)]/[0.8410(1-0.0002\Delta T)]^2$ [kg· s^{-1}·m^{-1}], where Pr is the Prandtl number and ΔT is the temperature difference relative to $T_0 = 26.85$ [^{o}C]. The expression is accurate for $T_0 \pm 10$ [^{o}C]. For a 7.5 [mm] diameter at 27 [^{o}C], $\beta_0 \approx 1.5$.

Transmission line parameters for the (W. Mason, 1928) solution. As this solution was originally derived assuming viscous losses only (Helmholtz, 1863),

$$\mathcal{Z} = \frac{s\rho_0}{A}\left[1 + \frac{2}{r_v(s)}\right] \text{ (lossy, linearized force equation)} \tag{A.64a}$$

$$\mathcal{Y} = \frac{sA}{\eta_0 P_0}, \text{ (lossless, linearized continuity equation)} \tag{A.64b}$$

where the lossless equation of state is used to calculate the continuity equation. These equations do not result in the correct propagation factor $\kappa(s)$. Instead, W. Mason (1928) approximated $\kappa(s)$ from Equation A.57,

$$\kappa(s) \approx \frac{s}{c_0}\left[1 + \frac{1}{r_v'(s)}\right] \neq \sqrt{\mathcal{Z}\mathcal{Y}}, \tag{A.65}$$

where Rayleigh's substitution to add the thermal effects is included via

$$r_v'(s) = r_v(s)\frac{\sqrt{\mu_0}}{\gamma_0'}. \tag{A.66}$$

To completely describe wave propagation in the duct, the characteristic impedance must still be calculated. In this case,

$$\frac{\mathcal{Z}}{\kappa} \neq \frac{\kappa}{\mathcal{Y}} \tag{A.67}$$

due to the method for including heat conduction. Therefore, each of these quantities gives a different solution for the characteristic impedance (typically assumed to be $z_0 = \sqrt{\mathcal{Z}/\mathcal{Y}} = \mathcal{Z}/\kappa = \kappa/\mathcal{Y}$).
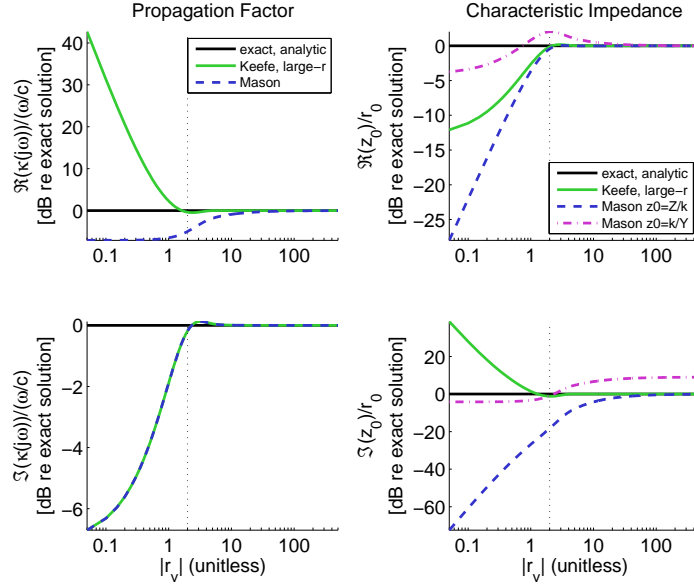

Figure A.5: The propagation function $\kappa(s)$ and characteristic impedance z_0 for different large-r approximations. These values are normalized as $\kappa/(\omega/c_0)$ and z_0/r_0, so that they are dimensionless functions of $|r_v|$ rather than frequency or radius (e.g. Keefe (1984)). Exact solutions (Keefe, 1984; Benade, 1968) are given, and compared with the analytic solution given here (Eqs. A.42a and A.42b). Finally, large-r approximations by Keefe (1984) and W. P. Mason (1927) are given. Note that Mason's z_0 can be expressed as $\mathcal{Z}/\kappa$ or $\kappa/\mathcal{Y}$, which gives two different answers because of the way he approximates κ. Keefe says his large-r approximation is valid for $r_v > 2$.

Figure A.5 shows the values for $|r_v|$ over which Keefe's and Mason's large-r approximations match the exact solution. Keefe (1984) recommends truncating the series approximation for $\Re(z_0)$ and $\Im(\kappa)$, so the values shown here match the large-r (fewer terms) curves from Figure A.2. As expected, for very large radii the propagation number and characteristic impedance approach the lossless case, $\kappa \to s/c_0$ and $z_0 \to r_0$. See Figure A.1 for $|r_v|$ values as a function of frequency and diameter. Above Keefe's cutoff of $|r_v| = 2$, the approximations are equally good for $\Im(\kappa)$ and $\Re(z_0)$ (taking the solution $z_0 = \mathcal{Z}/\kappa$). However, for $\Re(\kappa)$ and $\Im(z_0)$, Keefe's approximation is superior. Finally, it is interesting to note that, taking $z_0 = \kappa/\mathcal{Y}$, Mason's solution is not as good as the other approximations in the large-r regime, but is closer to the exact solution for the small-r regime.

Again, these approximations are typically unnecessary on a modern computer. However, it is useful to study them in order to understand historical results and put them in context.

A.3 Solutions for other constant-area geometries

Some authors (e.g. Stinson (1991)) have addressed lossy solutions for plane-wave propagation in arbitrary constant-area horn geometries. As the transmission-line parameters $\mathcal{Z}$ and $\mathcal{Y}$ are dependent upon the cross-sectional geometry of the horn, 'arbitrary' solutions often require more computation before they can be used. Cylindrical and parallel-plate geometries are by far the easiest to examine, as closed-form solutions for the transmission-line parameters may be found.

Richards (1986) compares the transmission-line solutions for a cylindrical horn with those for infinite parallel planes.[14] He found that for a wide range of useful sizes, these solutions are nearly identical. For geometries and frequencies where these solutions are approximately the same, Richards (1986) proposes that the duct size may be expressed in terms of a generalized radius,

$$a_0 = \frac{2A_0}{\Pi_0}, \tag{A.68}$$

where A_0 is the duct area and Π_0 is the duct perimeter. In the case of a cylindrical tube a_0 is equal to the tube radius, and in the case of infinite parallel plates a_0 is equal to the distance between the plates. Note that the generalized radius of Equation A.68 appeared in the results of Rayleigh (1896) and W. Mason (1928). Richards (1986) evaluates this formula theoretically in terms of two different geometries, and experimentally using ducts of atypical cross-sectional geometry.

A.3.1 Solution for infinite parallel plates

Consider two infinite parallel plates, with a uniform gap of height a_0 between them, and plane-wave flow in one direction. Viscothermal losses for this geometry were investigated by Rayleigh (1896) (Sec. 350). An easy-to-follow derivation of the parallel-plate solution is given by Richards (1986).

The transmission-line parameters are given by

$$\mathcal{Z}(s) = \frac{s}{c_0} r_0 \left[1 - \frac{2}{r_v} \tanh\left(\frac{r_v}{2}\right) \right]^{-1} \tag{A.69a}$$

$$\mathcal{Y}(s) = \frac{s}{c_0} \frac{1}{r_0} \left[1 + (\eta_0 - 1)\frac{2}{r_t} \tanh\left(\frac{r_t}{2}\right) \right], \tag{A.69b}$$

where the parameters are independent of the axial coordinate x. Similar to the cylindrical horn solution,

$$r_v(s) = a_0 \sqrt{\frac{s\rho_0}{\mu_0}} = r_t(s)/\sqrt{\mathrm{Pr}}, \tag{A.70}$$

and $r_0 = \rho_0 c_0 / A_0$ where A_0 is the area between the plates.

---

[14]Richards uses J_2/J_0 for the ratio of Bessel functions in the cylindrical solution, whereas the correct formula should have J_1/J_0.

A.3.2 Generalization to other geometries

Note the similarities between Equations A.42a and A.42b, and Equations A.69a and A.69b. Both of these solutions take the form

$$\mathcal{Z}(s) = \frac{s}{c_0} r_0 \left[1 - F(r_v) \right]^{-1} \tag{A.71a}$$

$$\mathcal{Y}(s) = \frac{s}{c_0} \frac{1}{r_0} \left[1 + (\eta_0 - 1)F(r_t) \right] \tag{A.71b}$$

$$r_v(s) = \frac{2A_0}{\Pi_0} \sqrt{\frac{s\rho_0}{\mu_0}} = r_t(s)/\sqrt{\mathrm{Pr}}. \tag{A.71c}$$

The function $F(\alpha)$ varies by geometry, such that

$$F_p(\alpha) = \frac{2}{\alpha} \tanh\left(\frac{\alpha}{2}\right) \quad \text{(parallel-plate)} \tag{A.72a}$$

$$F_c(\alpha) = \frac{2}{\alpha} \frac{I_1(\alpha)}{I_0(\alpha)} \quad \text{(cylindrical).} \tag{A.72b}$$

As Richards (1986) notes, for $\alpha = r_v$ or $\alpha = r_t = r_v/\sqrt{\mathrm{Pr}}$ values where $F_p \approx F_c$, these solutions are interchangeable. As these geometries are quite different, it follows that either equation may be used for an arbitrary geometry, as long as this condition is met. As Richards (1986) notes, in the large-r limit as $\alpha \to \infty$, the functions are approximately equivalent

$$F_p(\alpha) \approx \frac{2}{\alpha} \tag{A.73a}$$

$$F_c(\alpha) \approx \frac{2}{\alpha}. \tag{A.73b}$$

In the small-r limit as $\alpha \to 0$, the cylindrical and parallel-plate solutions are slightly different,

$$F_p(\alpha) \approx 1 - \frac{\alpha^2}{12} \tag{A.74a}$$

$$F_c(\alpha) \approx 1 - \frac{\alpha^2}{8}. \tag{A.74b}$$

Figure A.6 shows how the differences between the functions F_p and F_c affect the propagation function $\kappa = \sqrt{\mathcal{Z}\mathcal{Y}}$ and the characteristic impedance assuming a uniform-area horn, $z_0 = \sqrt{\mathcal{Z}/\mathcal{Y}}$ (Sec. A.2). Note that z_0 and r_0 (the surge resistance) depend on the cross-sectional area (and will vary with x for a variable-area horn of area $A(x)$). The parallel-plate solutions are expressed in decibels relative to the exact cylindrical solution (Keefe, 1984). For the entire r_v range, the discrepancies in κ and z_0 between the two geometries remain within a small [dB] range. The largest discrepancy between the solutions occurs in the transition region between small-r and large-r solutions, near $r_v = 2$. This makes sense, as the shape of the horn plays the largest role in the determination of the total boundary layer area in this r_v range. For very large-r solutions ($r_v > 10$),
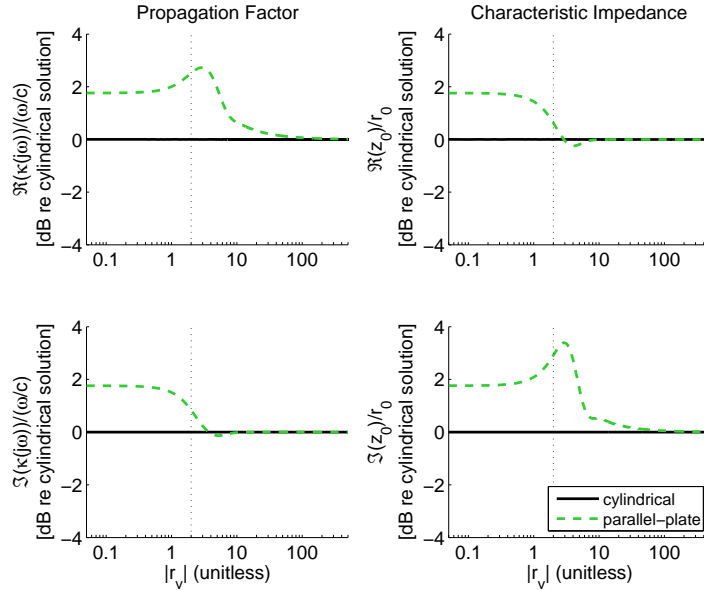
these solutions are nearly identical.

Figure A.6: The propagation function $\kappa(s)$ and characteristic impedance z_0 for wave propagation between infinite parallel plates, expressed in [dB] relative to the cylindrical-horn solutions (Keefe, 1984). These values are normalized as $\kappa/(\omega/c_0)$ and z_0/r_0, so that they are dimensionless functions of $|r_v|$ rather than frequency or area (e.g. Keefe (1984)). For very large-r ($r_v > 10$), these solutions are nearly identical. The largest discrepancy between the solutions occurs in the transition region between small-r and large-r solutions, near $r_v = 2$.

From Figure A.6, it appears that both the cylindrical and parallel-plate horn solutions may be generalized to an arbitrary geometry using the generalized radius given by Equation A.68. In most cases, this generalization will have far less error than the wrong choice of series expansion for the cylindrical horn (e.g. Figs. A.2 and A.5). For $r_v > 10$, it does not matter which solution is used, as they are identical. For smaller values of r_v, choosing the solution for the geometry most similar to that of the test system should give a reasonable approximation for viscous and thermal losses.

A.4   The Webster horn equation

The Webster horn equation (Webster, 1919) may be used to analyze a variable-area horn. The horn has a cross-sectional area function $A(x)$, where x is the axis of propagation. To cast this problem in one dimension, it is necessary to use the volume velocity $v(x,t) \leftrightarrow \mathcal{V}(x,\omega)$ (Eq. 3.1) and average pressure $\psi(x,t) \leftrightarrow \Psi(x,\omega)$ (Eq. 3.3) of an infinitesimal slice, as described in Section 3.1. The following results are derived under the quasi-static assumption that the slice width is much smaller than the wavelength.

Figure A.7 compares the volume-velocity slice for a variable-area horn with that for a constant-

area tube. The cross-sectional slice is perpendicular to the axis of flow at all points throughout the cross section; therefore, it takes the shape of a cap or lens, rather than a flat plane. This infinitesimally thin slice represents an iso-pressure surface, which is an equipotential surface for the volume velocity.

The Webster horn equation is typically given as

$$\frac{1}{A(x)} \frac{\partial}{\partial x} A(x) \frac{\partial p}{\partial x} = \frac{1}{c_0^2} \frac{\partial^2 p}{\partial t^2} \qquad \leftrightarrow \qquad \frac{1}{A(x)} \frac{\partial}{\partial x} A(x) \frac{\partial \mathcal{P}}{\partial x} = \frac{s^2}{c_0^2} \mathcal{P}, \tag{A.75}$$

where $\Psi = \mathcal{P}$ for iso-pressure surfaces of area $A(x)$. Typically, this equation is assumed to hold for slowly varying area functions $A(x)$. Keefe & Barjau (1999) state that if the horn profile changes too rapidly with x, the assumption of iso-pressure surfaces will break down. This condition may be taken to mean that $A(x)$ should be smooth, and that its changes dA/dx (in [m]) should be small compared to the wavelength $\lambda = c_0/f$ (in [m]) such that the plane-wave assumption holds.
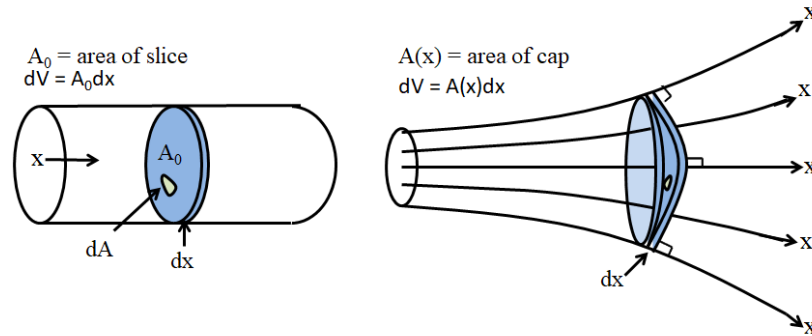
Figure A.7: Cross-sectional slice related to the volume velocity in a cylinder (left) and variable-area horn (right). The cross-sectional slice should be an iso-pressure curve, which must be orthogonal to the velocity flow lines (x) for the plane-wave mode (0th order mode). In the case of the variable-area horn, note that this surface is not a flat plane.

A.4.1 One-dimensional force equation (average pressure)

To cast the lossless force equation (conservation of momentum) into one-dimensional form, it must be averaged over the area of the slice. Note that $\hat{x}$ is defined as orthogonal to the iso-pressure slice,

in the $-\vec{\nabla}p$ direction. The force equation becomes

$$\vec{\nabla}p = -\rho_0 \frac{\partial \vec{u}}{\partial t}$$

$$\frac{1}{A(x)} \iint_{A_{slice}} dA\hat{x} \cdot \vec{\nabla}p = \frac{1}{A(x)} \iint_{A_{slice}} dA\hat{x} \cdot \left(-\rho_0 \frac{\partial \vec{u}}{\partial t}\right)$$

$$= -\frac{\rho_0}{A(x)} \frac{\partial}{\partial t}\left(\iint_{A_{slice}} \vec{u} \cdot \hat{x} dA\right)$$

$$= -\frac{\rho_0}{A(x)} \frac{\partial v}{\partial t}. \tag{A.76}$$

The left-hand side of this equation requires careful attention. Ideally, it will be equal to $\partial\psi/\partial x$, but this is the case only under two conditions:

1. The infinitesimal slice in question is iso-pressure ($p = \psi$ everywhere on the slice).

2. The differential slice thickness is constant over the whole slice (cannot vary with dA).

Under these conditions, the term $\hat{x} \cdot \vec{\nabla}p$ will factor out of the integral, and be equal to $\partial\psi/\partial x$.

Assume that the infinitesimally thick slices are bounded by adjacent iso-pressure contours. For the term $\hat{x} \cdot \vec{\nabla}p$ to be independent of dA, it is necessary that the infinitesimal thickness between adjacent iso-pressure contours not vary across the slice (e.g. dx does not depend on dA). If this condition holds, then the x component of the gradient will be equal to $\partial/\partial x$. If the slices are also iso-pressure, then $\partial p/\partial x$ will factor out of the integral. According to Agulló et al. (1999) and Keefe & Barjau (1999), condition (2) is met only for cylindrical and conical horns, which use cylindrical and spherical coordinate systems respectively. These coordinate systems are 'separable,' such that the differential length does not depend on the differential area (e.g. $dV = (dx)(dr)(rd\theta) = dxdA$ in cylindrical coordinates or $dV = (dr)(r\sin\phi d\theta)(rd\phi) = drdA$ in spherical coordinates).

If both conditions (1) and (2) are met, then

$$-\frac{\rho_0}{A(x)} \frac{\partial v}{\partial t} = \frac{1}{A(x)} \iint_{A_{slice}} dA\hat{x} \cdot \vec{\nabla}p$$

$$= \frac{1}{A(x)} \iint_{A_{slice}} \frac{\partial p}{\partial x} dA$$

$$= \frac{\partial p}{\partial x}\left(\frac{1}{A(x)} \iint_{A_{slice}} dA\right)$$

$$= \frac{\partial p}{\partial x}. \tag{A.77}$$

Under the assumption that iso-pressure curves exist and the average pressure $\psi = p$, this gives (in both the time and frequency domains)

$$\frac{\partial \psi}{\partial x} = -\frac{\rho_0}{A(x)} \frac{\partial v}{\partial t} \qquad \leftrightarrow \qquad \frac{\partial \Psi}{\partial x} = -\frac{s\rho_0}{A(x)} \mathcal{V}, \tag{A.78}$$

143

which corresponds to the lossless transmission line parameter $\mathcal{Z} = s\rho_0/A(x)$.

A.4.2 One-dimensional continuity equation (volume velocity)

To cast the lossless continuity equation (conservation of mass) into one-dimensional form, it must be integrated over the volume of the slice,

$$\vec{\nabla} \cdot \vec{u} = -\frac{1}{\eta_0 P_0} \frac{\partial p}{\partial t}$$

$$\iiint_{V_{slice}} dV \vec{\nabla} \cdot \vec{u} = \iiint_{V_{slice}} dV \left[-\frac{1}{\eta_0 P_0} \frac{\partial p}{\partial t} \right]. \tag{A.79}$$

Note that the density ρ_0 is assumed to be constant over the volume slice. Let the axial coordinate vary by δx, and let $\hat{n}$ be a vector normal to the surface of the volume slice, S_{slice}. Consider the left-hand side of Equation A.79. By the divergence theorem (Gauss' theorem) this equation becomes

$$\iiint_{V_{slice}} dV \vec{\nabla} \cdot \vec{u} = \iint_{S_{slice}} \vec{u} \cdot \hat{n} dS$$

$$= \iint_{A_{slice}(x+\delta x)} \vec{u}(x+\delta x) \cdot (\hat{x}) dA + \iint_{A_{slice}(x)} \vec{u}(x) \cdot (-\hat{x}) dA$$

$$= v(x+\delta x) - v(x), \tag{A.80}$$

the difference in volume velocities going into and out of the slice.[15]

Now consider the right-hand side of Equation A.79,

$$\iiint_{V_{slice}} dV \left[-\frac{1}{\eta_0 \rho_0} \frac{\partial p}{\partial t} \right] = -\frac{1}{\eta_0 P_0} \frac{\partial}{\partial t} \left[\iiint_{V_{slice}} p dV \right]. \tag{A.81}$$

Under condition (2) from the previous section, in the case where the infinitesimal thickness is uniform over the slice,

$$\iiint_{V_{slice}} p dV = \delta x \iint_{A_{slice}} p dA = \delta x A(x) \psi. \tag{A.82}$$

Putting these results together,

$$v(x+\delta x) - v(x) = -\frac{1}{\eta_0 P_0} \frac{\partial}{\partial t} \left[\delta x A(x) \psi \right]$$

$$\frac{v(x+\delta x) - v(x)}{\delta x} = -\frac{A(x)}{\eta_0 P_0} \frac{\partial \psi}{\partial t}. \tag{A.83}$$

---

[15] Note that the wall boundary condition for $\vec{u}$ means that $\vec{u} \cdot \hat{n} = 0$ at the horn walls.

Taking the limit as $\delta x \to 0$,

$$\frac{\partial v}{\partial x} = -\frac{A(x)}{\eta_0 P_0}\frac{\partial \psi}{\partial t} \qquad \leftrightarrow \qquad \frac{\partial \mathcal{V}}{\partial x} = -\frac{sA(x)}{\eta_0 P_0}\Psi, \qquad\qquad (A.84)$$

which corresponds to the lossless transmission line parameter $\mathcal{Y} = sA(x)/(\eta_0 P_0)$. Again, it is important to note that this derivation only holds if the infinitesimal thickness between iso-pressure curves remains uniform across the slice.

A.4.3   Webster equation for a conical horn (spherical coordinates)

This section presents an alternative derivation of the Webster horn equation beginning from the wave equation. This exercise is similar to the preceding derivations using the continuity of mass and momentum equations. It shows how the Webster horn equation may be derived without first casting these equations in terms of pressure and volume velocity. Additionally, the primitive solutions for wave propagation in a conical horn are presented.

The Webster horn equation may be derived by combining Equations A.78 and A.84. Another way to derive the Webster horn equation is to begin with the wave equation,

$$\nabla^2 p = \frac{1}{c_0^2}\frac{\partial^2 p}{\partial t^2}, \qquad\qquad (A.85)$$

and integrate both sides over the volume of the slice (as in the previous section). The Webster horn equation then follows from the form of the Laplacian (∇^2) in the chosen coordinate system. The left-hand side becomes

$$\iiint_{V_{slice}} dV \nabla^2 p = \iiint_{V_{slice}} dV \vec{\nabla} \cdot \vec{\nabla} p$$

$$= \iint_{S_{slice}} dS \hat{n} \cdot \vec{\nabla} p$$

$$= \left[\iint_{A_{slice}} dA \hat{x} \cdot \vec{\nabla} p\right]_{x+\delta x} + \left[\iint_{A_{slice}} dA(-\hat{x}) \cdot \vec{\nabla} p\right]_{x}. \qquad (A.86)$$

To proceed with simplifying this integral, it is necessary to specify the coordinate system and the locations of the iso-pressure curves. Therefore, the following derivation considers the case of a conical horn.

Shown in Figure A.8, a conical horn may be described by spherical coordinates (r, θ, ϕ). The radial spherical coordinate $r = R_0 + x$ corresponds the axial coordinate x of the horn; the mouth of the horn at $x = 0$ corresponds to the constant radius $r = R_0$. In this case, the infinitesimal slice width (dx) is not a function of θ or ϕ. The differential volume and x component of the gradient
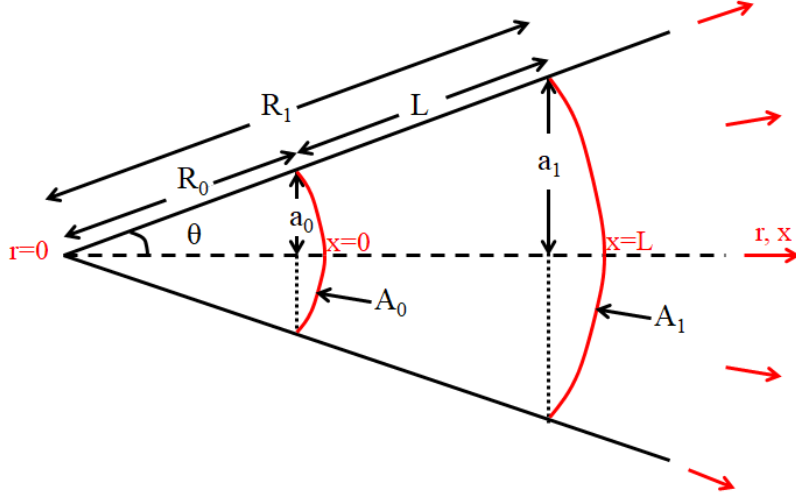
Figure A.8: Example of a conical horn of length L, beginning at $x = r - R_0 = 0$. The planar radii at the ends of the horn are specified by a_0 and a_1. The areas of the iso-pressure curves are given by the spherically convex areas A_0 and A_1.

are given by

$$
\begin{aligned}
dV &= (dr)(r\sin\phi\, d\theta)(r\, d\phi) \\
&= (dx)((R_0 + x)\sin\phi\, d\theta)((R_0 + x)\, d\phi) = (dx)(dA)
\end{aligned} \tag{A.87a}
$$

$$
\hat{x} \cdot \vec{\nabla} = \hat{r} \cdot \vec{\nabla} = \frac{\partial}{\partial r} = \frac{\partial}{\partial x}. \tag{A.87b}
$$

Thus, assuming iso-pressure surfaces at x and $x + \delta x$, the term $\hat{x} \cdot \vec{\nabla} p = \partial p/\partial x$ may be factored out of the integral. The left-hand side becomes

$$
\begin{aligned}
\iiint_{V_{slice}} dV \nabla^2 p &= \left[\iint_{A_{slice}} dA \frac{\partial p}{\partial x} \right]_{x+\delta x} - \left[\iint_{A_{slice}} dA \frac{\partial p}{\partial x} \right]_{x} \\
&= \delta x \frac{\partial}{\partial x} \left[\frac{\partial p}{\partial x} \iint_{A_{slice}} dA \right] \\
&= \delta x \frac{\partial}{\partial x} \left[A(x) \frac{\partial p}{\partial x} \right] \\
&= \delta x \frac{\partial}{\partial x} \left[A(x) \frac{\partial \psi}{\partial x} \right].
\end{aligned} \tag{A.88}
$$

The right-hand side of the wave equation becomes

$$
\iiint_{V_{slice}} dV \frac{1}{c_0^2} \frac{\partial^2 p}{\partial t^2} = \frac{1}{c_0^2} \frac{\partial^2}{\partial t^2} \iiint_{V_{slice}} dV\, p. \tag{A.89}
$$

For iso-pressure curves in spherical coordinates,

$$\iiint_{V_{slice}} dV \frac{1}{c_0^2} \frac{\partial^2 p}{\partial t^2} = \delta x \frac{1}{c_0^2} \frac{\partial^2}{\partial t^2} \iint_{A_{slice}} dA p$$

$$= \delta x \frac{A(x)}{c_0^2} \frac{\partial^2 \psi}{\partial t^2}. \tag{A.90}$$

Combining Equations A.88 and A.90 and dividing by δx yields the Webster horn equation

$$\frac{1}{A(x)} \frac{\partial}{\partial x} A(x) \frac{\partial \psi}{\partial x} = \frac{1}{c_0^2} \frac{\partial^2 \psi}{\partial t^2} \qquad \leftrightarrow \qquad \frac{1}{A(x)} \frac{\partial}{\partial x} A(x) \frac{\partial \Psi}{\partial x} = \frac{s^2}{c_0^2} \Psi. \tag{A.91}$$

For a conical horn, the area function is a conical section of a sphere, defined by the angular ranges of θ and ϕ. Therefore, it is some fraction of the surface area of a sphere, given by $4\pi R_0^2$ for radius R_0. Thus, the area function may be described by

$$A(x) = \frac{A_0}{R_0^2} (R_0 + x)^2 \tag{A.92}$$

such that $A(x)|_{x=0} = A_0$ describes the area of a cap (or lens) of spherical curvature at $r = R_0$. Applying this result to the frequency-domain Webster horn equation yields

$$\frac{1}{r^2} \frac{\partial}{\partial r} r^2 \frac{\partial \Psi}{\partial r} = \frac{s^2}{c_0^2} \Psi$$

$$\frac{\partial^2 \Psi}{\partial r^2} + \frac{2}{r} \frac{\partial \Psi}{\partial r} = \kappa^2 \Psi, \tag{A.93}$$

which is the same as the spherical wave equation. This equation gives results of the form

$$\Psi = \Psi^+ + \Psi^-$$

$$= \alpha_+ \frac{e^{-\kappa r}}{r} + \alpha_- \frac{e^{\kappa r}}{r}$$

$$= \alpha_+ \frac{e^{-\kappa(x+R_0)}}{x + R_0} + \alpha_- \frac{e^{\kappa(x+R_0)}}{x + R_0}, \tag{A.94}$$

where $\alpha_\pm$ are constants that depend on the horn's boundary conditions.

The lossless volume velocity wave equation differs from the pressure wave equation, according to Equation 3.5, and is given by

$$\frac{\partial^2 \mathcal{V}}{\partial r^2} - \frac{2}{r} \frac{\partial \mathcal{V}}{\partial r} = \kappa^2 \mathcal{V}. \tag{A.95}$$

The general solution for the volume velocity is given by

$$\mathcal{V} = \mathcal{V}^+ - \mathcal{V}^- \tag{A.96a}$$

$$\mathcal{V}^{\pm} = \beta_{\pm} e^{\mp \kappa r}(1 \pm \kappa r)$$

$$= \beta_{\pm} e^{\mp \kappa(x + R_0)}(1 \pm \kappa(x + R_0)), \tag{A.96b}$$

where $\beta \pm$ are constants that depend on the boundary conditions. The general solutions for $\mathcal{V}$ and Ψ may be verified via substitution into their respective wave equations.

From these general solutions, the direction-dependent characteristic admittance may be derived. It is given by

$$y_c^{\pm}(r, s) = \frac{\mathcal{V}^{\pm}}{\Psi^{\pm}} = \frac{\mathcal{Y}}{\kappa^2}\left(\kappa \pm \frac{1}{r}\right) = \frac{1}{\mathcal{Z}}\left(\kappa \pm \frac{1}{r}\right). \tag{A.97}$$

Thus, for a conical horn (recall that $y_0 = \sqrt{\mathcal{Y}/\mathcal{Z}}$ is the characteristic admittance for a uniform horn),

$$\kappa = \sqrt{\mathcal{Z}\mathcal{Y}} \tag{A.98a}$$

$$y_c^{\pm}(r, s) = \sqrt{\frac{\mathcal{Y}}{\mathcal{Z}}}\left(1 \pm \frac{1}{\kappa r}\right) = y_0(x, s)\left(1 \pm \frac{1}{\kappa r}\right). \tag{A.98b}$$

A.4.4   Curvilinear horn equation

If the differential thickness of a volume slice is not uniform over its area (meaning the differential volume is not separable, $dV \neq dAdx$), then the integrals of Equations A.86 and A.89 become more complicated. Agulló et al. (1999) and Keefe & Barjau (1999) use orthogonal curvilinear coordinates to address this issue when formulating the Webster horn equation.

The following discussion uses a 'pseudo-cylindrical' curvilinear coordinate system with variables (x, r, θ) to describe the variable-area horn in Figure A.7. This coordinate system is assumed to be orthogonal (Agulló et al., 1999; Keefe & Barjau, 1999). The differential volume and x component of the gradient may be described by

$$dV = (h_x dx)(h_r dr)(h_\phi d\phi) = (h_x dx)dA \tag{A.99a}$$

$$\hat{x} \cdot \vec{\nabla} = \frac{1}{h_x}\frac{\partial}{\partial x}, \tag{A.99b}$$

where h_x, h_r and h_ϕ are functions of (x, r, ϕ), which allow the differential thicknesses to vary with the other coordinates. Here x is the axis of flow, r is a pseudo-radius (which we allow to have some curvature, unlike the radius in cylindrical coordinates) and ϕ is a rotation angle with a range of 2π.

The curvilinear horn equation derived by Agulló et al. (1999) deals with the variable infinitesimal

148

thickness $h_x dx$ by using the averages (over the slice area $A(x)$) to separate the $\vec{\nabla} p$ and p terms from the integrals in Equations A.86 and A.89. These averages are given by

$$
\begin{aligned}
\langle h_x \rangle &= \frac{1}{A(x)} \iint_{A_{slice}} dA h_x = \frac{1}{A(x)} \iint_{A_{slice}} (h_r dr h_\phi d\phi) h_x \\
&= \frac{2\pi}{A(x)} \int_{R_{slice}} dr (h_r h_\phi h_x) \\
\left\langle \frac{1}{h_x} \right\rangle &= \frac{1}{A(x)} \iint_{A_{slice}} dA \frac{1}{h_x} \\
&= \frac{2\pi}{A(x)} \int_{R_{slice}} dr \left(\frac{h_r h_\phi}{h_x} \right).
\end{aligned}
$$

(A.100a)

(A.100b)

Using these results, the average slice thickness can be represented as $\langle h_x \rangle dx$, and the average x component of the gradient becomes $\langle 1/h_x \rangle \partial/\partial x$.

The left-hand side of the wave equation, given in Equation A.86, becomes

$$
\begin{aligned}
\iiint_{V_{slice}} dV \nabla^2 p &= \left[\iint_{A_{slice}} dA \hat{x} \cdot \vec{\nabla} p \right]_{x+\delta x} + \left[\iint_{A_{slice}} dA (-\hat{x}) \cdot \vec{\nabla} p \right]_x \\
&= \left[\iint_{A_{slice}} dA \frac{1}{h_x} \frac{\partial p}{\partial x} \right]_{x+\delta x} - \left[\iint_{A_{slice}} dA \frac{1}{h_x} \frac{\partial p}{\partial x} \right]_x \\
&= \left[\left\langle \frac{1}{h_x} \right\rangle \frac{\partial p}{\partial x} \iint_{A_{slice}} dA \right]_{x+\delta x} - \left[\left\langle \frac{1}{h_x} \right\rangle \frac{\partial p}{\partial x} \iint_{A_{slice}} dA \right]_x \\
&= \frac{\delta x}{\delta x} \left(\left[\left\langle \frac{1}{h_x} \right\rangle A(x) \frac{\partial p}{\partial x} \right]_{x+\delta x} - \left[\left\langle \frac{1}{h_x} \right\rangle A(x) \frac{\partial p}{\partial x} \right]_x \right) \\
&= \delta x \frac{\partial}{\partial x} \left[\left\langle \frac{1}{h_x} \right\rangle A(x) \frac{\partial \psi}{\partial x} \right].
\end{aligned}
$$

(A.101)

The right-hand side (Eq. A.89) becomes

$$
\begin{aligned}
\iiint_{V_{slice}} dV \frac{1}{c_0^2} \frac{\partial^2 p}{\partial t^2} &= \frac{1}{c_0^2} \frac{\partial^2}{\partial t^2} \iiint_{V_{slice}} dV p \\
&= \frac{1}{c_0^2} \frac{\partial^2}{\partial t^2} \iiint_{V_{slice}} dA (h_x dx) p \\
&= \delta x \langle h_x \rangle \frac{1}{c_0^2} \frac{\partial^2 p}{\partial t^2} \iint_{A_{slice}} dA \\
&= \delta x \langle h_x \rangle \frac{A(x)}{c_0^2} \frac{\partial^2 \psi}{\partial t^2}.
\end{aligned}
$$

(A.102)

This gives the curvilinear horn equation (Agulló et al., 1999; Keefe & Barjau, 1999)

$$\frac{1}{\langle h_x \rangle A(x)} \frac{\partial}{\partial x} \left[\left\langle \frac{1}{h_x} \right\rangle A(x) \frac{\partial \psi}{\partial x} \right] = \frac{1}{c_0^2} \frac{\partial^2 \psi}{\partial t^2}, \tag{A.103}$$

which corresponds to the lossless transmission-line parameters

$$\mathcal{Z} = \frac{s \rho_0}{A(x) \langle \frac{1}{h_x} \rangle} \tag{A.104a}$$

$$\mathcal{Y} = \frac{s A(x) \langle h_x \rangle}{\eta_0 P_0}. \tag{A.104b}$$

In the case of the conical horn (spherical coordinates), $h_x = 1$, and Equation A.103 reduces to Equation A.91.

Solutions to the curvilinear horn equation can be difficult to find, as it is not generally possible to define a single orthogonal curvilinear coordinate system for the entire horn. Agulló et al. (1999) and Keefe & Barjau (1999) address this issue by using 'local coordinates.' Locally, an orthogonal (but not separable) curvilinear coordinate system (such as spherical or 'oblate spheroidal') is used. An additional function is then used to map these local coordinate systems to the horn profile, relative to the axial coordinate x. This process is not addressed in detail here, as curvilinear horn models are not used in this thesis.

Excepting cases where $A(x)$ changes very quickly with x, the change in the Webster horn equation due to $\langle \frac{1}{h_x} \rangle$ and $\langle h_x \rangle$ is expected to be small (these quantities are approximately equal to 1). Due to the high computational cost of this method and the difficulty of defining iso-pressure curve locations and local coordinate systems for an arbitrary horn shape, this method seems impractical for many applications. Additionally, it makes assumptions about the iso-pressure curve locations based on their shape at the mouth of the horn, which may not be valid (Miller, 1991; Kartan, 2013).

A.4.5   Visco-thermal losses in a horn

Historically, visco-thermal losses have been incorporated into the Webster horn equation by substituting the lossy propagation factor κ in place of the lossless factor $\kappa = s/c_0$ (Keefe & Barjau, 1999; Mapes-Riordan, 1993). An intuitive extension of this theory is posed here, in terms of the transmission line parameters $\mathcal{Z}$ and $\mathcal{Y}$. Note that the lossy horn equation given here is only valid insofar as

$$\Psi = \frac{1}{\mathcal{Y}} \frac{\partial}{\partial x} \frac{1}{\mathcal{Z}} \frac{\partial \Psi}{\partial x} \approx \frac{1}{\mathcal{Y} \mathcal{Z}} \frac{1}{A(x)} \frac{\partial}{\partial x} A(x) \frac{\partial \Psi}{\partial x}, \tag{A.105}$$

which is true when the boundary layer is small compared to the horn radius, or the area function is very slowly varying (e.g. $r_v(x, s)$ is also very slowly varying). Approximations for the lossy horn equation may also be derived using the method of variation of parameters (Pierce, 1981) or the

Wentzel, Kramers, and Brillouin (WKB) approximation.

Recall that $r_v(s)$ and $r_t(s) = \sqrt{\mathrm{Pr}}r_v(s)$, the dimensionless parameters describing the viscous and thermal boundary layers. In a cylindrical horn, these parameters were proportional to the radius a_0 (where area $A_0 = \pi a_0^2$). However, this parameter may be more generally derived by relating the wavefront area to the perimeter of the wall boundary, as described in Section A.4.5 (Rayleigh, 1896; W. P. Mason, 1927; Richards, 1986). Therefore, we can generalize the parameter a_0 to

$$a_0 = \frac{2\pi a_0^2}{2\pi a_0} \rightarrow \frac{2A(x)}{\Pi(x)}, \tag{A.106}$$

where $A(x)$ is the wavefront area in the horn, and $\Pi(x)$ is the wavefront perimeter as a function of the axial coordinate x. Therefore, let

$$r_v(x,s) = \frac{2A(x)}{\Pi(x)}\sqrt{\frac{s\rho_0}{\mu}}. \tag{A.107}$$

Note that the wavefront area in a horn is generally a convex surface (e.g. Fig. A.7). Therefore, if the planar cross section of the horn is a circle with local radius a_0, then the perimeter $\Pi = 2\pi a_0$, but the wavefront area $A \neq \pi a_0^2$. Since the horn geometry is closer to the cylindrical than the infinite parallel-plate geometry described in Section A.4.5, the $\mathcal{Z}$ and $\mathcal{Y}$ parameters for a cylindrical waveguide should be used to calculate r_v.

Therefore, intuitively, the lossy solution for the curvilinear horn is

$$\mathcal{Z}(x,s) = \frac{s\rho_0}{A(x)\langle\frac{1}{h_x}\rangle}\left[1 - \frac{2}{r_v}\frac{I_1(r_v)}{I_0(r_v)}\right]^{-1} \tag{A.108a}$$

$$\mathcal{Y}(x,s) = \frac{sA(x)\langle h_x\rangle}{\eta_0 P_0}\left[1 + (\eta_0 - 1)\frac{2}{r_t}\frac{I_1(r_t)}{I_0(r_t)}\right], \tag{A.108b}$$

where $\mathcal{Z}$ and $\mathcal{Y}$ have gained factors of $\langle 1/h_x\rangle$ and $\langle h_x\rangle$ in a similar fashion to the lossless curvilinear transmission line parameters. This generalization is likely to hold in horns of circular cross section, or of reasonably smooth perimeter. Note that in these equations, $r_v(x,s)$ should be calculated according to Equation A.112. In the case of the conical horn, $\langle 1/h_x\rangle = \langle h_x\rangle = 1$. Note that, for many horns, it may be assumed that $\langle 1/h_x\rangle \approx \langle h_x\rangle \approx 1$.

Boundary layer ratio for the conical horn. Figure A.8 depicts a conical horn in a spherical coordinate system where $r = R_0 + x$. The wavefront area is given by

$$\iint_{A_{slice}} dA = \int_0^{2\pi} d\phi \int_0^{\theta_0} d\theta (r^2 \sin\theta)$$

$$= 2\pi r^2 \int_0^{\theta_0} \sin\theta d\theta$$

$$A(x) = 2\pi(1 - \cos\theta_0)(R_0 + x)^2. \tag{A.109}$$

Therefore, in Equation A.92, the area $A_0 = A(0) = 2\pi(1 - \cos\theta_0)R_0^2$. In the typical case where the planar radii a_0 and a_1 at both ends of the horn are specified, rather than the r coordinate value, R_0 and $\cos\theta_0$ may be calculated from

$$\sin\theta_0 = \frac{a_0}{R_0} = \frac{a_1}{R_0 + L} \tag{A.110a}$$

$$R_0 = \frac{a_0 L}{a_1 - a_0} \tag{A.110b}$$

$$\cos\theta_0 = \frac{\sqrt{R_0^2 - a_0^2}}{R_0} = \frac{\sqrt{L^2 - (a_1 - a_0)^2}}{L}. \tag{A.110c}$$

Furthermore, if a is the planar radius, then

$$\Pi(x) = 2\pi a(x) = 2\pi \sin\theta_0(R_0 + x). \tag{A.111}$$

Therefore, for the conical horn,

$$r_v(x, s) = \frac{2(1 - \cos\theta_0)(R_0 + x)}{\sin\theta_0}\sqrt{\frac{s\rho_0}{\mu}}. \tag{A.112}$$

This formula calculates the viscous boundary layer ratio as a function of axial depth in the conical horn in terms of the local (curved) wavefront area, using the generalized radius $2A/\Pi$.

APPENDIX B

TWO-PORT NETWORKS

Two-port network models make it possible to model a one-port or two-port transmission line using a concatenation of 2×2 matrices. In this thesis, two-port models are used for multiple purposes. One application is analysis of middle-ear network models, consisting of electrical network elements such as resistors, capacitors, and inductors. A second application is modeling the transmission of sound in variable-area horns, such as a probe tip or ear canal. In this thesis, two-port models for cylindrical and conical horns are used to approximate other variations in area.

B.1 Definitions and properties

Figure B.1 shows a general 'black box' two-port network in terms of the 'forces' and 'flows' at the input and output ports. For electrical, mechanical and acoustical systems, the 'force' variables are voltage (V), mechanical force (F), and average pressure (Ψ), respectively. The 'flow' variables are current (I), one-dimensional mechanical velocity (U), and volume velocity ($\mathcal{V}$). The direction of Flow_2 is defined as into the port. This simplifies the analysis of impedance matrices in the following sections.

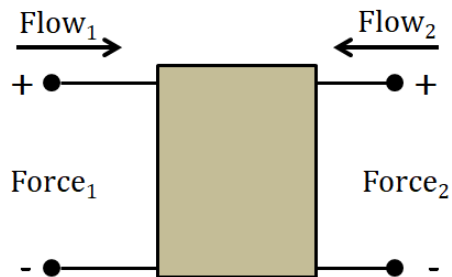

Figure B.1: A general two-port network showing the 'forces' and 'flows' at the input (1) and output (2). The direction of Flow_2 is defined as into the port, which simplifies the analysis of the impedance matrix.

B.1.1 Transmission ($ABCD$) and impedance matrices

Transmission through the 2-port network may be described by the following matrix equation:

$$\begin{bmatrix} \text{Force}_1 \\ \text{Flow}_1 \end{bmatrix} = T \begin{bmatrix} \text{Force}_2 \\ -\text{Flow}_2 \end{bmatrix} = \begin{bmatrix} A & B \\ C & D \end{bmatrix} \begin{bmatrix} \text{Force}_2 \\ -\text{Flow}_2 \end{bmatrix},$$
(B.1)

where the direction of Flow_2 is defined as into the port, as shown in Figure B.1. This convention is not widely used in the literature. However, it provides the correct direction of the volume velocity for the impedance matrix, thus simplifying the analysis. Transmission matrices may be concatenated from left to right via matrix multiplication,

$$T_{total} = \prod_{k=1}^{N} T_k = T_1 T_2 T_3 \ldots T_{N-1} T_N.$$
(B.2)

The impedance matrix, where the determinant $\Delta_T = AD - BC$, is given by[1]

$$\begin{bmatrix} \text{Force}_1 \\ \text{Force}_2 \end{bmatrix} = Z \begin{bmatrix} \text{Flow}_1 \\ \text{Flow}_2 \end{bmatrix} = \begin{bmatrix} z_{11} & z_{12} \\ z_{21} & z_{22} \end{bmatrix} \begin{bmatrix} \text{Flow}_1 \\ \text{Flow}_2 \end{bmatrix} = \frac{1}{C} \begin{bmatrix} A & \Delta_T \\ 1 & D \end{bmatrix} \begin{bmatrix} \text{Flow}_1 \\ \text{Flow}_2 \end{bmatrix}.$$
(B.3)

The input impedance of the two-port network when the far right end is 'blocked' ($\text{Flow}_2 = 0$) is given by $z_{11} = A/C$. If the network is terminated in a load impedance Z_L across the output terminals, then

$$Z_L = Z_2 = \frac{\text{Force}_2}{-\text{Flow}_2}.$$
(B.4)

At the input terminals, the impedance $Z_{in} = Z_1$ is related to the load impedance $Z_L = Z_2$ by

$$Z_{in} = \frac{AZ_L + B}{CZ_L + D} = z_{11} - \frac{z_{12} z_{21}}{z_{22} + Z_L} = \frac{\text{Force}_1}{\text{Flow}_1}$$
(B.5a)

$$Z_L = -z_{22} - \frac{z_{12} z_{21}}{Z_{in} - z_{11}} = \frac{\text{Force}_2}{-\text{Flow}_2}.$$
(B.5b)

The force transfer function is load-dependent, and given by

$$H = \frac{\text{Force}_2}{\text{Force}_1} = \frac{1}{A + B/Z_L}.$$
(B.6)

---

[1]In reverse, the transmission matrix may be expressed in terms of the elements of the impedance matrix by

$$\begin{bmatrix} \text{Force}_1 \\ \text{Flow}_1 \end{bmatrix} = \begin{bmatrix} A & B \\ C & D \end{bmatrix} \begin{bmatrix} \text{Force}_2 \\ -\text{Flow}_2 \end{bmatrix} = \frac{1}{z_{21}} \begin{bmatrix} z_{11} & \Delta_Z \\ 1 & z_{22} \end{bmatrix} \begin{bmatrix} \text{Force}_2 \\ -\text{Flow}_2 \end{bmatrix}.$$

B.1.2 Reciprocity

A network is reciprocal if the determinant $\Delta_T = 1$, and anti-reciprocal if $\Delta_T = -1$. When testing for reciprocity, it is important to note that for a product of matrices,

$$\Delta_{T_{total}} = \prod_{k=1}^{N} \Delta_{T_k} = \Delta_{T_1} \Delta_{T_2} \Delta_{T_3} \ldots \Delta_{T_{N-1}} \Delta_{T_N}. \tag{B.7}$$

A network containing traditional circuit elements (such as resistors, inductors and capacitors) in series and shunt configurations will always be reciprocal. The transmission matrices for series and shunt elements are given by

$$\text{Series impedance Z:} \quad \begin{bmatrix} 1 & Z \\ 0 & 1 \end{bmatrix} \quad \text{Shunt admittance Y:} \quad \begin{bmatrix} 1 & 0 \\ Y & 1 \end{bmatrix}. \tag{B.8}$$

Both of these matrices have determinants $\Delta_T = 1$, therefore, all traditional series and shunt impedances are reciprocal. According to Equation B.7, any concatenation of these elements will also be reciprocal. Two more components of import for network modeling include the transformer and gyrator.

Transformers may be used to describe a lever ratio or ratio of areas in a model. In general, the function of a transformer is to change the voltage (pressure) at some point along the transmission line (there is a compensatory change in the current or volume velocity). A transformer with a 'turns ratio' of N has the transmission matrix and determinant given by

$$\begin{bmatrix} A & B \\ C & D \end{bmatrix} = \begin{bmatrix} N & 0 \\ 0 & 1/N \end{bmatrix} \tag{B.9a}$$

$$\Delta_T = 1 - 0 = 1. \tag{B.9b}$$

Therefore, a transformer is a reciprocal circuit element. Note that by itself a transformer does not have an impedance matrix, as $1/C = 1/0$ is undefined.

A gyrator may be used to convert between electrical and mechanical/acoustical sections of a model, as its function is to swap the force and the flow quantities in a circuit. Therefore, a gyrator is a key component in the model of a loudspeaker (Kim & Allen, 2013). The transmission matrix and determinant of a gyrator are given by

$$\begin{bmatrix} A & B \\ C & D \end{bmatrix} = \begin{bmatrix} 0 & T_0 \\ 1/T_0 & 0 \end{bmatrix} \tag{B.10a}$$

$$\Delta_T = 0 - 1 = -1. \tag{B.10b}$$

Therefore, a gyrator is anti-reciprocal.

B.1.3   Reversibility

A reversible network has the same transmission parameters if its terminals are reversed. To reverse the terminals in Figure B.1, two operations must be performed. First, the matrix inverse must be taken, to solve for the output in terms of the input. Second, the directions of Flow_1 and Flow_2 must be reversed. This is calculated as

$$
\begin{bmatrix} \text{Force}_1 \\ \text{Flow}_1 \end{bmatrix} = \begin{bmatrix} A & B \\ C & D \end{bmatrix} \begin{bmatrix} \text{Force}_2 \\ -\text{Flow}_2 \end{bmatrix}
$$
$$
\begin{bmatrix} \text{Force}_2 \\ -\text{Flow}_2 \end{bmatrix} = \frac{1}{\Delta_T} \begin{bmatrix} D & -B \\ -C & A \end{bmatrix} \begin{bmatrix} \text{Force}_1 \\ \text{Flow}_1 \end{bmatrix}
$$
$$
\begin{bmatrix} \text{Force}_2 \\ \text{Flow}_2 \end{bmatrix} = \frac{1}{\Delta_T} \begin{bmatrix} D & B \\ C & A \end{bmatrix} \begin{bmatrix} \text{Force}_1 \\ -\text{Flow}_1 \end{bmatrix}. \tag{B.11}
$$

Therefore, for a network to be reversible, it must be true that

$$
\begin{bmatrix} A & B \\ C & D \end{bmatrix} = \frac{1}{\Delta_T} \begin{bmatrix} D & B \\ C & A \end{bmatrix}, \tag{B.12}
$$

meaning $A = D/\Delta_T$, $B = B/\Delta_T$, $C = C/\Delta_T$ and $D = A/\Delta_T$. The conditions for reversibility of a network are given by

$$
\text{Reciprocal } (\Delta_T = 1): D = A \tag{B.13a}
$$
$$
\text{Anti-reciprocal } (\Delta_T = -1): D = -A, \;\; B = C = 0. \tag{B.13b}
$$

If the network is not reciprocal or anti-reciprocal, it cannot be reversible (except for the trivial case where $A = B = C = D = 0$). Note that neither the gyrator nor the transformer (described in the previous section) is reversible.

B.2   Transmission matrices for acoustic horns

Transmission matrices for cylindrical tubes, conical horns, and step discontinuities in area are given in this section. Solutions for the cylindrical and conical horns are given in terms of the complex wave propagation factor $\kappa(x, s)$. In the case of lossless propagation, $\kappa = s/c_0$. Thus, the lossy equations are given in terms of hyperbolic functions (sinh, cosh), which become trigonometric functions (sin, cos) in the lossless case. For reference and comparison to other published models,

note that

$$\sin(x) = -j\sinh(jx) \tag{B.14a}$$

$$\cos(x) = \cosh(jx) \tag{B.14b}$$

$$\tan(x) = -j\tanh(jx). \tag{B.14c}$$

The general derivation for a two-port network given primitive pressure-wave solutions is given in Section 3.3.1. In the following sections, this general formula is adapted to specific geometries.

B.2.1 Uniform-area horn

In a horn of uniform area, the normalized forward- and backward-traveling waves and characteristic admittances are given by

$$\widehat{\Psi}^{\pm}(x, s) = e^{\mp \kappa x} \tag{B.15a}$$

$$y_c^{\pm}(x, s) = y_0. \tag{B.15b}$$

where the propagation number κ is constant over the length of the horn, and y_0 is the complex, frequency-dependent characteristic admittance incorporating thermoviscous losses.

Thus, Equation 3.38 becomes

$$
\begin{bmatrix} \Psi_1 \\ \mathcal{V}_1 \end{bmatrix} = -\frac{1}{2y_0}\begin{bmatrix} e^{-\kappa x_1} & e^{\kappa x_1} \\ y_0 e^{-\kappa x_1} & -y_0 e^{\kappa x_1} \end{bmatrix}\begin{bmatrix} -y_0 e^{\kappa x_2} & -e^{\kappa x_2} \\ -y_0 e^{-\kappa x_2} & e^{-\kappa x_2} \end{bmatrix}\begin{bmatrix} \Psi_2 \\ -\mathcal{V}_2 \end{bmatrix}
$$

$$
= -\frac{1}{2y_0}\begin{bmatrix} -y_0(e^{\kappa L} + e^{-\kappa L}) & -(e^{\kappa L} - e^{-\kappa L}) \\ -y_0^2(e^{\kappa L} - e^{-\kappa L}) & -y_0(e^{\kappa L} + e^{-\kappa L}) \end{bmatrix}\begin{bmatrix} \Psi_2 \\ -\mathcal{V}_2 \end{bmatrix}
$$

$$
= \begin{bmatrix} \cosh(\kappa L) & \frac{1}{y_0}\sinh(\kappa L) \\ y_0\sinh(\kappa L) & \cosh(\kappa L) \end{bmatrix}\begin{bmatrix} \Psi_2 \\ -\mathcal{V}_2 \end{bmatrix}, \tag{B.16}
$$

where the characteristic impedance $z_0 = 1/y_0$ and the tube length $L = x_2 - x_1$. Thus the $ABCD$ parameters for a cylindrical horn are

$$A = \cosh(\kappa L) \tag{B.17a}$$

$$B = z_0\sinh(\kappa L) \tag{B.17b}$$

$$C = \frac{1}{z_0}\sinh(\kappa L) \tag{B.17c}$$

$$D = \cosh(\kappa L). \tag{B.17d}$$

The determinant of this matrix is given by

$$\Delta_T = AD - BC = \cosh^2(\kappa L) - \sinh^2(\kappa L) = 1. \tag{B.18}$$

Therefore, a cylindrical horn is always reciprocal. Because $A = D$, a cylindrical horn is also reversible.

B.2.2   Conical horn

In a conical horn, the normalized forward- and backward-traveling waves and the direction-dependent characteristic admittances are given by

$$\widehat{\Psi}^{\pm}(r, s) = \frac{e^{\mp \kappa r}}{r} \tag{B.19a}$$

$$y_c^{\pm}(r, s) = y_0(r, s)\left(1 \pm \frac{1}{\kappa r}\right), \tag{B.19b}$$

where $\kappa(r, s)$ and $y_0(r, s)$ both vary with diameter over the length of the horn. These equations are exact for a lossless horn, and approximate for a lossy horn. Recall that $y_0(r, s) = \sqrt{\mathcal{Y}/\mathcal{Z}}$ is the characteristic admittance for a uniform horn of $A(r)$. The coordinate r is the radius in spherical coordinates, originating from a point at $r = 0$, as shown in Figure A.8. The horn axis $x = r - r_1$ may be defined as beginning at some initial point $r = r_1$, and ending at $r = r_2 > r_1$ such that the length of the horn $L = r_2 - r_1$.

For convenience, define $y_{0,1} = 1/z_{0,1} = y_0(r_1, s)$ and $y_{0,2} = 1/z_{0,2} = y_0(r_2, s)$. Thus, Equation 3.38 becomes

$$
\begin{aligned}
\begin{bmatrix} \Psi_1 \\ \mathcal{V}_1 \end{bmatrix} &= -\frac{r_2^2}{2y_{0,2}} \frac{1}{r_1 r_2} \begin{bmatrix} e^{-\kappa_1 r_1} & e^{\kappa_1 r_1} \\ y_{c,1}^+ e^{-\kappa_1 r_1} & -y_{c,1}^- e^{\kappa_1 r_1} \end{bmatrix} \begin{bmatrix} -y_{c,2}^- e^{\kappa_2 r_2} & -e^{\kappa_2 r_2} \\ -y_{c,2}^+ e^{-\kappa_2 r_2} & e^{-\kappa_2 r_2} \end{bmatrix} \begin{bmatrix} \Psi_2 \\ -\mathcal{V}_2 \end{bmatrix} \\
&= -\frac{r_2}{r_1} \frac{1}{2y_{0,2}} \begin{bmatrix} (-y_{c,2}^- e^{\Delta_{\kappa r}} - y_{c,2}^+ e^{-\Delta_{\kappa r}}) & -(e^{\Delta_{\kappa r}} - e^{-\Delta_{\kappa r}}) \\ (-y_{c,1}^+ y_{c,2}^- e^{\Delta_{\kappa r}} + y_{c,1}^- y_{c,2}^+ e^{-\Delta_{\kappa r}}) & -(y_{c,1}^+ e^{\Delta_{\kappa r}} + y_{c,1}^- e^{-\Delta_{\kappa r}}) \end{bmatrix} \begin{bmatrix} \Psi_2 \\ -\mathcal{V}_2 \end{bmatrix} \\
&= \begin{bmatrix} A & B \\ C & D \end{bmatrix} \begin{bmatrix} \Psi_2 \\ -\mathcal{V}_2 \end{bmatrix}
\end{aligned}
\tag{B.20a}
$$

$$\Delta_{\kappa r} = \kappa_2 r_2 - \kappa_1 r_1. \tag{B.20b}$$

Simplifying these expressions for the elements $ABCD$ yields

$$A = \frac{r_2}{r_1}\left[\cosh(\Delta_{\kappa r}) - \frac{1}{\kappa r_2}\sinh(\Delta_{\kappa r})\right] \tag{B.21a}$$

$$B = \frac{r_2}{r_1}\left(z_{0,2}\right)\sinh(\Delta_{\kappa r}) \tag{B.21b}$$

$$C = \frac{r_2}{r_1}\left(\frac{1}{z_{0,1}}\right)\left[\left(\frac{1}{\kappa r_1} - \frac{1}{\kappa r_2}\right)\cosh(\Delta_{\kappa r}) + \left(1 - \frac{1}{(\kappa r_1)(\kappa r_2)}\right)\sinh(\Delta_{\kappa r})\right] \tag{B.21c}$$

$$D = \frac{r_2}{r_1}\left(\frac{z_{0,2}}{z_{0,1}}\right)\left[\cosh(\Delta_{\kappa r}) + \frac{1}{\kappa r_1}\sinh(\Delta_{\kappa r})\right]. \tag{B.21d}$$

Note that this result is different from that of Mapes-Riordan (1993), which gives the horn transmission matrix parameters in terms of $z_{0,1}$ only, by making an incorrect substitution

$$\frac{z_{0,2}}{z_{0,1}} \neq \frac{r_1^2}{r_2^2} \quad \text{(lossy case)}, \tag{B.22}$$

which is not generally true in the presence of viscous and thermal losses. It is only true in the lossless case, when $z_0 = r_0 = \rho_0 c_0/A_0$ for a given area A_0.

It is also extremely important to note that this model applies to a lossy conical segment of any length. In the literature, misinformation about the lossy cone model has been propagated by use of the lossless model, where $\kappa = \kappa_1 = \kappa_2$ is constant throughout the cone. Historically, it has been considered necessary to break the lossy cone into many small subsections over which the diameter is assumed to be slowly varying, because the lossy propagation factor $\kappa(s) \neq s/c_0$ varies with diameter (Mapes-Riordan, 1993). However, this is simply not necessary, as the application of the boundary conditions during the derivation leads to a closed-form expression in terms of κ_1 and κ_2. Therefore, the lossy cone models published by both Mapes-Riordan (1993) and Kulik (2007) are incorrect.[2]

The determinant of the cone transmission matrix is given by

$$\Delta_T = AD - BC = \frac{z_{0,2}}{z_{0,1}}\frac{r_2^2}{r_1^2}, \tag{B.23}$$

which is equal to 1 only in the case of lossless propagation. Therefore, the lossless conical horn model is reciprocal but not reversible, and the lossy conical horn model is neither reciprocal nor reversible. Note that since the pressure functions used to analyze the lossy horn are approximations, this result does not prove that the lossy conical horn is not reciprocal, only that the model is. To

---

[2]Kulik (2007) attempted to derive an exact model for the lossy conical horn, beginning with the incorrect assumption that $\Delta_{\kappa r} = \kappa(r,s)L$. Using trigonometric identities, he found that $\Delta_{\kappa r} = \int_{r_1}^{r_2} \kappa(r,s)dr$, which is incorrect.

model the transformation from the large end to the small end, the transmission matrix is given by

$$
\begin{bmatrix} A' & B' \\ C' & D' \end{bmatrix} = \frac{1}{AD - BC} \begin{bmatrix} D & B \\ C & A \end{bmatrix}.
\tag{B.24}
$$

Considering Figure A.8, the axial coordinates r_1 and r_2 can be related to the planar diameters d_1 and d_2 at the ends of the conical horn. This is done using the relationship

$$
\sin(\theta_0) = \frac{d_1}{2r_1} = \frac{d_2}{2r_2}
\tag{B.25}
$$

which yields the equations

$$
r_1 = \frac{d_1 L}{d_2 - d_1}
\tag{B.26a}
$$

$$
r_2 = \frac{d_2 L}{d_2 - d_1}.
\tag{B.26b}
$$

Therefore, the ratio $r_2/r_1 = d_2/d_1$. For modeling, it is useful to cast these equations in terms of the planar diameters and their difference, $\Delta d = d_2 - d_1$. The $ABCD$ parameters become

$$
A = \frac{d_2}{d_1} \left[\cosh(\Delta_{\kappa d}) - \frac{\Delta d}{\kappa_2 d_2 L} \sinh(\Delta_{\kappa d}) \right]
\tag{B.27a}
$$

$$
B = \frac{d_2}{d_1} \left(z_{0,2} \right) \sinh(\Delta_{\kappa d})
\tag{B.27b}
$$

$$
C = \frac{d_2}{d_1} \left(\frac{1}{z_{0,1}} \right) \left[\frac{\Delta d}{L} \left(\frac{1}{\kappa_1 d_1} - \frac{1}{\kappa_2 d_2} \right) \cosh(\Delta_{\kappa d}) + \left(1 - \left(\frac{(\Delta d)}{L} \right)^2 \frac{1}{(\kappa_1 d_1)(\kappa_2 d_2)} \right) \sinh(\Delta_{\kappa d}) \right]
\tag{B.27c}
$$

$$
D = \frac{d_2}{d_1} \left(\frac{z_{0,2}}{z_{0,1}} \right) \left[\cosh(\Delta_{\kappa d}) + \frac{\Delta d}{\kappa_1 d_1 L} \sinh(\Delta_{\kappa d}) \right]
\tag{B.27d}
$$

$$
\Delta_{\kappa d} = \frac{L}{\Delta d} (\kappa_2 d_2 - \kappa_1 d_1).
\tag{B.27e}
$$

If $d_2 = d_1$, then $\Delta d = 0$, $\kappa_2 = \kappa_1 = \kappa$ and $\Delta_{\kappa d} = \kappa L$; in this case, the transmission matrix is equal to that of the uniform cylinder as expected. Additionally, in the limit as $L \to 0$, these parameters are well-behaved. For $\Delta_{\kappa d} \to 0$,

$$
\cosh(\Delta_{\kappa d}) \approx 1 + \frac{\Delta_{\kappa d}^2}{2} + \dots
\tag{B.28a}
$$

$$
\sinh(\Delta_{\kappa d}) \approx \Delta_{\kappa d} + \frac{\Delta_{\kappa d}^3}{6} + \dots,
\tag{B.28b}
$$

160

which leads to the well-behaved limits

$$A|_{L \to 0} = \kappa_1/\kappa_2 \tag{B.29a}$$

$$B|_{L \to 0} = 0 \tag{B.29b}$$

$$C|_{L \to 0} = 0 \tag{B.29c}$$

$$D|_{L \to 0} = \frac{z_{0,2}}{z_{0,1}} \frac{d_2^2}{d_1^2}, \tag{B.29d}$$

$$\Delta_{\kappa d}|_{L \to 0} = 0. \tag{B.29e}$$

For a lossless horn, the $ABCD$ matrix becomes the identity matrix, as $L \to 0$.

Due to the curvature of the wavefronts in the conical horn (e.g. Fig. A.8), special care must be given to calculations involving the wavefront area. The characteristic impedance $z_0(r, s)$ and propagation function $\kappa(r, s)$ should be calculated according to Equation A.44a, where the area is related to the planar diameter d by

$$A(d) = 2\pi \left(\frac{L}{\Delta d}\right)^2 \left[1 - \sqrt{1 - \left(\frac{\Delta d}{2L}\right)^2}\right] d^2, \tag{B.30}$$

where $\Delta d = d_2 - d_1$ as before. The perimeter function is defined by the planar diameter as

$$\Pi(d) = \pi d. \tag{B.31}$$

Finally, it should be noted that the length from the input plane to the output plane, L_0, is different from the length $L = r_2 - r_1$ between the curved wavefronts. These lengths are related by

$$L_0 = L \cos \theta_0 = L \sqrt{1 - \left(\frac{\Delta d}{2L}\right)^2}$$

$$L = \sqrt{L_0^2 + \left(\frac{\Delta d}{2}\right)^2}. \tag{B.32}$$

B.2.3   Step discontinuity

Karal (1953) modeled the impedance of a step discontinuity between two axially symmetric cylindrical horns of diameter d_1 and d_2, for $d_1 < d_2$. As for all of the two-port models presented in this section, this model applies to plane-wave propagation. Therefore, the wavelength of sound must be much larger than either diameter.

To maintain consistent notation, Ψ_1 and Ψ_2 are defined to be the plane-wave (0th-order) model. Here, $\Psi_{1,tot}$ and $\Psi_{2,tot}$ are used to indicate the total pressure across all modes. In general at a

junction, the pressure is assumed to be equal on both sides

$$\Psi_{1,tot} = \Psi_{2,tot}.$$

However, in the case of a step discontinuity, the higher-order modes that arise due to the spreading of the wave from the smaller tube to the larger tube should not necessarily be neglected. Thus Karal (1953) breaks the pressure into the plane-wave mode and the higher-order modes,

$$\Psi_1 + \Psi_{1,1...N} = \Psi_2 + \Psi_{2,1...N}. \tag{B.33}$$

It cannot be assumed that $\Psi_1 \neq \Psi_2$. Rather, some of the pressure is transferred between the plane-wave and higher-order modes at the discontinuity.

For frequencies and radii within the purview of this thesis, these higher-order modes are typically evanescent and decay within a few millimeters. Thus, the higher-order modes do not contribute to the axial flow of the volume velocity. Therefore, the plane-wave modes may be related by a series impedance,

$$\Psi_1 = \Psi_2 + Z\mathcal{V} \tag{B.34a}$$

$$\mathcal{V}_1 = \mathcal{V}_2. \tag{B.34b}$$

Karal (1953) finds this impedance to be an inductance,

$$Z = sL$$

$$L \approx \frac{8\rho_0}{3\pi^2 d_1} H(\alpha), \tag{B.35}$$

where $\alpha = d_1/d_2$ is the ratio of the diameters (which must fall between 0 and 1). Note that Karal's approximation of L leaves out a frequency-dependent term, and he does not justify the elimination of this term in his paper. Karal defines the function $H(\alpha)$ as

$$H(\alpha) = \frac{3\pi}{2} \sum_{n=1}^{\infty} \frac{J_1^2(\alpha x_n)}{\alpha x_n^3 J_0^2(x_n)}, \tag{B.36}$$

where x_n are the roots of the Bessel function $J_1(x_m) = 0$. The function $H(\alpha)$ will be considered in detail next.

The $ABCD$ matrix for this series inductance is given by

$$A = 1 \tag{B.37a}$$

$$B = sL \tag{B.37b}$$

$$C = 0 \tag{B.37c}$$

162

$$D = 1. \tag{B.37d}$$

The determinant of this matrix is

$$\Delta_T = AD - BC = 1. \tag{B.38}$$

Therefore, the Karal correction is reciprocal. Additionally, because $A = D$, the Karal correction is reversible.
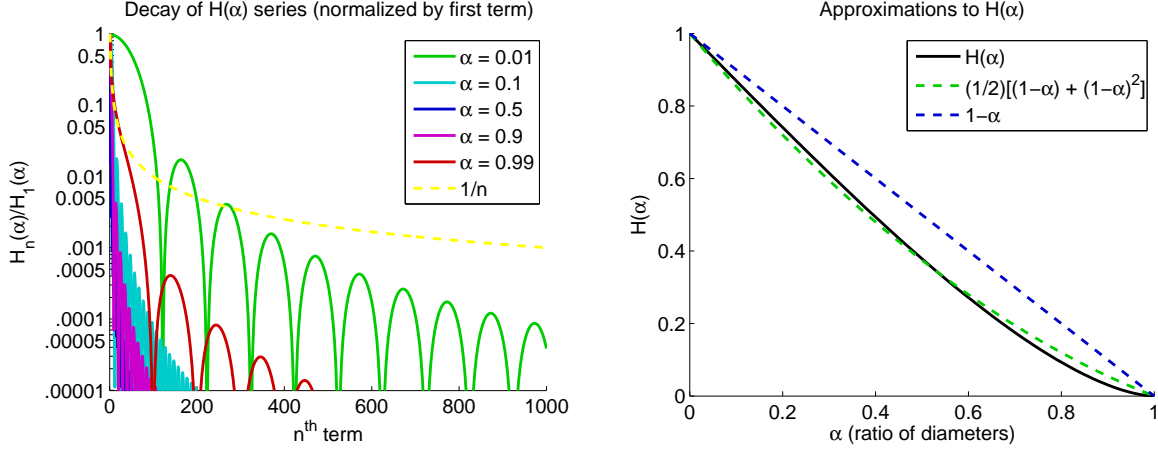
Figure B.2: Examining the series of $H(\alpha)$ from Equation B.35. The left plot shows the decay of the series terms, normalized by the $n = 1$ term. These terms are compared to the harmonic series $1/n$ to show that the series converges. The right plot shows $H(\alpha)$ (calculated using 1000 terms) and some common approximations to this function.

The terms of the sum $H(\alpha)$ are shown in the left plot of Figure B.2. The first 1000 terms of the series are plotted, normalized by the $n = 1$ term. These terms are compared to the harmonic series $1/n$ to show that the series converges. The series converges fastest for α values that are not extrema (e.g. close to 0 or 1). Indeed, for most calculations 50 terms will be sufficient.

The right plot shows $H(\alpha)$ (calculated using 1000 terms) and some common approximations to this function. The simplest approximation is given by

$$H(\alpha) \approx 1 - \alpha. \tag{B.39}$$

This approximation was used by Sondhi (1983) and is given in Puria (1991). A higher-order approximation is given by

$$H(\alpha) \approx \frac{1}{2}\left[(1 - \alpha) + (1 - \alpha)^2\right]. \tag{B.40}$$

This approximation[3] better fits the curvature of $H(\alpha)$. Of course, using modern computing, it is simple enough to save the function $H(\alpha)$ that has been calculated using the 1000-term series. When a particular value of α is specified, $H(\alpha)$ may be interpolated from the saved function.

---

[3]Given by Jont Allen (informal communication).

Some authors have found Karal's $H(\alpha)$ expression for the inductor to be an insufficient model for describing wave spreading from a small orifice, such as an in-the-ear probe with small central loudspeaker outlet (e.g. (Rasetshwane & Neely, 2015)).[4] This is not entirely surprising, as Karal (1953) drops an additional frequency-dependent term describing this inductor (in his Eq. 50) without any justification. Puria (1991) evaluated the Karal correction using a rigidly terminated cascade of 2-3 cylinders of varying area. He found that the Karal correction improves the reflectance model phase when included between the cylindrical models. He found that, in the case of a constriction (the middle tube having the smallest diameter), the Karal model alone did not adequately predict the cavity loss, as quantified by the magnitude reflectance. Note that Puria (1991) did not attempt to model this loss.

Rasetshwane & Neely (2015) use a two-cone model to account for the impedance of a step discontinuity. This model was fitted using an error-minimization algorithm, rather than a predetermined model based on the size of the discontinuity. It should be noted that the two-port parameters of the conical horn have a very different form form a series inductor. Benade (1988) indicates that the cone may be described by an initial shunt inductor, followed by a uniform transmission line accounting for delay, a transformer, and a second shunt inductor. The presence of a shunt branch indicates that the volume velocity is altered by the area change. Karal assumed that the area change does not affect the volume velocity, which may be an invalid assumption (particularly if there are viscous and thermal losses due the wall of the jump discontinuity).

Figures B.3 and B.4 compare Karal's model for a step discontinuity with the conical horn model. Both models are calculated for zero-length (just the step discontinuity) and for a tube or cone length of one radius away from the discontinuity. This is approximately the distance over which higher-order modes associated with the step discontinuity decay enough that they are negligible. The zero-length conical model is calculated by setting the length to `eps` (the smallest number) in Matlab. The step discontinuity is chosen to mimic the geometry of a measurement probe such as the ER10C; the step in diameter is taken to be 1 [mm] to 7.5 [mm].

Figure B.3 gives the $ABCD$ parameter magnitudes for the configurations described. The black solid lines show the Karal model, while the black dashed lines show a cone of length L= `eps` = 2.2204^{-16} [m]. The remaining four models have a physical length of 3.75 [mm]. The light blue line shows a tube model of this length for comparison. The blue solid and dashed lines show this tube preceded by the Karal inductor or zero-length cone, respectively. Finally, the red curve shows the model for a 3.75 [mm] cone connecting these diameters. Note that C is very small for all models, while A and D are on the order of 1, at least for low- to mid-frequencies. While the magnitude of B varies, it increases approximately linearly with frequency for all models, not just the Karal inductor alone.

Thus, these models are all very similar to each other, and to a uniform tube of some length. This is expected, as the Karal inductor is intended to add acoustic length due to the spreading

_____
[4]Historically, Mimosa Acoustics tried to use this correction to improve the calibration, but it did not seem to improve the Thévenin model.

inertance. In fact, for very small κL the $ABCD$ model of a tube is approximately

$$A = 1 \tag{B.41a}$$

$$B = z_0 \kappa L \tag{B.41b}$$

$$C = \frac{1}{z_0} \kappa L \tag{B.41c}$$

$$D = 1, \tag{B.41d}$$

where C will be much smaller than 1, since z_0 is usually quite large (for a 1 [mm] diameter, $\rho_0 c_0 / A_0 = 5.2 \times 10^8$, and for a 7.5 [mm] diameter, $\rho_0 c_0 / A_0 = 9.3 \times 10^6$). Note that $\kappa \approx s/c$ for 'large' diameters (e.g. Fig. A.1), so $B \propto s$. If more losses are present in the system, other powers of s (e.g. $\sqrt{s}$) will contribute more to B.

Consider Figure B.4. Note that the Karal model alone does not have an impedance matrix, because $C = 0$. The top-left plot shows the input impedance of these models given a 'blocked' termination condition. This plot indicates the effective length of each model, as the null frequency decreases with increasing acoustic length. It is apparent that a zero-length cone is acoustically longer than the Karal model. Therefore, if the Karal model is inadequate due to its effective length, cone models offer an increase in this length.
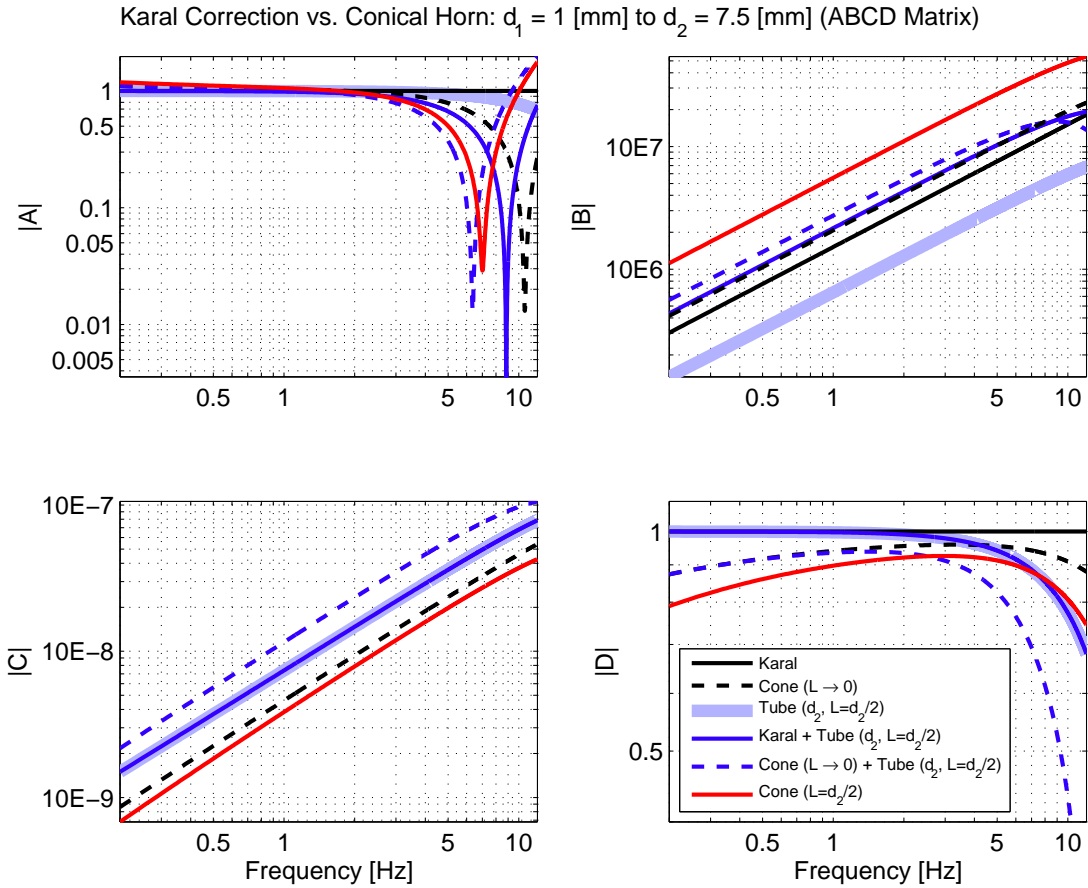
Figure B.3: Two-port matrix parameter magnitudes using different models for a step discontinuity of 1 [mm] to 7.5 [mm]. The black solid lines show the Karal model, while the black dashed lines show a cone of infinitesimal length (L= eps = 2.2204^{-16} [m]). The remaining four models have a physical length of 3.75 [mm]. The light blue line shows a tube model of this length for comparison. The blue solid and dashed lines show a tube of this length preceded by the Karal inductor or zero-length cone, respectively. Finally, the red curve shows the model for a 3.75 [mm] cone connecting these diameters.
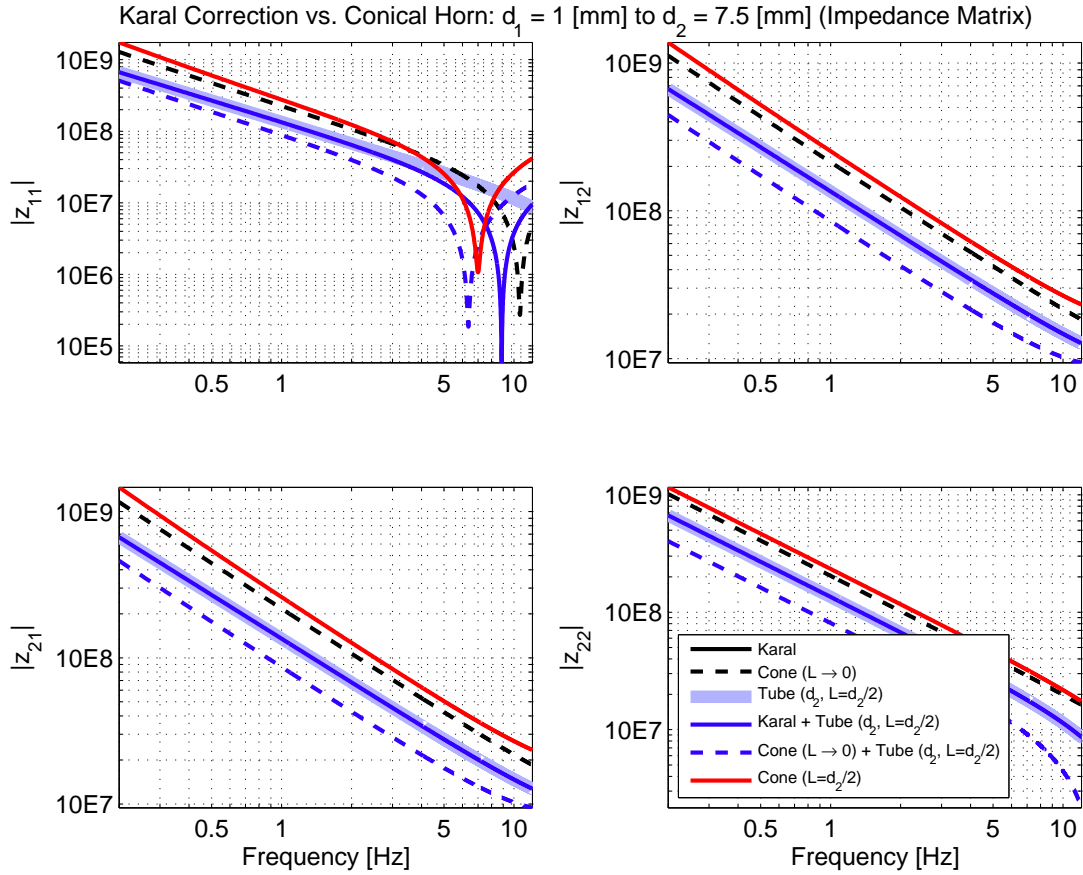
Figure B.4: Two-port matrix parameter magnitudes using different models for a step discontinuity of 1 [mm] to 7.5 [mm]. All elements of the impedance matrix for the Karal inductor (solid black, not shown) will be infinite, since its $ABCD$ matrix has C=0. The black dashed lines show a cone of infinitesimal length (L= $\texttt{eps}$ = 2.2204^{-16} [m]). The remaining four models have a physical length of 3.75 [mm]. The light blue line shows a tube model of this length for comparison. The blue solid and dashed lines show a tube of this length preceded by the Karal inductor or zero-length cone, respectively. Finally, the red curve shows the model for a 3.75 [mm] cone connecting these diameters.

B.3 Experimental determination of two-port parameters

The two-part parameters (e.g. the transmission or impedance matrix) of an unknown system may be experimentally measured in a number of ways. When measurements of the input or load impedance are available, deriving the two-port parameters becomes relatively simple. Other methods using 3-4 microphones (with and without calibrations) are described by Rodriguez et al. (2011) and previous works cited in that paper. In this thesis, two-port parameters are experimentally determined for cases where the input impedance may be measured, using a Thévenin-calibrated source.

B.3.1 Reciprocal networks

Reciprocal networks have the related properties

$$\Delta_T = 1 \quad \text{and} \quad z_{12} = z_{21}. \tag{B.42}$$

This can be seen by considering

$$\begin{bmatrix} A & B \\ C & D \end{bmatrix} = \frac{1}{z_{21}} \begin{bmatrix} z_{11} & \Delta_Z \\ 1 & z_{22} \end{bmatrix}, \tag{B.43}$$

where the determinant is given by

$$\begin{aligned}
\Delta_T &= \frac{z_{11}z_{22}}{z_{21}^2} - \frac{\Delta_Z}{z_{21}^2} \\
&= \frac{z_{11}z_{22}}{z_{21}^2} - \frac{(z_{11}z_{22} - z_{12}z_{21})}{z_{21}^2} \\
&= \frac{z_{12}z_{21}}{z_{21}^2}, \tag{B.44}
\end{aligned}$$

which is equal to 1 when $z_{12} = z_{21}$.

A reciprocal network may be characterized using three input impedance measurements Z_{in}, and three known load impedances Z_L. The load impedances may be measured or modeled, as needed. Define

$$\mathcal{T}_{SQ} = z_{12}z_{21} = z_{12}^2, \tag{B.45}$$

where both z_{12} and z_{21} are equal to the positive square root of $\mathcal{T}_{SQ}$. This gives three equations $k = 1, 2, 3$ in three unknowns,

$$Z_{kin} = z_{11} - \frac{\mathcal{T}_{SQ}}{z_{22} + Z_{kL}}. \tag{B.46}$$

Using a computational tool such as the `symbolic` package in Matlab or Octave, this gives the

unique solutions (e.g. Ramo et al. (2008))

$$z_{11} = \frac{Z_{1L}Z_{1in}Z_{2in} - Z_{1L}Z_{1in}Z_{3in} - Z_{1in}Z_{2L}Z_{2in} + Z_{1in}Z_{3L}Z_{3in} + Z_{2L}Z_{2in}Z_{3in} - Z_{2in}Z_{3L}Z_{3in}}{Z_{1L}Z_{2in} - Z_{1L}Z_{3in} - Z_{1in}Z_{2L} + Z_{1in}Z_{3L} + Z_{2L}Z_{3in} - Z_{2in}Z_{3L}}$$
(B.47a)

$$z_{22} = \frac{Z_{1L}Z_{1in}Z_{2L} - Z_{1L}Z_{1in}Z_{3L} - Z_{1L}Z_{2L}Z_{2in} + Z_{1L}Z_{3L}Z_{3in} + Z_{2L}Z_{2in}Z_{3L} - Z_{2L}Z_{3L}Z_{3in}}{Z_{1L}Z_{2in} - Z_{1L}Z_{3in} - Z_{1in}Z_{2L} + Z_{1in}Z_{3L} + Z_{2L}Z_{3in} - Z_{2in}Z_{3L}}$$
(B.47b)

$$\mathcal{T}_{SQ} = \frac{(Z_{1L} - Z_{2L})(Z_{1L} - Z_{3L})(Z_{1in} - Z_{2in})(Z_{1in} - Z_{3in})(Z_{2L} - Z_{3L})(Z_{2in} - Z_{3in})}{(Z_{1L}Z_{2in} - Z_{1L}Z_{3in} - Z_{1in}Z_{2L} + Z_{1in}Z_{3L} + Z_{2L}Z_{3in} - Z_{2in}Z_{3L})^2}$$
(B.47c)

$$z_{12} = \sqrt{\mathcal{T}_{SQ}}$$
(B.47d)

$$z_{21} = \sqrt{\mathcal{T}_{SQ}}.$$
(B.47e)

Some examples of reciprocal acoustic networks include lossless cylindrical and conical horns. When visco-thermal losses are present, cylindrical horns are reciprocal, but conical horns are not, as shown in Section B.2.2.

B.3.2   Anti-reciprocal networks

Anti-reciprocal networks have the related properties

$$\Delta_T = -1 \quad \text{and} \quad z_{12} = -z_{21}.$$
(B.48)

In this case, the quantity $\mathcal{T}_{SQ}$ becomes

$$\mathcal{T}_{SQ} = z_{12}z_{21} = -z_{12}^2.$$
(B.49)

The solutions for z_{11}, z_{22} and $\mathcal{T}_{SQ}$ are the same as the reciprocal case, and the off-diagonal impedance matrix terms are given by

$$z_{12} = -\sqrt{-\mathcal{T}_{SQ}}$$
(B.50a)

$$z_{21} = \sqrt{-\mathcal{T}_{SQ}}.$$
(B.50b)

B.3.3   Non-reciprocal networks

Because of the algebraic relationship $\mathcal{T}_{SQ} = z_{12}z_{21}$, it is not possible to determine the individual parameters z_{12} and z_{21} using a fourth set of input and load impedances (Z_{4in}, Z_{4L}). One solution to this problem is to measure the force transfer function with a known load impedance Z_{L4}. From

the transmission matrix, the load-dependent transfer function H is given by

$$\frac{\text{Force}_2}{\text{Force}_1} = \frac{1}{A + \frac{B}{Z_L}} = H. \tag{B.51}$$

Given a fourth known load Z_{4L} and the force transfer function H_4, it can be shown that

$$z_{21} = H_4 \left(z_{11} + \frac{z_{11} z_{22} - \mathcal{T}_{SQ}}{Z_{4L}} \right). \tag{B.52}$$

Once z_{21} is identified, it is easy to solve for $z_{12} = \mathcal{T}_{SQ}/z_{21}$.

Using three pairs of input and load impedance measurements, the final solutions for z_{12} and z_{21} become

$$z_{12} = \frac{Z_{4L} \left(Z_{1L} - Z_{2L} \right) \left(Z_{1L} - Z_{3L} \right) \left(Z_{1in} - Z_{2in} \right) \left(Z_{1in} - Z_{3in} \right) \left(Z_{2L} - Z_{3L} \right) \left(Z_{2in} - Z_{3in} \right)}{H_4 \mathcal{F} \left(Z_{1L} Z_{2in} - Z_{1L} Z_{3in} - Z_{1in} Z_{2L} + Z_{1in} Z_{3L} + Z_{2L} Z_{3in} - Z_{2in} Z_{3L} \right)} \tag{B.53a}$$

$$z_{21} = \frac{H_4 \mathcal{F}}{Z_{4L} \left(Z_{1L} Z_{2in} - Z_{1L} Z_{3in} - Z_{1in} Z_{2L} + Z_{1in} Z_{3L} + Z_{2L} Z_{3in} - Z_{2in} Z_{3L} \right)} \tag{B.53b}$$

$$\begin{aligned}
\mathcal{F} = &\; Z_{1L} Z_{1in} Z_{2L} Z_{3in} - Z_{1L} Z_{1in} Z_{2in} Z_{3L} + Z_{1L} Z_{1in} Z_{2in} Z_{4L} - Z_{1L} Z_{1in} Z_{3in} Z_{4L} \\
&- Z_{1L} Z_{2L} Z_{2in} Z_{3in} + Z_{1L} Z_{2in} Z_{3L} Z_{3in} + Z_{1in} Z_{2L} Z_{2in} Z_{3L} - Z_{1in} Z_{2L} Z_{2in} Z_{4L} \\
&- Z_{1in} Z_{2L} Z_{3L} Z_{3in} + Z_{1in} Z_{3L} Z_{3in} Z_{4L} + Z_{2L} Z_{2in} Z_{3in} Z_{4L} - Z_{2in} Z_{3L} Z_{3in} Z_{4L}. \tag{B.53c}
\end{aligned}$$

B.4 Application to Thévenin source parameters

The Thévenin equivalent circuit for a network is given by a 'force' source (e.g. voltage or pressure) and a series impedance. The equivalent force is equal to the force across the output terminals in the 'open circuit' (zero flow) condition. The equivalent impedance is equal to the impedance across the output terminals when all 'force' sources are replaced by short circuits. Such conditions may be easily enforced on two-port network models.

This section shows how the Thévenin equivalent parameters are related to loudspeaker model parameters. Additionally, modified Thévenin parameters are calculated for a Thévenin source cascaded with a known two-port network.

B.4.1 Source parameters for a loudspeaker

A classic example of an anti-reciprocal network is a loudspeaker, which converts an electrical signal to mechanical movement of a diaphragm, using a magnetic field and wire coil. Hunt (1954) models

the loudspeaker using a gyrator, as

$$
\begin{bmatrix} V_1 \\ I_1 \end{bmatrix} = \begin{bmatrix} A & B \\ C & D \end{bmatrix} \begin{bmatrix} F_2 \\ -U_2 \end{bmatrix}
$$

$$
\begin{bmatrix} V_1 \\ I_1 \end{bmatrix} = \begin{bmatrix} 1 & Z_e \\ 0 & 1 \end{bmatrix} \begin{bmatrix} 0 & T_0 \\ \frac{1}{T_0} & 0 \end{bmatrix} \begin{bmatrix} 1 & Z_m \\ 0 & 1 \end{bmatrix} \begin{bmatrix} F_2 \\ -U_2 \end{bmatrix}, \tag{B.54}
$$

where the signals are input voltage (V_1), input current (I_1), output force (F_2), and output mechanical velocity (U_2). The electrical impedance ($Z_e = V_1/I_1$) and mechanical impedance ($Z_m = -F_2/U_2$) are series elements on either side of the gyrator. The parameter $T_0 = B_0 l$ is a function of the coil length and magnetic field strength. This model has the impedance matrix

$$
\begin{bmatrix} V_1 \\ F_2 \end{bmatrix} = \begin{bmatrix} Z_e & -T_0 \\ T_0 & Z_m \end{bmatrix} \begin{bmatrix} I_1 \\ U_2 \end{bmatrix}, \tag{B.55}
$$

which shows that the loudspeaker model is anti-reciprocal, since $z_{21} = T_0 = -z_{12}$. The transmission matrix is given by

$$
\begin{bmatrix} V_1 \\ I_1 \end{bmatrix} = \frac{1}{T_0} \begin{bmatrix} Z_e & (Z_e Z_m + T_0^2) \\ 1 & Z_m \end{bmatrix} \begin{bmatrix} F_2 \\ -U_2 \end{bmatrix}. \tag{B.56}
$$

For a simple, ideal diaphragm of area A_0 moving with velocity U_2, the acoustic volume velocity is given by $\mathcal{V}_2 = U_2 A_0$. The conversion between mechanical and acoustical variables may be represented by a transformer, such that

$$
\begin{bmatrix} V_1 \\ I_1 \end{bmatrix} = \frac{1}{T_0} \begin{bmatrix} Z_e & (Z_e Z_m + T_0^2) \\ 1 & Z_m \end{bmatrix} \begin{bmatrix} \frac{1}{A_0} & 0 \\ 0 & A_0 \end{bmatrix} \begin{bmatrix} \Psi_2 \\ -\mathcal{V}_2 \end{bmatrix}. \tag{B.57}
$$

The Thévenin parameters for an arbitrary $ABCD$ matrix are given by

$$
\text{Force}_s = \text{Force}_2 \Big|_{\text{Flow}_2 = 0} = \frac{V_1}{A} \tag{B.58a}
$$

$$
Z_s = -\frac{\text{Force}_2}{\text{Flow}_2} \Big|_{V_1 = 0} = \frac{B}{A}. \tag{B.58b}
$$

Therefore, the mechanical (F_s, $Z_{s,m}$) and acoustical (Ψ_s, $Z_{s,a}$) source parameters are given in terms of the 'Hunt parameters' (Z_e, Z_m, T_0) by

$$
F_s = \frac{V_1 T_0}{Z_e} \qquad\qquad \Psi_s = F_s A_0 \tag{B.59a}
$$

$$
Z_{s,m} = \frac{(Z_e Z_m + T_0^2)}{Z_e} \qquad\qquad Z_{s,a} = Z_{s,m} A_0^2. \tag{B.59b}
$$

Note that the Norton equivalent source flow is given by $\text{Flow}_s = \text{Force}_s / Z_s$.

A loudspeaker with acoustic delay. If there is an acoustic system between the diaphragm and the measured load, the relationship between the Thévenin parameters (Force$_s$, Z_s) and the electro-mechanical parameters of the loudspeaker (Z_e, Z_m, T_0) becomes more complicated. In this case, the two-port matrix equation becomes

$$\begin{bmatrix} V_1 \\ I_1 \end{bmatrix} = \frac{1}{T_0} \begin{bmatrix} Z_e & (Z_e Z_m + T_0^2) \\ 1 & Z_m \end{bmatrix} \begin{bmatrix} \frac{1}{A_0} & 0 \\ 0 & A_0 \end{bmatrix} \begin{bmatrix} A & B \\ C & D \end{bmatrix} \begin{bmatrix} \Psi_2 \\ -\mathcal{V}_2 \end{bmatrix}, \tag{B.60}$$

where the parameters $ABCD$ characterize an acoustic transmission line, which may be of varying area.

An example of this is a hearing-aid loudspeaker such as the magnetic balanced-armature receiver modeled by Kim & Allen (2013). In this case, the loudspeaker diaphragm is housed in a rectangular box with a short cylindrical port. Kim & Allen (2013) model this acoustic portion as a shunt compliance representing the volume of the box housing the diaphragm, and a uniform tube transmission line representing the port.

B.4.2 Revised calibration including a known two-port network

Consider the case where a known two-port network ($ABCD$) is added to a Thévenin-calibrated system. An example of this is adding a variable-area probe tip to the Thévenin-calibrated probe developed in Chapter 4. In this case, the system may be represented via the matrix equation

$$\begin{bmatrix} \text{Force}_1 \\ \text{Flow}_1 \end{bmatrix} = \begin{bmatrix} A' & B' \\ C' & D' \end{bmatrix} \begin{bmatrix} \text{Force}_2 \\ -\text{Flow}_2 \end{bmatrix}$$

$$\begin{bmatrix} \text{Force}_s \\ \text{Flow}_s \end{bmatrix} = \begin{bmatrix} 1 & Z_s \\ 0 & 1 \end{bmatrix} \begin{bmatrix} A & B \\ C & D \end{bmatrix} \begin{bmatrix} \text{Force}_2 \\ -\text{Flow}_2 \end{bmatrix}. \tag{B.61}$$

The modified source parameters are given by

$$\text{Force}'_s = \frac{\text{Force}_s}{A'} = \frac{\text{Force}_s}{A + Z_s C} \tag{B.62a}$$

$$Z'_s = \frac{B'}{A'} = \frac{B + Z_s D}{A + Z_s C}, \tag{B.62b}$$

where $ABCD$ are the two-port parameters of the known network between the original point of calibration and the measurement load.

This calculation could be used to analyze pressure measurements made with a microphone placed at the output of the known two-port network. For measurements made at the original point of Thévenin calibration, load impedance calculations will be identical to Equation B.5b.

172

APPENDIX C

POLE-ZERO FITTING

This appendix appeared in Robinson (2013), and is repeated here for convenience. A vector fitting procedure developed by Gustavsen & Semlyen (1999) is used to fit complex, frequency domain data to a function of the form shown in Equation 3.88. The vector fitting procedure is an iterative two step process, which converts a nonlinear least squares problem to a linear least squares problem by introducing an unknown scaling function Θ, having known poles. Let the iteration index of the algorithm be denoted by m=1,2,...,M. Note that the pole order of the algorithm is fixed; if some error criterion is not met, the algorithm may be re-run with a greater number of poles N_p. On each iteration, a least squares problem is solved based on the following equations:

$$H_m(s) = \sum_{i=1}^{N_p} \frac{c_{i,m}}{s - a_{i,m-1}} + d_m + e_m s \tag{C.1a}$$

$$\Theta_m(s) = \sum_{i=1}^{N_p} \frac{b_{i,m}}{s - a_{i,m-1}} + 1. \tag{C.1b}$$

These equations are linear in their unknowns $c_{i,m}$, d_m, e_m, and $b_{i,m}$. Both $\Theta_m(s)$ and $H_m(s)$ share the same known poles $a_{i,m-1}$, which have either been determined in the previous iteration or initialized by the user. It is important that $\Theta_m(s)$ and $H_m(s)$ have the same poles because the poles algebraically cancel when a ratio of the functions is taken in a later step of the algorithm (Eq. C.3). The algorithm iterates to converge on the unknown poles $A_i = a_{i,M}$ of the fit $\hat{F}(s) = F_M(s)$ (which are a nonlinear unknown in Eq. 3.88). The initial poles $a_{i,0}$ are the 'starting poles' of the algorithm; their selection will be described below.

The vector fitting method relates Equations C.1a and C.1b to the measured data $F(\omega_k)$ at a given frequency index k via

$$\Theta_m(s)\Big|_{s=j\omega_k} F(\omega_k) = H_m(s)\Big|_{s=j\omega_k}. \tag{C.2}$$

When evaluated over the many available frequency points of $F(\omega)$, Equation C.2 results in an over-determined linear problem in the unknowns $c_{i,m}$, d_m, e_m, and $b_{i,m}$. At each algorithm step, the current fit is given by

$$F_m(s) = \frac{H_m(s)}{\Theta_m(s)} \tag{C.3}$$

using the estimated values of $c_{i,m}$, d_m, e_m, and $b_{i,m}$. This fit is related to the data via

$$F(\omega) \approx F_m(s)\Big|_{s=j\omega} \qquad \text{(C.4)}$$

and should improve with iteration.

Because $H_m(s)$ and $\Theta_m(s)$ share the same poles, by construction there is a perfect cancellation in Equation C.3. Thus, upon iteration, the zeros of $\Theta_m(s)$ become the poles of $F_m(s)$. To see this, consider the product forms of Equations C.1a and C.1b for a non-zero e_m,

$$H_m(s) = \frac{e_m \prod_{i=1}^{N_p+1}(s - z_{i,m})}{\prod_{i=1}^{N_p}(s - a_{i,m-1})} \qquad \text{(C.5a)}$$

$$\Theta_m(s) = \frac{\prod_{i=1}^{N_p}(s - a_{i,m})}{\prod_{i=1}^{N_p}(s - a_{i,m-1})}, \qquad \text{(C.5b)}$$

where $z_{i,m}$ are the zeros of $H_m(s)$, $a_{i,m}$ are the zeros of $\Theta_m(s)$, and $a_{i,m-1}$ are the known poles of both functions. Substituting Equations C.5a and C.5b for Equation C.3 yields

$$F_m(s) = \frac{H_m(s)}{\Theta_m(s)} = \frac{e_m \prod_{i=1}^{N_p+1}(s - z_{i,m})}{\prod_{i=1}^{N_p}(s - a_{i,m})}. \qquad \text{(C.6)}$$

Thus, on each iteration the zeros of the scaling function $\Theta_m(s)$ become the poles of the fitted function $F_m(s)$. On the last iteration, the poles $a_{i,M}$ become the poles of $F_M(s) = \hat{F}(s)$ (Eq. 3.88) such that $A_i = a_{i,M}$. Gustavsen & Semlyen found that it is better to calculate the remaining quantities C_i, D, and E via the least squares procedure outlined by Equation C.2, using $a_{i,M}$ as the starting poles. Thus, the final quantities $C_i = c_{i,M+1}$, $D = d_{M+1}$, and $E = e_{M+1}$ are the result of a partial iteration.

An appropriate selection of starting poles $a_{i,0}$ is necessary for the convergence of the vector fitting method. For a function with resonance peaks, such as the reflectance, Gustavsen & Semlyen (1999) suggest that the starting poles (complex conjugate pairs $a_{i,0} = -\alpha_{i,0} \pm j\beta_{i,0}$, with $\alpha_{i,0} = \beta_{i,0}/100$ advised) be linearly distributed over the frequency range of the data. The linear problem can become ill-conditioned if the starting poles are real. Large differences between the starting poles and the best fit poles of the response can cause large differences between $\Theta_m(s)$ and $H_m(s)$ resulting in poor least squares solutions (Gustavsen & Semlyen, 1999).

If the least squares procedure returns unstable poles ($\text{Re}\{a_{i,m}\} > 0$), their real parts are reflected to the left half s-plane before the next iteration. Due to this, the error will not always decrease monotonically with iteration. Depending on the application, it may also be beneficial to impose additional properties. For example, one might force the impedance to be minimum-phase, instead of merely stable. This could be done by inverting the real part of any zero that appears in the RHP, similar to the procedure for enforcing stability of the poles. Such a constraint may cause an increase in error, but could have utility for physical modeling.

The error depends on the starting pole values due to noise in the data. Additionally, due to the smoothness of the reflectance function and the number of available parameters, there exist multiple non-unique fits yielding reasonable fit errors (e.g. within a certain MSE tolerance). Thus the poles (of an already low error fit) may vary with iteration, resulting in non-monotonic error. Typically, significant MSE improvement over the first few iterations occurs only for low pole orders (e.g. $N_p < 10$ over a 0.1 to 10 [kHz] range). For high pole orders (e.g. $N_p > 20$ over the same range) the fitting procedure achieves close to its lowest MSE within one iteration. When the order is approximately known, as it is here, the starting poles better cover the entire frequency range, causing the fit to commonly converge within a few iterations. For low orders of poles, more iterations may be necessary to migrate the poles to their best fit locations.

APPENDIX D

MIDDLE-EAR PRESSURE STUDY DETAILS

D.1 Data labels

Measuring the reflectance, eight trials each of AMEP and NMEP conditions were similarly inter-leaved. During each trial, up to eight test-retest measurements were made, for a total of approximately 64 measurements per condition (AMEP or NMEP) in each ear. The subjects are given names beginning with 'N' (experiment order) and 'S' (final presented subjects in order of decreasing NMEP), and measurement test sets are delineated 'M01' through 'M16.' Of these 16 test sets, 8 are measured in the AMEP condition, and 8 are measured in the NMEP condition. The final number (1-8) labels each test-retest measurement. For the purposes of this appendix, the data is labeled as follows:

$$\underbrace{\text{N01}}_{\text{subject}} \quad \overbrace{\text{M01}}^{\text{test (01-16)}} \quad \underbrace{1}_{\text{retest (1-8)}}$$
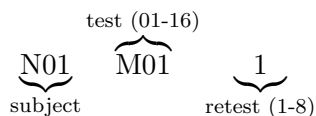
Table D.1 shows the correspondence between 'N' labels assigned by Thompson et al. (2015), and 'S' labels used in Robinson et al. (2016), which ordered the labels according to decreasing NMEP TPP.

D.2 Choosing lowest-noise measurements

To select the test-retest measurements with the least noise, we chose the measurement having the shortest path through the complex reflectance plane ($\Re\{\Gamma\}$ vs. $\Im\{\Gamma\}$). For test-retest measurements of the same insertion, this appears to be a very effective method to find the measurement with the

Table D.1: Subjects included in the NMEP study (Robinson et al., 2016) who were able to induce repeatable NMEPs, listed in order of decreasing NMEP.

S	1	2	3	4	5	6	7	8
N	11	01	04	14	08	06	13	02
μ_{NMEP} [daPa]	-65	-107	-123	-129	-156	-156	-266	-384

least noise, as it minimizes large deviations due to noise, and minimizes noise loops in the complex plane. *For varying insertions, this method may not be expressly applied, as delay due to the residual ear canal length is directly related to the path length of the complex reflectance curve.*

For comparison three de-noising criteria are proposed:

1. Complex path length in the reflectance domain (L_Γ).

2. Complex path length in the admittance domain (L_Y).

3. Closeness to the mean across frequency, where the minimum deviation from the mean is

$$\varepsilon = \min_m \sum_k |\Gamma_m(\omega_k) - \bar{\Gamma}(\omega_k)|^2 \tag{D.1}$$

for a set of test-retest measurements with indices $m = 1...M$.

Three different approaches are shown. In Figure D.1, the test-retest measurements are low noise, and appear to be similar to each other. In this case, most of the measurements appear to be acceptable for use in the data analysis. In Figure D.2, the measurements are noisy, although they do appear to be similar to each other, especially at high frequencies. From these plots, it is clear that these three methods will select some of the lowest noise measurements, but the complex length estimates L_Γ and L_Y perform best (for measurement set N04M02 they select the same curve). This makes sense, as the mean curve may be affected by large amounts of noise, especially at low frequencies. We chose to use L_Γ for measurement selection because we typically perform pole-zero fitting in the reflectance domain, and reflectance values, which are contained within the unit circle on the complex plane, have a small dynamic range across frequency and are thus more numerically stable (Robinson et al., 2013).

Finally, Figure D.3 shows an instance where the test-retest measurements do not appear to be in good agreement with each other. A few measurements are noisy, but many of the curves seem reasonably smooth. We hypothesize that two primary factors may contribute to disagreement between curves of the same test-retest set.

- *Change in middle ear condition.* In this experiment, subjects were asked to induce NMEP using the Toynbee maneuver. If a subject was unable to hold the induced pressure, the response of the system would change during measurement for the same probe insertion. In the case of Figure D.3, measurement set N04M05 was obtained in the 'normal' condition, which means (a) the subject may have experienced small changes in pressure due to normal resting state (e.g. yawning between measurements), or (b) the middle ear pressure may not have completely equalized prior to measurement and continued to change (e.g. through yawning or normal breathing between measurements)

- *Change in probe location ('drift').* The probe may have shifted slightly due to change in posture or other movement of the subject. This could produce small changes in the REC

Figure D.1: Selection of best (least noisy) measurement from the test-retest set N01M01. The measurements labeled L_Γ and L_Y are selected because they have the shortest path lengths in the complex Γ and Y planes. The measurement labeled Mean Γ is chosen because it sits the closest to the mean complex reflectance curve, across frequency. Here all 8 measurements appear to be low noise and in agreement with each other.

length between the probe and the TM. Changes in REC length have the most pronounced effects on the complex reflectance (change in phase due to differing delay), and the low-frequency absorbance level (due to losses in the ear canal). Measurements with significant noise and drift may indicate probe insertions that are not very deep (i.e. they are loose).

We conclude that this complex path length method to determine the best measurements is most effective for a set of measurements that are very similar (excepting noise), meaning that they are from the same probe insertion with a constant middle ear condition. In the future, we may be able to use the complex path length method for other applications.

D.3 Tympanometry results

Tables D.2, D.3 and D.4 give the details of the tympanograms measured by Suzanne Thompson, for each subject. Note that ears N01 and N02 (S2 and S8) were measured on two separate occasions, giving different tympanometry results for the WAI study (Robinson et al., 2016) and the DPOAE study Thompson et al. (2015). Any differences between the tympanometry results in the two studies are highlighted in red in Table D.3.
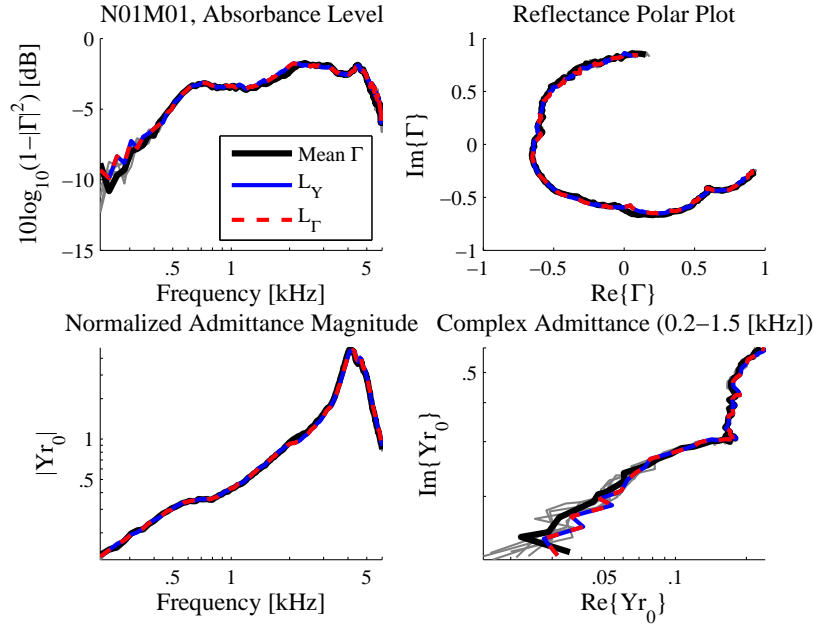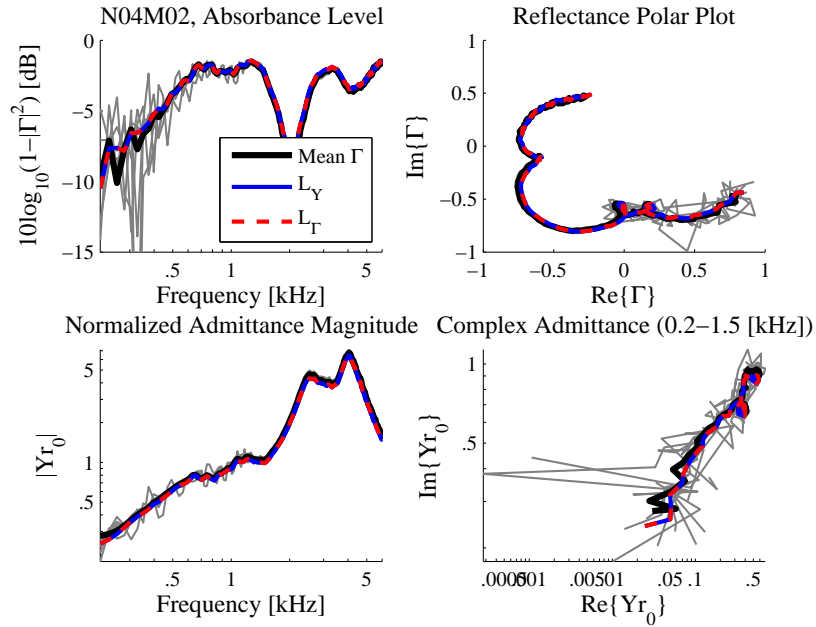
Figure D.2: Selection of best (least noisy) measurement from the test-retest set N04M02. The measurements labeled L_Γ and 'L_Y are selected because they have the shortest path lengths in the complex Γ and Y planes. The measurement labeled Mean Γ is chosen because it sits the closest to the mean complex reflectance curve, across frequency. Here many measurements are noisy, and both methods select curves that appear less noisy. The path-length determined measurements appear to be less noisy than the measurement of closest proximity to the mean.

Table D.2: Table of tympanometric results, reproduced from Thompson (2013). Note that for the WAI study, the TPPs were different for ears N01 (S2) and N02 (S8).

	Normal			NMEP		
Subject	μ_{TPP} [daPa]	σ_{TPP}	Range [daPa]	μ_{TPP} [daPa]	σ_{TPP}	Range [daPa]
N01	1	9	[-20, 5]	-271	30	[-305, 230]
N02	0	9	[-20, 25]	-324	95	[-385, -120]
N04	4	3	[0, 10]	-123	18	[-150, -90]
N06	-1	6	[-10, 5]	-157	13	[-180, -140]
N08	6	7	[0, 20]	-145	46	[-201, -55]
N11	4	4	[-5, 10]	-65	12	[-80, -50]
N13	-8	7	[-5, 0]	-262	39	[-345, 230]
N14	1	13	[-15, 20]	-129	30	[-185, -90]
Avg.	1	7	[-20, 25]	-185	35	[-385, -50]
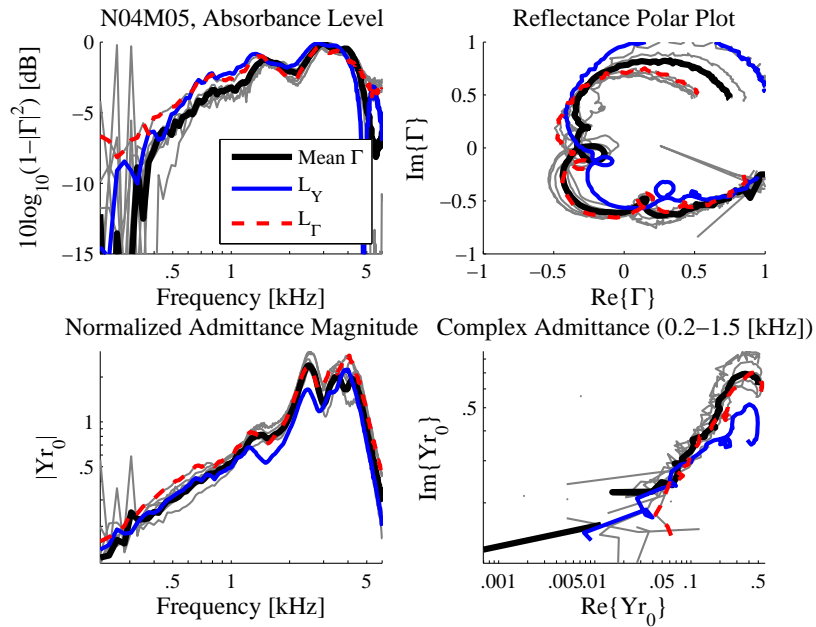
Figure D.3: Selection of best (least noisy) measurement from the test-retest set N04M05. The measurements labeled L_Γ and L_Y are selected because they have the shortest path lengths in the complex Γ and Y planes. The measurement labeled Mean Γ is chosen because it sits the closest to the mean complex reflectance curve, across frequency. Here the measurements are not in good agreement with each other. This may be due to slight changes in probe position (drift) or middle ear pressure. The three methods given are not as reliable in this instance, and all three methods select very different curves.

Table D.3: TPP Values (dPa). Values from .pdf file of tympanograms sent by Suzanne Thompson. Mean, standard deviation, and range values that differ from Table 1 are colored red; for most ears, these differences are small and may be due to differences in calculation (e.g. standard deviation normalized by N vs. N-1). The tympanometry results for ears N01 and N02 pertain only to the WAI study performed by Thompson, and thus are different from the pressures used in Thompson et al. (2015).

Ear	1	2	3	4	5	6	7	8	μ_{TPP}	σ_{TPP}	Median	Range
N01 (Normal)	0	5	-20	5	5	-5	5	0	-1	9	2.5	[-20, 5]
N02 (Normal)	5	0	0	0	5	5	-5	-5	1	4	0	[-5, 5]
N04 (Normal)	5	5	5	10	0	5	0	5	4	3	5	[0, 10]
N06 (Normal)	5	-5	-5	-10	5	0	-5	5	-1	6	-2.5	[-10, 5]
N08 (Normal)	20	5	10	10	5	0	0	0	6	7	5	[0, 20]
N11 (Normal)	10	0	(0)	(5)	5	-5	5	5	3	5	5	[-5, 10]
N13 (Normal)	5	(bad)	(bad)	-20	(bad)	-10	-5	-10	-8	9	-10	[-20, 5]
N14 (Normal)	15	-15	5	-15	10	-5	-5	20	1	13	0	[-15, 20]
N01 (NMEP)	-100	-80	-110	-145	-130	(-90)	-130	-70	-107	27	-105	[-145, -70]
N02 (NMEP)	(bad)	-385	-385	-380	-140	-385	-385	-385	-384	92	-385	[-385, -140]
N04 (NMEP)	-120	-120	-110	-140	-150	-130	-125	-90	-123	18	-122.5	[-150, -90]
N06 (NMEP)	-160	(-145)	-180	-140	-165	-160	(bad)	-145	-156	14	-160	[-180, -140]
N08 (NMEP)	-180	-135	-55	-210	-150	-120	-135	-165	-144	46	-142.5	[-210, -55]
N11 (NMEP)	-60	-80	-60	-50	-65	-65	-55	-85	-65	12	-62.5	[-85, -50]
N13 (NMEP)	(bad)	-290	-235	-260	-235	-245	-255	-345	-266	39	-255	[-345, -235]
N14 (NMEP)	-185	-90	-95	-120	-140	-130	-135	-140	-129	30	-132.5	[-185, -90]

Table D.4: C_{TM} Values (mL). Values from .pdf file of tympanograms sent by Suzanne Thompson. We compare the eardrum compliance values estimated by tympanometry to those estimated via pole-zero factorization.

Ear	1	2	3	4	5	6	7	8	$\mu_{C_{TM}}$	$\sigma_{C_{TM}}$	Median	Range
N01 (Normal)	0.7	0.5	0.5	0.4	0.5	0.5	0.7	0.7	0.56	0.12	0.5	[0.4, 0.7]
N02 (Normal)	0.6	0.6	0.7	0.7	0.6	0.6	0.6	0.7	0.64	0.05	0.6	[0.6, 0.7]
N04 (Normal)	0.9	1.0	1.0	1.0	0.8	0.8	1.0	1.2	0.96	0.13	1.0	[0.8, 1.2]
N06 (Normal)	0.5	0.6	0.6	0.6	0.5	0.5	0.5	0.9	0.59	0.14	0.55	[0.5, 0.9]
N08 (Normal)	0.9	0.8	0.7	0.9	1.0	1.0	1.0	1.0	0.91	0.11	0.95	[0.8, 1.0]
N11 (Normal)	0.6	0.6	0.7	0.6	0.6	0.6	0.6	0.5	0.6	0.05	0.6	[0.5, 0.7]
N13 (Normal)	0.4	(bad)	(bad)	0.5	(bad)	0.4	0.4	0.5	0.44	0.05	0.4	[0.4, 0.5]
N14 (Normal)	0.7	0.8	0.8	0.8	0.8	0.9	0.9	0.8	0.81	0.06	0.8	[0.7, 0.9]
N01 (NMEP)	0.8	0.5	0.5	0.5	0.5	0.5	0.6	0.6	0.56	0.11	0.5	[0.5, 0.8]
N02 (NMEP)	(bad)	0.1	0.2	0.1	0.7	0.1	0.4	0.2	0.26	0.22	0.2	[0.1, 0.7]
N04 (NMEP)	1.1	1.1	1.1	1.2	0.8	1.0	1.1	1.2	1.08	0.13	1.1	[0.8, 1.2]
N06 (NMEP)	0.5	0.5	0.5	0.6	0.5	0.5	(bad)	0.5	0.51	0.04	0.5	[0.5, 0.6]
N08 (NMEP)	0.9	1.0	1.0	0.8	0.9	1.0	1.0	0.9	0.94	0.07	0.95	[0.8, 1.0]
N11 (NMEP)	0.6	0.7	0.6	0.6	0.7	0.7	0.6	0.7	0.65	0.05	0.65	[0.6, 0.7]
N13 (NMEP)	(bad)	0.4	0.4	0.3	0.4	0.4	0.4	0.2	0.36	0.08	0.4	[0.2, 0.4]
N14 (NMEP)	0.8	0.8	0.8	0.9	0.9	0.9	0.9	1.0	0.88	0.07	0.9	[0.8, 1.0]

REFERENCES

Abur, D., Horton, N. J., & Voss, S. E. (2014). Intrasubject variability in power reflectance. *Journal of the American Academy of Audiology*, *25*(5), 441–448.

Agulló, J., Barjau, A., & Keefe, D. H. (1999). Acoustic propagation in flaring, axisymmetric horns: I. a new family of unidimensional solutions. *Acta Acustica United with Acustica*, *85*(2), 278–284.

Agulló, J., Barjau, A., & Martínez, J. (1988). Alternatives to the impulse response h(t) to describe the acoustical behavior of conical ducts. *The Journal of the Acoustical Society of America*, *84*(5), 1606–1612.

Allen, J. B. (1986). Measurement of eardrum acoustic impedance. *Peripheral Auditory Mechanisms*, 44–51.

Allen, J. B. (2016). *An Invitation to Mathematical Physics and its History.* Retrieved 2017-09-24, from `http://jontalle.web.engr.illinois.edu/uploads/298/anInvitation.pdf`

Allen, J. B., Jeng, P. S., & Levitt, H. (2005). Evaluation of human middle ear function via an acoustic power assessment. *Journal of Rehabilitation Research & Development*, *42*, 63–78.

Allen, J. B., & Sondhi, M. M. (1979). Cochlear macromechanics: Time domain solutions. *The Journal of the Acoustical Society of America*, *66*(1), 123–132.

Amir, N., Shimony, U., & Rosenhouse, G. (1995). A discrete model for tubular acoustic systems with varying cross section–the direct and inverse problems. part 1: theory. *Acta Acustica United with Acustica*, *81*(5), 450–462.

Aron, M., Floyd, D., & Bance, M. (2015). Voluntary eardrum movement: A marker for tensor tympani contraction? *Otology & Neurotology*, *36*(2), 373–381.

Atkinson, K. E., & Shampine, L. F. (2008). Algorithm 876: Solving fredholm integral equations of the second kind in matlab. *ACM Transactions on Mathematical Software (TOMS)*, *34*(4), 1–20. (Article 21)

Bance, M., Makki, F. M., Garland, P., Alian, W. A., van Wijhe, R. G., & Savage, J. (2013). Effects of tensor tympani muscle contraction on the middle ear and markers of a contracted muscle. *The Laryngoscope*, *123*(4), 1021–1027.

Benade, A. H. (1968). On the propagation of sound waves in a cylindrical conduit. *The Journal of the Acoustical Society of America*, *44*(2), 616–623.

Benade, A. H. (1988). Equivalent circuits for conical waveguides. *The Journal of the Acoustical Society of America*, *83*(5), 1764–1769.

Beranek, L. L., & Mellow, T. J. (2012). *Acoustics: Sound Fields and Transducers.* Academic Press.

Bluestone, C. D., & Klein, J. O. (2007). *Otitis Media in Infants and Children.* People's Medical Publishing House - USA.

Brune, O. (1931). Synthesis of a finite two-terminal network whose driving-point impedance is a prescribed function of frequency. *Studis in Applied Mathematics*, *10*, 191–236.

Burdiek, L. M., & Sun, X. M. (2014). Effects of consecutive wideband tympanometry trials on energy absorbance measures of the middle ear. *Journal of Speech, Language, and Hearing Research*, *57*(5), 1997–2004.

Caflisch, R. E. (1981). An inverse problem for toeplitz matrices and the synthesis of discrete transmission lines. *Linear Algebra and its Applications*, *38*, 207–225.

Campbell, G. A. (1922). Physical theory of the electric wave filter. *Bell System Technical Journal*, *1*(2), 1–32.

Charaziak, K. K., & Shera, C. A. (2017). Compensating for ear-canal acoustics when measuring otoacoustic emissions. *The Journal of the Acoustical Society of America*, *141*(1), 515–531.

Claerbout, J. F. (1985). *Fundamentals of Geophysical Data Processing.* Blackwell Scientific Publications.

Fallon, J. B., Irvine, D. R. F., & Shepherd, R. K. (2008). Cochlear implants and brain plasticity. *Hearing Research*, *238*(1), 110–117.

Farmer-Fedor, B. L., & Rabbitt, R. D. (2002). Acoustic intensity, impedance and reflection coefficient in the human ear canal. *The Journal of the Acoustical Society of America*, *112*, 600–620.

Feeney, M. P., Grant, I. L., & Marryott, L. P. (2003). Wideband energy reflectance measurements in adults with middle-ear disorders. *Journal of Speech, Language, and Hearing Research*, *46*(4), 901–911.

Feeney, M. P., Hunter, L. L., Kei, J., Lilly, D. J., Margolis, R. H., Nakajima, H. H., ... others (2013). Consensus statement: Eriksholm workshop on wideband absorbance measures of the middle ear. *Ear and Hearing*, *34*, 78s–79s.

Feeney, M. P., & Keefe, D. H. (1999). Acoustic reflex detection using wide-band acoustic reflectance, admittance, and power measurements. *Journal of Speech, Language, and Hearing Research*, *42*(5), 1029–1041.

Feeney, M. P., & Keefe, D. H. (2001). Estimating the acoustic reflex threshold from wideband measures of reflectance, admittance, and power. *Ear and Hearing*, *22*(4), 316–332.

Feeney, M. P., Keefe, D. H., & Marryott, L. P. (2003). Contralateral acoustic reflex thresholds for tonal activators using wideband energy reflectance and admittance. *Journal of Speech, Language, and Hearing Research*, *46*(1), 128–136.

Feeney, M. P., Keefe, D. H., & Sanford, C. A. (2004). Wideband reflectance measures of the ipsilateral acoustic stapedius reflex threshold. *Ear and Hearing*, *25*(5), 421–430.

Goll, E., & Dalhoff, E. (2011). Modeling the eardrum as a string with distributed force. *The Journal of the Acoustical Society of America*, *130*(3), 1452–1462.

Gopinath, B., & Sondhi, M. M. (1971). Inversion of the telegraph equation and the synthesis of nonuniform lines. *Proceedings of the IEEE*, *59*(3), 383–392.

Groon, K. A., Rasetshwane, D. M., Kopun, J. G., Gorga, M. P., & Neely, S. T. (2015). Air-leak effects on ear-canal acoustic absorbance. *Ear and Hearing*, *36*(1), 155–163.

Grüneisen, E., & Merkel, E. (1922). Schallgeschwindigkeit in luft und wasserstoff von 0 c. und 1 atm. *Annalen der Physik*, *371*(21), 344–364.

Gustavsen, B., & Semlyen, A. (1999). Rational approximation of frequency domain responses by vector fitting. *Power Delivery, IEEE Transactions on*, *14*(3), 1052–1061.

Haghighatshoar, S., Taghizadeh, M. J., & Asaei, A. (2015). A new identity for the least-square solution of overdetermined set of linear equations. *arXiv preprint arXiv:1502.07695*.

Helmholtz, H. (1863). On the influence of friction in the air on sound motion. *Verhandl. Naturhist. Med. Ver. Heidelberg*, *3*, 16–20.

Holmquist, J., & Olen, L. (1980). Evaluation of Eustachian tube function. *The Journal of Laryngology & Otology*, *94*(01), 15–23.

Honjo, I., Kumazawa, T., & Honda, K. (1981). Simple impedance test for Eustachian tube function. *Archives of Otolaryngology*, *107*(4), 221–223.

Hunt, F. V. (1954). *Electroacoustics: The Analysis of Transduction, and its Historical Background*. Acoustical Society of America.

Hunter, L. L., Feeney, M. P., Lapsley Miller, J. A., Jeng, P. S., & Bohning, S. (2010). Wideband reflectance in newborns: Normative regions and relationship to hearing-screening results. *Ear and Hearing*, *31*(5), 599–610.

Karal, F. C. (1953). The analogous acoustical impedance for discontinuities and constrictions of circular cross section. *The Journal of the Acoustical Society of America*, *25*(2), 327–334.

Kartan, S. (2013). *Green's function derivations for specific acoustic admittances and impedances*. Urbana, IL: University of Urbana Champaign. (MS Thesis)

Keefe, D. H. (1984). Acoustical wave propagation in cylindrical ducts: Transmission line parameter approximations for isothermal and nonisothermal boundary conditions. *The Journal of the Acoustical Society of America*, *75*(1), 58–62.

Keefe, D. H. (1996). Wind-instrument reflection function measurements in the time domain. *The Journal of the Acoustical Society of America*, *99*(4), 2370–2381.

Keefe, D. H. (2015a). Acoustical transmission-line model of the middle-ear cavities and mastoid air cells. *The Journal of the Acoustical Society of America*, *137*(4), 1877–1887.

Keefe, D. H. (2015b). Human middle-ear model with compound eardrum and airway branching in mastoid air cells. *The Journal of the Acoustical Society of America*, *137*(5), 2698–2725.

Keefe, D. H., & Barjau, A. (1999). Acoustic propagation in flaring, axisymmetric horns: Ii. numerical results, wkb theory, and viscothermal effects. *Acta Acustica United with Acustica*, *85*(2), 285–293.

Keefe, D. H., & Benade, A. H. (1983). Wave propagation in strongly curved ducts. *The Journal of the Acoustical Society of America*, *74*(1), 320–332.

Keefe, D. H., Bulen, J. C., Arehart, K. H., & Burns, E. M. (1993). Ear-canal impedance and reflection coefficient in human infants and adults. *The Journal of the Acoustical Society of America*, *94*, 2617–2638.

Keefe, D. H., Hunter, L. L., Feeney, M. P., & Fitzpatrick, D. F. (2015). Procedures for ambient-pressure and tympanometric tests of aural acoustic reflectance and admittance in human infants and adults. *The Journal of the Acoustical Society of America*, *138*(6), 3625–3653.

Keefe, D. H., Ling, R., & Bulen, J. C. (1992). Method to measure acoustic impedance and reflection coefficient. *The Journal of the Acoustical Society of America*, *91*, 470–485.

Keefe, D. H., Sanford, C. A., Ellison, J. C., Fitzpatrick, D. F., & Gorga, M. P. (2012). Wideband aural acoustic absorbance predicts conductive hearing loss in children. *International Journal of Audiology*, *51*(12), 880–891.

Keefe, D. H., & Simmons, J. L. (2003). Energy transmittance predicts conductive hearing loss in older children and adults. *The Journal of the Acoustical Society of America*, *114*, 3217–3238.

Kei, J., Sanford, C. A., Prieve, B. A., & Hunter, L. L. (2013). Wideband acoustic immittance measures: Developmental characteristics (0 to 12 months). *Ear and Hearing*, *34*, 17s–26s.

Kim, N., & Allen, J. B. (2013). Two-port network analysis and modeling of a balanced armature receiver. *Hearing Research*, *301*, 156–167.

Kirchhoff, G. (1868). On the influence of heat conduction in a gas on sound propagation. *Ann. Phys. Chem.*, *134*, 177–193.

Kringlebotn, M. (1988). Network model for the human middle ear. *Scandinavian Audiology*, *17*(2), 75–85.

Kulik, Y. (2007). Transfer matrix of conical waveguides with any geometric parameters for increased precision in computer modeling. *The Journal of the Acoustical Society of America*, *122*(5), EL179–EL184.

Kusse, B. R., & Westwig, E. A. (2010). *Mathematical Physics: Applied Mathematics for Scientists and Engineers*. John Wiley & Sons.

Lapsley Miller, J., Reed, C., Robinson, S., Perez, Z., & Jeng, P. (2017). Pure-tone audiometry with forward-pressure level calibration leads to clinically-relevant improvements in test-retest reliability. *Ear and Hearing*. (under review)

Lauxmann, M., Eiber, A., Haag, F., & Ihrle, S. (2014). Nonlinear stiffness characteristics of the annular ligament. *The Journal of the Acoustical Society of America*, *136*(4), 1756–1767.

Lewis, J. D., McCreery, R. W., Neely, S. T., & Stelmachowicz, P. G. (2009). Comparison of in-situ calibration methods for quantifying input to the middle ear. *The Journal of the Acoustical Society of America*, *126*(6), 3114–3124.

Lewis, J. D., & Neely, S. T. (2015). Non-invasive estimation of middle-ear input impedance and efficiencya). *The Journal of the Acoustical Society of America*, *138*(2), 977–993.

Lundberg, K. H., Miller, H. R., & Trumper, R. L. (2007). Initial conditions, generalized functions, and the laplace transform: Troubles at the origin. *IEEE Control Systems Magazine*, *27*(1), 22–35.

Lynch, T. J., Nedzelnitsky, V., & Peake, W. T. (1982). Input impedance of the cochlea in cat. *The Journal of the Acoustical Society of America*, *72*(1), 108–130.

Mapes-Riordan, D. (1993). Horn modeling with conical and cylindrical transmission-line elements. *Journal of the Audio Engineering Society*, *41*(6), 471–484.

Marshall, L., Heller, L. M., & Westhusin, L. J. (1997). Effect of negative middle-ear pressure on transient-evoked otoacoustic emissions. *Ear and Hearing*, *18*(3), 218–226.

Mason, W. (1928). The propagation characteristics of sound tubes and acoustic filters. *Physical Review*, *31*(2), 283–295.

Mason, W. P. (1927). A study of the regular combination of acoustic elements, with applications to recurrent acoustic filters, tapered acoustic filters, and horns. *Bell System Technical Journal*, *6*(2), 258–294.

McCreery, R. W., Pittman, A., Lewis, J., Neely, S. T., & Stelmachowicz, P. G. (2009). Use of forward pressure level to minimize the influence of acoustic standing waves during probe-microphone hearing-aid verification. *The Journal of the Acoustical Society of America*, *126*(1), 15–24.

Mermelstein, P. (1967). Determination of the vocal-tract shape from measured formant frequencies. *The Journal of the Acoustical Society of America*, *41*(5), 1283–1294.

Milazzo, M., Fallah, E., Carapezza, M., Kumar, N. S., Lei, J. H., & Olson, E. S. (2017). The path of a click stimulus from ear canal to umbo. *Hearing Research*, *346*, 1–13.

Miles, J. W. (1947). The diffraction of sound due to right-angled joints in rectangular tubes. *The Journal of the Acoustical Society of America*, *19*(4), 572–579.

Miller, D. A. B. (1991). Huygens's wave propagation principle corrected. *Optics Letters*, *16*(18), 1370–1372.

Møller, A. R. (1960). Improved technique for detailed measurements of the middle ear impedance. *The Journal of the Acoustical Society of America*, *32*(2), 250–257.

Møller, A. R. (1961). Network model of the middle ear. *The Journal of the Acoustical Society of America*, *33*(2), 168–176.

Møller, A. R. (1983). *Auditory Physiology*. New York, New York: Academic Press, Inc.

Monroy, G. L., Shelton, R. L., Nolan, R. M., Nguyen, C. T., Novak, M. A., Hill, M. C., ... Boppart, S. A. (2015). Noninvasive depth-resolved optical measurements of the tympanic membrane and middle ear for differentiating otitis media. *The Laryngoscope*, *125*(8), E276–E282.

Mukerji, S., Windsor, A. M., & Lee, D. J. (2010). Auditory brainstem circuits that mediate the middle ear muscle reflex. *Trends in Amplification*, 170–191.

Murakami, S., Gyo, K., & Goode, R. L. (1997). Effect of middle ear pressure change on middle ear mechanics. *Acta Oto-Laryngologica*, *117*(3), 390–395.

Myers, E. N., Murakami, S., Gyo, K., Goode, R. L., et al. (1998). Effect of increased inner ear pressure on middle ear mechanics. *Otolaryngology–Head and Neck Surgery*, *118*(5), 703–708.

Nakajima, H. H., Pisano, D. V., Roosli, C., Hamade, M. A., Merchant, G. R., Mahfoud, L., ... Merchant, S. N. (2012). Comparison of ear-canal reflectance and umbo velocity in patients with conductive hearing loss: A preliminary study. *Ear and Hearing*, *33*(1), 35–43.

Neely, S. T., & Gorga, M. P. (1998). Comparison between intensity and pressure as measures of sound level in the ear canal. *The Journal of the Acoustical Society of America*, *104*(5), 2925–2934.

Nguyen, C. T., Jung, W., Kim, J., Chaney, E. J., Novak, M., Stewart, C. N., & Boppart, S. A. (2012). Noninvasive in vivo optical detection of biofilm in the human middle ear. *Proceedings of the National Academy of Sciences*, *109*(24), 9529–9534.

Nguyen, C. T., Robinson, S. R., Jung, W., Novak, M. A., Boppart, S. A., & Allen, J. B. (2013). Investigation of bacterial biofilm in the human middle ear using optical coherence tomography and acoustic measurements. *Hearing Research*, *301*, 193–200.

Nguyen, C. T., Tu, H., Chaney, E. J., Stewart, C. N., & Boppart, S. A. (2010). Non-invasive optical interferometry for the assessment of biofilm growth in the middle ear. *Biomedical Optics Express*, *1*(4), 1104–1116.

O'Connor, K. N., & Puria, S. (2008). Middle-ear circuit model parameters based on a population of human ears. *The Journal of the Acoustical Society of America*, *123*(1), 197–211.

Onchi, Y. (1949). A study of the mechanism of the middle ear. *The Journal of the Acoustical Society of America*, *21*(4), 404–410.

Pang, X. D., & Peake, W. T. (1986). How do contractions of the stapedius muscle alter the acoustic properties of the ear? In *Peripheral Auditory Mechanisms* (pp. 36–43). Springer.

Parent, P., & Allen, J. B. (2007). Wave model of the cat tympanic membrane. *The Journal of the Acoustical Society of America*, *122*(2), 918–931.

Parent, P., & Allen, J. B. (2010). Time-domain "wave" model of the human tympanic membrane. *Hearing Research*, *263*(1-2), 152–167.

Pascal, J., Bourgeade, A., Lagier, M., & Legros, C. (1998). Linear and nonlinear model of the human middle ear. *The Journal of the Acoustical Society of America*, *104*(3), 1509–1516.

Pierce, A. D. (1981). *Acoustics: An Introduction to its Physical Principles and Applications*. McGraw-Hill New York.

Prieve, B. A., Calandruccio, L., Fitzgerald, T., Mazevski, A., & Georgantas, L. M. (2008). Changes in transient-evoked otoacoustic emission levels with negative tympanometric peak pressure in infants and toddlers. *Ear and Hearing*, *29*(4), 533–542.

Prieve, B. A., Vander Werff, K. R., Preston, J. L., & Georgantas, L. (2013). Identification of conductive hearing loss in young infants using tympanometry and wideband reflectance. *Ear and Hearing*, *34*(2), 168–178.

Puria, S. (1991). *A theory of cochlear input impedance and middle ear parameter estimation.* New York, NY: City University of New York. (PhD Thesis)

Puria, S., & Allen, J. B. (1998). Measurements and model of the cat middle ear: evidence of tympanic membrane acoustic delay. *The Journal of the Acoustical Society of America*, *104*, 3463–3481.

Rabinowitz, W. M. (1981). Measurement of the acoustic input immittance of the human ear. *The Journal of the Acoustical Society of America*, *70*, 1025–1035.

Ramo, S., Whinnery, J. R., & Van Duzer, T. (2008). *Fields and Waves in Communication Electronics.* John Wiley & Sons.

Rasetshwane, D. M., & Neely, S. T. (2011). Inverse solution of ear-canal area function from reflectance. *The Journal of the Acoustical Society of America*, *130*(6), 3873–3881.

Rasetshwane, D. M., & Neely, S. T. (2015). Reflectance measurement validation using acoustic horns. *The Journal of the Acoustical Society of America*, *138*(4), 2246–2255.

Rasetshwane, D. M., Neely, S. T., Allen, J. B., & Shera, C. A. (2012). Reflectance of acoustic horns and solution of the inverse problem. *The Journal of the Acoustical Society of America*, *131*(3), 1863–1873.

Rayleigh. (1896). *The Theory of Sound, Volume 2.* (J. W. Strutt, Third Baron Rayleigh. Reprinted (1945), Dover, New York)

Recio-Spinoso, A., Fan, Y., & Ruggero, A. (2011). Basilar-membrane responses to broadband noise modeled using linear filters with rational transfer functions. *IEEE Transactions on Biomedical Engineering*, *58*(5), 1456–1465.

Richards, W. B. (1986). Propagation of sound waves in tubes of noncircular cross section. *NASA TP 2601*, 1–30.

Robinson, S. R. (2013). *Characterizing middle ear reflectance via pole-zero fitting.* Urbana, IL: University of Urbana Champaign. (MS Thesis)

Robinson, S. R., Nguyen, C. T., & Allen, J. B. (2013). Characterizing the ear canal acoustic impedance and reflectance by pole-zero fitting. *Hearing Research*, *301*, 168–182.

Robinson, S. R., Thompson, S., & Allen, J. B. (2016). Effects of negative middle ear pressure on wideband acoustic immittance in normal-hearing adults. *Ear and Hearing*, *37*(4), 452–464.

Rodriguez, S., Gibiat, V., Lefebvre, A., & Guilain, S. (2011). The three-measurement two-calibration method for measuring the transfer matrix. *The Journal of the Acoustical Society of America*, *129*(5), 3056–3067.

Rosowski, J. J., Carney, L. H., Lynch III, T. J., & Peake, W. T. (1986). The effectiveness of external and middle ears in coupling acoustic power into the cochlea. In *Peripheral Auditory Mechanisms* (pp. 3–12). Springer.

Rosowski, J. J., Nakajima, H. H., Hamade, M. A., Mahfoud, L., Merchant, G. R., Halpin, C. F., & Merchant, S. N. (2012). Ear-canal reflectance, umbo velocity, and tympanometry in normal-hearing adults. *Ear and Hearing*, *33*(1), 19–34.

Rronenberg, J., Ben-Shoshan, J., & Wolf, M. (1993). Perforated tympanic membrane after blast injury. *Otology & Neurotology*, *14*(1), 92–94.

Schairer, K. S., Ellison, J. C., Fitzpatrick, D., & Keefe, D. H. (2007). Wideband ipsilateral measurements of middle-ear muscle reflex thresholds in children and adultsa). *The Journal of the Acoustical Society of America*, *121*(6), 3607–3616.

Scheperle, R. A., Goodman, S. S., & Neely, S. T. (2011). Further assessment of forward pressure level for in situ calibration. *The Journal of the Acoustical Society of America*, *130*(6), 3882–3892.

Scheperle, R. A., Neely, S. T., Kopun, J. G., & Gorga, M. P. (2008). Influence of in situ, sound-level calibration on distortion-product otoacoustic emission variability. *The Journal of the Acoustical Society of America*, *124*, 288–300.

Schroeder, M. R. (1967). Determination of the geometry of the human vocal tract by acoustic measurements. *The Journal of the Acoustical Society of America*, *41*(4B), 1002–1010.

Sessler, G. M., & West, J. E. (1962). Self-biased condenser microphone with high capacitance. *The Journal of the Acoustical Society of America*, *34*(11), 1787–1788.

Shahnaz, N., Bork, K., Polka, L., Longridge, N., Bell, D., & Westerberg, B. D. (2009). Energy reflectance and tympanometry in normal and otosclerotic ears. *Ear and Hearing*, *30*(2), 219–233.

Shanks, J. E., & Lilly, D. J. (1981). An evaluation of tympanometric estimates of ear canal volume. *Journal of Speech, Language, and Hearing Research*, *24*(4), 557–566.

Shanks, J. E., Lilly, D. J., Margolis, R. H., Wiley, T. L., & Wilson, R. H. (1988). Tympanometry. *Journal of Speech and Hearing Disorders*, *53*(4), 354–377.

Shanks, J. E., & Shohet, J. (2009). Tympanometry in clinical practice. *Handbook of Clinical Audiology*, 157–188.

Shaver, M. D., & Sun, X. M. (2013). Wideband energy reflectance measurements: effects of negative middle ear pressure and application of a pressure compensation procedure. *The Journal of the Acoustical Society of America*, *134*(1), 332–341.

Shaw, E. A. G. (1977). Eardrum representation in middle-ear acoustical networks. *The Journal of the Acoustical Society of America*, *62*(S1), S12–S12.

Shaw, E. A. G. (1980). The acoustics of the external ear. *Acoustical Factors Affecting Hearing Aid Performance*, 3–24.

Shaw, E. A. G., & Stinson, M. R. (1981). Network concepts and energy flow in the human middle-ear. *The Journal of the Acoustical Society of America*, *69*(S1), S43–S43.

Shaw, E. A. G., & Stinson, M. R. (1983). The human external and middle ear: Models and concepts. In *Mechanics of Hearing* (pp. 3–10). Springer.

Shera, C. A., & Zweig, G. (1991). Phenomenological characterization of eardrum transduction. *The Journal of the Acoustical Society of America*, *90*(1), 253–262.

Siegel, J. H. (1994). Ear-canal standing waves and high-frequency sound calibration using otoacoustic emission probes. *The Journal of the Acoustical Society of America*, *95*(5), 2589–2597.

Simmons, L. F. G., & Johansen, F. C. (1925). On the transmission of air-waves through pipes. *The London, Edinburgh, and Dublin Philosophical Magazine and Journal of Science*, *50*(297), 553–570.

Sondhi, M. M. (1983). An improved vocal tract model. In *Proceedings of the 11th ica* (Vol. 4, pp. 167–170).

Sondhi, M. M., & Gopinath, B. (1971). Determination of vocal-tract shape from impulse response at the lips. *The Journal of the Acoustical Society of America*, *49*(6B), 1867–1873.

Sondhi, M. M., & Resnick, J. R. (1983). The inverse problem for the vocal tract: Numerical methods, acoustical experiments, and speech synthesis. *The Journal of the Acoustical Society of America*, *73*(3), 985–1002.

Souza, N. N., Dhar, S., Neely, S. T., & Siegel, J. H. (2014). Comparison of nine methods to estimate ear-canal stimulus levels. *The Journal of the Acoustical Society of America*, *136*(4), 1768–1787.

Staelin, D. H., Morgenthaler, A. W., & Kong, J. A. (1998). *Electromagnetic Waves*. Upper Saddle River, NJ: Prentice-Hall, Inc.

Stepp, C. E., & Voss, S. E. (2005). Acoustics of the human middle-ear air space. *The Journal of the Acoustical Society of America*, *118*, 861–871.

Stevens, E. H. (1902). Ueber schallgeschwindigkeit in luft bei gewöhnlicher und bei hoher temperatur und in verschiedenen dämpfen. *Annalen der Physik*, *312*(2), 285–320.

Stinson, M. R. (1991). The propagation of plane sound waves in narrow and wide circular tubes, and generalization to uniform tubes of arbitrary cross-sectional shape. *The Journal of the Acoustical Society of America*, *89*(2), 550–558.

Stinson, M. R., & Lawton, B. W. (1989). Specification of the geometry of the human ear canal for the prediction of sound-pressure level distribution. *The Journal of the Acoustical Society of America*, *85*(6), 2492–2503.

Stokes, G. G. (1845). On the theories of internal friction of fluids in motion. *Trans. Camb. Philos. Soc.*, *8*, 287–305.

Sun, X. M., & Shaver, M. D. (2009). Effects of negative middle ear pressure on distortion product otoacoustic emissions and application of a compensation procedure in humans. *Ear and Hearing*, *30*(2), 191–202.

Thompson, S. (2013). *Impact of negative middle ear pressure on distortion product otoacoustic emissions*. New York, NY: City University of New York. (PhD Thesis)

191

Thompson, S., Henin, S., & Long, G. R. (2015). Negative middle ear pressure and composite and component distortion product otoacoustic emissions. *Ear and Hearing*, *36*(6), 695–704.

Tideholm, B., Carlborg, B., Jönsson, S., & Bylander-Groth, A. (1998). Continuous long-term measurements of the middle ear pressure in subjects without a history of ear disease. *Acta Oto-Laryngologica*, *118*(3), 369–374.

Vanhuyse, V. J., Creten, W. L., & Van Camp, K. J. (1975). On the w-notching of tympanograms. *Scandinavian Audiology*, *4*(1), 45–50.

Van Rhijn, A. (2003). Integrated circuits for high performance electret microphones. In *Audio Engineering Society Convention 114.*

Van Valkenburg, M. E. (1960). *Introduction to Modern Network Synthesis.* New York, NY: John Wiley and Sons.

Van Valkenburg, M. E. (1964). *Modern Network Synthesis.* New York, NY: John Wiley & Sons, Inc.

Voss, S. E., & Allen, J. B. (1994). Measurement of acoustic impedance and reflectance in the human ear canal. *The Journal of the Acoustical Society of America*, *95*, 372–384.

Voss, S. E., Horton, N. J., Woodbury, R. R., & Sheffield, K. N. (2008). Sources of variability in reflectance measurements on normal cadaver ears. *Ear and Hearing*, *29*(4), 651–665.

Voss, S. E., Merchant, G. R., & Horton, N. J. (2012). Effects of middle-ear disorders on power reflectance measured in cadaveric ear canals. *Ear and Hearing*, *33*(2), 195–208.

Voss, S. E., Rosowski, J. J., Merchant, S. N., & Peake, W. T. (2000). Acoustic responses of the human middle ear. *Hearing Research*, *150*(1-2), 43–69.

Voss, S. E., Rosowski, J. J., Merchant, S. N., & Peake, W. T. (2001). Middle-ear function with tympanic-membrane perforations. ii. a simple model. *The Journal of the Acoustical Society of America*, *110*, 1445-1452.

Voss, S. E., Stenfelt, S., Neely, S. T., & Rosowski, J. J. (2013). Factors that introduce intrasubject variability into ear-canal absorbance measurements. *Ear and Hearing*, *34*, 60s–64s.

Webster, A. G. (1919). Acoustical impedance and the theory of horns and of the phonograph. *Proceedings of the National Academy of Sciences*, *5*(7), 275–282.

Weece, R., & Allen, J. (2010). A method for calibration of bone driver transducers to measure the mastoid impedance. *Hearing Research*, *263*(1), 216–223.

Wegel, R., & Lane, C. (1924). The auditory masking of one pure tone by another and its probable relation to the dynamics of the inner ear. *Physical Review*, *23*(2), 266–285.

Withnell, R. H., Jeng, P. S., Waldvogel, K., Morgenstein, K., & Allen, J. B. (2009). An in situ calibration for hearing thresholds. *The Journal of the Acoustical Society of America*, *125*, 1605-1611.

Youla, D. (1964). Analysis and synthesis of arbitrarily terminated lossless nonuniform lines. *IEEE Transactions on Circuit Theory*, *11*(3), 363–371.

Zwislocki, J. (1953). Acoustic attenuation between the ears. *The Journal of the Acoustical Society of America*, *25*, 752–759.

Zwislocki, J. (1957). Some impedance measurements on normal and pathological ears. *The Journal of the Acoustical Society of America*, *29*, 1312–1317.

Zwislocki, J. (1962). Analysis of the middle-ear function. part i: Input impedance. *The Journal of the Acoustical Society of America*, *34*, 1514–1523.